Boiling on a Tube Bundle:
Heat Transfer, Pressure Drop and Flow Patterns

PAR

Francesco AGOSTINI

laurea in ingegneria meccanica, Università degli studi di Bergamo, Dalmine, Italie
et de nationalité italienne

ÉCOLE POLYTECHNIQUE
FÉDÉRALE DE LAUSANNE

Suisse
2008

To Angelo, Lucia and Nicoló

"Oltre il fiume,
Oltre il confine,
Oltre ogni oltre,
Vai senza timore"

Abstract

The complexity of the two-phase flow in a tube bundle presents important problems in the design and understanding of the physical phenomena taking place. The working conditions of an evaporator depend largely on the dynamics of the two-phase flow that in turn influence the heat exchange and the pressure drop of the system. A characterization of the flow dynamics, and possibly the identification of the flow pattern in the tube bundle, in thus expected to lead to a better understanding of the phenomena and to reveal on the mechanisms governing the tube bundle. Therefore, the present study aims at providing further insights into two-phase bundle flow through a new visualization system able to provide for the first time a view of the flow in the core of a tube bundle. In addition, the measurement of the light attenuation of a laser beam through the two-phase flow and measurement of the high frequency pressure fluctuations with a piezo-electric pressure transducer are used to characterize the flow. The design and the validation of this new instrumentation also provided a method for the detection of dry-out in tube bundles. This was achieved by a laser attenuation technique, flow visualization, and estimation of the power spectrum of the pressure fluctuation. The current investigation includes results for two different refrigerants, R134a and R236fa, three saturations temperatures $T_{sat} = 5$, 10 and 15 °C, mass velocities ranging from 4 to $40\,kg/sm^2$ in adiabatic and diabatic conditions (several heat fluxes). Measurement of the local heat transfer coefficient and two-phase frictional pressure drop were obtained and utilized to improve the current prediction methods. The heat transfer and pressure drop data were supported by extensive characterization of the two-phase flow, which was to improve the understanding of the two-phase flow occurring in tube bundles.

Keywords: bundle boiling, pool boiling, heat transfer, two-phase flow, visualization, pressure drop, spectral analysis, Wilson Plot

Version Abrégée

La complexité des écoulements diphasiques au sein d'un faisceau de tubes soulève de nombreux problèmes de compréhension des phénomènes physiques y prenant place, et par suite, de dimensionnement. Les conditions de fonctionnement d'un évaporateur sont fortement liées à la dynamique de l'écoulement diphasiques qui influence le transfert de chaleur et les pertes de pression dans le système. La caractérisation de la dynamique de l'écoulement et l'identification des régimes d'écoulement permettent une meilleure compréhension des phénomènes et mécanismes physiques dominant le faisceau. Cette étude présente des résultats obtenus au moyen d'une nouvelle technique de visualisation permettant d'observer pour la première fois l'écoulement directement au sein du faisceau. De plus, des mesures par atténuation de l'intensité lumineuse d'un laser, associées à des mesures des fluctuations de pression à hautes fréquences obtenues au moyen d'un capteur piézo-électrique permettent de caractériser l'écoulement. Cette approche permet la détection de l'assèchement dans les faisceaux de tubes par l'utilisation d'une technique d'atténuation de l'intensité lumineuse d'un laser, la visualisation des écoulements et l'estimation de la puissance spectrale des fluctuations de pression. La présente étude couvre deux différents réfrigérants, R134a et R236fa, trois températures de saturation, $T_{sat} = 5$, 10 and 15 °C, des vitesses surfaciques massiques comprises entre 4 et $40\,kg/sm^2$ et une large gamme de flux de chaleur (conditions adiabatiques et diabatiques). Des mesures locales du coefficient de transfert de chaleur et des pertes de pression diphasiques par frottement ont été réalisées et mises en parallèle avec l'étude approfondie des caractéristiques de l'écoulement double phase. Cette étude permet d'améliorer la compréhension des régimes d'écoulement diphasiques à l'intérieur des faisceaux de tubes ainsi que les méthodes de prédiction.

Mots clés: ébullition en faisceau, ébullition en vase, transfert de chaleur, écoulement diphasique, visualisation, pertes de pression, analyse spectrale, Méthode de Wilson.

Acknowledgements

I would like to express my gratitude to my thesis committee, Prof. Rakesh Chawla, EPFL, Prof. John R. Thome, EPFL, who gave me the opportunity to perform this investigation at EPFL, Prof. Anthony M. Jacobi, University of Illinois, and Prof. Gherhardt Ribatski, Universidade de São Paulo.
My gratitude goes to all those people who contributed in different ways to this thesis, special thanks to Dr. Navid Borhani and to Laurent Chevalley.

Above all I would like to thank all my friends, my family and the "great schatzi" for their unremitting support, affection and love. Thank you for the happiness you bring around me!

Francesco Siddharta Luigi Agostini
Lausanne, May 2008

Contents

List of Figures

List of Tables

Nomenclature

Greek letters

α	Heat transfer coefficient	$[W/m^2K]$
Δ	Difference	$[-]$
δ	Film thickness	$[mm]$
λ	Dimensionless mass velocity	$[-]$
λ	Friction factor multiplier	$[-]$
λ	Thermal conductivity	$[W/mK]$
λ	Wave length	$[nm]$
μ	Dynamic viscosity	$[kg/m.s]$
ρ	Density	$[kg/m^3]$
σ	Surface tension	$[N/m]$
σ	Variance	
τ	Time lag	$[s]$
ε	Void fraction	$[-]$
ξ	Dimensionless parameter	$[-]$

Roman letters

$\dot{m}$	Mass flow rate	$[kg/s]$
$\dot{V}_G$	Volumetric flow rate	$[m^3/s]$
$\dot{V}$	Volumetric flow rate	$[m^3/s]$
A	Area	$[m^2]$
Bo	Bond number	$[-]$
c_p	Specific heat at constant pressure	$[J/kgK]$
Cap	Capillary number	$[-]$
D	Diameter	$[mm]$
d	Axial distance	$[mm]$
Eu	Euler number	$[-]$
f	Frequency	$[Hz]$

f	Friction factor	
Fr	Froude number	$[-]$
G	Mass flux	$[kg/s.m^2]$
g	Gravity acceleration	$[m/s^2]$
GOD	Goodness of fit	
h	Enthalpy	$[J/kg]$
h	Height	$[mm]$
j	Superficial velocity	$[m/s]$
Ja	Jacob number	$[-]$
L	Lenght	$[mm]$
M	Molecular weigth	$[kg/kmol]$
N	Number of samples	$[-]$
N	Number of tube rows	
n	Sample	$[-]$
Nu	Nusselt number	$[-]$
P	Dimensionless pressure	$[-]$
P	Perimeter	$[mm]$
p	Pressure	$[Pa]$
p	Probability	
PDF	Probability density function	
PIV	Particle image velocimetry	
Pr	Prandtl number	$[-]$
PSD	Power spectral density	
Q	Power	$[W]$
q	Heat flux	$[W/m^2]$
R	Roughness parameter	$[\mu m]$
R	Thermal resistance	$[m^2 K/W]$
r	Radius	$[mm]$
R_{xx}	Autocorrelation	
Re	Reynolds number	$[-]$
Ri	Richardson number	$[-]$
RMS	Root mean square	
S	Velocity ratio	$[-]$
s	Tube pitch	$[mm]$

T	Time period	$[s]$
t	Time	$[s]$
t	Turbulent	
U	Global heat transfer coefficient	$[W/m^2K]$
u	Velocity	$[m/s]$
V	Drift velocity	$[m/s]$
We	Weber number	$[-]$
x	Vapor quality	$[-]$
X_{tt}	Martinelli parameter	$[-]$

Subscript

acc	Acceleration
acq	Acquisition
b	Bubble
c	Convective
cb	Convective boiling
$char$	Characteristic
d	Departure
e	External
f	Friction
fil	Filter
G	Gas
Gn	Gnielinski
h	Hydraulic
h	Hydrostatic
i	Inlet
i	Internal
L	Liquid
l	Laminar
m	Momentum
max	Maximum
min	Minimum
o	Outer
or	Outer root
pb	Pool boiling

r	Reduced
ref	Reference
res	Resonance
s	Slug
s	Static
$samp$	Sampling
sat	Saturation
sub	Sub-cooling
wat	Water

Chapter 1

Introduction

The multiphase scientific community, with increasingly more complex industrial applications, is conducting extensive studies in the field of two-phase flow and heat transfer. The goal is to better understand the mechanisms characterizing two-phase flow and evaporation on a dense array of tubes typical of heat exchangers and the link between the flow and heat transfer. Thermo-physical properties of the evaporating fluid play a strong role in the physical phenomena during evaporation. However, current available prediction methods can only be applied to specific fluids and with well-defined conditions mainly obtained through applied research. Often the resulting prediction methods available in literature are purely empirical. The basic physical phenomena of two-phase flow are well known in simple internal flow geometries but for more complex geometries, like flow over tube bundles, many questions still remain and wait to be solved by the scientific community. Consequently, a development of a more fundamental research approach is mandatory to tackle this complex problem.

The complexity of the two-phase flow in a tube bundle presents important problems in the design and understanding of the physical phenomena taking place. The working conditions of an evaporator depend largely on the dynamics of the two-phase flow that in turn influence the heat exchange and the pressure drop. A characterization of the flow dynamics, and possibly the identification of the flow pattern in tube bundle, will lead to a better understanding of the phenomena and reveal the mechanisms governing the heat transfer process in a tube bundle.

The aim of the present investigation is to better understand the mechanisms linked to two-phase flow and evaporation on a dense array of tubes in heat exchangers. The first stage of this work was a literature review, to clearly identify possible measurement techniques and define a starting point for the development of new experimental techniques. Three different techniques capable of providing quantitative information about the two-phase flow were designed, tested and developed. These techniques lead to the measurement of:

⋄ the fluctuation of the local pressure signals from high frequency piezoelectric pressure transducers;

⋄ the attenuation of a low power laser beam crossing the two-phase flow by means of a photodiode;

⋄ the visualization of two-phase flow structures with high speed video recording and analysis. This, for the first time, provided visual access to the core of a tube bundle under evaporation test conditions.

The bundle boiling LTCM stand was designed and built in a previous study by Robinson and Thome [63] and numerous boiling data were obtained under adiabatic conditions, mainly with enhanced tubes. In the present study the LTCM facility was modified, allowing the installation of the new instrumentation and the visualization system. The experimental campaign focused on plain copper tubes in adiabatic and diabatic tests with two different refrigerant fluids: R134a and R236fa. A new database, under adiabatic conditions, was obtained and employed to refine existing frictional pressure drop models. As well as a

comparison with existing models, a verification of the flow pattern map approach was shown. This new study provide extensive new information on the behavior of two-phase flow in tube bundles, and provides a solid base for further instrumentation development in this field. Local heat transfer coefficients were measured to obtain new local heat transfer data. The new results were then used to develop new prediction methods for two-phase pressure drops and boiling heat transfer, based in part on the new flow observations.

The thesis is organized as follow:

◇ *Chapter 1* · Introduction.

◇ *Chapter 2* · Definition of the main variables and the basic equations used in two-phase flow.

◇ *Chapter 3* · State of the art review on tube bundle flow pattern classification and on flow regimes identification techniques.

◇ *Chapter 4* · Description of the test facility and the instrumentation.

◇ *Chapter 5* · Discussion of the experimental results concerning two-phase flow characterization. The analysis of the laser-photodiode signals, the piezo-electric pressure signals and the high speed flow visualization are presented.

◇ *Chapter 6* · The experimental results concerning pressure drop in tube bundles are discussed and compared to existing two-phase pressure drop correlations.

◇ *Chapter 7* · An analysis of the local heat transfer data is presented and compared with existing prediction methods.

◇ *Chapter 8* · The conclusions of this study are summarized.

Chapter 2

Fundamental Definitions and Flow Parameters

This chapter introduces the primary variables used throughout this work and derives some simple relationships between them for the case of one-dimensional flow. To distinguish between gas and liquid phases, the subscripts G and L are used respectively. Basic equations for two-phase flows are also introduced at the end of the chapter.

2.1 Two-phase flow

Classical thermodynamics tell us that a phase is a macroscopic state of matter which is homogeneous in chemical composition and physical structure; e.g. a gas, a liquid or solid of a pure component. Two-phase flow is the simplest case of multi-phase flow in which two phases of a pure component are present. In internal convective vaporization and condensation processes, the vapor and liquid are in simultaneous motion inside the pipe. The resulting two-phase flow is generally more complicated physically than single-phase flow. In addition to the usual inertia, viscous, and pressure forces present in single-phase flow, two-phase flows are also affected by interfacial tension forces, the wetting characteristics of the liquid on the tube wall, and the exchange of momentum between the liquid and vapor phases in the flow.

2.2 Vapor quality

The vapor quality x is defined as the vapor mass flow rate $\dot{m}_G \, kg/s$ divided by the total mass flow rate $\dot{m}_G + \dot{m}_L$:

$$x = \frac{\dot{m}_G}{\dot{m}_G + \dot{m}_L} \tag{2.1}$$

When phase change does not take place in the channel, one needs to measure the mass flow rate of each phase, and the quality is then determined for the entire channel. In case there is a phase change in the channel, e.g. if the channel is heated and boiling takes place, then the quality will increase (inverse for condensation) downstream with the flow. Since often there is no thermal equilibrium between the phases, one cannot calculate the quality merely by knowing the inlet quality and the heat flux from the wall. Unfortunately, it is very difficult to measure or calculate with precision the quality of the liquid-vapor mixture flowing in a channel where a change of phase takes place. However a fictitious quality, the so called thermodynamic equilibrium quality, can be calculated by assuming that both phases are

saturated, i.e., that their temperatures are equal to the saturation temperature corresponding to their common pressure. The so-called thermodynamic equilibrium quality can be calculated as:

$$x = \frac{h_z - h_L}{h_{LG}} \tag{2.2}$$

where $h_L \, J/kg$ is the enthalpy of the saturated liquid, $h_{LG} \, J/kg$ is the latent heat of vaporization, and $h(z) \, J/kg$ is the enthalpy at a cross section z. This can be calculated from:

$$h(z) = h_{in} + \frac{1}{\dot{m}} \int_{in}^{z} q(z) dz \tag{2.3}$$

where $h_{in} \, J/kg$ is the enthalpy of the fluid at the inlet and $q(z) \, W/m$ is the heat input per unit length of channel.

2.3   Void fraction

In two-phase flow, void fraction is one of the most important parameters to be defined. It defines the cross-sectional area occupied by each phase. As it determines mean velocities of the liquid and the vapor phases, it represents a fundamental parameter in the calculation of pressure drop, flow pattern transitions and heat transfer coefficients. The void fraction of the vapor is defined as:

$$\varepsilon = \frac{A_G}{A_G + A_L} \tag{2.4}$$

where A_G is the sum of areas occupied by voids and A_L is the sum of areas occupied by the liquid. The total cross-sectional area of the channel is called A.

2.4   Velocities

In two-phase flow there are a number of velocities that can be defined. Also, in general, the phases will not have the same velocity and there will be a relative velocity between them.

2.4.1   Mass velocity

The mass velocity G is defined as the mass flow rate $\dot{m}$ divided by the cross-sectional area of the flow channel:

$$G = \frac{\dot{m}}{A} \tag{2.5}$$

Considering the continuity law, the mass velocity is the expression of the mean flow velocity multiplied by the mean density. The mass velocity has units of $kg/m^2 s$. For a tube bundle, G is the mass velocity at the minimum cross-sectional area of the channel including blockage of the tubes.

2.4.2   True average velocities

The true average velocities (also called actual velocities) of the phases u_G and u_L are the velocities by which the phases actually travel. The cross sectional average true velocities are determined by the

volumetric flow rates $\dot{V}_G$ and $\dot{V}_L$ m^3/s of the vapor and liquid divided by the cross-sectional areas occupied by the respective phases:

$$u_G = \frac{\dot{V}_G}{A_G} = \frac{\dot{V}_G}{\varepsilon A} \qquad u_L = \frac{\dot{V}_L}{A_L} = \frac{\dot{V}_L}{(1-\varepsilon)A} \tag{2.6}$$

From the equation of continuity, it is possible to define liquid and vapor true mean velocities referred to their own cross sectional areas and their own mass flow rates as follows:

$$u_G = \frac{x}{\varepsilon}\frac{\dot{m}}{\rho G A} = \frac{G}{\rho_G}\frac{x}{\varepsilon} \qquad u_L = \left(\frac{1-x}{1-\varepsilon}\right)\frac{\dot{m}}{\rho L A} = \left(\frac{G}{\rho_L}\frac{1-x}{1-\varepsilon}\right) \tag{2.7}$$

2.4.3 Superficial velocities

The superficial velocities (also called volumetric fluxes) of the phases j_G and j_L are defined as the volumetric flow rate of the phase through the total cross-sectional area of the two-phase flow. It might also be expressed as the phase velocity if it would flow alone in the entire cross section. Thus:

$$j_G = \frac{\dot{V}_G}{A} = \frac{G}{\rho_G}x = \varepsilon u_G \qquad j_L = \frac{\dot{V}_L}{A} = \frac{G}{\rho_L}(1-x) = (1-\varepsilon)u_L \tag{2.8}$$

The total superficial velocity is defined as:

$$j = j_G + j_L \tag{2.9}$$

2.4.4 Drift velocities

The drift velocities of the phases V_{Gj} and V_{Lj} are defined as the true average velocity of the phase in relation to the total superficial velocity, namely:

$$V_{Gj} = u_G - j \qquad V_{Lj} = u_L - j \tag{2.10}$$

The drift fluxes of the phases j_{Gj} and j_{Lj} are defined as:

$$j_{Gj} = \varepsilon V_{Gj} = \varepsilon(u_G - j) \qquad j_{Lj} = (1-\varepsilon)V_{Lj} = (1-\varepsilon)(u_L - j) \tag{2.11}$$

It follows:

$$j_{Gj} + j_{Lj} = 0 \tag{2.12}$$

2.5 Definition of non-dimensional numbers

The principal non-dimensional numbers used in the present study are defined below. Different definitions of the main non-dimensional numbers, particularly for the Reynolds and Froude number, can be found in the literature. In order to be coherent in this work, the following definitions are used throughout this work:

2.5.1 Reynolds number

The Reynolds number represents the ratio of the inertial forces to the viscous forces. For the particular case of forced convection inside a tubular channel, the liquid Reynolds number for a single-phase in a channel can be expressed in the following form:

$$Re_L = \frac{\rho_L u_L D_h}{\mu_L} \tag{2.13}$$

where D_h is the hydraulic diameter defined as the ratio of the cross-sectional A to the wetted perimeter P_L:

$$D_h = \frac{4A}{P_L} \tag{2.14}$$

D_h for the liquid and gas phases is expressed in the following form:

$$D_h|_L = \frac{4A_L}{P_L} = \frac{4(1-\varepsilon)A}{P_L} \qquad D_h|_G = \frac{4A_G}{P_L} = \frac{4\varepsilon A}{P_L} \tag{2.15}$$

Considering one-dimensional flow and using the definition of the true mean velocity from equation Eq. (2.6) the liquid and gas Reynolds numbers in a two-phase flow can be expressed as:

$$Re_L = \frac{GD_h|_L}{\mu_L} \frac{1-x}{1-\varepsilon} = \frac{4G(1-x)A}{\mu_L P_L} \qquad Re_G = \frac{GD_h|_G}{\mu_G} \frac{x}{\varepsilon} = \frac{4GxA}{\mu_G P_L} \tag{2.16}$$

2.5.2 Nusselt number

The Nusselt number expresses the ratio of convective to conduction temperature gradient. In internal forced convection, the reference length is the tube diameter:

$$Nu = \frac{\alpha D}{\lambda} \tag{2.17}$$

where h is the heat transfer coefficient,D is the tube diameter and λ is the thermal conductivity.

2.5.3 Liquid Froude number

The Froude number represents the ratio of the inertia forces to the gravitational forces. The general expression is:

$$Fr = \frac{u^2}{gL} \tag{2.18}$$

2.5.4 Liquid Weber number

The liquid Weber number expresses the ratio of inertia to surface tension forces. As for the Nusselt number, the reference length is the tube diameter. It is expressed for liquid phase as:

$$We_L = \frac{\rho_L u_L^2 D}{\sigma} \tag{2.19}$$

2.5.5 Prandtl number

The Prandtl number is the ratio between the momentum diffusivity and the thermal diffusivity. It is expressed for a liquid and gas as:

$$Pr_L = \frac{c_{pL}\mu_L}{\lambda_L} \qquad Pr_G = \frac{c_{pG}\mu_G}{\lambda_G} \tag{2.20}$$

2.5.6 Capillary number

The Capillary number is the ratio between Weber and Reynolds number, and represents a ratio between viscous force and surface tension force:

$$Cap = \frac{We}{Re} \tag{2.21}$$

2.5.7 Richarson number

The Richarson number is the ratio between the buoyancy force and the inertial force:

$$Ri = \frac{\Delta \rho g L}{\rho u^2} \tag{2.22}$$

2.5.8 Martinelli parameter

The Martinelli parameter is defined as the ratio between the theoretical pressure gradients which would occur if either fluid were flowing alone in the pipe with the original flow rate of each phase. The Martinelli parameter X_{tt} is calculated as:

$$X_{tt}^2 = \frac{\Delta p_L}{\Delta p_G} \tag{2.23}$$

X_{tt}^2 is void fraction independent and is a measure of the degree to which the two-phase mixture is closer to being a liquid, i.e. $X_{tt}^2 \gg 1$, or to being a gas, i.e. $X_{tt}^2 \ll 1$. The subscript tt is sometimes used and signifies that both phases are turbulent. Modeling the pressure drop of each phase with its superficial velocity and friction factors in the classical form:

$$f_L = C_L Re_L^{(-n)} \qquad f_G = C_G Re_G^{(-m)} \tag{2.24}$$

and assuming the same friction model for both phases (both turbulent or both laminar) which means that m = n and CL = CG, equation (2.33) reduces to:

$$X_{tt}^2 = \left(\frac{1-x}{x}\right)^{(2-n)} \left(\frac{\mu_L}{\mu_G}\right)^n \left(\frac{\rho_G}{\rho_L}\right) \tag{2.25}$$

Chapter 3

State of the Art Review

A state of the art review is presented here. The first part will focus specifically on tube bundle flow pattern classification, whilst the second part will analyze the techniques developed through the years by the two-phase community for flow regime identification. Experimentally, it is much more difficult to investigate two-phase flows over tube bundles than for internal tube flows. Hence, the results of this review will be used to develop three methods, that will be implement simultaneously, to determine local flow patterns.

3.1 Flow patterns and their transition in two phase flow

Two phase flow plays an important role in advanced energy conversion systems. The quantity of energy involve (for example: pressure drop, heat transfer rates, rates of chemical reaction, etc. depend strongly on the flow regime). Thus, in order to better model these flows, this demands greater understanding of the physics of the flow, and also of the ability to predict the flow regimes.

Hubbard and Dukler [29] concretize the concept of flow patterns giving the following definition: *in single phase flow the phase boundaries are defined by the dimensions of the conduit in which flow takes place. Two phase flow is complicated by the fact that the phase boundaries are determined not only by the position of the walls but by the distribution of the phase in the flow space. Furthermore, this distribution varies with flow rate, fluid properties, conduit size, shape and other factors. Each of these distributions is called a Flow Regime.* Vince and Lahey [28] state: *flow regime maps represent a convenient way to indicate the phase distribution of a two-phase mixture. Flow regime boundaries can be indicated on a plot with parameters commonly measured or calculated.*

The prediction or the identification of flow regimes in two phase flow is one of the most important problems in the design and operation of two phase systems. To underline the importance of the problem, Noghrehkar et al. [16] stated: *it has been estimated that nearly half of all process heat exchangers operate in two-phase flow, however, our understanding of two-phase flow is far from satisfactory. Historically, it has been difficult to develop an accurate method because flow regimes have been judged mostly on a basis of visual observation. In such cases the models suffer of a lack of objectiveness.* Lin and Hanratty [33]: *gas and liquid flowing in a horizontal pipeline show a number of interfacial configurations, called flow patterns.*

This situation is universally accepted in the two phase community which consciously recognizes such limitations. From this point of view, it is desirable to develop more objective methods of flow pattern identification. The expression *more objective* and *not objective* is used: all the "objective" techniques are calibrated through visual measurements which are intrinsically subjective. Fluctuations and their spectral analysis in the two-phase flow field have catalyzed over the years with more and more interest, as this appears to be a powerful tool to more objectively detect flow patterns.

3.1.1 Flow patterns

On the last 60 years, several attempts to characterize flow patterns in tube bundles have been carried out. Historically, the main technique employed in this task has been visual observation. Flow pattern maps have been proposed by several authors, and usually, there is a simple plot of the superficial velocity of the liquid versus that of the gas, with boundaries between regimes drawn based on observations. Below the more important studies are mentioned.

Diehl [1]

Diehl [1] has been a pioneer in defining the existence of different flow regimes. Without presenting a flow pattern map, he identified in a condenser, for down-flow, two possible flow regimes: annular flow and misting flow.

NEL research [2], [3], [4], and [6]

The National Engineering Laboratory (NEL) performed an extensive study on heat exchanger design [5] and research. Studying pressure drop and heat transfer on the shell side of a heat exchanger prototype, Sutherland and Murray [2] presented a series of images from the experimental investigation: see Fig. (3.1)-Fig. (3.5). The authors did not classify the possible flow patterns and the test section (only 1 column of tubes) is far from being representative of a real heat exchanger.

For vertical up and down flow in another tube bundle test section, Grant and Murray [3] identified by visual observation, as reported in Fig. (3.6): *bubbly, slug* and *spray* flows. The authors, using an air-water mixture, identified a change from bubbly flow (the liquid phase filled the channel with the gas phase dispersed in the liquid as discrete bubbles) at low qualities to slug flow (intermittent slugs of liquid were propelled cyclically through the bundle by the gas) in the quality range from 1 to 10% and then to spray flow (the liquid phase was entrained as droplets in the gas stream) at higher qualities. A flow pattern map based on visual observations was presented, refer to Fig. (3.7), where the plot was done in terms of the parameters used by Baker (see [3]).

Similarly, Grant and Murray [4] using the same facility as in [3], studied the possible flow patterns in the case of horizontal two-phase flow. They identified the following distinct regimes:

  ⋄ *Spray flow*

  ⋄ *Stratified spray flow*: the liquid tended to separate from the gas phase and flow along the bottom of the bundle, but a part of the gas phase was mixed, as bubbles, in the liquid layer.

  ⋄ *Stratified flow*: complete separation of the two phases.

  ⋄ *Bubbly flow*.

The representation of the different flow regimes is given in Fig. (3.8). A flow map is presented in terms of Baker (see [3]) parameters modified according to Bell (see [3]) as shown in Fig. (3.9). It is basically a plot of $j_G.(\rho_G/\rho_L)^{1/2}$ against $j_L.(\rho_L.\mu_L)^{1/3}/\sigma$. A global summary and analysis of the work carried out at National Engineering Laboratories [2], [3], [4], is presented in the paper of Grant and Chisholm [6]. They proposed the same data presented previously but rearranged the two-phase flow pattern maps into new parameters and classifications (e.g. the slug flow it was now classified as intermittent), see Fig. (3.10).

Kondo and Nakajima [7], Kondo [8]

Kondo and Nakajima [7] and Kondo [8] identified bubbly, slug and froth flows in an air-water bundle facility with vertical upward flow. They did not propose a new classification or a new flow pattern
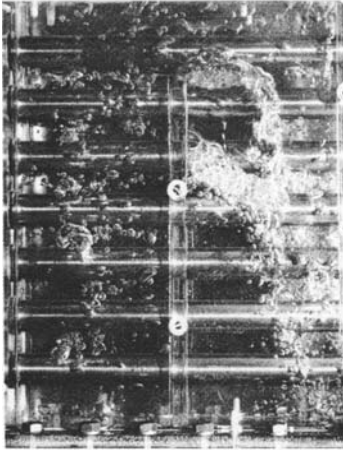
Figure 3.1: $G_L = 537 \, [kg/s.m^2]$, $x = 0.035\%$, Sutherland and Murray [2]
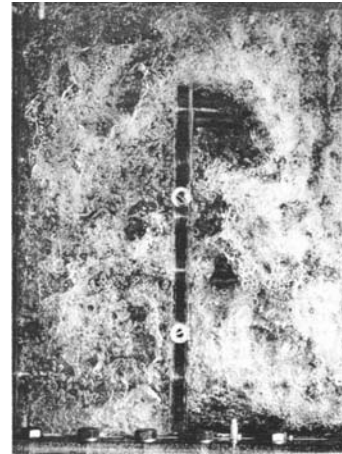
Figure 3.2: $G_L = 885 \, [kg/s.m^2]$, $x = 0.088\%$, Sutherland and Murray [2]
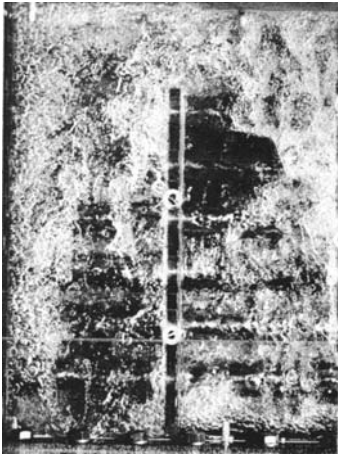
Figure 3.3: $G_L = 204 \, [kg/s.m^2]$, $x = 1.43\%$, Sutherland and Murray [2]
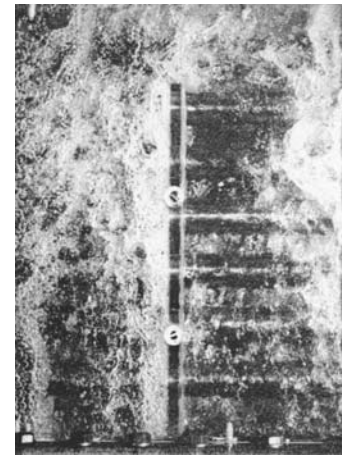
Figure 3.4: $G_L = 204 \, [kg/s.m^2]$, $x = 5.23\%$, Sutherland and Murray [2]
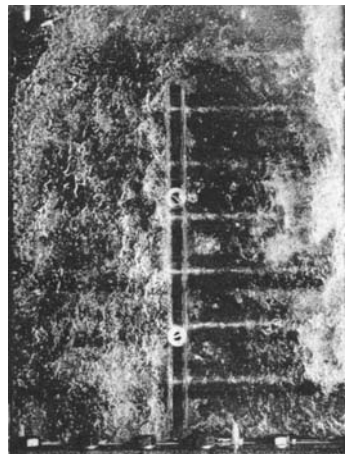
Figure 3.5: $G_L = 182 \, [kg/s.m^2]$, $x = 9.16\%$, Sutherland and Murray [2]
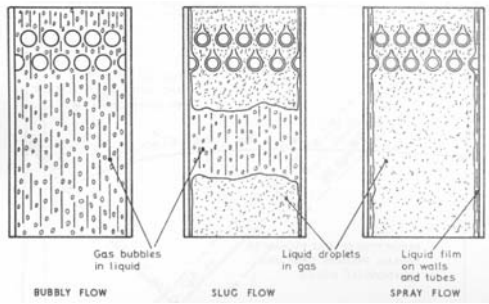
Figure 3.6: Flow pattern, up-flow, Grant and Murray [3]
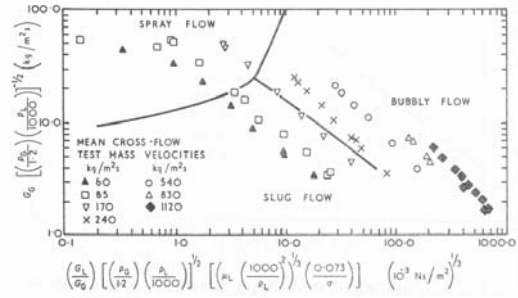
Figure 3.7: Flow regime map, up-flow, Grant and Murray [3]
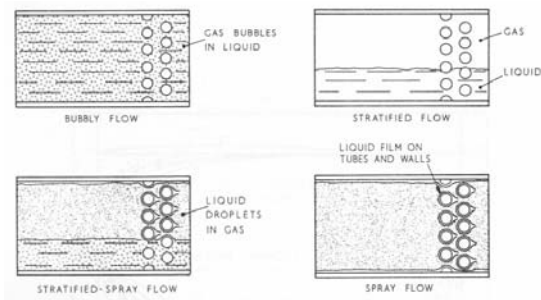
Figure 3.8: Flow pattern, horizontal-flow, Grant and Murray [4]
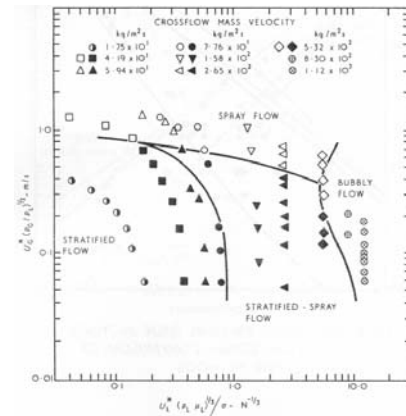
Figure 3.9: Flow regime map, horizontal-flow, Grant and Murray [4]
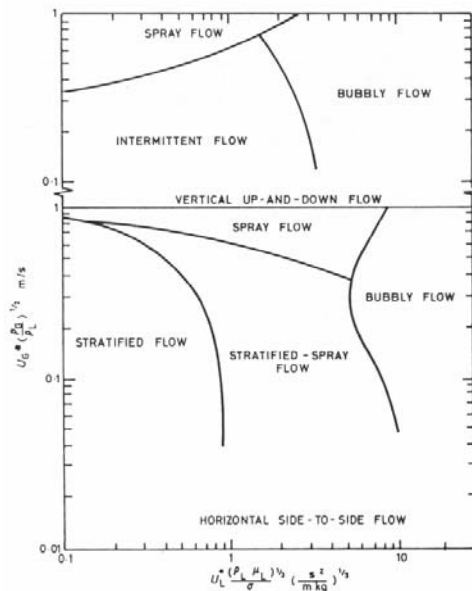
Figure 3.10: Flow regime map, up/down-flow, Grant and Chisholm [6]

map, but their work supports what was previously proposed by Grant and Chisholm [6]. An interesting representation of the different flow patterns was presented and supported with photographic material as in Fig. (3.11). The top figure is characteristic for low flow rates, where bubbles are much smaller in diameter than the tube diameter and are rather uniformly distributed in the water phase. The shape of the bubbles is elliptical. This flow regime is classified as *bubbly flow*. Passing now to the central figure, the authors noticed that as the air flow rate increased, some of the bubbles coalesced and filled up the tube clearance, so that the height and length of the bubbles were comparable. This flow regime was classified as *slug flow*. The bottom figure represents the flow at high air flow rates, where height and width of the large bubbles are several times the tube pitch; this flow regime is classified as *froth flow*.
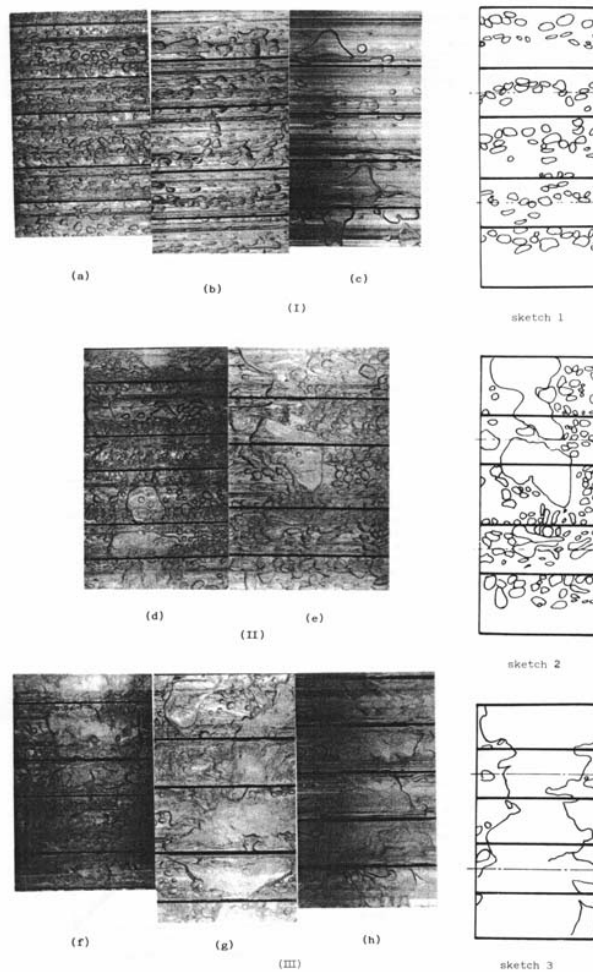
Figure 3.11: Flow patterns (I. bubbly; II. slug; III. froth), Kondo and Nakajima [7]

Pettigrew et al. [9], [10], [11]

Pettigrew et al. [9], [10], [11], studying the vibration of tube bundles in two-phase cross flow, added some new information regarding flow patterns for vertical upward flow. The authors stated that some knowledge of the flow regime is necessary to understand flow-induced vibrations. They compared their data, classified by visual observation, with the flow pattern map of Grant [5]. The flow map, shown in Fig. (3.12), is plotted in terms of the Martinelli parameter against the gas dimensionless velocity. The

authors stated that bubbly flow appears to prevail at void fractions below 90%. Intermittent flow was observed at higher void fraction, roughly above 90%.
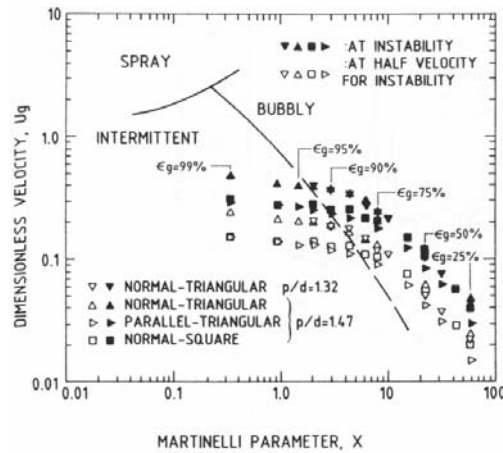
Figure 3.12: Flow regime map, Pettigrew et al. [9]

Ulbrich and Mewes [12]

For vertical upward flow, Ulbrich and Mewes [12] proposed a classification of the flow patterns by the use of visual observation and by the statistical analysis of the pressure drop time signals. The following classifications were proposed:

- ⋄ *Bubble*: dispersed gas distributed as discrete small bubbles in the continuous liquid phase, whose diameters are less than the characteristic spacing between the tubes and generally uniform in size;

- ⋄ *Intermittent*: irregular and alternating motion of the liquid and gas; the direction of the liquid flow changes in an erratic and irregular manner from up-flow to down-flow and vice versa. The liquid flows downwards not only as a film but also as units of liquid which occupy much of the cross-sectional area. Gas flows not only as spherically or elliptically capped bubbles but also as large flattened and irregular bubbles, whose height is several times greater than the tube diameter and their width is equivalent to the tube clearance);

- ⋄ *Dispersed*: regular dispersed droplets, which are carried out from the gas, initially above the tube bundle, and then also between the tubes. The dispersed flow regime is subdivided as: intermittent-dispersed (part of the liquid flows as irregular moving units) and annular dispersed (liquid flows as a thin film, with surface waves occupying the tube wall or the shell wall.

A representation is given in Fig. (3.13). Ulbrich and Mewes compared their database with the flow pattern maps available in the literature, and proposed a new flow pattern map in terms of superficial velocities. The final classification lead to three regimes: bubble, intermittent and dispersed. A representation of the proposed flow pattern map, with plotted experimental data points obtained from the authors, is given in Fig. (3.14).

Lian et al. [13]

In the field of tube bundles vibrations, Lian et al. [13] proposed a classification according to the available literature: *bubbly*, *churn turbulent* and *dispersed droplet*.
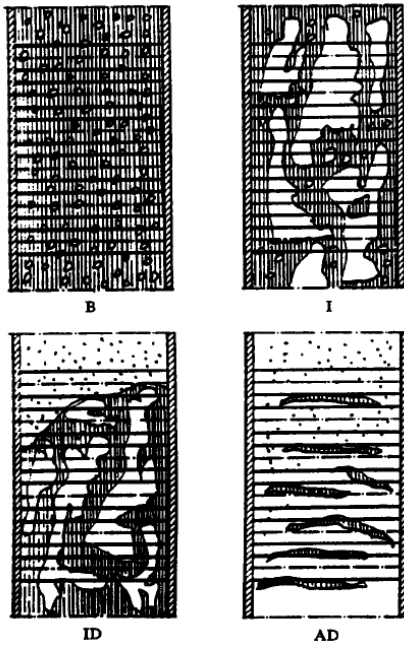
Figure 3.13: Flow pattern (B. bubble; I. intermittent; ID. intermittent dispersed; AD. annular dispersed), Ulbrich and Mewes [12]
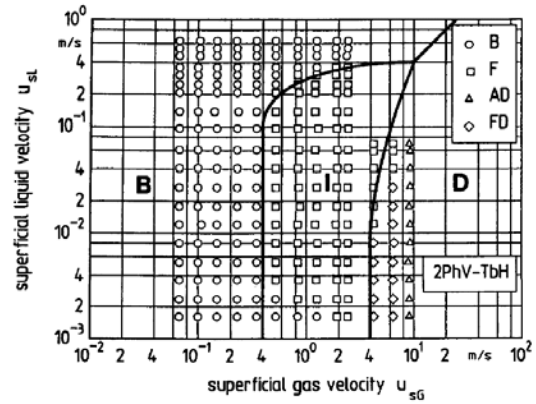
Figure 3.14: Flow regime map, Ulbrich and Mewes [12]

Xu et al. [14], [15]

Visual observation of vertical up, down and horizontal flow in a tube bundle was carried out in the experimental investigation of Xu et al. [14], [15]. For a two phase down flow across their tube bundle, Fig. (3.15), the following classifications were given:

◇ *Falling film*: the superficial velocities of the gas and liquid were low, and the liquid formed a film around the tube wall and the inside wall of the shell continuously; the film contained no gas bubbles, and the gas flowed through free areas between tubes; the surface of the film was wavy and the gas contained very few or no liquid droplets;

◇ *Intermittent*: gas moved at higher velocity; the gas liquid interface was disturbed by waves traveling in the flow direction, the continuous liquid film was intermittently cut off between the tubes by the gas; when the velocity of liquid was increased, the gas phase was entrained as bubbles in the liquid;

◇ *Annular*: the tube wall and the inside wall of the shell were covered by an annular liquid film; at a high gas velocity, some liquid was entrained as bubbles in the liquid;

◇ *Bubbly*: similar to the falling film flow, but the liquid film became thicker and contained small dispersed air bubbles; the film moved faster.

In the case of up flow, their schematic diagrams are shown in Fig. (3.16) with the following descriptions:

◇ *Churn*: at low superficial velocities of liquid and gas, it was controlled by gravity force and was much more chaotic;

◇ *Intermittent*: the two phase flow became periodically unstable; when a pulse appeared, parts of tubes were wetted by an annular liquid film, the others were filled with discrete bubbles;
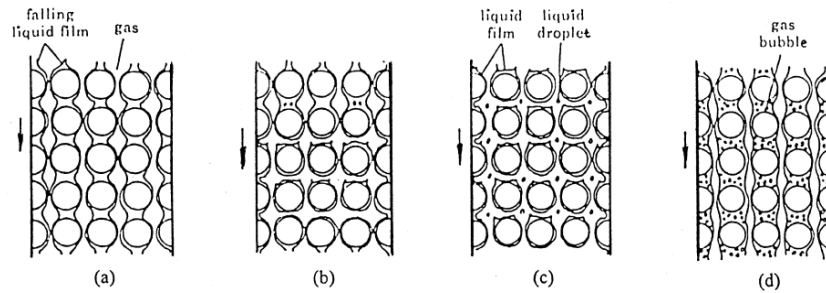
Figure 3.15: Flow patterns (a. falling film; b. intermittent; c. annular; d. bubbly) for down-flow, Xu et al. [14]
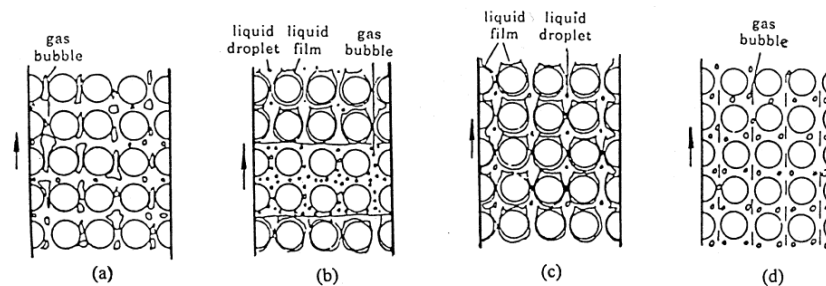
Figure 3.16: Flow patterns (a. churn; b. intermittent; c. annular; d. bubbly) for up-flow, Xu et al. [14]

⋄ *Annular*: same behavior as down flow;

⋄ *Bubbly*: the gas phase was uniformly distributed in the form of discrete bubbles in a continuous liquid phase.

In the case of horizontal flow, the authors seemed to be able to distinguish between *annular, bubbly, intermittent* and *stratified* flows. Flow pattern maps for vertical up and vertical down flows were proposed plotting the experimental observations in terms of liquid and gas superficial velocities: Fig. (3.17).

Noghrehkar et al. [16]

Noghrehkar et al. [16] used the probability density function (PDF) of local void fraction fluctuations as a flow regime indicator. From the experimental data obtained, the following classifications were given: *bubbly, intermittent* and *annular* flow. The authors proposed different flow maps in terms of superficial velocities for in-line, Fig. (3.19) and staggered configurations, Fig. (3.20). According to the presented maps, as the superficial liquid velocity increases, the transition from the bubbly to the intermittent flow pattern occurs at higher gas velocities for the staggered configuration compared to the in-line one. Noghrehkar et al. pointed out that the use of only visual observations as a flow regime indicator can lead to false considerations: using the PDF method, the authors observed different flow patterns near the shell wall from than at the inside of the bundle. Hence, this point out the need to make such measurements at the "heart" of the bundle and not at its perimeter.

Burnside et al. [18] and Iwaki et al. [19]

The latest developments in flow regime identification were oriented towards a characterization of the velocity fields inside the bundle using particle image velocimetry measurements. This work was done by Burnside et al. [18] and Iwaki et al. [19]; see Fig. (3.21). They tested a very short bundle butted up against a plexiglass end plate in order to view the flows.
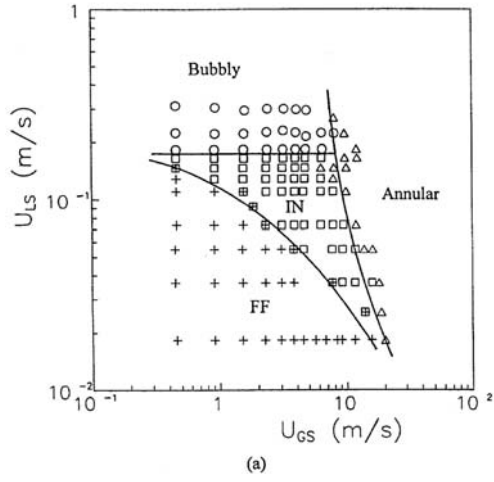
Figure 3.17: Flow regime map: down-flow, Xu et al. [14]
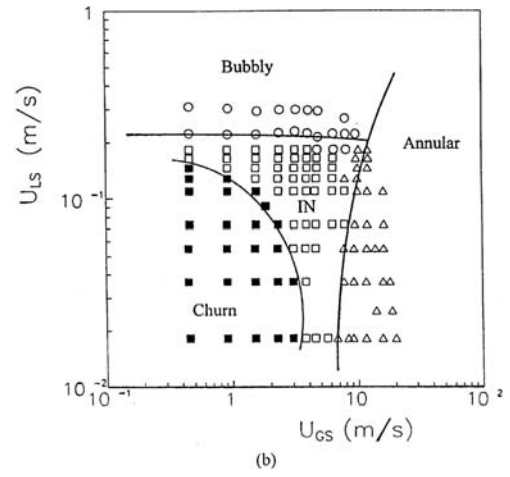
Figure 3.18: Flow regime map: up-flow, Xu et al. [14]
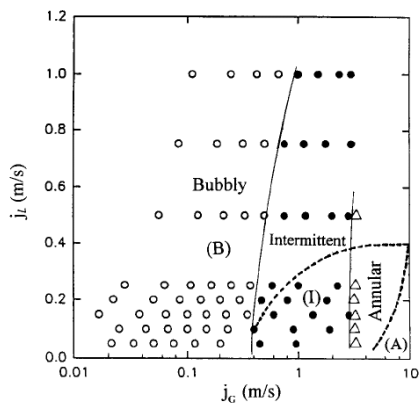
Figure 3.19: Flow regime map, in-line, Noghrehkar et al. [16]
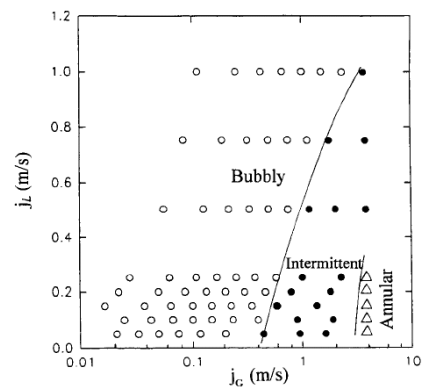
Figure 3.20: Flow regime map, staggered, Noghrehkar et al. [16]
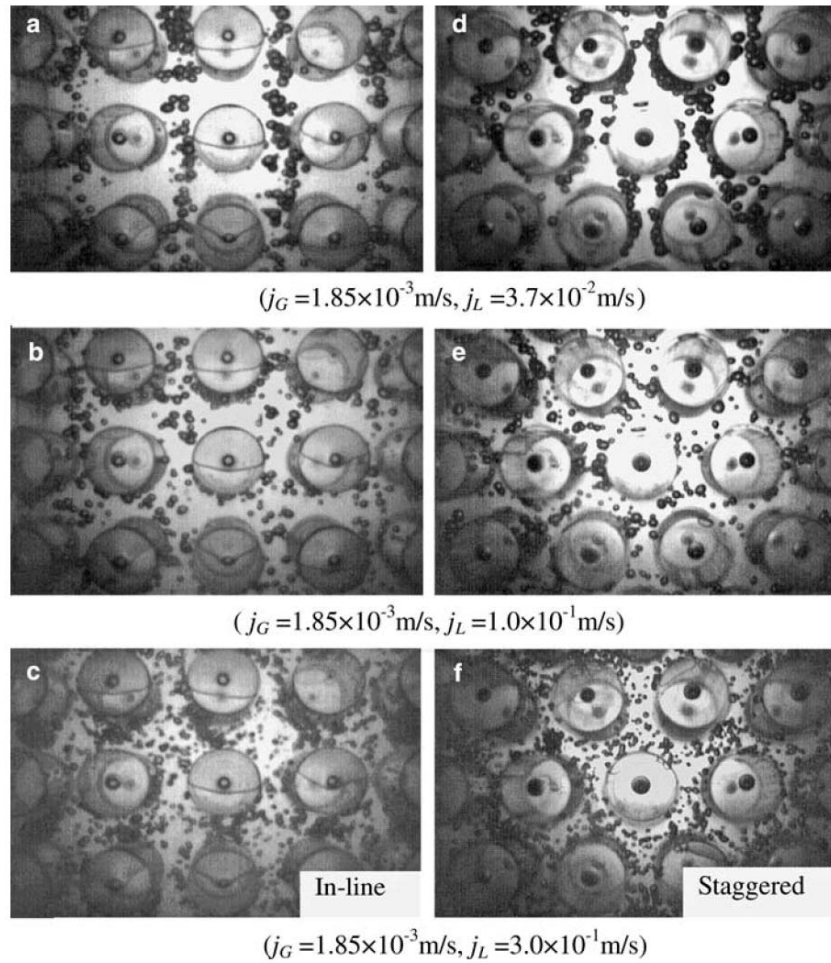
Figure 3.21: Visualized flow patterns using a strobe light: in-line vs staggered, Iwaki et al. [19]

Khushnood et al. [20], Ribatski and Thome [21]

Two recent papers review the work on tube bundles, one by Khushnood et al. [20] who focused on vibrations in tube bundles and the other by Ribatski and Thome [21]. From the work of Ribatski and Thome [21], the comparison of the flow maps according to subjective and objective methods was made. The different flow pattern maps are confronted in Fig. (3.22) and Fig. (3.23). An analysis unveils important discrepancies between the different methods. As stated from Ulbrich and Mewes [12], the three flow pattern maps proposed by Grant and Murray [3], Grant and Chisholm [6] and Pettigrew et al. [9], [10], [11] are practically identical and differ only in the coordinate system used. For this reason, just one of them is employed as reference: Grant and Chisholm [6]. A summary of the literature analyzed in this section is presented in Table (3.1).
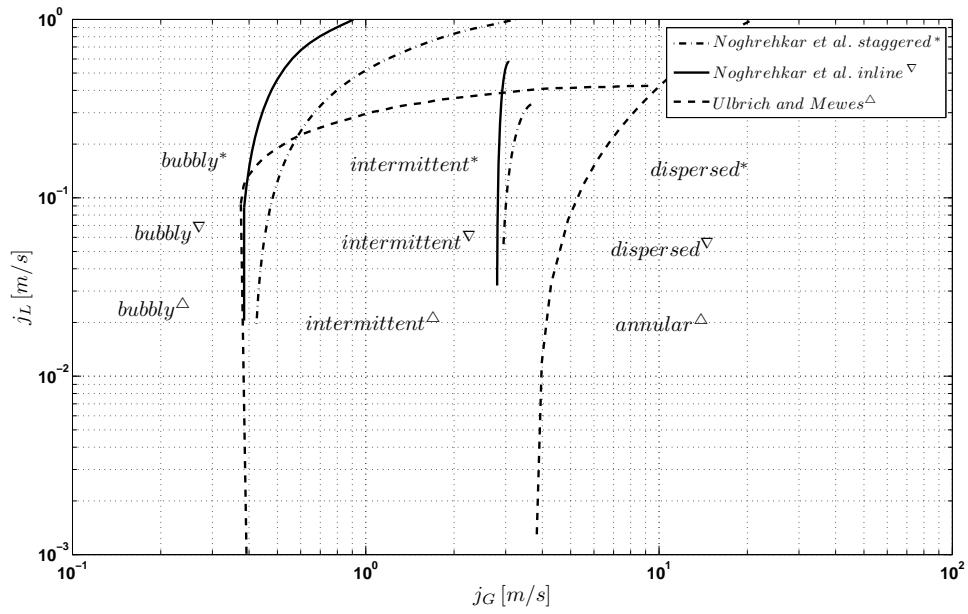
Figure 3.22: Shell side flow pattern map, Noghrehkar et al. [16] vs. Ulbrich and Mewes [12]
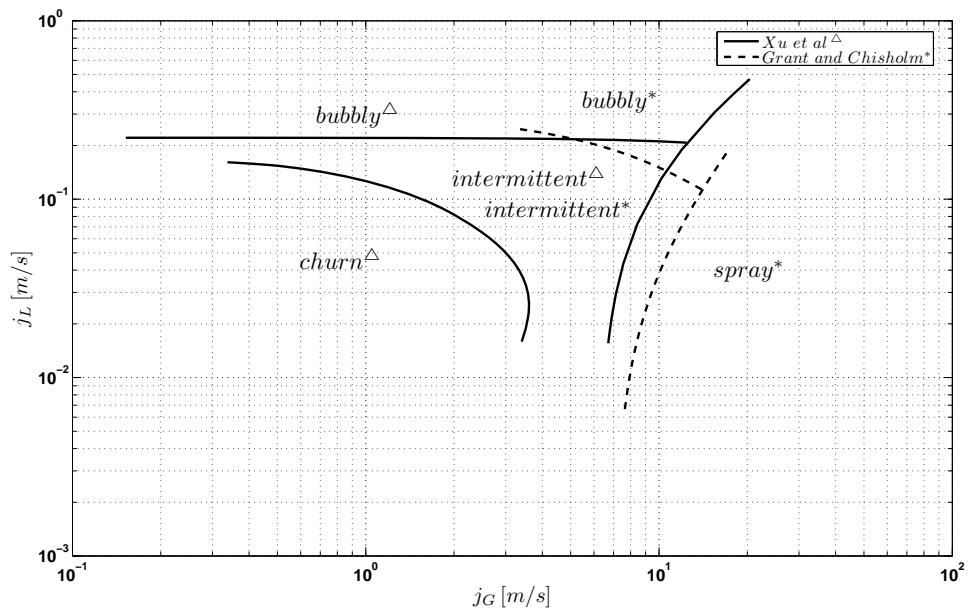
Figure 3.23: Shell side flow pattern map, Xu et al. [14], [15] vs. Grant and Chisholm [6]

Table 3.1: Two-phase flow pattern studies for tube bundles: literature summary

Author	Fluid Pressure/Temperature	Flow direction	Tube bundle characteristics	Test conditions	Flow pattern
Diehl [1]	Air–Water 101 [kPa] Air–Water and wetting agent 101 [kPa] Air–Sugar solution 101 [kPa] Pentane 207 − 620 [kPa] Methane-Pentane 123 [kPa] Methane-Propylene glycol 64 − 159 [kPa]	↑	5x17 tubes in square in-line array $s/D = 1.25$ $D = 12.7$ [mm] 2x16 tubes in 45° triangular layout $s/D = 1.33$ $D = 19.05$ [mm]	$G \leq 1110\,[Kg/s.m^2]$ $x = 0.006 − 0.99991\,[−]$	Annular; Misting
Sutherland and Murray [2]	Air–Water 101 [kPa]	↑↓	1x7 tubes $D = 19.1$ [mm]	$G_L = 185 − 990\,[Kg/s.m^2]$ $G_G = 0.15 − 18\,[Kg/s.m^2]$	[-]
Grant and Murray [3]	Air–Water 101 [kPa]	↑↓	4x11 tubes in equilateral triangular layout; segmentally baffled heat exchanger $s/D = 1.25$ $D = 19.1$ [mm]	$G = 60 − 1120\,[Kg/s.m^2]$	Bubbly; Slug; Spray
Grant and Murray [4]	Air–Water 101 [kPa]	→	4x11 tubes in equilateral triangular layout; segmentally baffled heat exchanger $s/D = 1.25$ $D = 19.1$ [mm]	$G = 20 − 1120\,[Kg/s.m^2]$	Spray; Stratified-spray; Stratified; Bubbly
NEL meeting 28.11.73 [5]	[-]	[-]	Heat exchanger	[-]	[-]
Grant and Chisholm [6]	Air–Water 101 [kPa]	↑↓→	4x11 tubes in equilateral triangular layout; segmentally baffled heat exchanger $s/D = 1.25$ $D = 19.1$ [mm]	$G_\rightarrow = 20 − 1120\,[Kg/s.m^2]$ $G_{\uparrow\downarrow} = 20 − 1120\,[Kg/s.m^2]$ $x = 0.002 − 0.94\,[−]$	↑↓.Bubbly; Intermittent; Spray →.Bubbly; Spray; Stratified-spray; Stratified
Kondo and Nakajima [7] Kondo [8]	Air–Water 101 [kPa]	↑	5x(7/9/11/13/15/20) tubes in staggered equilateral layout $s/D = 1.4/1.28/1.08$ $D = 25$ [mm]	$G_G = 0.018 − 0.6\,[m/s]$ $G_L = 0.32 − 3.2\,[m/s]$ $x = 0.005 − 0.9\,[−]$	Bubbly; Slug; Froth

Reference	Fluid / Pressure	Flow direction	Geometry	Mass flux / Quality	Flow patterns
Pettigrew et al. [9], [10], [11]	Air-Water 101 [kPa]	↑	$D = 19.05\,[mm]$ 8/10 tube rows a. Normal-Triangular (30°) $s/D = 1.32$ b. Normal-Triangular (30°) $s/D = 1.47$ c. Parallel-Triangular (60°) $s/D = 1.47$ d. Normal-Square (90°) $s/D = 1.47$	$G_a = 238 − 1012\,[Kg/s.m^2]$ $G_b = 45 − 1200\,[Kg/s.m^2]$ $G_c = 28 − 775\,[Kg/s.m^2]$ $G_d = 29 − 1013\,[Kg/s.m^2]$ $x \simeq 0 − 1\,[−]$	Bubbly; Intermittent
Ulbrich and Mewes [12]	Air-Water 101 − 140 [kPa]	↑	5x10 tubes in square in-line array $s/D = 1.5\; D = 20\,[mm]$	$G = 1.6 − 650\,[Kg/s.m^2]$ $x = 0.0001 − 0.89\,[−]$	Bubbly; Intermittent; Dispersed (Intermittent-dispersed & Annular-dispersed)
Lian et al. [13]	Air-Water 101 [kPa]	↑	5x20 tubes in-line array $s/D = 1.75\; D = 25.4\,[mm]$	$G \simeq 100 − 600\,[Kg/s.m^2]$ $x \simeq 0 − 1\,[−]$	[−]
Xu et al. [14], [15]	Air-Water Air-Oil 101 − 200 [kPa]	↑↓→	Segmentally baffled heat exchanger 5x20 tubes in square in-line array $s/D = 1.28\; D = 9.79\,[mm]$	$G = 37 − 658\,[Kg/s.m^2]$ $x = 0.001 − 0.94\,[−]$	↓.Falling film; Intermittent; Annular; Bubbly ↑. Churn; Intermittent; Annular; Bubbly →. Annular; Bubbly; Intermittent; Stratified
Noghrehkar et al. [16]	Air-Water 101 [kPa]	↑	5x24 tubes in square in-line array 5x26 tubes in equilateral triangular layout $s/D = 1.47\; D = 12.7\,[mm]$	$G = 50 − 1000\,[Kg/s.m^2]$ $x = 0 − 0.85\,[−]$	Bubbly; Intermittent; Annular
Burnside et al. [18]	Air-Water 101 [kPa]	↑	17x17 column kettle reboiler $s/D = 1.34\; D = 19\,[mm]$	[−]	[−]
Iwaki et al. [19]	Air-Water 101 [kPa]	↑	5x20 tubes in-line array 5x20 tubes in staggered array $s/D = 1.5\; D = 15\,[mm]$	$G_L = 64 − 692\,[Kg/s.m^2]$ $G_G = 0.002 − 0.009\,[Kg/s.m^2]$ (max area) $x \leqslant 0.02$	Bubbly
Khushnood et al. [20]	Lit. review				Bubble; Intermittent; Dispersed

| Ribatski and Thome [21] | Lit. review | | | [-] |

Flow pattern recognition is achieved by the analysis of various experimental parameters. A review is provided by Noghrehkar et al. [16], Bertola [38], Rajković et al. [35]. The main types of instrumentation employed in flow pattern identification are: X-ray attenuation, absolute and differential pressure transducers, electrical resistive and impedance void probes, fiber optic probes and visual recording devices.

The techniques of identification from processing of the measured signals are: visual inspection of the flow, shape analysis, fluctuation analysis, statistical moments, PDF, PSD, correlation dimension, space-time analysis and fractal techniques, namely by estimating the correlation dimension.

An overview of the techniques available in the two-phase community for the classification of flow patterns is presented here. The goal is to give a fuller understanding about the origins of the approaches and data analysis methods employed in the present experimental work.

3.1.2 Fluctuations in two phase flow: milestones of the two phase flow spectral analysis, the chordal void fraction analysis

The study of Jones and Zuber [24]

Jones and Zuber state: *two phase flow is a macroscopic conglomeration and not to be treated on the whole as a single fluid. Hence, point differentials are not adequate in themselves to completely describe the system behavior because, at one instant, one phase exists and one set of relations would hold, whereas, at the next instant the fluid will change and the alternate set of equations would govern.* Extensive experimental campaigns are required and necessary to allow a better understanding of the phenomenon. The authors propose a simplification of the overall flow pattern classification suggested by the statistical data and the development of an objective flow pattern discriminator for the three major classifications: *bubbly flow, slug flow* and *annular flow.* The data suggest that in the overall view, slug flow is a simple transitional flow, periodically fluctuating between bubbly flow and annular flow, and thus is simply a recurring time combination of the latter two independent regimes.

The authors identified the chordal void fraction, measured by a X-ray technique, as the sensible quantity to characterize the flow. Experiments were carried out in an air/water facility under adiabatic conditions. The test section was a rectangular vertical channel. The X-ray technique was earlier introduced and developed by Pike et al. [40]. Jones and Zuber point out that considerable fundamental information regarding the structure of two-phase flow may be obtained from the statistical behavior of the void fraction. From this point of view, the work of Akagaw et al. [43], [44] and [45] support this hypothesis by showing a direct correlation between void fraction and pressure drop fluctuations in two-phase flows. The link between these two physical quantities will be found to be of fundamental interest. A more extensive and detailed description of the work is available in the PhD thesis of Jones [22] and in the paper of Jones and Zuber [23].

Probability Density Function (PDF) Jones and Zuber expect the following behavior according to the paper of Delhaye from the 1969 (see [24]):

⋄ *Bubbly-like flows*: single peaked PDF at low void fractions with a large count ratio, n_i/N occuring at low void fraction while small ratios would exist in $\Delta\varepsilon_i$'s at higher values of ε.

⋄ *Annular-like flows*: single peaked PDF at high void fraction with a large count ratio at high void fraction.

⋄ *Slug-like flows*: twin peaked PDF with one at low void fraction characteristic of bubbly flow, and one at high void fraction characteristic of annular flow. The data suggest that in an overall view, neglecting the fine structure, slug flow is simply a transitional flow, periodically fluctuating between bubbly flow and annular flow, and thus is simply a recurring time combination of the latter two *independent* regimes.

These expectations gained a strong support from their experimental campaign. Jones and Zuber noted that the transition from bubbly to slug flow was delineated by the appearance of a second maximum in the PDF at high void fractions. The authors stated: *absolutely no subjectiveness was required to determine the appearance or disappearance of bridging along the measurement chord. It is felt that the probability density method presented an uniquely objective method for flow pattern determination.*

Furthermore, one can say the following:

◇ *Slug-like flow*: localized condition characterized by the appearance of two separate and statistically significant localized maxima in the void fraction PDF. *The two key expressions are "localized condition" and "statistically significant". A flow pattern could occur at one point in, say, rod bundle, another flow pattern could occur in another region. In order to be statistically significant, the maximum involved must be clearly existent when taken in consideration of the local measurement irregularities of the PDF.*

◇ *Bubbly and Annular flows*: it would simply be determined by the non-occurrence of slug flow coupled with the appropriate void fraction. If the low-void half of the PDF is analyzed, it is difficult to determine the difference between a slug and typical a bubbly flow situation. Similarly for the high-void half, it looks and behaves quite like annular flow. Therefore, it is suggested that slug flow may be treated as a transition flow which occurs in a periodic time combination of bubbly and annular-like flows.

Jones and Zuber were also able to determine the slug residence time by the PDF technique. The ratio of slug residence time to bubble residence time t_s/t_b was computed as the ratio of the two peaks of the probability density function encountered in slug flow. A graphical representation of the results is given in Fig. (3.24), Fig. (3.25) and Fig. (3.26). The PDF function is plotted as a function of the void fraction respectively for bubbly, annular and slug flows.
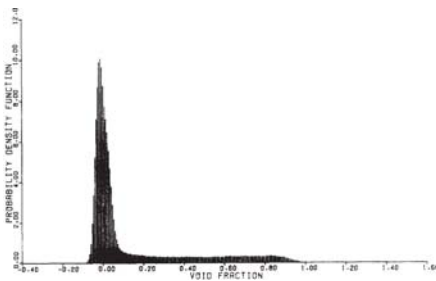
Figure 3.24: Bubbly-like flow, Jones and Zuber [24]
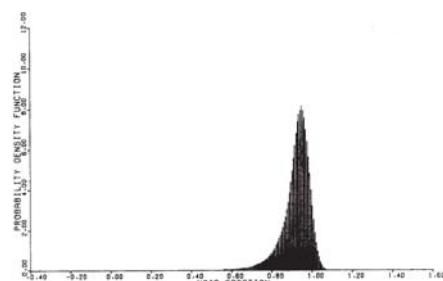
Figure 3.25: Annular-like flow, Jones and Zuber [24]
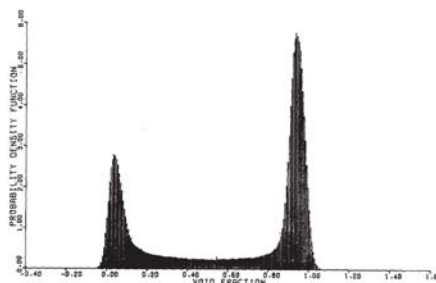
Figure 3.26: Slug-like flow, Jones and Zuber [24]

Power spectral densities (PSD)   Following the need to estimate the slug and bubble length (L_s, L_b), Jones and Zuber estabilished another milestone in the statistical analysis of two phase flow. The importance of the power spectral density of the chordal average void fraction was stated. If the frequency f is obtained by the frequency analysis of the void fraction signal in the time domain, the period between two successive slugs T^* can be evaluated as a reciprocal. Knowing the t_s/t_b ratio by the PDF analysis and the measured void fraction, then:

$$L^* = u_G T^* = \frac{j_G}{\varepsilon}\frac{1}{f} \qquad L_s = L^*\frac{1}{1 + \frac{t_s}{t_b}} \qquad L_b = L^*\frac{1}{1 + \frac{t_b}{t_s}} \tag{3.1}$$

(L^* is the distance between the center of two succesives slugs)

The slug frequency is obtained by the frequency analysis of the void fraction signal in the time domain. The *PSD* of the void fraction signal brings the following information:

⋄ *Slug*: the PSD in this flow pattern indicates strong periodicity, although the spectra are apparently continuous rather than discrete.

⋄ *Bubbly and Annular*: The maximum magnitude of fluctuations in slug flow is larger than the one of either bubbly flow or annular flow. Alternatively, the void fluctuations in bubbly flow appear as completely random with no periodicity. For annular flow the periodicity was not at all definite as the one shown for slug flow, and amounted to a small percentage of void fraction.

The basis of the work carried out from Jones surely constitutes a big step in the development of an analysis technique to investigate the two-phase behavior. However, the X-ray technique is technically difficult to manage, costly and not generally open to the scientific community. The strongest limitation is the impossibility to simply apply it to industrial facilities.

The Alekseev et al. [31] study

This study is situated in the same general field as the work of Jones. A β-ray technique was employed and coupled with the measurement of temperature fluctuations. Experiments were carried out in a vertical circular channel. The authors did not specify the nature of the fluid used. The authors, applying statistical and spectral analysis to the temperature fluctuations and void fraction, arrived at similar conclusions as above. This paper provides important support to the work of Jones and Zuber [24], and demonstrates that PDF analysis can be successfully applied to a wider family of signals than just X-ray.

The Vince and Lahey [28] study

This study is a further step in the development of the approach of Jones and Zuber [24]. The experimental results are representative for air/water mixtures with adiabatic conditions in a circular, vertical channel. The X-ray attenuation technique was selected to provide the statistical data. Six chordal void fractions were acquired on the cross section of a vertical tube. Fig. (3.27) refers to the proposed flow regime classification for vertical two-phase flow: Vince and Lahey included the *churn turbulent* flow to the Jones and Zuber [24] classification.

The authors stated that the statistical moments of the acquired signals completely quantify the information contained in the two-phase flow. The authors use the first four statistical moments (mean; variance; skewness; kurtosis), defined in appendix A, to characterize the void fraction density distribution. *These moments have physical significance and can be related to the various two-phase flow regimes. The variance of the void distribution should be small in bubbly and annular flows. These flows should also be leptokurtic*
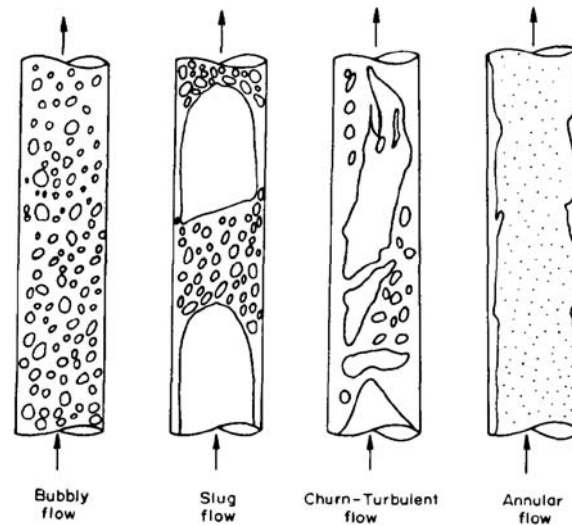
Figure 3.27: Flow regimes classification, vertical flow, Vince and Lahey [28]

and possess (positive or negative) skewness. Slug flow void distributions, on the contrary, should have a large variance but small skewness. The slug flow void distribution is normally platykurtic. Flow regime identification should thus be possible with these moments.

These moments can be computed from the measured channel chordal void fraction, and can be used to get information on flow regime. Further comments are made below:

PDF and PSD results:

⋄ Bubbly flow indicates unimodal PDF. A sharp peak is also observed at zero void fraction due to the measurement associated with liquid phase only. For slug flows the PDF becomes bimodal. *The circular conduit geometry used in this study indicates that the number of modes possessed by a PDF is not adequate for the flow regime identification. However, calculations of the moments can provide an objective indicator.*

⋄ About the slug-flow regime, the PSD indicates a specific behavior: a sharp peak of large magnitude is observed at low frequencies. As expected the peak moves at higher frequencies as the liquid velocity increases.

⋄ Statistical moments of the PDF distribution seem to provide a tool for flow pattern recognition. The authors state: *any practical flow regime indicator should be independent of fluid velocity.* Thus, the authors compare the data acquired at zero liquid flow with the ones at non-zero. In such a case, the authors wanted to provide a methodology to detect the two phase flow pattern by the use of only the chordal average void fraction signal. This approach should allow a *"simple"* measurement and flow pattern identification without having to take care of the main fluid parameters.

⋄ The analysis of the PSD data added new information about the nature of the two phase flow according to the flow pattern. A wide band in the low amplitude spectrum was found to be associated with *bubbly flow*. A low frequency peak of large amplitude was associated with the characteristic frequency of *slug flow*. A medium width band with an amplitude spectrum corresponded to *annular flow*. The authors stated that: *annular flow is composed of the frequencies of the liquid film thickness variation and roll waves moving along the liquid film/vapor interface, and thus produces a spectrum of medium width, which increases with the liquid velocity.*

◇ *All moments associated with the PSD exhibit a strong dependence on superficial liquid velocity. This characteristic is very undesirable for a flow regime indicator because any correlation would require knowledge about the liquid superficial velocity. Void fraction measurements are sufficiently difficult, the requirement of a simultaneous liquid velocity measurement renders the use of PSD moments impractical. Moreover, only the variance of the PSD has possibilities for a flow regime indicator. The skewness and kurtosis are essentially independent of the flow regime. As a result, the moments of the PSD are not considered to be as valuable as the moments of the PDF for the flow regime identification.*

◇ *Due to low velocity studies, the frictional pressure drop is very small. Thus a differential pressure measurement will then produce an accurate estimate of the global void fraction.*
Concluding, the authors point that the PDF variance appears to be the best flow regime indicator and recommended it as first choice.

The Lowe and Rezkallah [47] study

In this paper the authors investigate two-phase flow under micro-gravity conditions. Experiments were done with water and air under adiabatic conditions. A concave parallel plate capacitance sensor was employed to measure the chordal two-phase void fraction. The PDF of the void fraction signals was computed afterwards. For comparable flow regimes, the results optimally matched the results of Jones and Zuber [24] as visible in Fig. (3.28), Fig. (3.29) and Fig. (3.30) and constitutes a valid and authoritative support to the PDF approach. Furthermore, the analysis continues with the characterization of transitions between flow regimes by PDF analysis and visual observation. The authors proposed and verified a flow pattern map based on an objective flow indicator to predict the transitions between the different flow regimes.
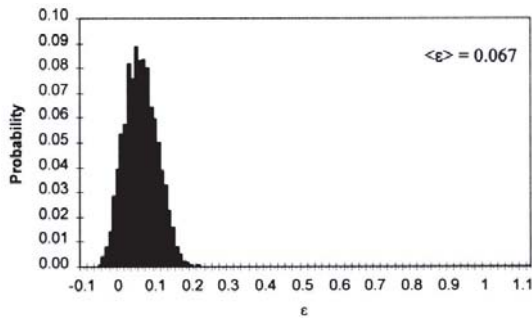
Figure 3.28: Bubbly-like flow, Lowe and Rezkallah [47]
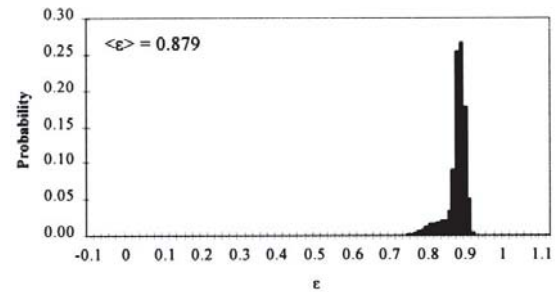
Figure 3.29: Annular-like flow, Lowe and Rezkallah [47]
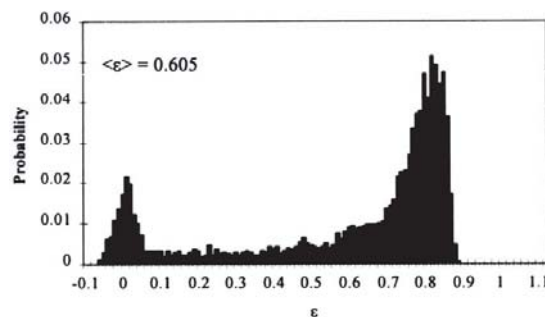
Figure 3.30: Slug-like flow, Lowe and Rezkallah [47]

3.1.3   Local void fraction analysis

Noghrehkar et al. [16]

Their test stand was a horizontal tube bundle with upward flow. Experiments were carried out under adiabatic conditions with air and water. An electrical resistivity void probe was employed to measure the local void fraction. With this instrument, the change in electrical conductivity of the fluid was measured. From this point of view, experiments with air and water lead to a suitable experimental technique: the difference of electrical resistivity of the two fluids is significant. This is not the same for liquid refrigerants and their vapors as used in the present thesis: the change in electrical conductivity for a fluid and its vapor is usually not measurable.

The signal provided from the descibed instrumentation was post-processed by the PDF approach. The flow patterns identified were: *bubbly, intermittent* and *annular* and showed the well-known PDF distributions. From the obtained database, flow regime maps were constructed using the PDF technique.

An intermittent flow regime existed within the staggered bundle over a wide range of homogeneous void fractions, but the void fluctuation amplitude remained very low near the wall, which is representative for bubbly flow. Even under the same flow conditions, the flow regimes that exist near the shell wall and well inside the bundle can be quite different. Visual observation of the flow from outside the bundle showed the passage of numerous small bubbles under the flow conditions tested, which would be interpreted as bubbly flow, but the flow regime inside the bundle was in fact intermittent flow. From this the author stated a fundamental point: *visual observations from outside the tube bundle may not reveal the actual flow regime existing inside the bundle under certain flow conditions.* What is remarkable is that the PDF of local void fractions was successfully used in an objective manner to identify the two-phase flow regimes and to construct a flow regime map.

3.1.4   Pressure fluctuations as a flow regime indicator

If the void fraction represents an important feature for flow pattern identification, the pressure drop should not be underestimated. Already starting from the work of Akagawa [43], [44] and [45], a correlation between void and the pressure drop fluctuations in two phase flow has been shown.

The Hubbard and Dukler [29] study

The work of Jones and Zuber [24] represented a milestone in terms of an objective flow regime indicator. Similarly, the two-phase community has developed similar techniques based on the analysis of the pressure fluctuations.

The first attempt in this direction was that of Hubbard and Dukler [29] although related work has been performed by Nishikawa et al. [42]. Hubbard and Dukler [29] used the spectra of wall pressure fluctuations to discriminate between various flow regimes in the case of horizontal flow. Their paper anticipates historically the one of Jones. Hubbard and Dukler [29], stating that *the spectral distribution of the wall pressure fluctuations provided a suitable parameter for flow regime characterization*, thus recognized the capability of spectral analysis. Hubbard and Dukler [29] performed a set of tests in adiabatic conditions with water and air. The channel was circular and horizontal. All the spectral distributions were seen to fall into three broad categories, characterized by the manner in which the energy in the wall pressure fluctuation was distributed among the frequencies observed. It appears that the multitude of flow regime types described in the literature may be redundant. The flow regimes were classified as *separated flow, intermittent flow* and *dispersed flow*.

The character of the trace was distinguished by only two variables, the amplitude of the fluctuations

and their frequency. The authors pointed that the magnitude and frequency of the pressure oscillations encountered in two-phase flow required pressure measuring devices having good frequency response and generating a continuous output signal capable of being recorded. In analyzing the pressure records, pressure fluctuations were analyzed. That is, if p is the instantaneous pressure and $\overline{p}$ is the time average pressure, the quantity $(p - \overline{p})^2$ is subjected to spectral analysis. The analysis provided the frequency distribution of the energy in these fluctuations. These distributions where employed to characterize the flow regimes. The capability of spectral analysis of the wall pressure fluctuations was developed successfully for the characterization and identification of two-phase flow regimes.

Weisman et al. [32]

The authors experimentally investigated air-water mixtures and evaporating Freon 113 in a horizontal circular channel. The following classification was assumed: *plug/bubble*, *stratified*, *wavy*, *slug* and *annular* Visual criteria were established for each of the flow patterns.
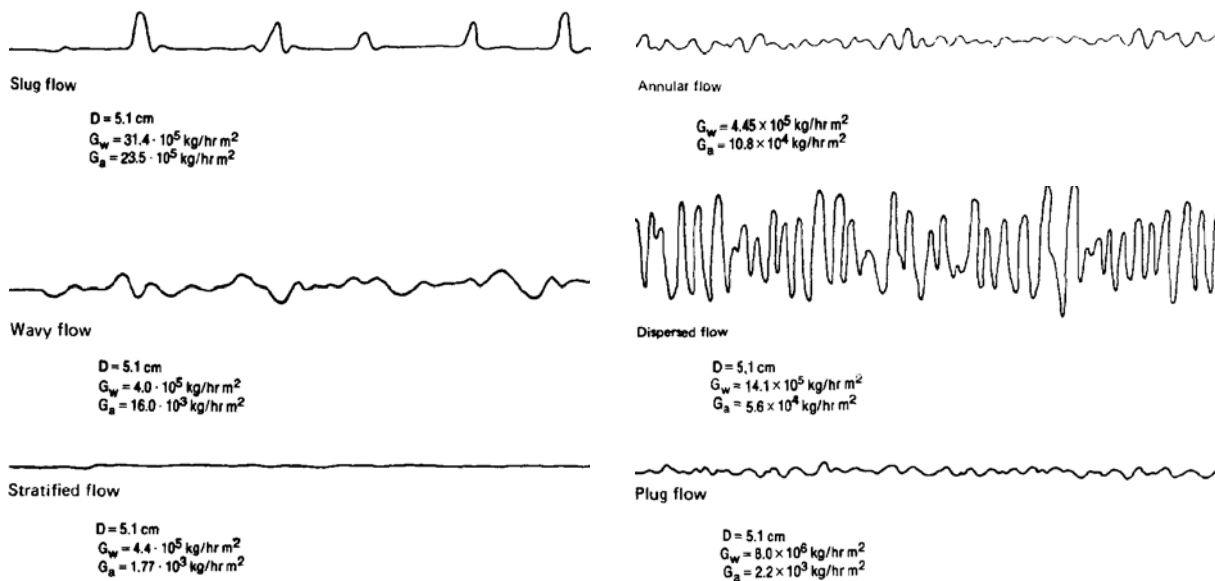
Figure 3.31: Pressure drop fluctuations traces, Weisman et al. [32]

The authors decided to develop relatively simple criteria which could be readily applied to oscillograph traces of pressure drop as reported in Fig. (3.31). The authors propose a criterion for determining flow patterns on the basis of the pressure drop fluctuations. This method was developed for air-water flows and it is based on water and air mass velocities, on the frequency content of the signal, and on the ratio of the amplitude of the trace to the amplitude of a standard slug flow. The method proved to be good at investigated conditions but less so for more complex geometries.

Tutu [25]

An analysis of pressure signals concerning adiabatic air-water flow in a vertical circular channel was presented. The pressure signals from two piezoresistive pressure transducers, axially separated by half of the diameter of the pipe, were registered. The author demonstrated that this approach is capable of characterizing the flow pattern through PDF and statistical quantities of the measured signal. The same concept developed for the void fraction was applied to dynamic pressure signals. In Fig. (3.32), the

pressure transducer layout is depicted. The non-dimensional pressure drop p_{21}^*, see Table 3.2, is bound between 0 and 1, any excursion must be addressed to dynamic effects: *acceleration* and *wall friction*.
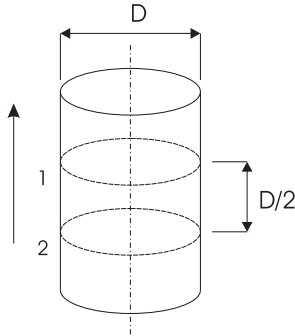
Figure 3.32: Pressure transducers layout installation

p_2, p_1	Pressure signal from lower and upper pressure transducer
$p_2 - p_1$	Pressure drop signal
Δp_s	Hydrostatic pressure component
$p_{21}^* = \frac{p_2 - p1}{\Delta p_s}$	Non-dimensional pressure drop

Table 3.2: Sensible quantities

The subsequent PDF analysis of the pressure drop signal and visual support leads to the successive flow pattern classification. A plot of the PDF traces, for the different flow regimes, as function of p_{21}^*, is given in Fig. (3.33). A comparison with experimental results available in the open literature is possible thanks to the following first approximation $(1 - p_{21}^*) \sim \varepsilon$. Thus, regarding flow pattern identification one can say:

◇ *Bubbly-like flows (1-2)*: characterized by a single peaked PDF centered in the neighborhood of $p_{21}^* = 1 - \varepsilon$ where ε is the average void fraction.

◇ *Slug flow (3-4)*: the PDF is bimodal. The smaller peak corresponds to the passage of Taylor bubbles and is located in the neighborhood of $p_{21}^* = 0$; the larger peak corresponds to the bubbly liquid slugs and is located around $p_{21}^* = 1$.

◇ *Churn regime (5-6) and Annular flow (7)*: the PDF is still bimodal but the magnitude of the peaks is rethat are now degenerating into longer and more frequently occurring gas pockets.

◇ *Annular churn (8)*: similar to annular flow (7) but with a skewness decreased by a factor two. It is expected that for higher air flow rates, the distribution will be even more symmetric.

The analysis of the RMS shows that during the annular regime it is much smaller (almost an order of magnitude) than during churn flow, so the discrimination between the two regimes is easy: $RMS(annular) \ll RMS(churn)$. The authors showed that pressure drop signals, together with statistical quantities can be used to discriminate between the various flow regimes. Further details are also presented in Tutu [39].

Jain and Roy [37]

Static pressure fluctuations at the test section outer wall and instantaneous chordal-average void fraction, were studied in vertical up-flow through concentric annular test sections. R-113, under evaporating conditions, was tested. In this study, the big challenge was the experimental technique proposed: matched piezo-electric pressure transducers for the pressure fluctuation measurements, and a linearized dual-beam X-ray system for the vapor fraction measurements. A sketch of the instrumentation layout is given in Fig. (3.34). This measurement matching results in a set of information of fundamental importance for the evaluation of the experimental technique in two-phase flow; a redundant set of measurements allows a cross checking of the results. Furthermore, the fluctuating static pressure at any point in the flow field consists of contributions from near field sources and from the acoustic pressure field generated far upstream due to turbulent flow through valves, elbows, restrictions, pump and so on. The innovative
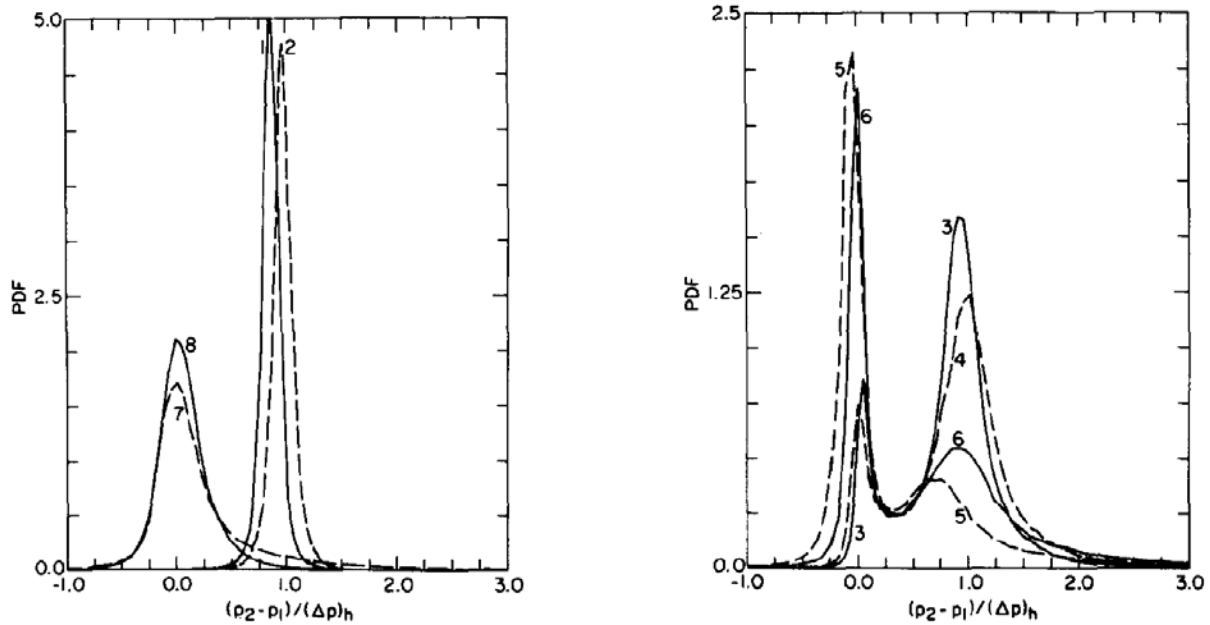
Figure 3.33: PDF of the pressure drop (1-2. bubbly; 3-4. slug; 5-6. churn; 7. annular; 8. annular/churn), Tutu [25]

idea of the authors was to measure only the near-field source contributions. They proposed a *coherence technique* employing two pressure transducers with identical responses. This technique is based on the postulate that at any axial location in the test section, the far-field source generated contribution is uniform over the flow cross-section. According to visual observations, the authors proposed a classification by the following regimes: *bubbly, churn-turbulent-slug* and *churn-turbulent-annular* flows. Their work is summarized below:

Wall static pressure fluctuations   The pressure fluctuation PDFs for bubbly, churn-turbulent-slug and churn-slug-annular flows showed that the obtained curves could be reasonably fitted by a Gaussian distribution as in Fig. (3.35). From a statistical point of view, the Gaussian distributions differ from the fourth moment, the Kurtosis. The presented plot shows an increasing Kurtosis going from bubbly flow to churn turbulent-slug-annular flow and then through churn turbulent slug flow. From the oscillogram analysis, several peaks of comparable magnitudes were identified for *bubbly flow*, a single dominant low-frequency peak at the frequency passage of the slug for the *churn turbulent-slug regime* and a low-frequency peak for the *churn turbulent-slug-annular regime* with a total spectral energy considerably smaller than the ones in the other flow regimes.

Chordal-average vapor fraction fluctuations   The analysis of the PDFs given in Fig. (3.36) leads them to the following considerations:

⋄ *Bubbly*: A single, narrow-peaked distribution occurs in the low vapor fraction region. The small width of the distributions suggests the presence of a relatively homogeneous flow field in the time domain for this flow regime.

⋄ *Churn turbulent-slug regime*: A single, wide-peaked distribution. The larger width of the distribution suggests the presence of a heterogeneous flow field (in terms of vapor agglomeration size and spatial distribution) in the time domain. In this case, the well known double peaked distribution
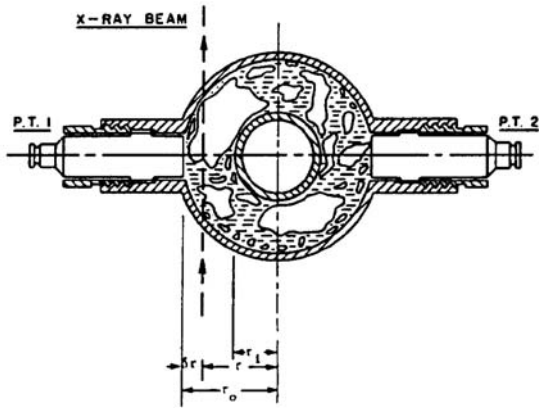
Figure 3.34: Test section view, instrumentation layout (P.T.1-2. piezoelectric pressure transducers), Jain and Roy [37]
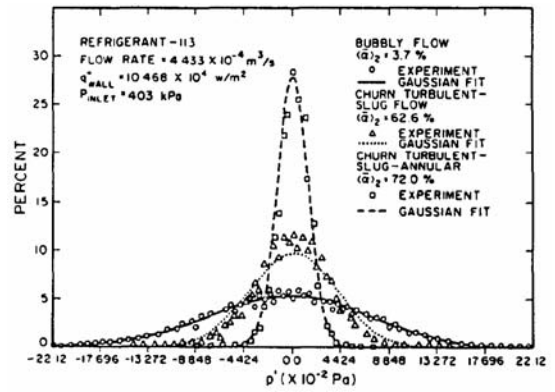
Figure 3.35: PDFs of wall static pressure fluctuations, Jain and Roy [37]
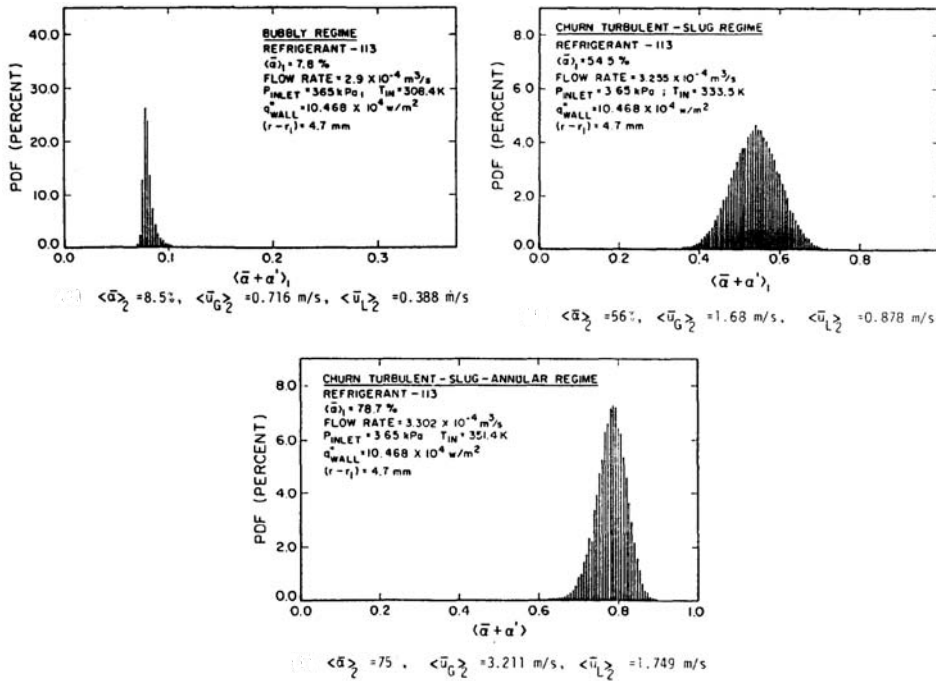
Figure 3.36: PDF of the chordal-average vapor fractions, Jain and Roy [37]

cannot be obtained because of the presence of a relatively high vapor fraction churn turbulent fluid in between the vapor slugs, in place of a very low vapor fraction fluid in air-water experiments.

◇ *Churn turbulent-slug-annular regime*: A single peaked PDFs distribution in the high vapor fraction region. The distribution is much narrower in comparison to the one obtained for the churn turbulent-slug regime.

Coherence of pressure-vapor fraction fluctuations

◇ *Bubbly*: The coherence function indicates a weak correlation between the wall pressure fluctuations and the vapor fluctuation. It appears reasonable to postulate that a part of the wall static pressure fluctuations in bubbly flow is caused by the vapor fraction fluctuations in adjacent regions.

◇ *Churn turbulent-slug regime*: A strong peak was measured. A strong correlation between the passage of vapor slugs and the wall pressure fluctuations was underlined.

◇ *Churn turbulent-slug-annular regime*: The correlation was considered to be rather weak. The effect of the interfacial waves as felt by the outer wall probably becomes considerably dampened due to the presence of a frothy mixture in-between.

This paper constitutes a key reference in our present research field. Firstly, the fluid is a one component boiling flow, which is a big step compared to the main part of the two-phase literature which investigates only air-water mixtures. Secondly, the authors developed two redundant objective experimental techniques for two-phase flow identification proposing and carrying out a strong analysis of the obtained data.

Matsui [27]

Matsui focused on pressure signals as they are relatively easy to obtain and contain sufficient information on the peculiar features of low patterns and conditions in two-phase flow. His experiments covered adiabatic nitrogen-water mixture in a vertical circular channel. The author selected differential pressure fluctuations as the quantity to identify flow patterns. This closely follows the considerations of Jain and Roy [37]. Therefore, differential pressure transducers were installed in such a way that it was possible to differentiate between short and long scales: this follows the work of Tutu [25], [39]. The layout is given in Fig. (3.37) and the computed pressure drops are summarized in Table (3.3).
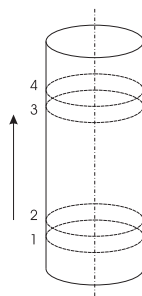
Figure 3.37: Pressure transducers layout installation

R scale	Δp_a Δp_b	$p_1 - p_2$ $p_3 - p_4$
L scale	Δp_c Δp_d	$p_1 - p_3$ $p_2 - p_4$

Table 3.3: Pressure transducers measurement scheme

The author introduced a new approach discriminating between short and long scales:

⋄ *Small intervals - R scale*: They are chosen as the inside radius of the pipe, in order to discriminate a spherical cup bubble or a cluster of small bubbles with half the length of the inside tube diameter. Calling $\widetilde{d}$ the axial distance between the probes, it follows: $\widetilde{d_{12}} = \widetilde{d_{34}} = D/2$

⋄ *Long intervals - L scale*: They are one order of magnitude larger in respect to the R scale to discriminate a developed gas slug, so that: $\widetilde{d_{13}} = \widetilde{d_{24}} \gg D/2$.

Their approach allowed for a more detailed analysis of the two-phase flow bringing to a clear distinction between flow patterns by the analysis of the pressure drop PDF. Their volumetric void fraction was obtained using cut-off valves; a photographic technique was employed for the visual observations. Where Δp_i is the difference of pressure between a pair of pressure transducers i. Δp_{i0} is the differential pressure. We define a non dimensional pressure drop as:

$$\Delta P_i = \Delta p_i / \Delta p_{i0} \qquad (3.2)$$

Assuming that the acceleration and frictional pressure components satisfy $(\Delta p_{acc}, \Delta p_f) \ll (\Delta p_{i0} - \overline{\Delta p_i})$; the term $(1 - \overline{\Delta P_i})$ represents approximately the average void fraction in the section i. The PDF is therefore applied to the quantity: $\Delta P_i^* = 1 - \Delta P_i$. On the L-scale, the pressure measurements indicated low fluctuations, so from ΔP_{LONG}^* it was possible to estimate the average void fraction.
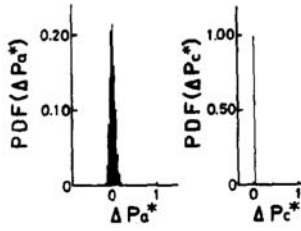
Figure 3.38: Bubbly flow, Matsui [27]
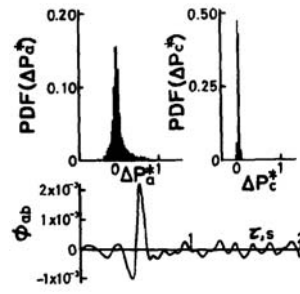
Figure 3.39: Spherical cap bubble flow, Matsui [27]
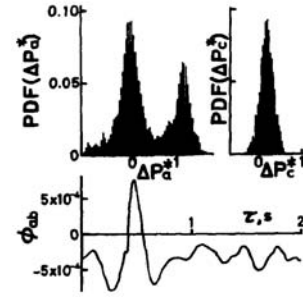
Figure 3.40: Slug flow, Matsui [27]
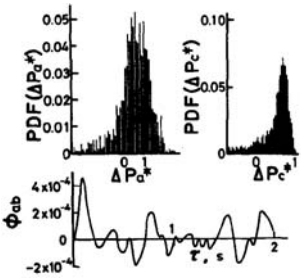
Figure 3.41: Froth flow, Matsui [27]
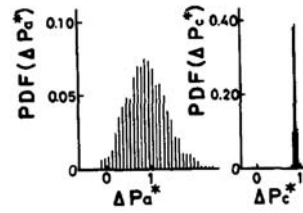
Figure 3.42: Annular flow, Matsui [27]
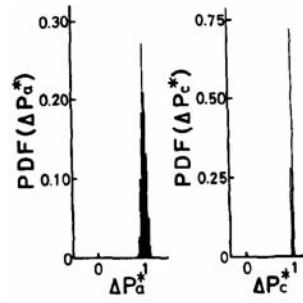
Figure 3.43: Mist flow, Matsui [27]

The beauty of the employed method is that the R-scale and L-scale analysis are complementary, so that when the information from one scale is not sufficient, the other can be used. Results in terms of PDF are reported in Fig. (3.38), Fig. (3.39), Fig. (3.40), Fig. (3.41), Fig. (3.42) and Fig. (3.43). This paper demonstrates the ability to recognize flow regimes through the statistical analysis of static pressure signals. Similarly, the successive work of Matsui [41] and [34] supports the technique be developed in parallel with that of Tutu [25] and [39].

Lin and Hanratty [33]

The authors of this paper describe how a pair of pressure transducers can be used to detect the presence of slugs. They propose that the differential pressure drop is more suited for detecting flow patterns which are steady with respect to time rather than for intermittent flows. The pressure in the front of the slug is low and increases sharply to a much higher value behind the slug. The pressure gradient behind the slug is small, but the pressure remains high. This type of pressure behavior was used to identify the slugs. The upstream pressure measurement detected a blockage from the characteristics of the pressure signal. The downstream pressure measurement was used to determine whether the slug remained coherent. An air-water mixture and boiling R-113 were employed as test fluids.

Two strain gauge pressure transducers with a flat frequency response up to $2\,kHz$ were used. The location of the transducers was such that they were located 200 pipe diameters away from the entry in order to allow the development of the flow. Two sets of parallel wire conductance probes were additionally used during the experiments to measure the heights and velocities of waves and pseudo-slugs. The acquisition system, coupled with the instrumentation, could provide a frequency response up to $1\,[kHz]$.
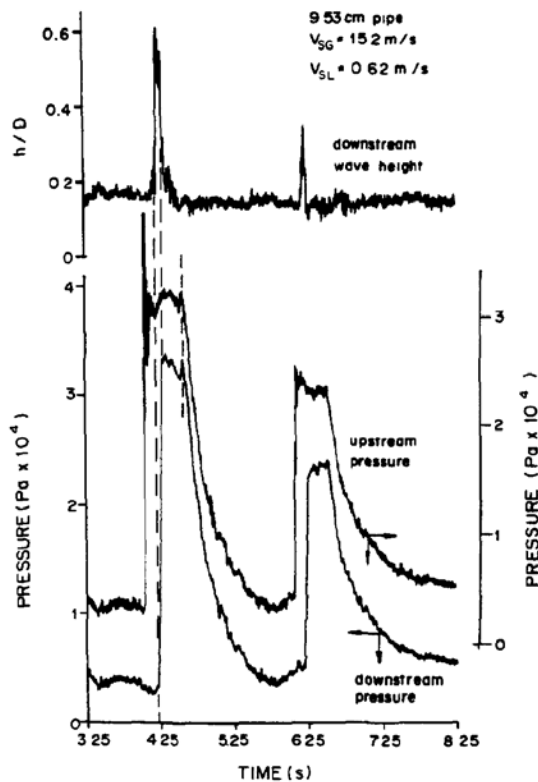
Figure 3.44: Wave-height and pressure-fluctuation measurements in slug flow, Lin and Hanratty [33]
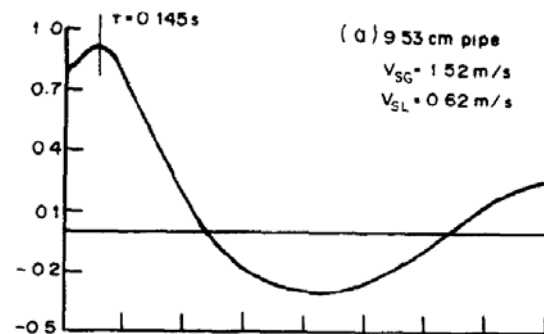
Figure 3.45: Dimensionless cross-correlation function, Lin and Hanratty [33]

Their measurements allowed an evaluation of the height of the liquid to the pipe diameter h/D to be obtained. A plot of wave-height compared to pressure fluctuation relative is presented in Fig. (3.44). The time delay between the arrivals of the two pressure signals gives a means of measuring the slug velocity. It is interesting to note that the use of pressure transducer pairs allows the propagation direction of the pressure wave to be determined by cross-correlation; hence eliminating ambiguities caused by possible pressure reflections from downstream. Analyzing the pressure record and the cross-correlation pressure plot, the authors pointed out that once the slug passes through both pressure taps, the pressure values

at both taps are almost identical.

Ito et al. [36]

These authors investigated air-water adiabatic two phase flows in a vertical circular channel. The authors pointed out that caution is required for the identification of the flow patterns because the flow configuration is quite complex due to the high degrees of freedom, and because the researcher's subjectivity is likely to influence the classification of the flow pattern. This study can be classified as different in respect to conventional discrimination methods using diagrams and parameters. The purpose of this study was to provide a one-dimensional simplified numerical model of the flow pattern and transition in an isothermal vertical pipe, and to explain fundamental aspects, such as the physical reason for the appearance of the flow pattern and for the transition from bubbly flow to annular flow. In this model the flow configuration is represented by the void wave pattern in the flow direction and the irregular bubble movement. The mutual interaction between bubbles in the local space does not attract attention. The numerical results were validated through the result of an experimental campaign. The flow behavior was observed with a high speed video camera. The PDF of the differential pressure signal was used to identify the flow pattern. The authors classified the flow pattern as: *bubbly, slug, churn* and *annular* flow. This simplified $1D$ model shows one approach that is capable of capturing the investigated two-phase phenomena.

Liebenberg et al. [30]

The experimental conditions are for a condensing refrigerant fluid in horizontal circular internally finned tube. This paper represents one of the more complete and recent applications of the spectral analysis for the objective determination of flow patterns. Pressure traces were sampled. Their character was distinguished by the amplitude of the fluctuations and their frequency. Some flow regimes, like stratified and wavy flow, can be detected from the time traces of the wall pressure oscillations without the need to consider the power spectrum. As visible in Fig. (3.46) the traces have characteristic "triangular" pulses with much larger amplitudes than the other flow patterns. However, the pressure time records were not sufficient to distinguish the other regimes. In such cases, the PSD distribution of the wall pressure is employed, see Fig. (3.47).

The authors point out that: *the pressure traces are typical examples of signals that are neither periodic nor transient (from a statistical point of view), thus rendering classical Fourier series analysis ineffective. A PSD distribution of the pressure traces would render a suitable generalized harmonic analysis.*

At this point it is important to point out that the authors remind us that there are distinct similarities between the PSDs of the different refrigerant fluids. Focusing on smooth-tubes, a classification according to the frequency content of the signal is proposed. Their flow pattern identification technique, applied in the field of condensation, could be transposed to evaporation.

3.1.5   Recent developments in objective flow regime identification

The identification and classification of two-phase flow patterns through signal analysis is still open to new techniques and concepts. The aim is to take a further step in the direction of objective flow regime identification by finding new methods capable of overcoming the limitations of more classical approaches such as statistical, PDF and PSD analysis.

◇ Franca et al. [46] experimented on the use of a fractal technique: analyzing the results in terms of correlation coefficients and Hurst analysis, the authors demonstrated that fractal techniques offer a promising way to objectively classify flow patterns.

◇ Rajković et al. [35] combined concepts from nonlinear dynamics theory, spectral operator theory and information theory to produce a method for the identification of flow regimes in two-phase
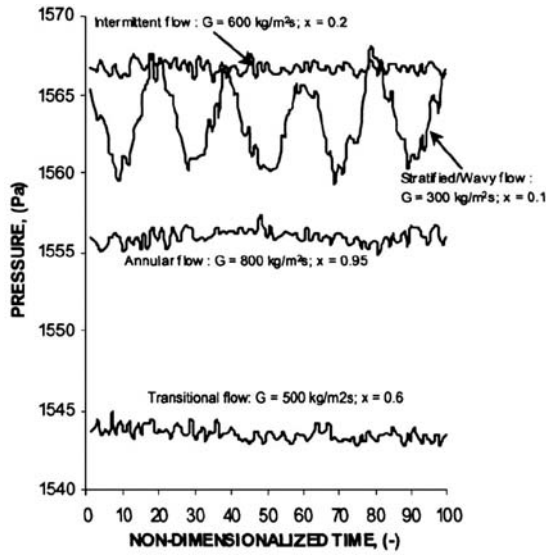
Figure 3.46: Sample wall pressure (gauge pressure), condensing R407 in a smooth tube, Liebenberg et al. [30]
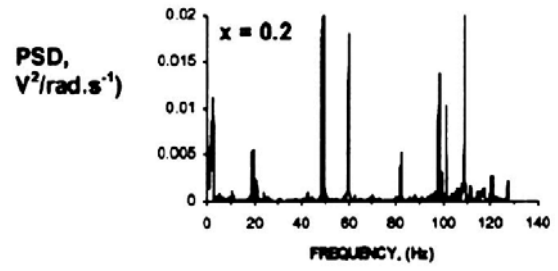
Figure 3.47: Example of PSD distribution and observed flow pattern for intermittent (slug and plug) flow, Liebenberg et al. [30]

flows. The flow regimes were classified according to their complexity, where the complexity was defined via the Gibbs-Boltzman-Shannon entropy.

◇ As a last significative example, Finally, Bertola [38], focusing on the plug and slug flow transition phenomena, successfully identified the phase density function as a basis of a method able to distinguish between different flow patterns.

All these methods appear to be promising and powerful, but they still have not found wide use in the two-phase community. Table (3.4) summarizes all the studies mentioned in this section.

Table 3.4: Two-phase fluctuations analysis: literature

Author	Fluid	Flow direction	Tube characteristics	Test conditions	Instrumentation	Sensible quantity	Flow pattern
Jones and Zuber [22], [23], [24]	Air-Water Adiabatic	↑	Rectangular channel $4.98x63.50\,[mm]$	$j = 0 - 37\,[m/s]$ $j_G = 0 - 33.1\,[m/s]$ $j_L = 0 - 3.05\,[m/s]$	X-ray $f_{response} > 1\,[kHz]$	Linearized void PDF; PSD	Bubbly; Slug; Annular (transitional)
Tuttu [25]	Air-Water Adiabatic	↑	Circular channel, PVC $D_i = 52.2\,[mm]$	$j_G = 0.085 - 11.76\,[m/s]$ $j_L = 0.011 - 0.874\,[m/s]$	Piezo pressure transducer $f_{response} = 65\,[kHz]$ $f_{samp} = 3.2 - 25\,[kHz]$ $f_{fil} = 1.6 - 12.5\,[kHz]$	Pressure/pressure drop fluctuations PDF; Statistical moments (first 4) order	Bubbly; Slug; Annular; Churn
Tuttu [39]	=	=	=	$[-]$	= $f_{samp} = 12.5\,[kHz]$ $f_{fil} = 5\,[kHz]$	=	Bubble-slug transition
Matsui [27]	Nitrogen-Water Adiabatic	↑	Circular channel, Plastic $D_i = 22\,[mm]$	$j_G = 0 - 10\,[m/s]$ $j_L = 0 - 1.5\,[m/s]$	Piezo pressure transducer $f_{res} = 600\,[kHz]$ $f_{samp} = 0.1\,[kHz]$ $f_{fil} = 20\,[Hz]$	Differential pressure fluctuations PDF; Cross correlation; Variance; Mean	Bubbly; Slug; Annular; Mist
Matsui [34]	=	=	=	$j_G = 0 - 12.5\,[m/s]$ $j_L = 0 - 0.49\,[m/s]$	=	Statisticals moments (first 2)	Bubbly; Slug; Annular; Mist (automatic identification)
Matsui [41]	Nitrogen-Water Adiabatic	→	Circular channel, Plastic $D_i = 20\,[mm]$	$j_G = 0 - 40\,[m/s]$ $j_L = 0.03 - 3\,[m/s]$	=	Differential pressure fluctuations PDF; Variance; Statistical moments (first 2)	Bubble; Plug; Slug; Annular; Separated
Vince and Lahey [28]	Air-Water Adiabatic	↑	Circular channel $D_i = 25.4\,[mm]$	$j_G = 0 - 4.24\,[m/s]$ $j_L = 0 - 0.5\,[m/s]$	X-ray $f_{fil} = 0.1\,[kHz]$	Chordal average void PDF; PSD; Statistical moments (first 4)	Bubbly; Slug; Churn; Annular
Hubbard and Dukler [29]	Air-Water Adiabatic	→	Circular channel, Pyrex type $D_i = 25.4 - 12.7\,[mm]$	$G = 0.136 - 60.76\,[kg/s.m^2]$ $\dot{m}_G = 0.0001 - 0.069\,[kg/s]$ $\dot{m}_L = 0.0121 - 2.14\,[kg/s]$	Fast response transducer sensing pressure $f_{samp} = 31.25\,[Hz]$	Spectral distribution of wall pressure fluctuations	Separated; Intermittent; Dispersed

Reference	Fluid / Condition		Geometry	Operating conditions	Measurement technique	Analysis	Flow patterns
Liebenberg et al. [30]	R22 R407c R134a Condensat.	→	Circular metallic finned tube $D_i=17.27[mm]$ $D_o=19.05[mm]$	$G=300-800[kg/m^2.s]$ $x_i=0.05-0.15[-]$ $x_o=0.85-0.95[-]$ $T_{sat}=40[°C]$	Pressure transducer Video recording $f_{acq}<140[Hz]$	PSD; Amplitude	Intermittent; Annular; Mist; Stratified; Wavy
Alekseev et al. [31]	[-]	←	Circular channel $D_i=7.6[mm]$	$j=0.05-0.52[m/s]$ $x_i=<0-0.064[-]$ $q=0.8.10^6[W/m^2]$ $p=0.4.10^6-2.9.10^6[Pa]$ $T=20-170[°C]$	β-ray $f_{acq}=80[Hz]$ Temperature $f_{acq}=80[Hz]$	Chordal void Spectral quantities	[-] (Frothlike flows)
Weisman et al. [32]	Air-Water Freon 113 Evaporation	→	Circular channel, Glass $D_i=12/25/51[mm]$	$G_G=0.14-56[kg/s.m^2]$ $G_L=14-14.10^3[kg/s.m^2]$	Pressure transducer	Pressure drop fluctuations Frequency and amplitude analysis	Plug-bubble; Stratified; Wavy; Slug; Annular; Dispersed
Lin and Hanratty [33]	Air-Water Adiabatic	→	Circular channel $D_i=25.4/95.3[mm]$	$j_G=0-70[m/s]$ $j_L=[-][m/s]$ $D_i=2.54[mm]$ $j_G=0-33[m/s]$ $j_L=0.166-1.01[m/s]$ $D_i=9.53[mm]$	Strain gauge pressure transducer $f_{response}=2[kHz]$ $f_{acq}=1[kHz]$ Parallel wire conductance probes	Pressure Amplitude; Cross-correlation	Slug
Rajković et al. [35]	Air-Water Adiabatic	→	Circular channel $D_i=25/50[mm]$	$j_G=0.32-6.5[m/s]$ $j_L=1.11[m/s]$	Absolute and differential pressure transducer diaphragm type (sub-miniature wet/wet) $f_{response}=5[kHz]$	Pressure fluctuaction Spatiotemporal decomposition: flow regime identification by complexity identification (by Gibbs-Boltzman-Shannon entropy)	Elongated bubble (plug); Slug (and transition)
Ito et al. [36]	Air-Water Adiabatic	←	Circular channel $D_i=14[mm]$	$j_G=0.02-19.02[m/s]$ $j_L=0.054-0.162[m/s]$	Pressure transducer High speed camera recording	Differential pressure signal PDF	Bubbly; Slug; Churn; Annular

Reference	Fluid; Condition	Flow	Geometry	Flow conditions	Technique	Measured quantities	Flow regimes
Jain and Roy [37]	R113; Evaporation	↑	Annular channel $D_a = 13.4\,[mm]$; $D_o = 38.1\,[mm]$ Plexiglass (Pressure measurements); $D_o = 38.1\,[mm]$ Pyrex; Alluminium (X-ray measurements)	$\dot{V}_i = 2.72.10^{-4} - 5.32.10^{-4}\,[m^3/s]$; $p_i = 350.10^3 - 410.10^3\,[Pa]$; $q_a = 1.047.10^5 - 1.31.10^5\,[W/m^2]$; $\Delta T_{sub,i} = 8.3 - 69.4\,[K]$	Piezo pressure transducer (PCB); X-ray; Capacitance probe; $f_{cut-off} = 40\,[Hz]$	Pressure/Differential pressure fluctuations; Intensity (RMS); PDF; Autopower spectral density function; Instantaneous chordal average void fraction; PDF; Autopower spectral density function; Volume-averaged mean vapor fraction	Bubbly; Slug; Churn; Annular
Bertola [38]	Air-Water; Adiabatic	→	Circular channel $D_i = 80\,[mm]$	$j_G = 0.3 - 8\,[m/s]$; $j_L = 0.6 - 2\,[m/s]$	Single-fiber optical probe $f_{samp} = 2\,[kHz]$	Statistical quantities; Phase density function time series; PDF; PSD	Gas-liquid intermittent subregimes and transition: Plug (or elongated bubble flow); Slug flow
Pike et al. [40]	Steam-Water; Adiabatic Evaporation	→	Circular channel	$[-]$	X-ray	Chordal average void	Annular (experiments were focused on the experimental technique development)
Nishikawa et al. [42]	Air-Water; Adiabatic	↑	Circular channel, Acrylic resin $D_i = 26\,[mm]$	$j_G = 0.03 - 8\,[m/s]$; $j_L = 0.01 - 3\,[m/s]$	Strain gage pressure transducers $f_{response} < 15\,[Hz]$	Pulsating pressure; Standard deviation; Frequency fluctuations; Spectral density	Bubbly; Slug; Froth; Annular (transitions)

Reference	Fluid / Conditions	Dir.	Geometry	Superficial velocities	Measurement technique	Analysis parameters	Flow patterns
Akagawa et al. [43], [44], [45]	Air-Water Adiabatic	↑	Circular channel, PVC $D_i = 27.6\,[mm]$	$j_G = 0.1 - 2\,[m/s]$ $j_L = 0 - 1.5\,[m/s]$	Differential pressure transducers Electrod probes Quick shut-off valves $f_{response} < 20\,[Hz]$	Pressure drop fluctuactions Probability distribution; Mean; Standard deviation; Amplitude; Power spectrum Void fluctuactions Volumetric mean void fraction	Slug
Nogherehkar et al. [16]	Air-Water Adiabatic	↑	Horizontal tube bundle Upward cross-flow $D_o = 12.7\,[mm]$ $s/D = 1.47$ Staggered (equilater) 5 x 26 In-line 5 x 24	$j_G = 0.02 - 3.9\,[m/s]$ $j_L = 0.05 - 1\,[m/s]$	Resistivity void probe $f_{samp} = 5\,[kHz]$	Local void fluctuaction PDF	Bubbly; Intermittent; Annular
Franca et al. [46]	Air-Water Adiabatic	→	Circular channel, Plexiglas $D_i = 19\,[mm]$	$j_G = 0.24 - 16.45\,[m/s]$ $j_L = 0.36 - 6.80\,[m/s]$	Variable differential reluctance pressure transducers $f_{res} = 5\,[kHz]$	Transient pressure drop PDF; PSD; Correlation dimension ν; Hurst dimension H (fractals technique)	Wavy; Plug; Slug; Annular
Lowe and Rezkallah [47]	Air-Water Adiabatic Microgravity	[−]	Circular channel $D_i = 9.525\,[mm]$	$j_G = 0.10 - 20.94\,[m/s]$ $j_L = 0.03 - 3.03\,[m/s]$	Concave parallel plate capacitance sensor $f_{res} = 100\,[kHz]$ $f_{char} = 100\,[kHz]$ $f_{char} < 100\,[kHz]$ $f_{samp} = 1024\,[Hz]$ High speed camera	Void fraction time trace PDF	Bubbly; Slug; Transitional; Annular

3.2   Void fraction prediction method

Combining the continuity equations for the liquid and gas phases, and accounting for the definition of cross-sectional vapor quality and velocity ratio S (ratio of mean gas velocity to the mean liquid velocity), the void fraction ε is obtained:

$$\varepsilon = \left[1 + S \frac{\rho_G}{\rho_L} \left(\frac{1-x}{x} \right) \right]^{-1} \tag{3.3}$$

In the case of homogeneous flow, the velocity ratio is equal to 1 and equation Eq. (3.3) can be solved. As pointed by Ribatski and Thome in [49], several authors have measured void fraction values significantly different than those predicted by the homogeneous model. Ribatski and Thome in [49] reviewed the models proposed in literature. The Feenstra et al. [50] model is employed in the present thesis as the void fraction prediction method, since they found that this was able to predict void fractions for tube bundles. By non-dimensional analysis, the authors identified four dimensionless groups governing the velocity ratio. Fitting their experimental data, Feenstra et al. obtained:

$$S = 1 + 25.7(Ri\,Cap)^{1/2} \left(\frac{s}{D} \right)^{-1} = \frac{u_G}{u_L} \tag{3.4}$$

In this model, the basic length scale is assumed to be the gap between two tubes a. The pitch velocity is also considered. From these assumptions it follows that:

$$Ri = \frac{(\rho_L - \rho_G)^2 g\,a}{G^2} \qquad Cap = \frac{\mu_L u_G}{\sigma} \tag{3.5}$$

where Ri is the Richardson number (ratio between buoyancy force and inertial force) and Cap is the the Capillary number (ratio between Weber and Reynolds number, it represents a ratio between the viscous force and the surface tension force).
An iterative procedure is needed for the computation: a guess value of the gas velocity u_G is imposed and then the parameters defined through equations Eq. (3.5), Eq. (3.4) are evaluated. The void fraction ε is now known by Eq. (3.3). Finally a new value of the gas velocity is re-computed by Eq. (3.26), closing the loop of the iterative procedure.

3.3   Pressure drop

3.3.1   Single phase pressure drops in tube bundles

The single phase pressure drop, can be split into two main contributions:

- ◇ Gravitational component, since the tube bundle configuration is vertical, the difference of pressure due to the action of the column of liquid must be evaluated. This component is expressed as follows:

$$\Delta p_h = \rho g h \tag{3.6}$$

- ◇ Fluid friction on the tubes, shell walls and the blockage effect induced by the presence of the tubes.

Focusing on the frictional component: the single phase pressure drop across tube bundle is a function of the mass velocity of the fluid through the bank bundle, its geometry and dimensions, and the physical properties of the fluid. A generic non-dimensional parameter ξ can be introduced:

$$\Delta p_f = \xi N \frac{G^2}{2\rho} \tag{3.7}$$

where $\xi = \xi(Re, geometry)$ and N characterizes the number of tube rows in the bundle. This last parameter is mostly defined as the number of major restrictions to the fluid flow. It can be defined in different ways according to the employed approaches. The Reynolds number Re is defined as follows using the minimal cross-sectional area of the flow to calculate G:

$$Re = \frac{GD}{\mu} \tag{3.8}$$

Geometry
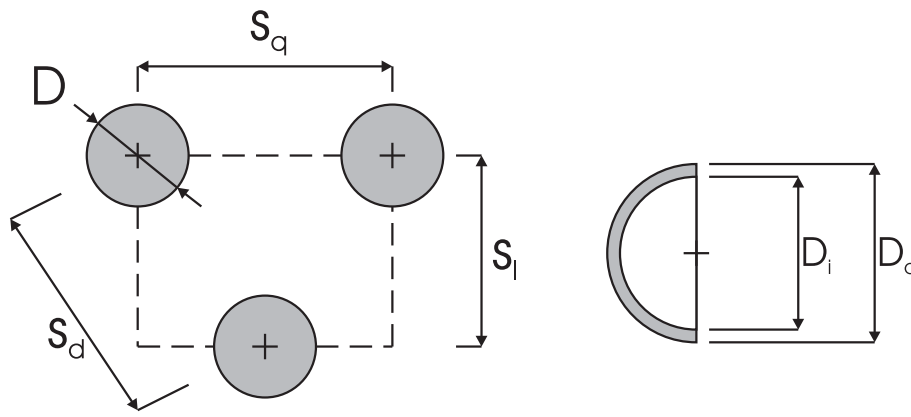
Figure 3.48: Arrangement

The parameters s_q, s_l, s_d are the transverse, longitudinal and diagonal spacings. They are usually divided by the tube diameter in order to obtain the non-dimensional parameters a, b and c. The geometry of the tube bundle in non-dimensional form is represented as:

$$a = \frac{s_q}{D_o} \qquad b = \frac{s_l}{D_o} \qquad c = \frac{s_d}{D_o} \tag{3.9}$$

The equivalent diameter of the tube bundle can be computed as follow:

$$d_{gb} = 4 \frac{Flow\,Area}{Heated\,Perimeter} = \left(\frac{4ab}{\pi} - 1\right) D_o \tag{3.10}$$

The following distinctions are made:

$$b \geq \frac{1}{2}\sqrt{2a+1} \qquad \text{Staggered with narrowest cross section perpendicular to the flow direction}$$

$$b < \frac{1}{2}\sqrt{2a+1} \qquad \text{Staggered with narrowest cross section along the diagonal}$$

For a staggered configuration, with narrowest cross section perpendicular to the direction of the flow, equations Eq. (3.11) are valid. They link together the free stream velocity u_f, the velocity in the narrowest cross section u_e, and the average velocity in the constriction u_v:

$$u_v = \frac{1}{\left(1 - \frac{\pi}{4a}\right)} u_f \qquad u_e = \frac{a}{(a-1)} u_f \tag{3.11}$$

The most used correlations to predict single-phase frictional pressure drop on plain tube bundles are the ones presented by Žukauskas & Ulinska [52] and Gaddis & Gnielinski [53].

Žukauskas and Ulinska

As previously pointed out, a non-dimensional parameter ξ is defined in order to describe the pressure drop through a tube bundle. Žukauskas calls this parameter ξ the Euler number Eu, which represents the ratio between the pressure forces and the inertia forces. Using the Euler number, the single phase pressure drop, can be computed:

$$\Delta p_f = Eu N_R \frac{G^2}{2\rho} \tag{3.12}$$

In this case, the parameter N becomes the number of tube rows N_R. Equations of the Euler number are given for different ranges of the Reynolds number below:

$$3 < Re \leq 10^3 \qquad \frac{Eu}{k_1} = 0.795 + \frac{0.247\,10^3}{Re} + \frac{0.335\,10^3}{Re^2} - \frac{0.155\,10^4}{Re^3} + \frac{0.241\,10^4}{Re^4} \tag{3.13}$$

$$10^3 < Re < 2.10^6 \qquad \frac{Eu}{k_1} = 0.245 + \frac{0.339\,10^4}{Re} - \frac{0.984\,10^7}{Re^2} + \frac{0.132\,10^{11}}{Re^3} - \frac{0.599\,10^{13}}{Re^4} \tag{3.14}$$

where k_1 is a parameter accounting for geometry. It is a function of the aspect ratio $\left(\frac{a}{b}\right)$. For a triangular equilateral array such as ours, $\left(\frac{a}{b}\right) = \left(\frac{2}{\sqrt{3}}\right)$ and $k_1 \approx 1$, thus the influence of this parameter can be neglected.

Gaddis and Gnielinski

Gaddis and Gnielinski approached the problem by considering a superposition of laminar and turbulent components. Equation (Eq. (3.7)) is written in this case as:

$$\Delta p_f = \xi_i N_W \frac{G^2}{2\rho} \tag{3.15}$$

N is assumed to be the number of minor restrictions encountered by the fluid N_W. For our geometrical arrangement, it corresponds to the number of tube rows N_R, as in equation (Eq. (3.12)). The parameters ξ_i and Eu are the same quantity. ξ is written in the following form:

$$\xi_i = \underbrace{\xi_{i,l} f_{zn,l}}_{l} + \underbrace{(\xi_{i,t} f_{z,t} + f_{n,t})[1 - e^{\left(-\frac{Re+200}{1000}\right)}]}_{t} \tag{3.16}$$

These correlations were developed for generic tube bundle geometries. Since different tube bundles are geometrically and fluid-dynamically dissimilar, the arrangement factors f are dependent on the geometry of the tube bundle: the relative transverse (a) and longitudinal (b) spacing. Considering first the laminar term, the pressure drop coefficient is expressed as:

$$\xi_{i,l} = \frac{f_{a,l}}{Re} \tag{3.17}$$

The arrangement factor for a staggered arrangement with the narrowest cross section along the diagonal is:

$$f_{a,l} = \frac{280\pi[(b^{0.5} - 0.6)^2 + 0.75]}{(4ab - \pi)a^{1.6}} \tag{3.18}$$

In an similar way for the turbulent component:

$$\xi_{i,t} = \frac{f_{a,t}}{Re^{0.25}} \tag{3.19}$$

The arrangement factor for a staggered arrangement with the narrowest cross section along the diagonal leads to:

$$f_{a,t} = 2.5 + \frac{1.2}{(a - 0.85)^{1.08}} + 0.4\left(\frac{b}{a} - 1\right)^3 - 0.01\left(\frac{a}{b} - 1\right)^3 \tag{3.20}$$

The coefficient $f_{zn,l}$ accounts for the effect of temperature dependency on the physical constant and the number of rows of tubes for the laminar component. For the turbulent case, $f_{z,t}$ accounts for the temperature dependency. The parameter $f_{n,t}$ incorporates the effects of inlet and outlet pressure drops in turbulent flows when the number of rows of tubes is small.

The number of rows seems to only have an importance in the case of non iso-thermal flows; in this case the acentric factor will act for $N_R < 10$.

3.3.2 Two-phase pressure drop in tube bundles

The two-phase flow pressure drop comprises for three different components: static, momentum (or dynamic) and frictional. For an evaporating flow, the static component is generally dominant when the flow moves in the vertical direction and at low mass velocities. The dynamic component accounts for the loss of momentum experienced by the flow during vaporization. The static and momentum components are similar to those used in evaluating void fraction. The pressure drop can be written as:

$$\Delta p = \Delta p_s + \Delta p_m + \Delta p_f \tag{3.21}$$

Considering a discretized domain of a physical two phase system where z is the coordinate in the vertical direction, one obtains:

$$\Delta p_s = \sum_i \left[\rho_L \left(1 - \frac{\varepsilon_{i+1} + \varepsilon_i}{2}\right) + \rho_G \left(\frac{\varepsilon_{i+1} + \varepsilon_i}{2}\right)\right] g\Delta z_i \tag{3.22}$$

$$\Delta p_m = G^2 \left\{\left[\frac{(1-x)^2}{\rho_L(1-\varepsilon)} + \frac{x^2}{\rho_G\varepsilon}\right]_{out} - \left[\frac{(1-x)^2}{\rho_L(1-\varepsilon)} + \frac{x^2}{\rho_G\varepsilon}\right]_{in}\right\} \tag{3.23}$$

Experimentally, the frictional pressure drop can be backed out as the difference between the total measured pressure drop and the sum of the static and momentum pressure drop computed as in Eq. (3.22) and Eq. (3.23). In the literature, several methods and correlations to compute the frictional pressure drop in tube bundle are available; as described by Ribatski and Thome in [49]. One of the most recent methods was developed at LTCM by Consolini et al. [51]. This method put its basis on the single phase pressure drop with a two-phase multiplier. The single phase friction factor for tube bundle f_1, according to Žukauskas and Ulinska [52], can be computed in terms of Euler number:

$$f_1 = \frac{1}{4} Eu \tag{3.24}$$

where Eu is defined by Eq. (3.13), Eq. (3.14). Generically, Eq. (3.12) written in terms of the friction factor and the Reynolds number are:

$$f = \frac{1}{4} \frac{\Delta p \, 2\rho}{G^2 N_R} \qquad Re = \frac{GD}{\mu} \tag{3.25}$$

Now considering two-phase flow, in order to extend generic equations of single phase to two-phase flow, the single phase density and viscosity are replaced by the following mixing values based on the void fraction:

$$\rho = \rho_L(1 - \varepsilon) + \rho_G \varepsilon \qquad \mu = \mu_L(1 - \varepsilon) + \mu_G \varepsilon \tag{3.26}$$

They then correlated the homogeneous friction factor f_1 to a two-phase friction factor f_2, to be found in place of f in Eq. (3.25), through a multiplier λ:

$$\lambda = \frac{f_2}{f_1} \tag{3.27}$$

where:

$$\lambda = \Lambda + (1 - \Lambda)(2x - 1)^2 \qquad \Lambda = \left(\frac{G}{G_{ref}} \right)^{-1.5} \tag{3.28}$$

and $G_{ref} = 400 \, kg/sm^2$. At this point f_2 is evaluated and the two-phase frictional pressure drop is calculated as:

$$\Delta p_{f,i} = 4 \frac{f_2 G^2}{2\rho} \qquad \Delta p_f = \sum_i \Delta p_{f,i} \tag{3.29}$$

3.4 Heat transfer

In literature forced flow-boiling heat transfer on tube bundles no well-validated general method for predicting heat transfer can be found. A global review of methods available is summarized in the work of Ribatski and Thome in [49]. Many studies present different heat transfer trends and dependencies from the basic parameters such as heat flux, mass velocity, vapor quality, etc. Shah in [55] underlines apparent conflicts in literature that show different behaviors according to the authors. The method developed at LTCM for plain tubes, presented by Thome and Robinson in [54], considers an asymptotic method for predicting the local bundle boiling heat transfer coefficient:

$$\alpha_o = \left(\alpha_{o,pb}^2 + \alpha_{o,cb}^2 \right)^{1/2} \tag{3.30}$$

where the first term is the nucleate boiling heat transfer coefficient and the second term is the convective boiling heat transfer coefficient. The nucleate boiling term $\alpha_{o,pb}$ is predicted using the Cooper correlation Eq. (7.15); the convective heat transfer coefficients were assumed to be the same as a thin film flow of thickness δ over the tubes in the bundle:

$$\alpha_{o,cb} = 4.032 \, Re_{\delta}^{0.236} Pr_L^{0.4} \left(\frac{\lambda_L}{\delta} \right) \tag{3.31}$$

The LTCM method, cover only plain tubes with the refrigerant R134a. A more recent method, proposed by Shah [55], was developed starting from a broader database. The author identified three possible regimes: *intense boiling regime* (heat transfer depends on heat flux), *convective boiling regime* (heat transfer depends on heat flux and mass velocity) and *convective regime* (heat transfer affected by mass velocity only). Shah defined afterwards a set of equations for each regime.

Chapter 4

Experimental Set-up

The existing LTCM bundle boiling facility has been modified and adapted to the new test conditions and measurement methods. The flow pattern instrumentation and visualization systems have been successfully integrated into the bundle boiling facility. A description of the test stand and the instrumentation will now be given.

4.1 General description

The objective of the experimental part of this study was to run bundle boiling evaporation and adiabatic two-phase flow tests. A wide range of experimental conditions over smooth tubes was investigated in order to obtain accurate values of two-phase pressure drops, local heat transfer coefficient values, video-recordings of the two-phase flow, and high frequency laser and pressure signals. These were then used to characterize the two-phase flow. The ranges of the experimental conditions are summarized in Table 4.1.

Experimental test conditions	
Test fluid	$R134a$, $R236fa$
Saturation temperature	T_{sat}=5, 10, 15 [°C]
Tube diameter	D_o=18.87 $[mm]$, D_i=16.00 $[mm]$
Tube pitch	s=22.22 $[mm]$
Tube layout	Staggered equilater
Vapor quality	x=0.1-0.9 $[-]$
Mass velocity	G=4, 10, 20, 30, 36 $[kg/sm^2]$
Heat flux	q_o=0, 7000, 12000, 21000 $[W/m^2]$

Table 4.1: Experimental conditions for bundle boiling tests

The existing LTCM test loop, developed by Casciaro and Robinson [63], has been adapted to be able to run these tests. The modifications consisted in limiting the diabatic part to the lower half of the tube bundle compared to the configuration of Robinson [63]. This allowed the installation of the flow pattern detection instrumentation in the adiabatic part.

The bundle boiling facility consists of a circulating loop supplying a flow of refrigerant to the bundle test section and a water loop that acts as the heat source for boiling the refrigerant. A pumping system controls the refrigerant mass flow rate. The flow is driven through a pre-heater, where the inlet conditions

of the test section are imposed in terms of vapor quality. After the test section and before re-entering the pumping system, a condensing system brings the fluid to sub-cooled conditions. The water circuit supplies heat at controlled conditions. The circuits are highly instrumented. General information about the basic configuration is available in [63]. A scheme of the refrigerant and of the water circuits are depicted in Fig. (4.1) and Fig. (4.2) respectively. An image of the test stand is given in Fig. (4.3)
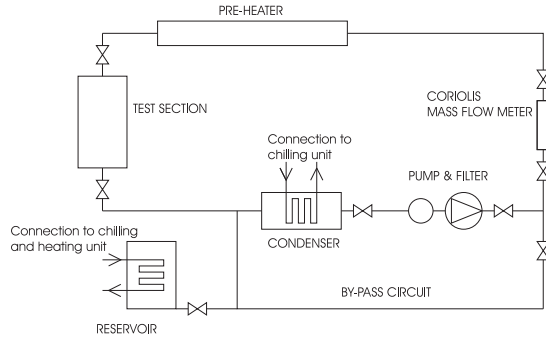
Figure 4.1: Refrigerant circuit scheme
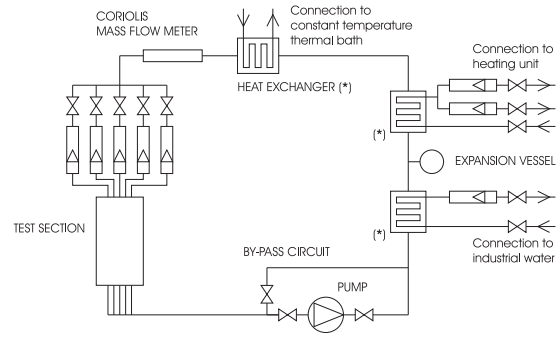
Figure 4.2: Water circuit scheme

A cross section of the test section is shown in Fig. (4.5). The test section is housed by a reinforced stainless steel box $107\,mm$ wide, $268\,mm$ high and $1067\,mm$ long. The walls of the box have a thickness of $20\,mm$. In the center of the test section is a bundle of 20 smooth copper tubes over which the refrigerant flow evaporates. The tubes have an outer diameter $D_o = 18.87\,mm$ and an internal diameter tube of $D_i = 16.00\,mm$. The bundle is eight rows high in a staggered, equilateral triangle layout with a pitch $s_q = 22.22\,mm$, Fig. (4.4). The tube length over which the heat transfer takes place measures $1027\,mm$. From Fig. (4.5) it can be seen that the tube bundle is subdivided into four groups of five tubes, with three tubes on the bottom and two tubes on top per group. Each group of five tubes represents one pass of the water flow along the length of the test section. Thus, in the original configuration, there were four passes of the water through the test section. In the new configuration just the two bottom passes are connected to the water circuit; the two top groups are not. These two zones will be referred to respectively as the diabatic and adiabatic zones. There are still four passes but just the bottom two are connected to the water circuit. The water direction is from the bottom to the top of the test section. The refrigerant enters at the bottom of the test section, being distributed by a perforated tube and a flat perforated distribution plate.

Considering the diabatic zone, within the two tube passes, there are stainless steel rods of $8\,mm$ diameter centered in each tube. A copper element is wrapped along all the length of the rod, generating a spiral. The rod increases the heat source water velocity and therefore also the water side heat transfer coefficient. The spiral wrap on the rod mixes the water to avoid a non-uniform water temperature distribution.

In Fig. (4.5) the central water circuit is instrumented, this provides local measurements of water temperature from thermocouples installed at three axial positions for each pass for a total of six along the flow circuit. At each position, a set of two thermocouples is placed. One is installed in the upper part of the annulus and one in the bottom part. Additionally, for each water circuit and for each pass, there is a thermocouple that measures the inlet and outlet temperatures.

4.2   Flow pattern instrumentation

In the adiabatic zone of the test stand, indicated in Fig. (4.5), two different sections are indicated as A-A and B-B. Their schematic representation are given in Fig. (4.6) and Fig. (4.7).
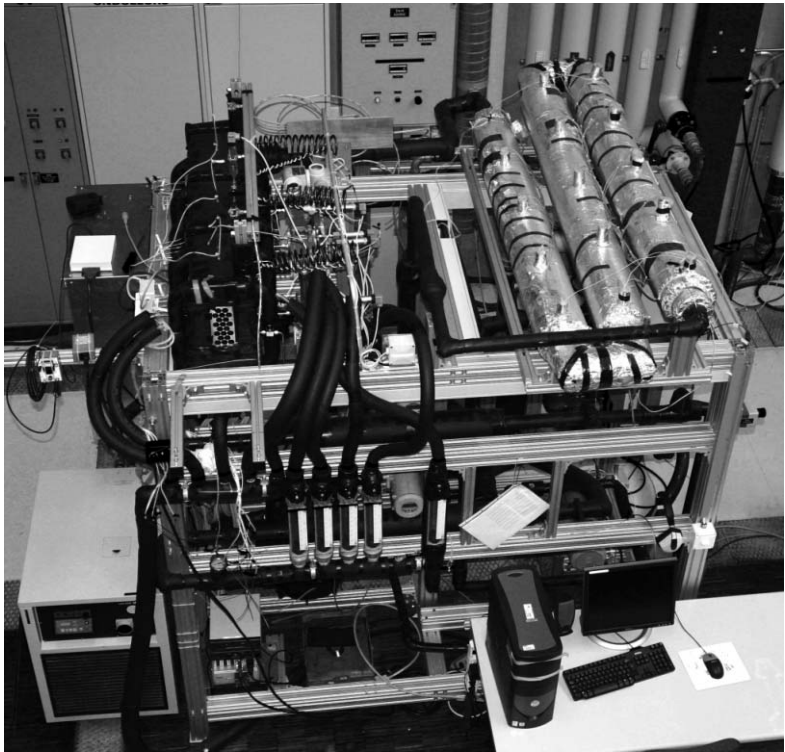
Figure 4.3: Bundle boiling test stand
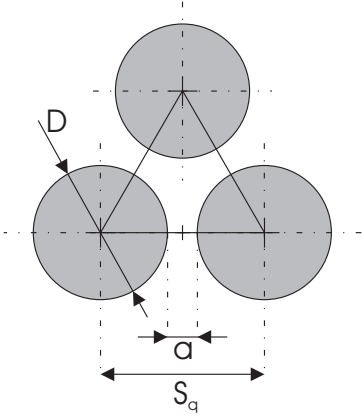
Figure 4.4: Tube layout
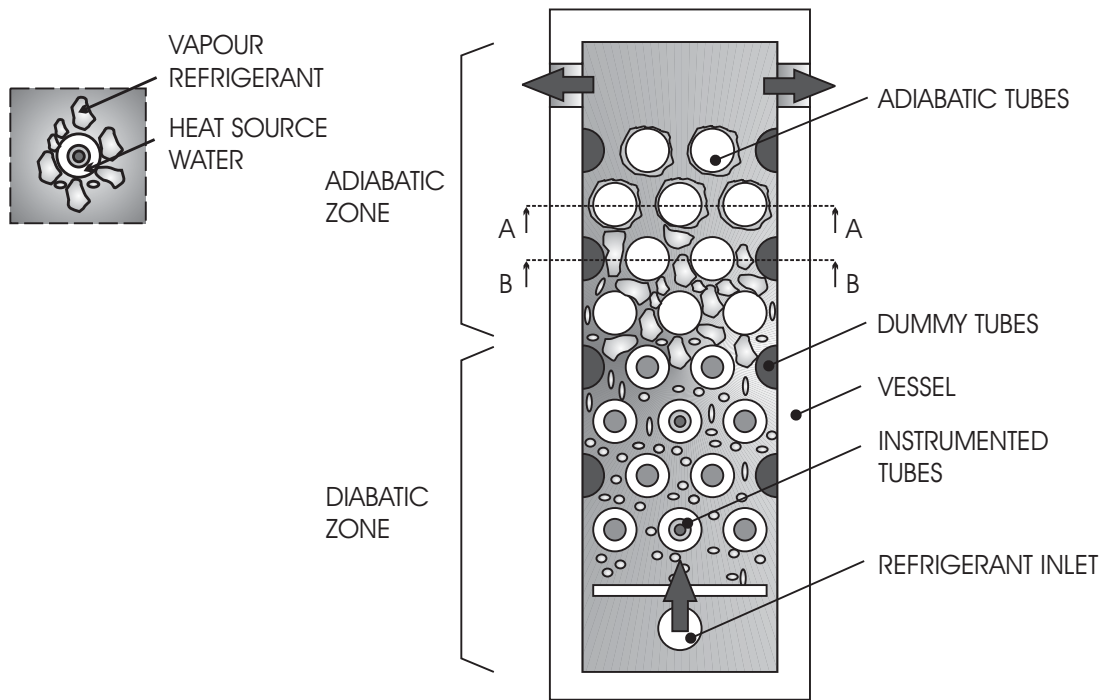
Figure 4.5: Test section layout
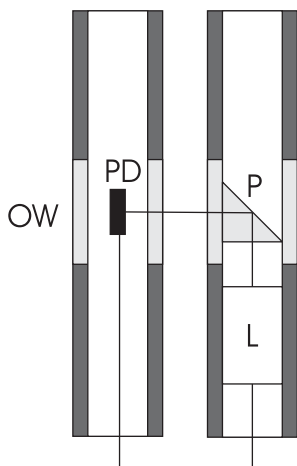
Figure 4.6: Section B-B (OW: optical window; PH: photodiode; P: prism; L: laser source).
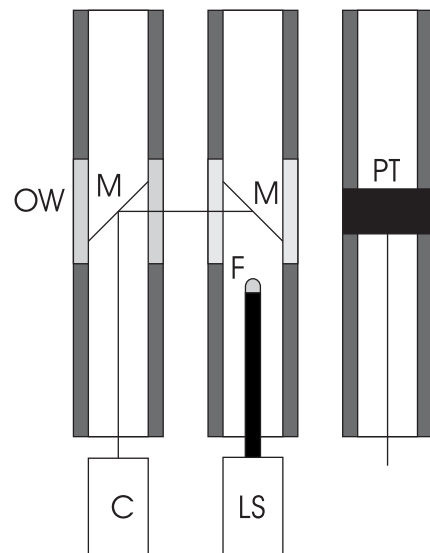
Figure 4.7: Section A-A (OW: optical window; M: mirror; PT: piezo-electric pressure transducer; C: camera; LS: light source; F: fiber optic).

4.2.1 Laser system

Considering the section B-B, two tubes are used to house the laser system that constitutes the laser-light signal two-phase detector. A more detailed layout of the laser system in section B-B is presented in Fig. (4.8) to Fig. (4.11). Inside the right tube, the laser source is mounted. The laser beam is aligned along the tube axis to reach a right angle prism at the midplane. The beam is thus deviated by 90°, passing through the optical window and exiting the tube where it encounters the two-phase flow. The beam then passes through the optical window of the second tube and on to a miniature photodiode. The photo-diode converts the intensity of incident light into voltage, and a wiring system brings the electrical signal outside the test section to the data acquisition system.

Laser

A laser-diode with a wavelength of $\lambda = 635\,nm$ and a power output of $P_o = 1\,mW$ was installed. It generates an elliptical beam profile with an aperture of 4x1.5 mm. The laser is driven by a DC power supply of $5\,V$ and $0.3\,A$.

Prism

The prism made of BK7 fused silica glass. Its size is 5.0x5.0x5.0 $\pm\,0.2\,mm$. It is characterized by a surface quality of $40-20$ scratch & dig, a surface flatness of $\lambda/4$ at $633\,nm$ and an angle tolerance of $\pm 5\,arcmin$. The two catheti are un-coated and the hypotenuse is coated with aluminium.

Photodiode

Several photo-diodes were tested. The most suitable for our application works in a spectral range of $\lambda = 350-1100\,nm$ with a maximum sensitivity at $\tilde{\lambda} = 850\,nm$. The radiant sensitive area measures $7.45\,mm^2$ and the dimensions of the radiant sensitive area are 2.73x7.73 mm.

Optical window

The optical window is made from a borosilicate glass tube (glass type 3.3) with an outer diameter $D_o = 19 \pm 0.20\,mm$ and wall thickness $WT = 1.2 \pm 0.05\,mm$. The transmissivity at a wave length of $\lambda = 635\,nm$ is $> 92\%$.

4.2.2 Piezo-electric & Visualization system

A detailed layout of section A-A is presented in Fig. (4.12). The tube at the extreme right is instrumented with a piezo-electric pressure transducer. The component is installed at the same axial position as the laser system. The remaining two tubes are designed to allow visual access to the test section by the use of a system of mirrors. Two elliptical mirrors are installed at an axial distance along the two tube, corresponding to the midplane of the test section. The casing, where the elliptical mirror is installed, has a rectangular optical window of $10\,mm$ high and $12.70\,mm$ wide, as visible in Fig. (4.13). One tube brings the light to the area of interest. A fiber optic cable brings the light along the tube axis just in front of the elliptical mirror. The light is reflected by the mirror, crosses the optical window and passes through the tube interspace with the two-phase flow. Inside the tube, a paper filter is wrapped around the optical window: this allows a more uniform distribution of the light in the zone of interest. The resulting image is captured by the second mirror and is reflected along the tube axis. A high speed digital camera, focused on the mirror, is installed externally for making video recordings. The tubes are internally ribbed in such a way as to avoid light reflections, as explained in appendix C.

PHOTO-DIODE

CASING

ANTI-CONDENSING
AIR FLOW

O-RING GROOVE

COPPER TUBE

PRISM

OPTICAL WINDOW

REFRIGERANT FLOW
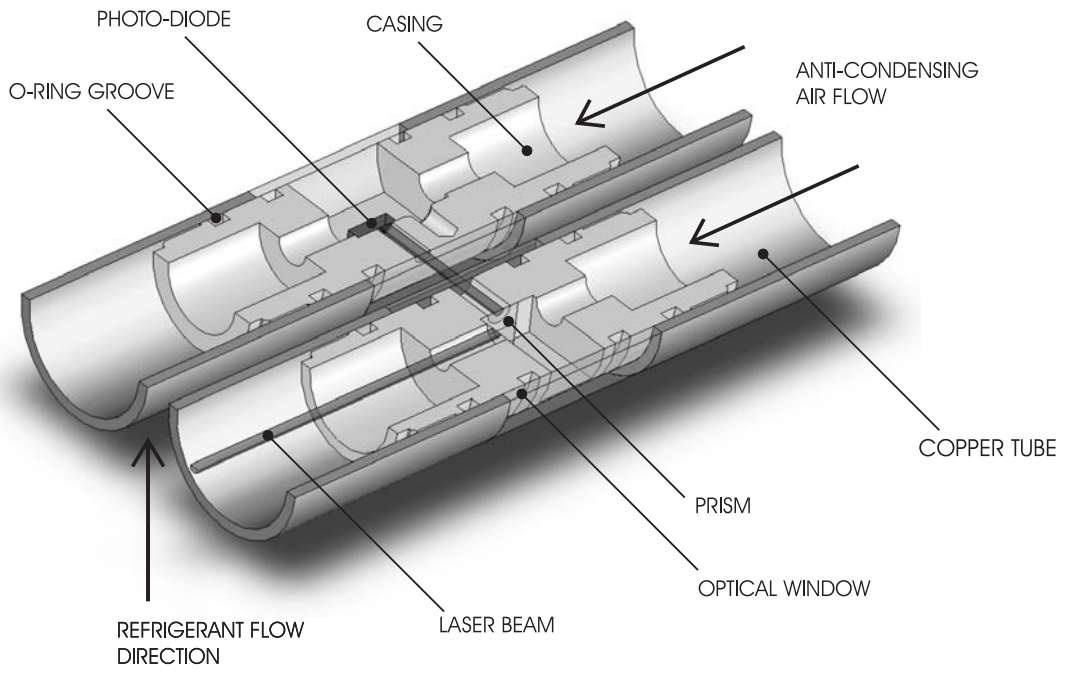DIRECTION

LASER BEAM

Figure 4.8: Section B-B, laser system layout

Figure 4.9: Photo-diode casing, front view
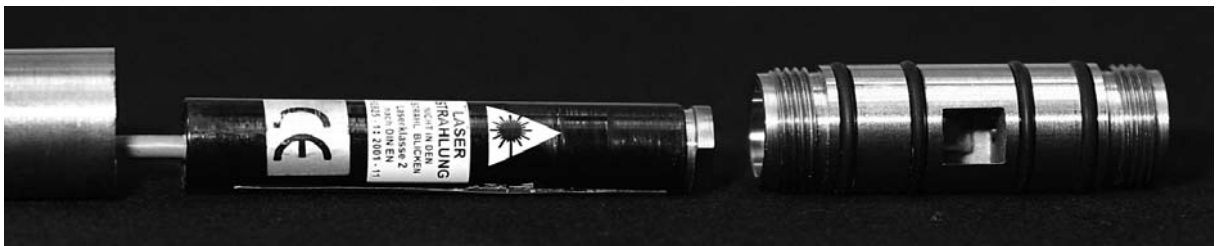

Figure 4.10: Photo-diode casing, back view
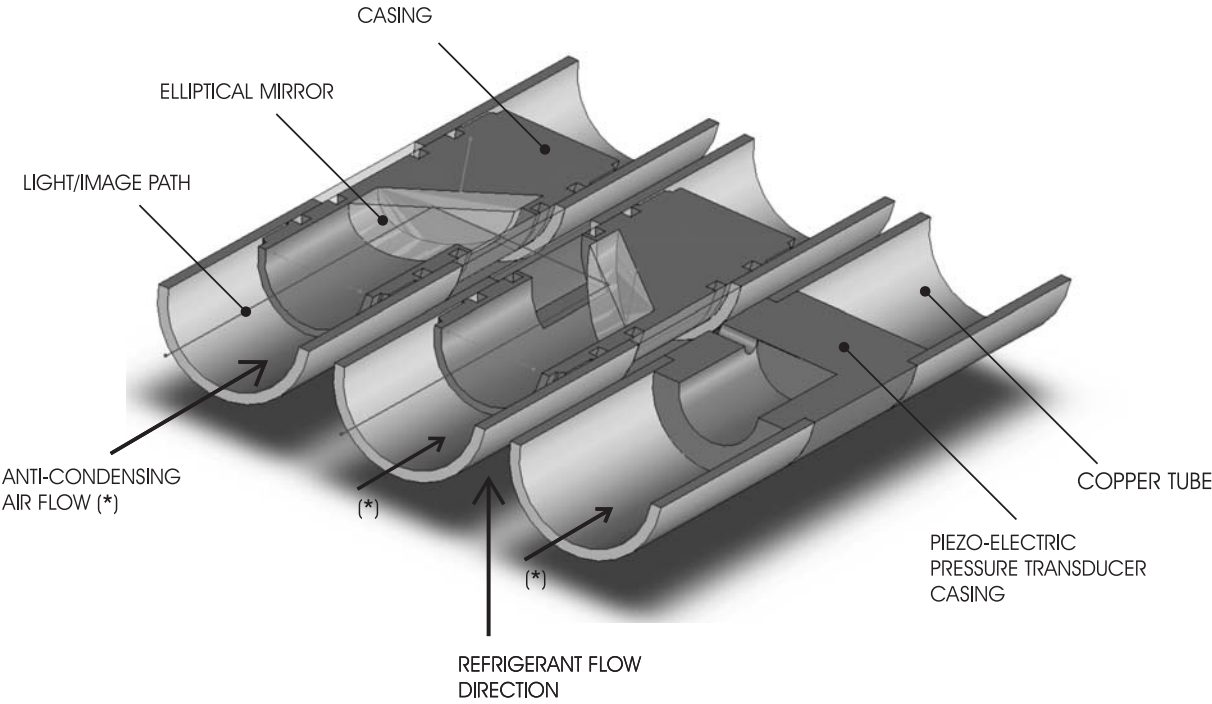

Figure 4.11: Laser-prism casing

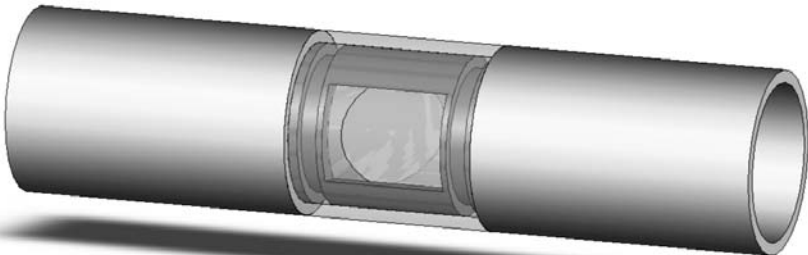Figure 4.12: Section A-A, camera system and piezo-electric pressure transducer layout

Figure 4.13: Elliptical mirror/optical window

Light source and optics

The cold light source is $20\,V$ with $150\,W$ and equipped with an IR filter. The optic source comprises a single flexible light guide fiber optic cable that is $1000\,mm$ long and $5\,mm$ diameter.

High speed camera

The high speed camera is capable of frame rates up to $120000\,fps$; it has a 10-bit CMOS sensor with $17\,\mu m$ pixels and adjustable shutter speeds of $16.7\,ms$ to $4\,\mu s$.

Piezo-electric pressure transducer

The sensing element is made of quartz, housed in a stainless steel casing and works in compression. The sensitive area measures $4.95\,mm^2$, with a diameter of $D = 2.51\,mm$. The measurement range for an output voltage of $\pm 5\,V$ is $690\,kPa$. The sensitivity $(-40/+20\%)$ is $7.3\,mV/kPa$. The sensor can resist pressures up to $1720\,kPa$ with a resolution of $0.035\,kPa$ and a resonance frequency of $\geq 250\,kHz$. The accuracy is $\leq 1\,\%\,FS$.

Elliptical mirror

The mirror is constructed from glass fused silica glass. The cut angle is $45°$, with a minor axis of $14.00 \pm 0.25\,mm$, a major axis $19.80 \pm 0.25\,mm$ and a thickness of $6.00 \pm 0.25\,mm$. A surface quality of $20 - 10$ scratch & dig and the surface flatness is $\lambda/10$ at $633\,nm$ is present. The angle of incidence is $45°$. The mirror has a dielectric coating, with a reflectivity HR of $> 99\%$ at $450 - 650\,nm$.

4.3 Instrumentation and measurement accuracies

4.3.1 Data acquisition system

All measurements are made with a computer equipped with a *National Instruments* data acquisition system. The system is split into two sub-systems. Two acquisition cards were installed on the PC, one for high frequency signal measurements (photo diode and piezo-pressure transducer) and the other one for low frequency response instrumentation like thermocouples and pressure transducers.

For the high frequency measurements, a PCI-6143 card was installed. This card provides 8 differential channels with an ADC resolution of $16\,bits$, a sampling rate of $250\,kS/s$ per channel and an input range of $\pm 5\,V$. A shielded I/O connector block SCB-68 allows different configurations of connections according to the signal source type. The connection scheme is reported in Fig. (4.14). The signal from the piezo-electric pressure transducer is a ground referenced signal. It is connected to the building system ground and is therefore already connected to a common ground point with respect to the PCI. The signal is differential: each input signal is tied to the positive input of the instrumentation amplifier and its reference signal, or return, is tied to the negative input of the instrumentation amplifier. The piezo-electric pressure transducer PCB-ICP-M105C02 is connected to the connector box through a sensor signal conditioner PCB-480E09: amplification x1, 10, 100 with a frequency range of $15 \cdot 10^{-5} - 100\,kHz$ in case of amplification x1, 10 while instead $15 \cdot 10^{-5} - 50\,kHz$ in case of amplification x100. The piezo electric system is powered by a power supply PCB-ICP-M105C02. The signal from the photodiode element BPW34B is a floating signal source; it is not connected in any way to the building ground system. In this case, a bias resistor connects the negative signal input to the analog input ground which itself is connected to the ground of the data acquisition card. A resistor of $100\,K\Omega$ is installed; this resistor provides a return path for the $200\,pA$ bias current. If a return path is not provided (as tested), the

instrumentation amplifier bias current stores up stray capacitances, resulting in uncontrollable drift and possible saturation of the amplifier.

Concerning the low frequency instrumentation, a PCI-6259 was installed. This card provides 32 differential channels with ADC resolution of $16\,bits$ and a sampling rate of $1\,MS/s$ aggregate. A SCXI-1000 module with four bays is connected to this card. For the acquisition computer, each of the four bays has a 32 channel voltage measurement card (type 1102). The total number of acquisition channels is thus 128. Each channel of this system has a computer programmable gain: 1 for 0 to $10\,V$ signal (pressure transducer and mass flow meter) and 100 for low voltage signals (thermocouples). The signals can be adjusted to the 0 to 10V range of the acquisition card in the computer. A 2Hz low pass frequency filter is also included in the card for each channel. This helps to diminish the measurement noise and does not affect the steady-state measurements of this study. At the end of the acquisition chain, a terminal block with 32 sockets is connected to the 1102 card. Each card has its own terminal block. The cold junction for every thermocouple is made in this terminal block at the socket. The material of this socket is copper for both poles ($+$ and $-$) such that the continuity of the two different specific materials of the thermocouple is broken at this point located inside the terminal block. The temperature of the 32 cold junctions is maintained uniform with a metallic plate and is measured by the system via an RTD installed in the middle. Additionally, all the terminal blocks are placed in a closed cupboard away from external thermal influences. In order to measure a test parameter in a channel, 100 acquisitions are made in $0.02\,s$ ($50\,Hz$ electric period) and the average of these 100 values is calculated during the acquisition. The result is the measured value of this channel. By this way, any noise from alternating current on the measured signal is removed. This value is stored and the system steps to the next channel. With this measurement method, the theoretical channel measurement frequency is 50 channels per second, but due to the switching time between channels, the actual frequency is 10 channels per second. In total, it thus takes $4.3\,s$ to measure all the channels of the acquisition computer once. To obtain one data point, 30 of such acquisition cycles are recorded and averaged.
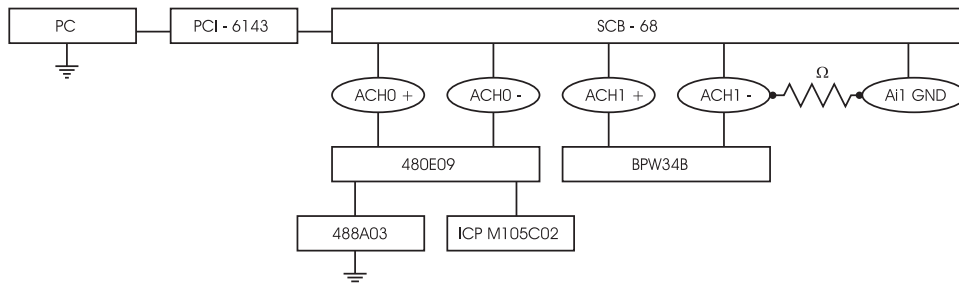
Figure 4.14: PCI-6143 configuration

4.3.2 Thermocouples

Type K thermocouples ($NiCr/NiAl$) are used. They are calibrated in a thermal bath: the reference is provided by a reference platinum thermometer. The maximum deviation resulting from the calibration is $0.03\,K$. See Gstöhl [61] for more details.

4.3.3 Pressure transducers

Absolute pressure transducers are employed for monitoring the operating conditions and for security reasons. The operating ranges are between $0 - 20\,bar$ and $0 - 40\,bar$. Accuracies of $\pm 0.4\,\%\,FS$ and $\pm 0.1\,\%\,FS$ respectively were given by the supplier. These transducers are calibrated in the laboratory

with a calibration balance. The deviation is always smaller than the one specified by the supplier.

Differential pressure transducers with working ranges of $\pm 40\,bmar$ are installed for pressure drop measurements. An accuracy of $\pm 0.1\,\%\,FS$ is given by the supplier. The instruments are calibrated in the laboratory with a water column.

4.3.4   Flow meter

Two Coriolis mass flow meters are installed on the bundle boiling test facility with a range of $0-1.67\,kg/s$. The uncertainty in the measurement is provided by the constructor using the equation: $\Delta \dot{m}/\dot{m} \leq \pm (0.15 + S/\dot{m})\,\%$, where $S = 8.3\,10^{-3}\,kg/s$ is a constant depending from the mass flow meter.

The air-water test facility is equipped with variable area flow meters. For air, they range from $0.5 - 50\,Nl/h$, $4 - 40\,Nl/h$ and $50 - 500\,Nl/h$ with an accuracy of $2.5\,\%\,FS$; for water from $0.5 - 50\,l/h$, $4 - 40\,l/h$ and $40 - 400\,Nl/h$ with an accuracy of $2.5\,\%\,FS$.

4.3.5   Heat transfer: measurement accuracies

q_o	7000 $[W/m^2]$	12000 $[W/m^2]$	21000 $[W/m^2]$
$\delta q_o \%$	$\pm\ 8\%$	$\pm\ 5\%$	$\pm\ 4\%$
$\delta \alpha_o \%$	$\pm 12\%$	$\pm\ 8\%$	$\pm\ 6\%$

Table 4.2: Heat flux and local heat transfer coefficient experimental uncertainties

A rigorous uncertainty analysis is presented in appendix F.

According to Eq. (7.10) the internal heat transfer coefficient α_i is calculated from the Gnielinski correlation and the corrective multiplier C_i. The relative uncertainty in the value of C_i corresponds approximately to the relative uncertainty of the internal heat transfer coefficient. $\delta C_i \% = \pm 8\%$ for 95.4% confidence interval. The relative uncertainties of the heat flux and of the local refrigerant heat transfer coefficient are reported in Table 4.2, the values refer to 95.4% confidence interval.

Chapter 5

Flow Patterns

This chapter discusses experimental results concerning the characterization of two-phase flow in the tube bundle. The analysis of the laser-photodiode signals, the piezo-electric pressure signals and the image processing from the visualization are presented.

5.1 Flow pattern: General statement

The following two-phase classification of flow in tube bundles is assumed: *bubbly flow*, *intermittent flow* and *dispersed flow*.

5.2 Laser and pressure signals

The instrumentation was installed at different positions, see Fig. (4.5) but the measured quantities represent essentially the same physical phenomena. The pressure and laser instrumentation were installed in the adiabatic zone, which allows us to assume that the signals are representative of the same physical phenomena, since in the adiabatic zone no heat exchange takes place. As the distance between the two measurement points is only limited to a pitch value, the effect of the pressure drop is negligible. The sampling frequency for the laser-diode and for the piezo-electric transducer was set to $f_{samp} = 10\,kHz$ over a time interval of $t_{samp} = 10\,s$. This time interval was sufficient to sample the investigated two-phase flow phenomena based on a preliminary study.

Before being installed in the bundle boiling facility, the instrumentation for flow pattern identification was tested over a wide range of conditions with air-water tests. This allowed evaluation of the instrumentation prior to tests with refrigerants in the main facility. The tests were carried out at somewhat similar geometric conditions. A detailed description and discussion of these air-water results is given in Appendix C.

As apparent from the state of the art review, Chapter 3, and from the air-water tests in Appendix C, statistical quantities derived from the pressure and laser signals appear to be sufficient to characterize the flow.

5.2.1 Raw signal

Compared to air-water tests in horizontal tubes, flow patterns in the bundle boiling facility could not be readily identified from the structure of their signal. From this point of view, the techniques presented in literature that use simple criteria for flow pattern identification, like simple amplitude analysis, lose their

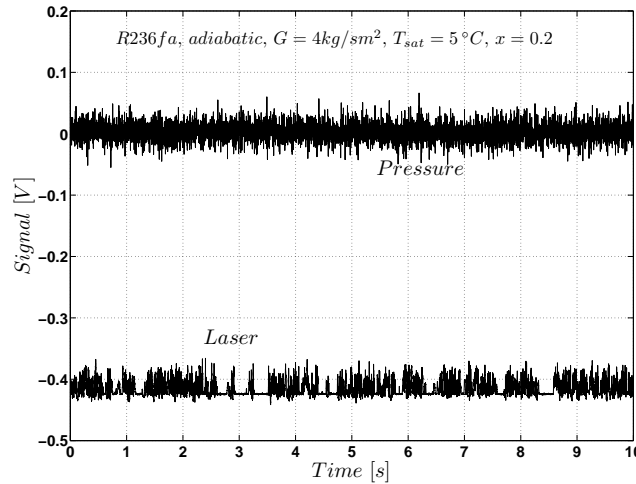applicability in complex geometries. An example of a characteristic raw signals is shown in Fig. (5.1).

Figure 5.1: Laser-pressure raw signals

5.2.2 Laser vs. pressure signal correlation

Unlike air-water experiments inside a horizontal tube, the laser and pressure signals measured in the bundle boiling facility do not show a strong correlation. As shown in Fig. (5.2), the two signals have a small correlation. This can be due to two factors: either a variation of the two-phase flow in between the two measurement points, or a different response of the instrumentation to the same phenomena. Since the instrumentation is installed in the adiabatic zone, the second hypothesis is the more probable. This means that the two instruments react in a different way to the flow field, or, a structure detected from the laser could not be detected from the pressure and vice-versa. Furthermore, due to secondary flow, a given two phase structure encountering the first transducer may not encounter the second. This hypothesis will be confirmed later by image analysis.

5.2.3 Statistical moments

The laser and pressure signals were analyzed to determine their statistical moments. A representative plot of the first four statistical moments of the laser signal are given in Fig. (5.3), Fig. (5.4), Fig. (5.5) and Fig. (5.6). What is evident is that the value increases to a steady value with increasing vapor quality at the same mass velocity. The standard deviation is small for all the cases and exhibits the same trend as the mean. The skewness and the kurtosis remain positive for almost all the cases and tend to constant values close to zero (indicating normal distribution) for higher vapor qualities. A massive analysis of all the data points acquired for the different refrigerants, for both laser and pressure, did not show clear trends that could be used to indicate a flow pattern effect. Changing the saturation temperature, the behavior remains unchanged and shows similar trends. No sensible variations in the moments were visible when passing from 5 to 15 °C.

5.2.4 Probability density function

The PDFs of the laser and pressure signals were computed using the method presented in appendix A. According to literature, the PDF of the laser and pressure signals should show a well known distribution.
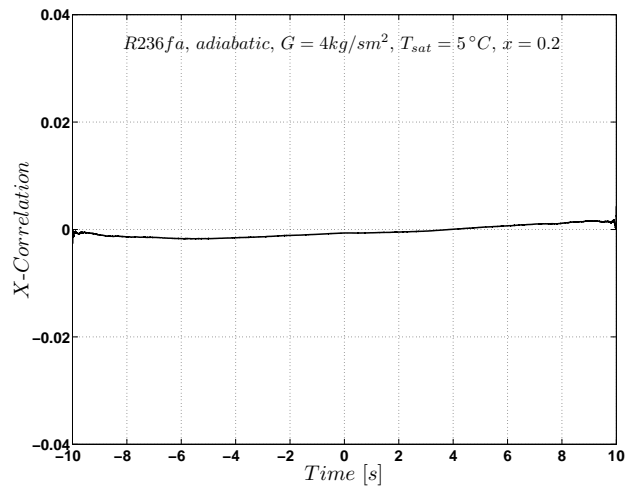
Figure 5.2: Cross-Correlation between the laser and pressure signals
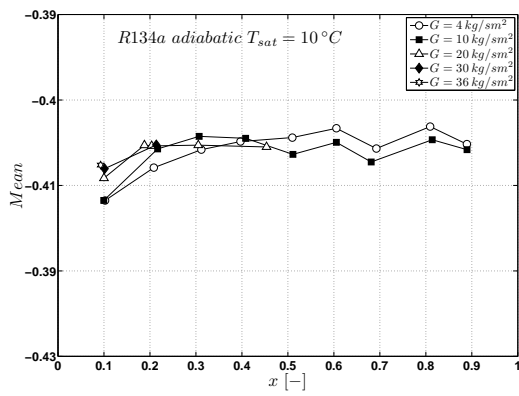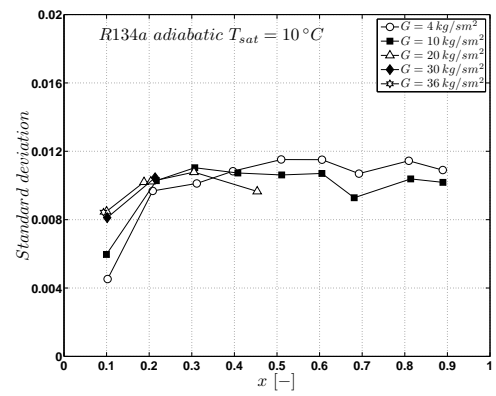

Figure 5.3: Laser mean

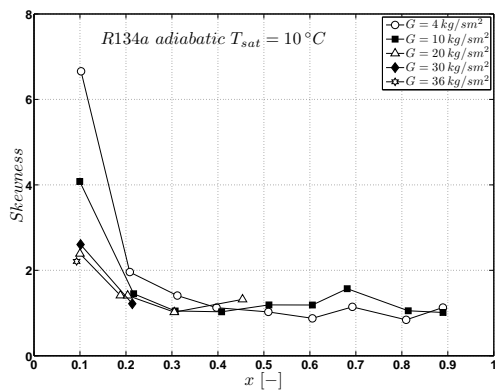
Figure 5.4: Laser standard deviation
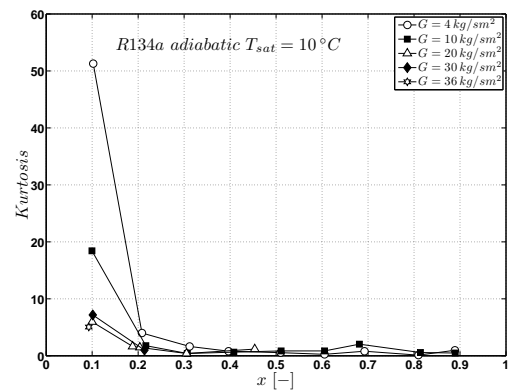

Figure 5.5: Laser skewness

Figure 5.6: Laser kurtosis

The analysis is presented below.

Laser signal: Dry-out detection

Fig. (5.7) and Fig. (5.8) show the PDF of all the experimental data points measured for R134a and R236fa. From these plots, three groups of signals are identifiable. The three groups represent three saturation temperatures: 5, 10 and 15 °C. It can be seen that the absolute mean signal amplitude decreases with increasing saturation temperature. This effect can be attributed to two different factors: a change in the surface tension of the saturated fluid and a change of the optical properties of the fluid. The surface tension acts on the bubble dimension; a decrease of this physical quantity with an increase of temperature will reduce the diameter of the bubbles. Therefore, due to the increased absorption of the transmitted light as a result of smaller bubbles, one would expect the peak of the photo diode voltage PDF to move to a lower absolute value as the temperature increases. Furthermore, the light passing through a two-phase mixture encounters phenomena such as reflection, refraction and absorption. The physical quantities governing these phenomena are temperature dependent, see Table (5.1), therefore resulting in changes in the measured voltage.
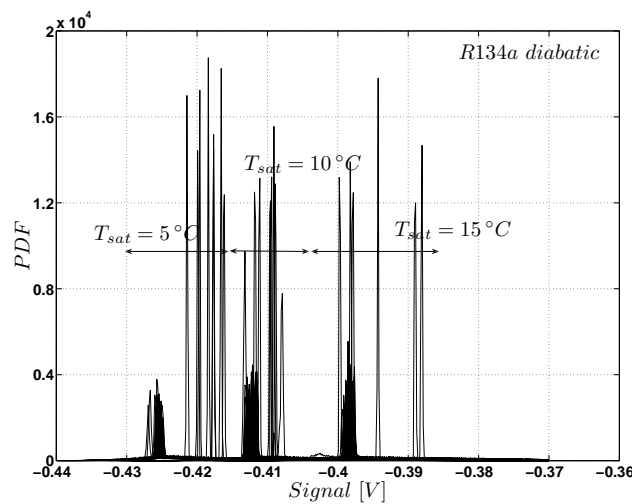
Figure 5.7: Laser PDF, diabatic R134a, dry-out detection

T [°C]	n_L	n_G	$(n_L + n_G)/2$
20.3	1.2356	1.0032	1.1194
29.7	1.2304	1.0041	1.1173
39.4	1.2234	1.0058	1.1146
49.7	1.2160	1.0077	1.1119
59.9	1.2083	1.0103	1.1093

Table 5.1: R134a liquid-vapor refractive indexes (n), [56]

We now focus on a single group of laser PDF for different vapor qualities but at the same saturation temperature, heat flux and mass velocity, Fig. (5.9). As can be seen, the PDF for the $x \simeq 1$ cases exhibit some peaks at higher absolute voltages that are almost one order of magnitude bigger in amplitude than other features. Since light attenuation is a function of its absorption by the fluid, and is expected to
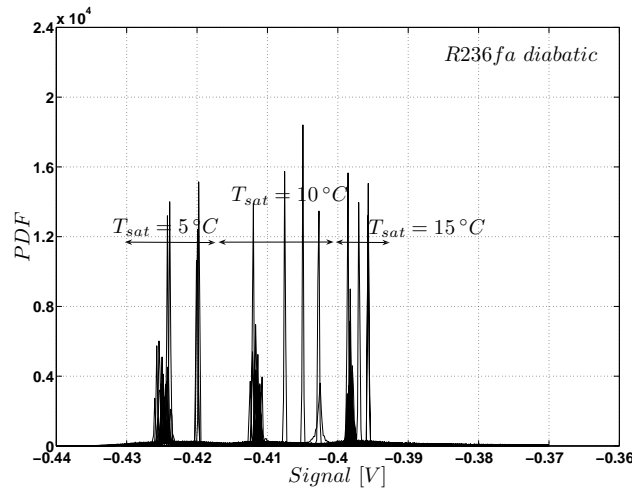
Figure 5.8: Laser PDF, diabatic R236fa, dry-out detection

be higher for the liquid phase than for gas phase, it is evident that in such a case just the gas phase is present. This implies a dry-out condition. These cases were cross-checked with the temperature distribution along the water circuit. In Fig. (5.10), the profile of the water temperature along the circuit for four different inlet vapor qualities, ranging from $x = 0.6$ to $x = 0.9$, are plotted. With an imposed heat flux of $7000 \, W/m^2$, the vapor quality at the measurement point ranges from slightly less than 1 to a dry-out condition of $x = 1$. This can be clearly seen from Fig. (5.10): a lower inlet vapor quality results in a vapor quality smaller than 1 at the measurement point. The water temperature profile in this case develops as expected by following a parabolic distribution along the circuit. An increase in inlet vapor quality results in dry-out at the measurement point; this can be seen from Fig. (5.10) for the inlet vapor quality of $x = 0.7$ and 0.8, where the water temperature profile becomes flat from at point b. Although the two curves still follow a parabolic profile for the first part of the circuit, they suddenly get flat at a well defined location. This is because part of the bundle is in the dry-out condition. This produces a dramatic drop of the shell-side heat transfer coefficient in such areas. A lower heat transfer coefficient signifies a lower heat flux, thus leading to an almost constant water temperature. A further increase of inlet vapor quality to $x = 0.9$, produces an earlier dry-out in the tube bundle, as indicated by label a in Fig. (5.10). Coming back to the laser signal, the PDF analysis seems to be good way of identifying dry-out conditions but it does not indicate any changes in flow regime over the present test conditions.

In Fig. (5.11) and Fig. (5.12), the experimental data are plotted in terms of superficial gas and liquid velocities for R134a and R236fa, respectively. Each plot displays conditions of heat flux ranging from 0 to $21000 \, W/m^2$, saturation temperatures of 5, 10, $15 \, °C$, and mass fluxes from 4 to $36 \, kg/sm^2$. On the same plots, the experimental points approaching conditions of dry-out are marked with black circles. The dry-out zone appears to be well-defined and similar for the two investigated fluids; a qualitative line indicating the border between dry-out and non-dry-out is placed on the plots. A data point was defined as a *dry-out point* if and only if it simultaneously respected the conditions of a flat water profile and a laser PDF peak. The definition of the *dry-out zone* constitutes an important achievement in the field of bundle boiling evaporation, because it enables one to identify conditions of very poor heat transfer and also indicates where a change in the heat transfer model must be made.

For non-dry-out conditions, the PDFs are similar; they usually exhibit a single-peak that is characteristic of bubbly flow for almost all the experimented conditions. The positions of the peak change; however, no coherent trend can be observed, Fig. (5.9). Although, it was easy to identify changes in the two-phase distribution of air-water flows, it is not possible here: the PDF exhibit only small changes of intensity and the mean values remain almost constant for all the experimental conditions. PDF analysis
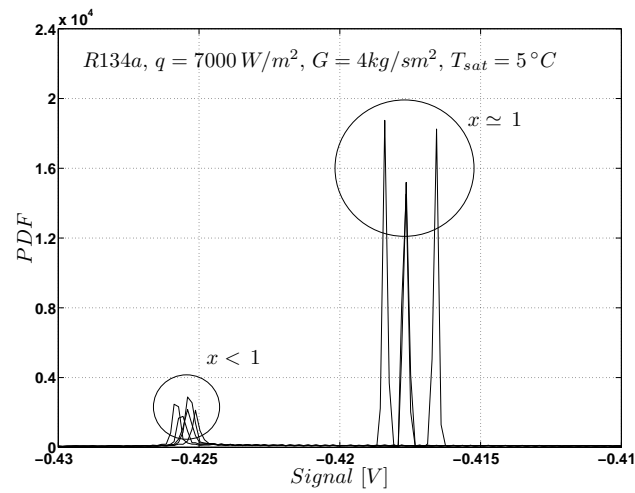
Figure 5.9: Dry-out detection, laser PDF for different vapor qualities
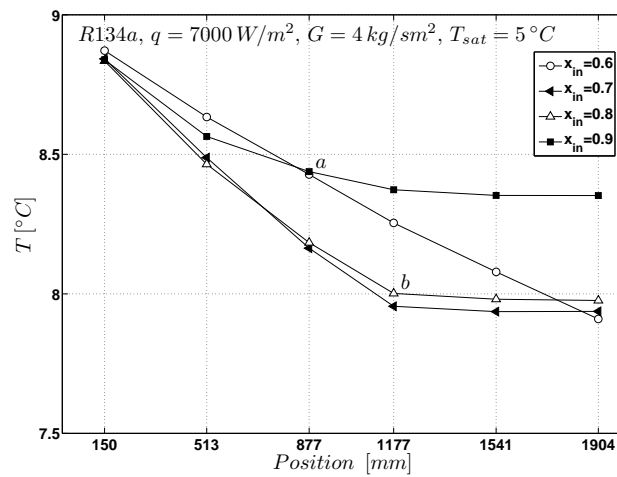

Figure 5.10: Dry-out, water temperature as a function of position along the water circuit
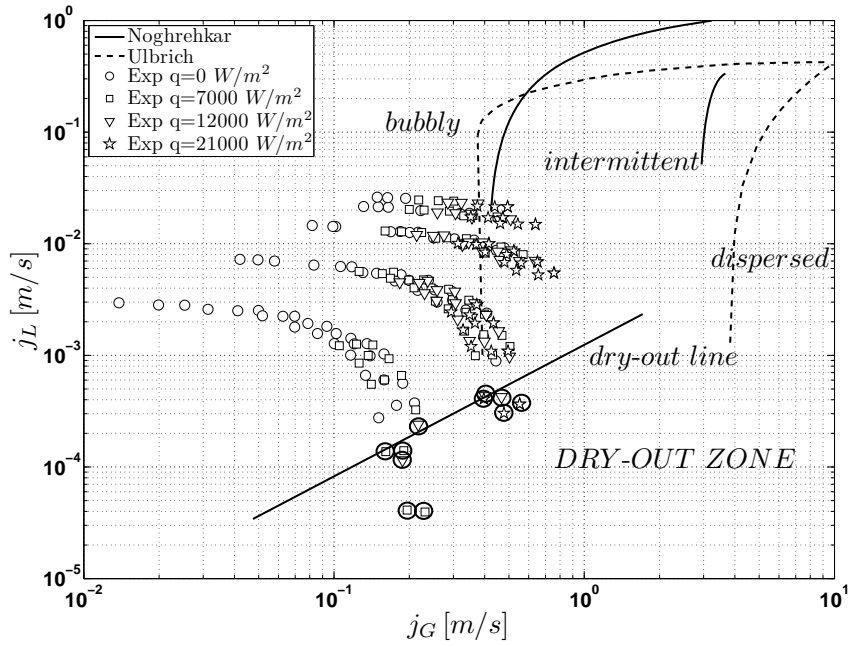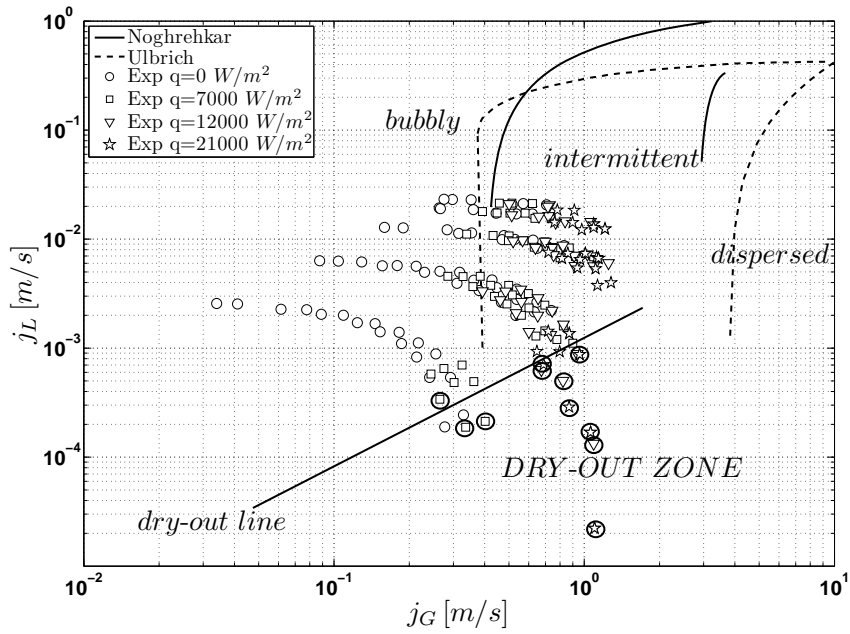
Figure 5.11: Flow map, R134a

Figure 5.12: Flow map, R236fa

is widely employed for air-water flows by the two-phase community, this seems to be a valid approach, as demonstrated by the preparatory experimental campaign for air-water flows described in appendix C, but it is probably not the best approach for two-phase flows in tube bundles. To investigate all possibilities in terms of PDF analysis, the method presented in Aprin [57] was applied to the measured laser signal. This method is applicable to binary signals such as those from electronic devices that digitize the signal intensities into binary. Therefore, the laser time record was converted into a binary signal and the treatment defined by Aprin was applied. The signal was split into time blocks of $0.02\,s$ and a void parameter was then computed for each block. This was the ratio of the time where the signal reached the threshold value relative to the total time window. The PDF of this void distribution was then computed. It was found that although the method was not sensitive to the time window size, it was highly dependent on the intensity threshold used to binarize it, Fig. (5.13). In other words, different PDF results are obtained from different thresholds, leading to a lack of robustness.
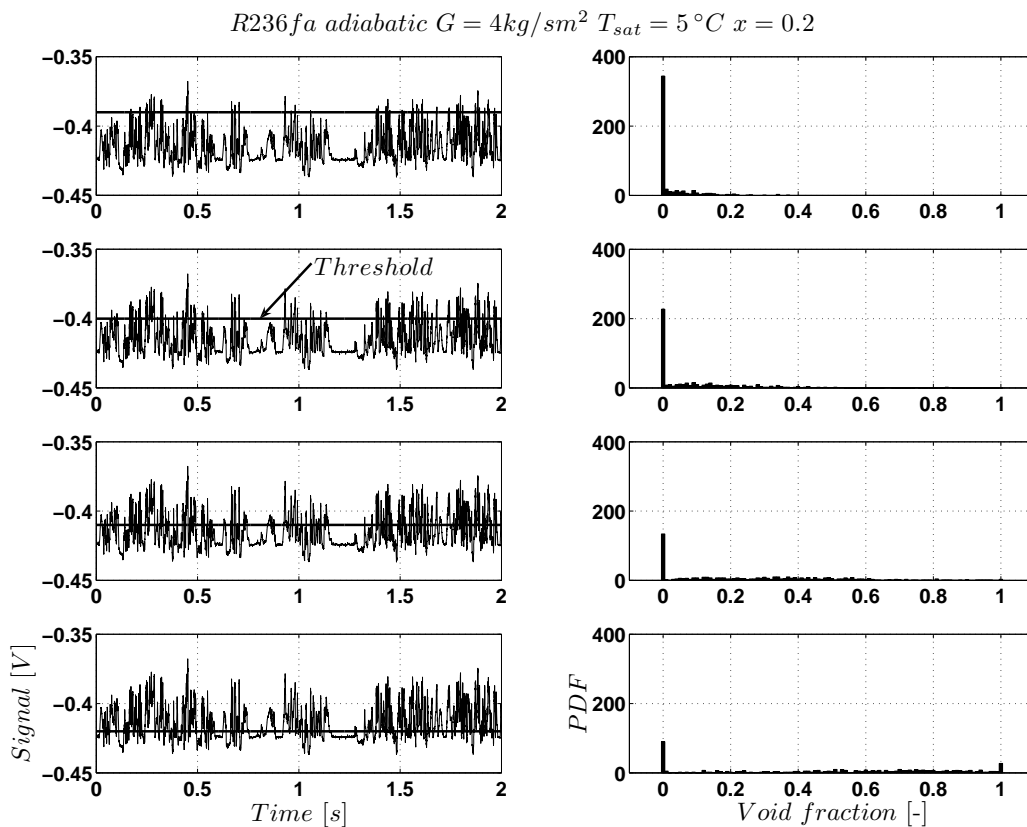
Figure 5.13: Threshold analysis

Pressure signal

Although the same analysis was carried out on the pressure signals, it did not lead to any sensible conclusions for characterizing the two-phase flow patterns. Concerning dry-out, the PDF of the pressure signal differs from the laser one. There is no sharp variation of the PDF that can be used to identify dry-out; the PDF smoothly changed from non dry-out to dry-out. Therefore, the pressure signal PDF seems to be unable to clearly identify the dry-out condition from other phenomena that could indicate changes in flow pattern. To have a clearer view of the PDF distribution, contour plots of the PDF are

shown in Fig. (5.14). In each sub-graph the PDF intensity is plotted: along the abscissa we have the local vapor quality at the investigated point and the signal intensity on the ordinate .

Each sub-graph row refers to the same saturation temperature, ranging from 5 to 15 °C, and each column to the same mass velocity varying from 4 to $30\,kg/sm^2$. Variations in the PDF intensity and shape are present but they do not seem to follow any particular trends. At the lowest investigated mass velocity, $4\,kg/sm^2$, for all the vapor qualities, the PDF of the pressure exhibits a single sharp peak and flat tails characteristic of a high kurtosis distribution. For all other mass velocities, the PDF exhibited a distribution that ranged from a single sharp peak to a double peak, with generally smaller kurtosis characteristic of a more rounded distribution. The different PDF profiles are randomly linked to the flow conditions and for this reason they can not be employed as possible flow regime indicators. The detailed distribution of the PDFs, grouped according to heat flux for R236fa at $T_{sat} = 15\,°C$ are shown in Fig. (5.15) to Fig. (5.18). The results for other saturation temperatures and for R134a are not reported here since they show similar features as those presented above. Examples of possible PDF distributions for fixed conditions are given in the subplots A, J, Q and U of Fig. (5.15); these correspond, respectively, to the experimental points at G=4, 10, 20 and $30\,kg/sm^2$ for a vapor quality of x=0.1. These experimental points, according to existing flow pattern maps like Noghrehkar et al. [16] and Ulbrich & Mewes [12] and to visual observations, should fall in the same flow regime but the pressure PDF seem to be unable to identify these phenomena. the exact reason for this appears to be that no significant variation in two-phase flow structure is occurring in this two-phase bundle flow.
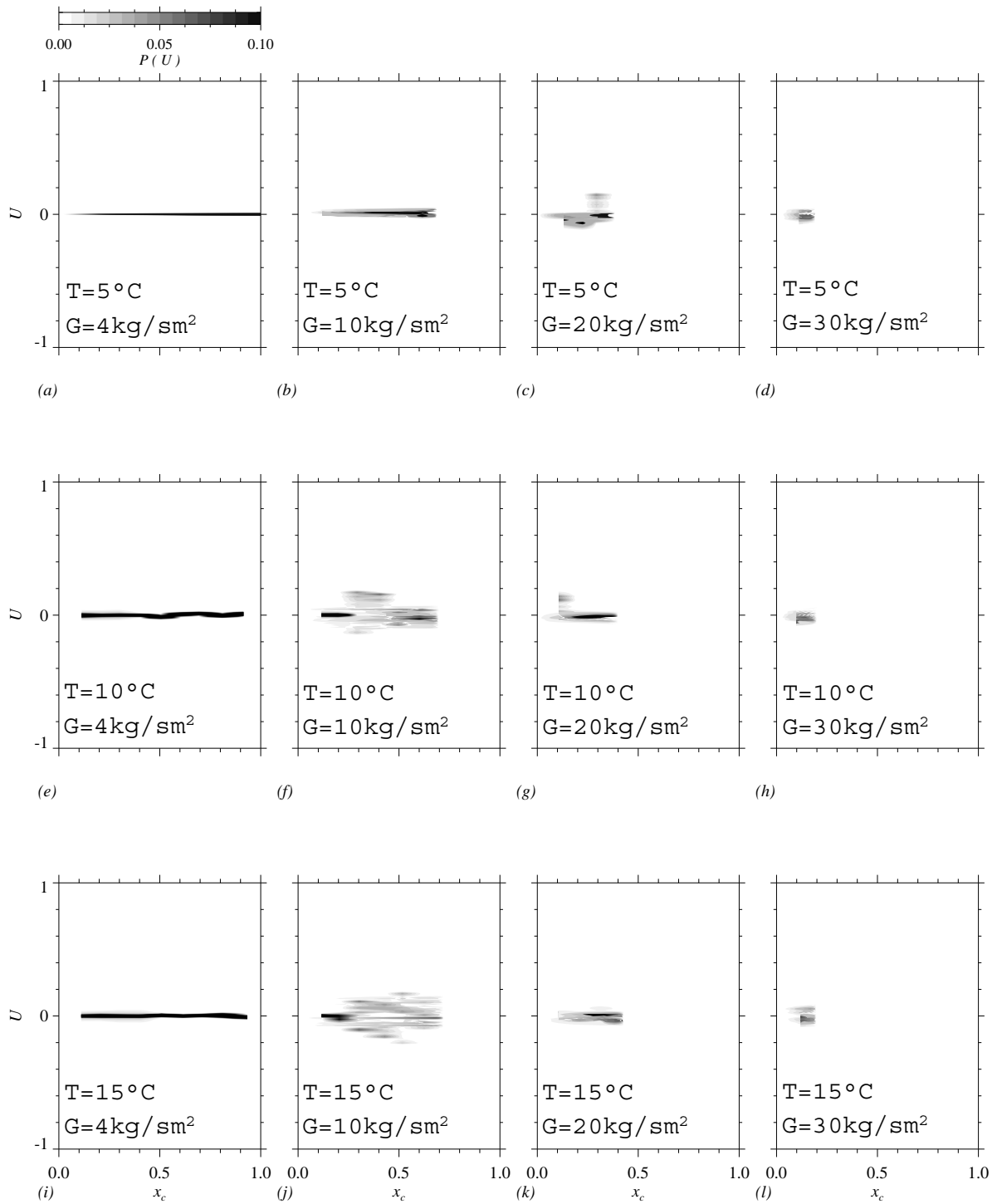
Figure 5.14: PDF pressure contour plots, R236fa, adiabatic
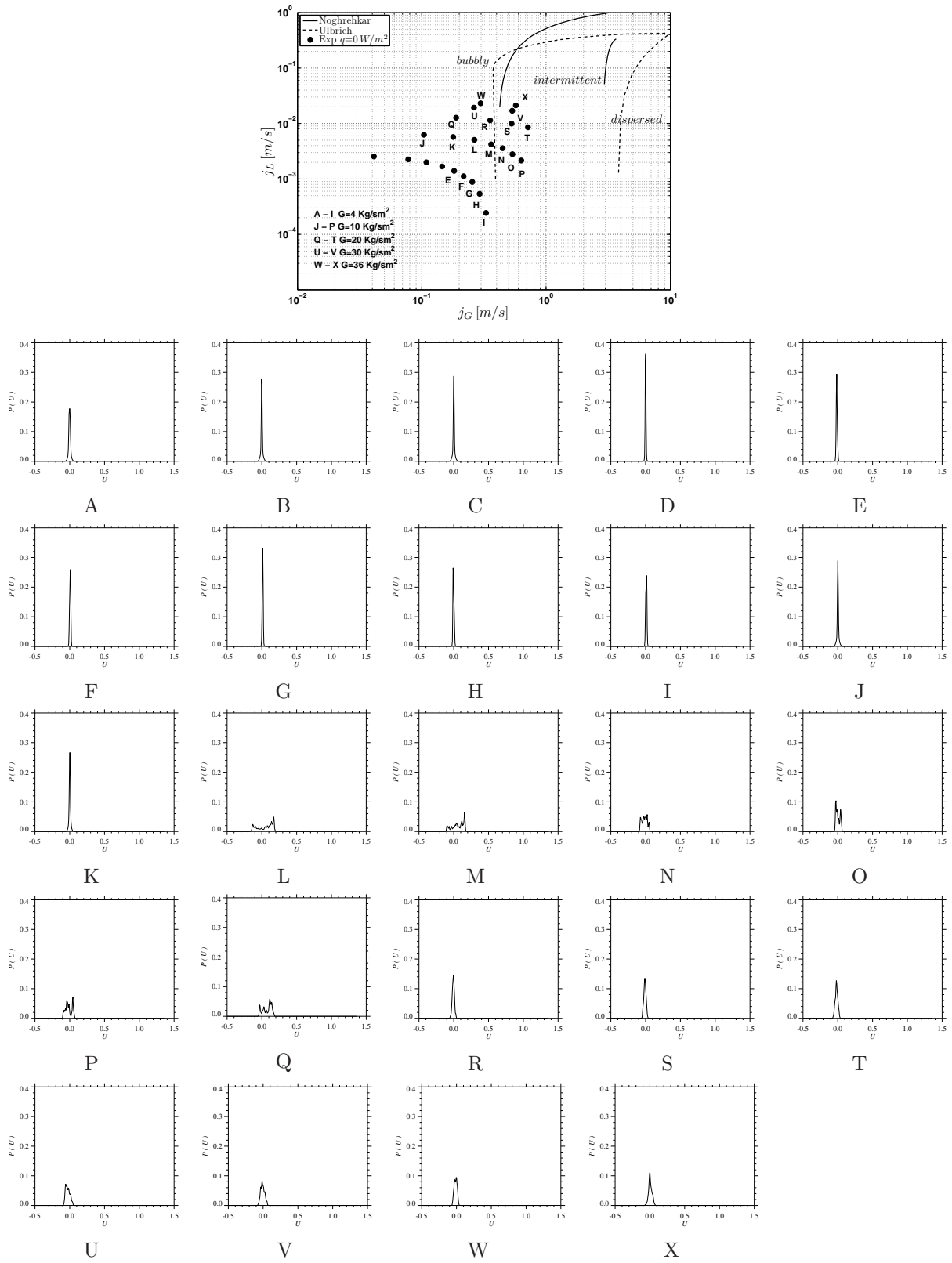
Figure 5.15: PDF of the pressure, adiabatic R236fa, T_{sat}=10 °C

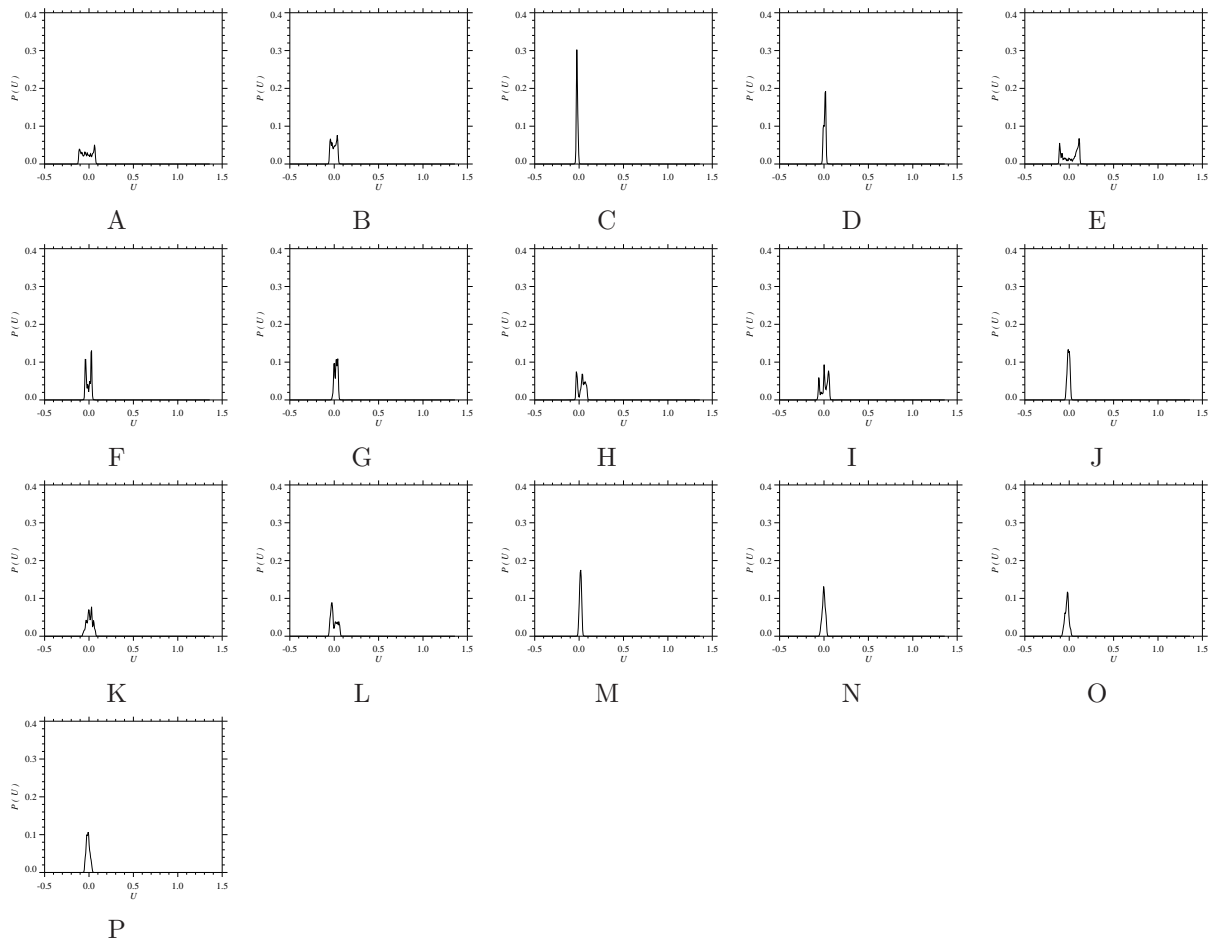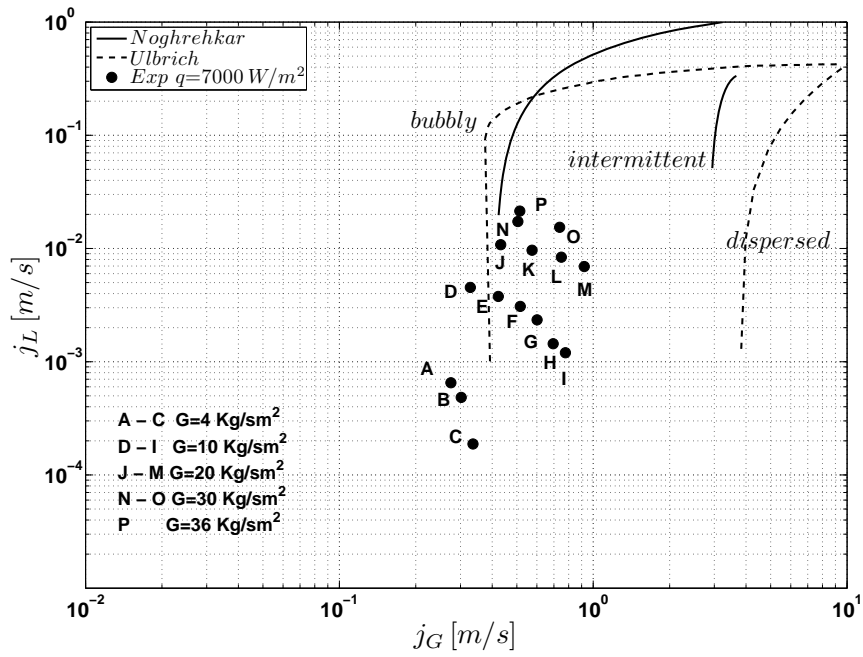Figure 5.16: PDF of the pressure, q=7000 $[W/m^2]$, R236fa, T_{sat}=10 °C
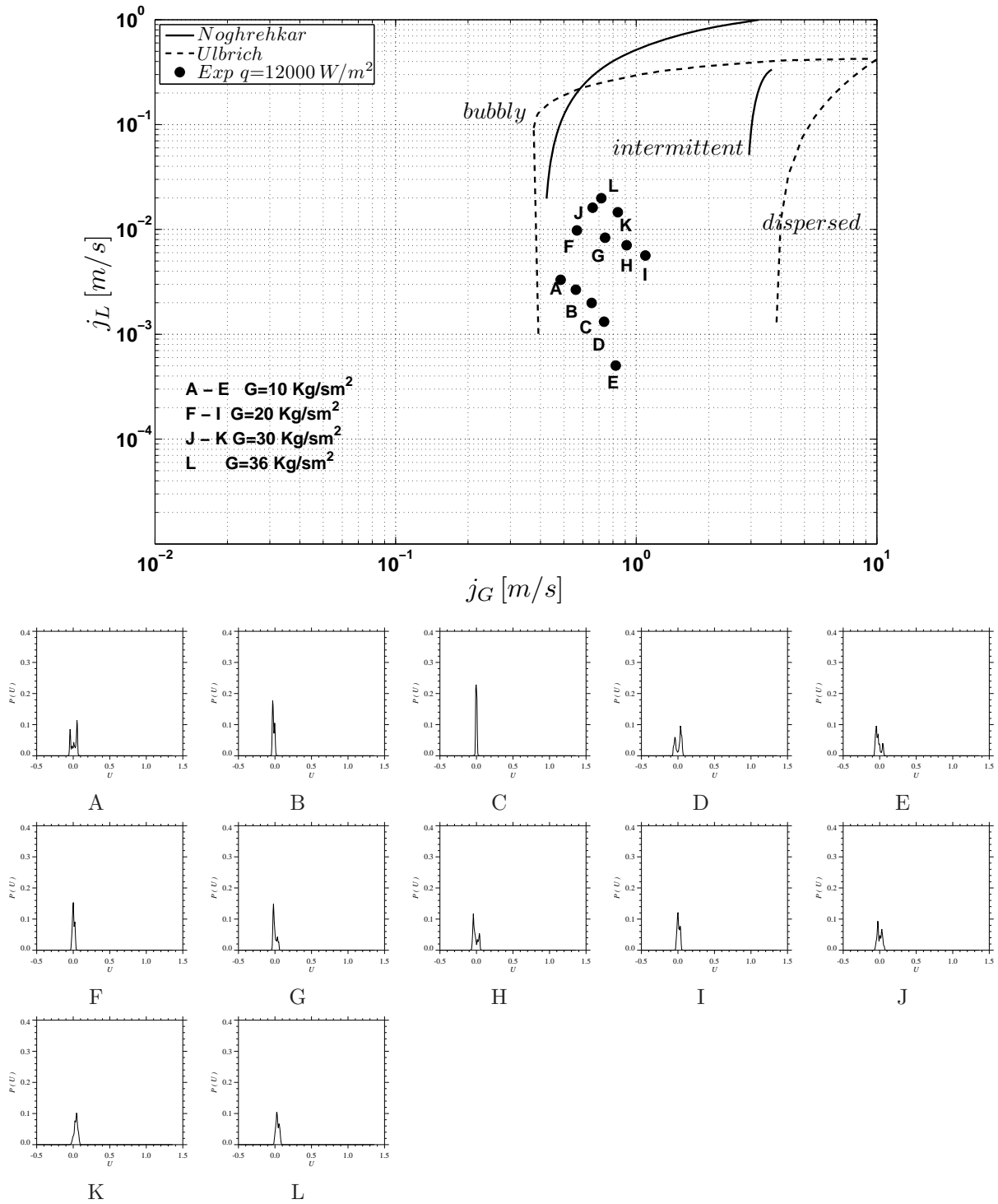
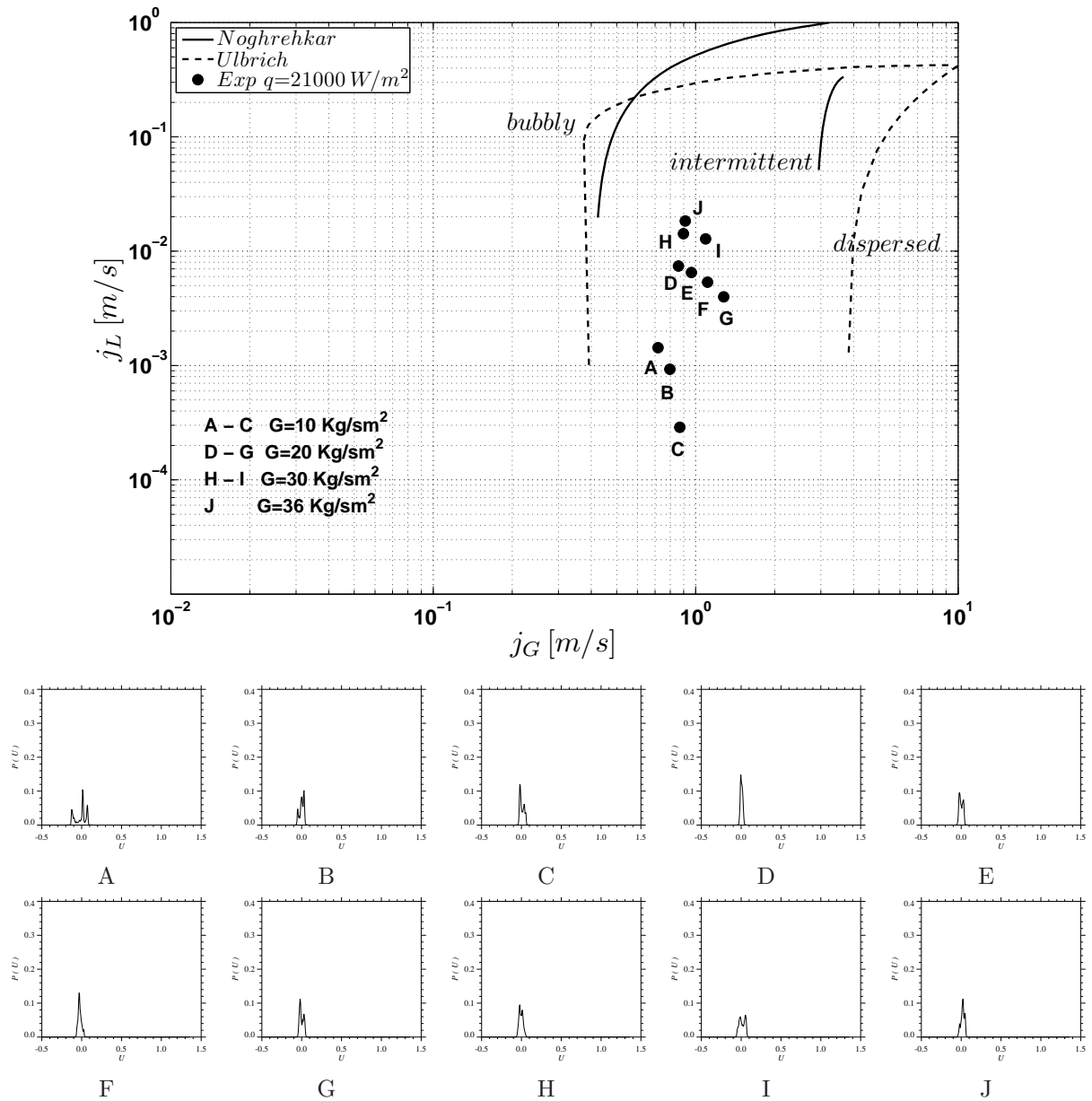Figure 5.17: PDF of the pressure, q=12000 $[W/m^2]$, R236fa, T_{sat}=10 °C

Figure 5.18: PDF of the pressure, q=21000 $[W/m^2]$, R236fa, T_{sat}=10 °C

5.2.5 Power spectrum

Power spectrum analysis was carried out on the laser and pressure signals. The sampling frequency $f_{samp} = 10000\,Hz$ led to a Nyquist frequency of $5000\,Hz$. The original signal, of length $10\,s$, was filtered with an anti-aliasing Kaiser filter, where the cut-off frequency was set at 0.96 times the Nyquist frequency. The signal was then split into 192 records of 2048 samples; the scheme assumes a 0.5 overlap ratio between successive records. The fast Fourier transform (FFT) then lead to a frequency resolution of $39.35\,Hz$ in the final spectra.

Laser signal

No sensible information could be extracted from the FFT power spectra of the laser signal.

Pressure signal

Power spectrum contour plots of the pressure signal are presented in Fig. (5.20) to Fig. (5.23). Each figure collects all the data for the same heat flux level, while each sub-figure represents a contour plot of the power spectrum intensity as a function of the local vapor quality and frequency. Considering one figure, each row represents the same saturation temperature and each column the same mass velocity. For each condition, where a condition is identified by a specific heat flux, temperature and mass velocity, important features were identified. In all, four different modes were observed, and identified as A, B, C and D.

A. Fig. (5.19)A shows two features. Firstly, a component at approximatively $200\,Hz$, whose frequency increases with increasing vapor quality. Secondly, well defined high frequency modes that disappear above a certain vapor quality.

B. Similar to A, however, the high frequency components only appear at higher vapor qualities in Fig. (5.19)B.

C. A high frequency component that decreases in frequency with increasing vapor qualities, highlighted in Fig. (5.19)C.

D. An increase in the level of background noise across the spectrum; possibly indicative of chaotic activity, highlighted in Fig. (5.19)D.
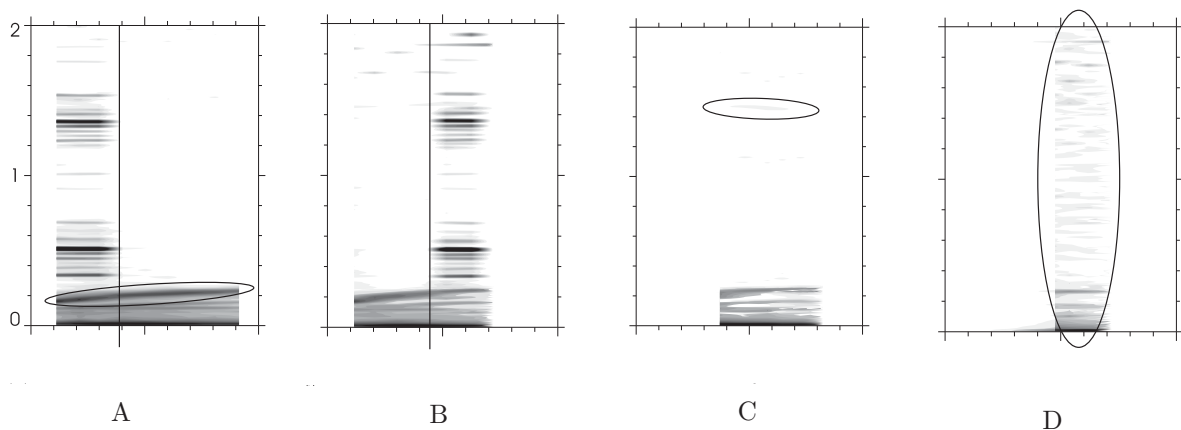

Figure 5.19: Power spectrum pressure modes, R236fa
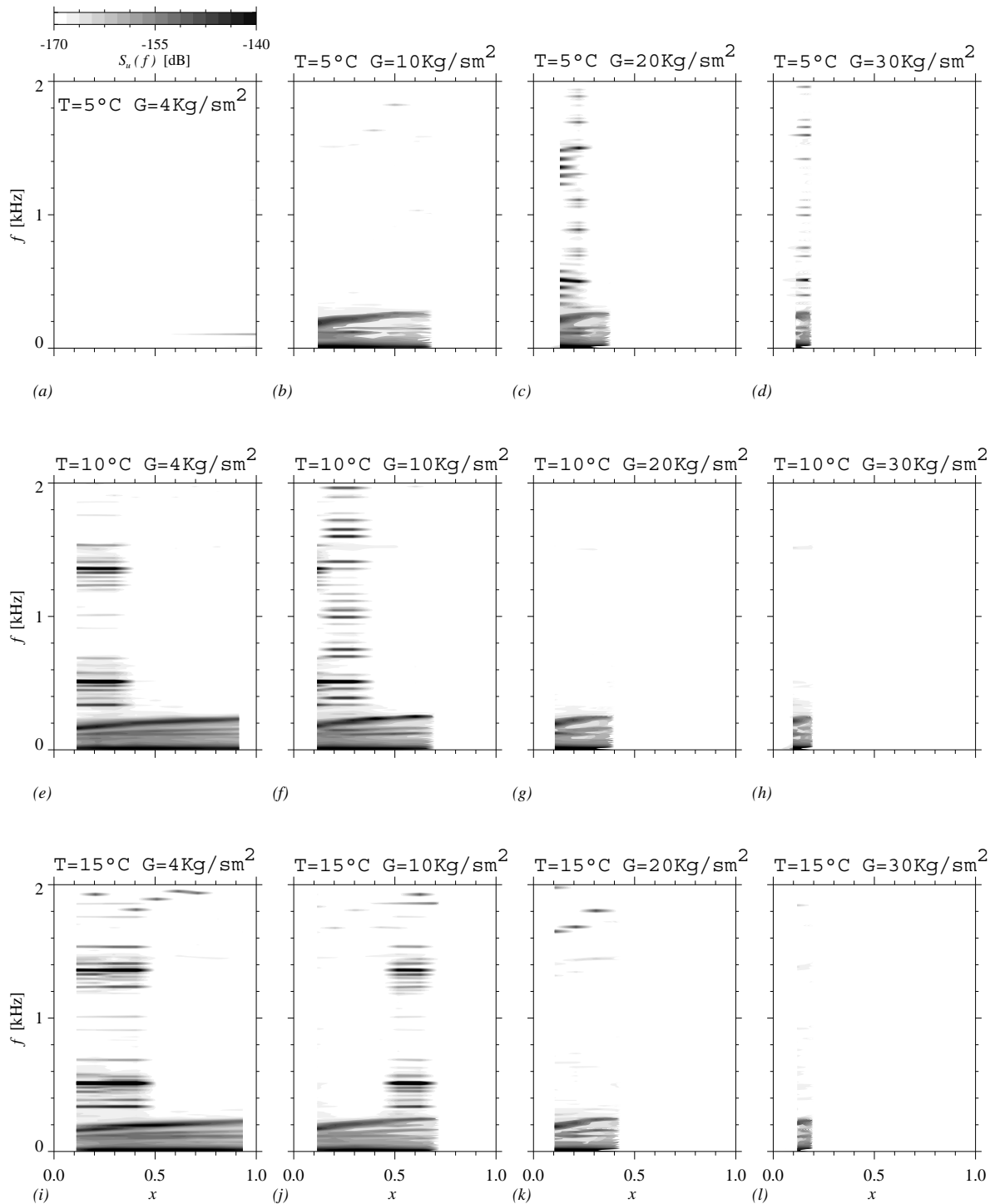
Figure 5.20: Power spectrum of the pressure, R236fa, adiabatic
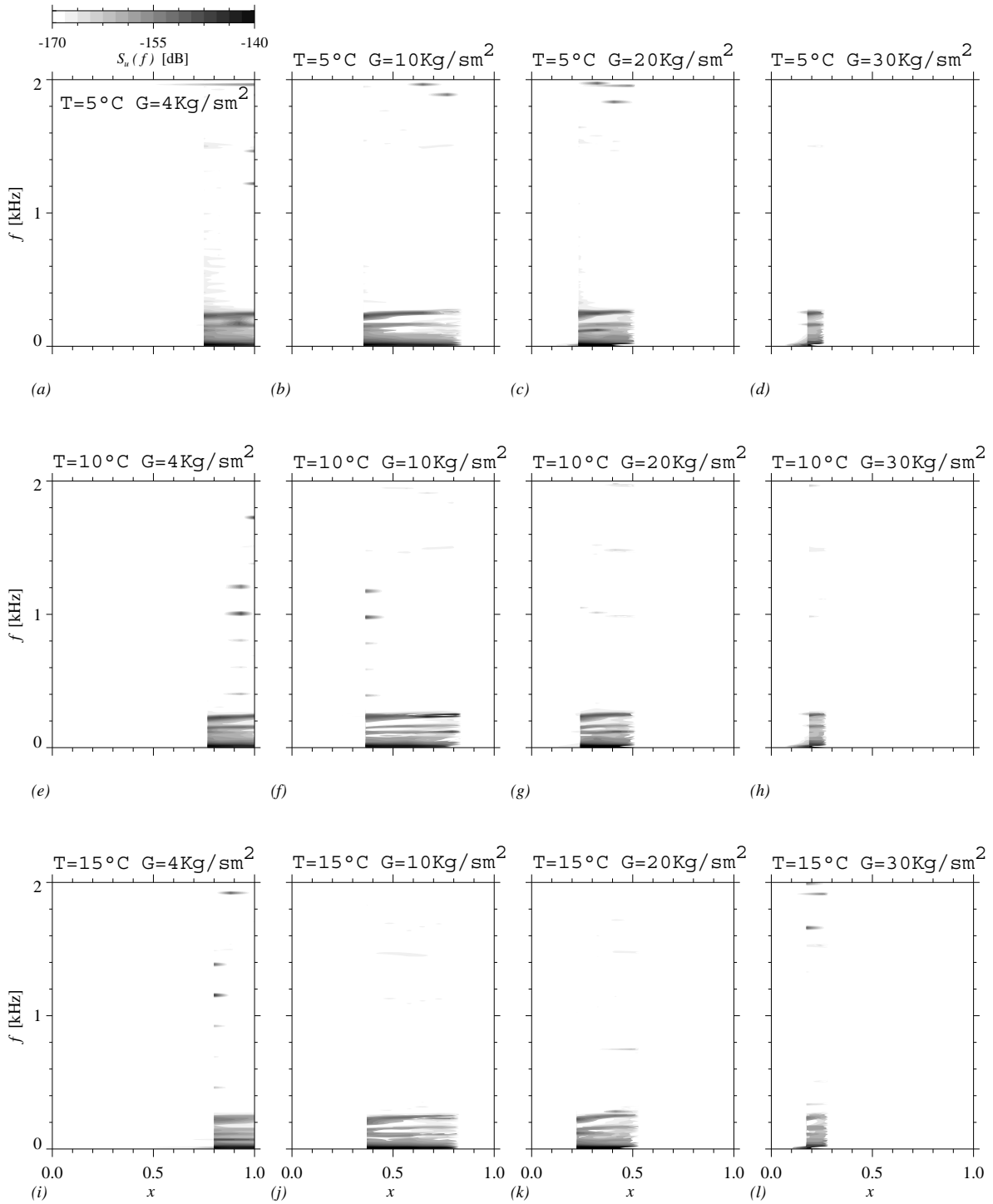
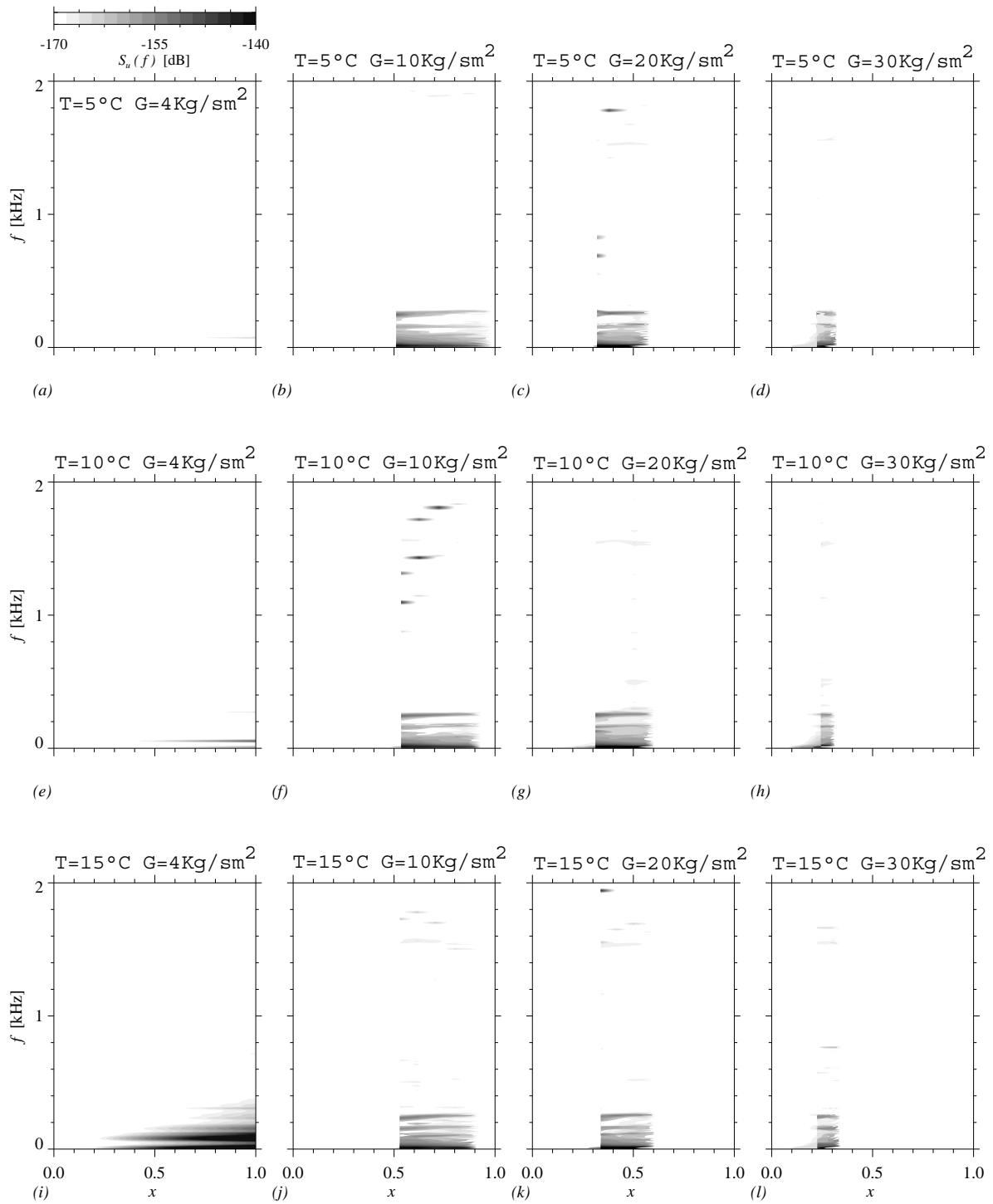Figure 5.21: Power spectrum of the pressure, R236fa, $q = 7000\,W/m^2$

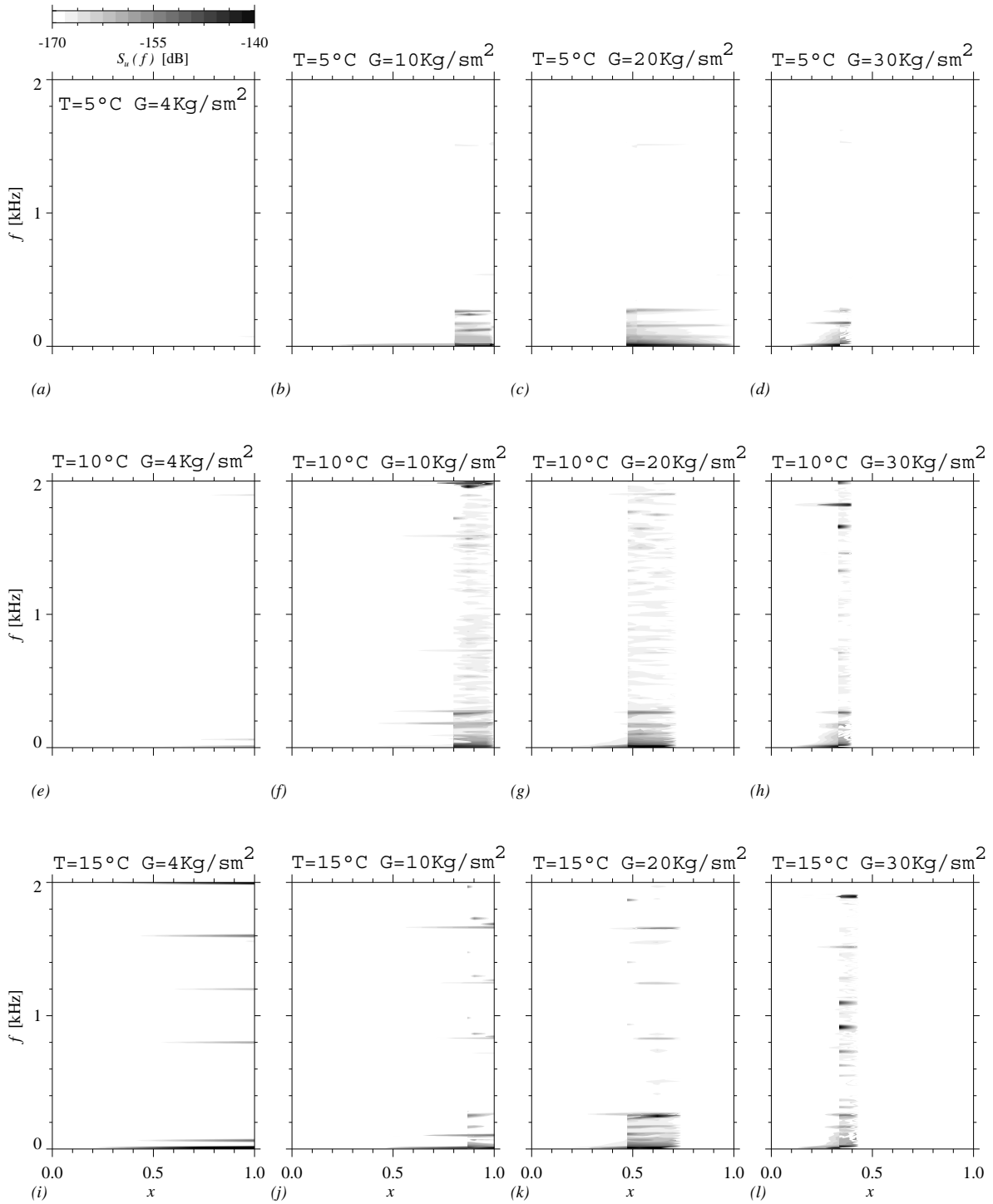Figure 5.22: Power spectrum of the pressure, R236fa, $q = 12000 \, W/m^2$

Figure 5.23: Power spectrum of the pressure, R236fa, $q = 21000\,W/m^2$

5.3   High speed video recordings

The sampling frequency of the high speed camera was $f_{samp} = 6\,kHz$ over a time interval of $t_{samp} = 4\,s$; the frame size was 256x256 $pixels$. In Fig. (5.24), a characteristic image of the two-phase flow is depicted. The setup of the visual system allows the acquisition of images covering an elliptical area with a semimajor axis of $a = 6.35\,mm$ and a semiminor axis of $b = 5.00\,mm$. The line $\overline{AB}$, defined at the midplane, was used as the reference for the image analysis.
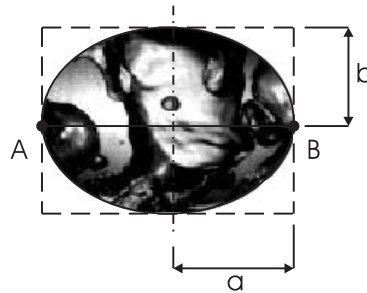

Figure 5.24: Field of view geometry

The novel approach used to evaluate the video recordings was to extract the pixel line $\overline{AB}$ from each image and to plot it over time. This results in an image where the abscissa is the line $\overline{AB}$ and the ordinate is the time. This allows a better and easier visual analysis of the results at the narrowest gap between the tubes. The concept is depicted in Fig. (5.25), where over an interval of time $\Delta t = (t^* - t_0)$, a structure moves up through $\overline{AB}$. Plotting this in a time dependent diagram results in a single image where structures crossing $\overline{AB}$ become inverted.
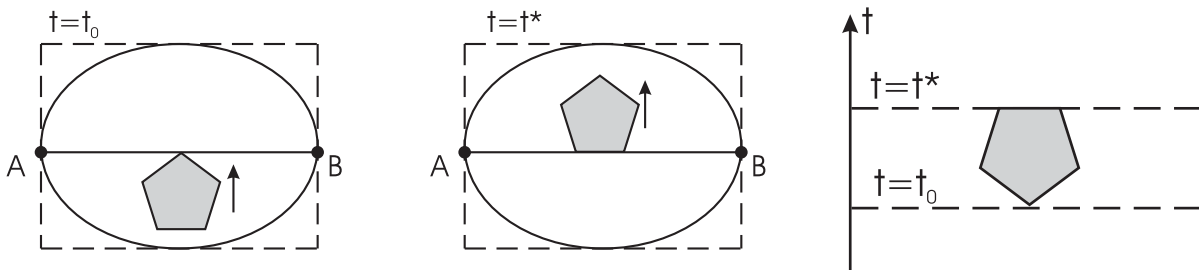
Figure 5.25: Image analysis concept

The resulting video observation is characteristic of the flow at the seventh tube row. These are depicted in Fig. (5.26), Fig. (5.28), Fig. (5.29) and Fig. (5.30) for a representative sample of the experiments: R236fa, T_{sat}=10 °C. The results are grouped according to the heat flux level and to the saturation temperature. In each image, a sketch of a flow map in terms of superficial gas and liquid velocities is shown; this provides a direct link between the visual observation and its experimental conditions. According to the literature, mainly on the basis of air-water experiments, the classification of *bubbly*, *intermittent* and *dispersed* is assumed. Bubbly flow is defined as a gas distributed as discrete small bubbles in the continuous liquid phase. The diameter of these bubbles is less than the characteristic spacing between tubes and should be generally uniform size. Dispersed flow manifests itself as an irregular and alternating motion of the liquid and gas. However, in the present study, the dispersed region was not covered because it was out of the range of possible measurements.

Considering the presented range of experimental conditions, the visualization of the tube bundle indicated that bubbly flow did not manifest itself as expected. Due to the low gas velocities typical of this

regime, the flow appears as a continuous liquid phase characterized by the presence of vapor bubbles of limited size. Vertically the gas bubbles are confined by the narrow gap between the tubes, whilst in the direction of the tube axis no confinement is present. At the measurement point, considered as representative, the bubbles are much bigger than the tube interspace and are not generally uniform in size. This can be expected in diabatic conditions: at a small inlet vapor quality, for example less then 0.1, we would expect a kind of bubbly flow. In such a case, a bubble rising from the bottom of the bundle will encounter all the tube rows where evaporation is taking place. New gas structures will be generated and then generally interact and coalescence will take place, leading to the observed patterns. Therefore, the flow pattern changes across the tube bundle, at least in diabatic conditions. So, if a bubbly flow, as defined in literature, is present at the bottom of the bundle, this will not be the case at the measurement location.

Superimposed on the vertical motion are secondary effects that manifest themselves on the gas structures and are visible in the figures, see for example points A, B, J of Fig. (5.26). The lateral movement indicates recirculation effects. This is generally more visible at low vapor qualities where the gas structures are well identifiable and trackable.

Following an ideal line of constant mass velocity and increasing vapor quality, an increase of the gas structure dimensions is notable; they get closer to each other in a chaotic and irregular motion until they cover all the visual area in continuous fashion. Liquid slugs appear randomly for intermediate conditions. This is visible for example in Fig. (5.26) at a mass velocity of $10\,kg/sm^2$ with a vapor quality ranging from 0.1 to 0.7.

At high vapor superficial velocities, the gas phase is dominant and covers all the visual area. A wavy surface indicates the presence of a liquid film all around the tube, that is a sort of "annular flow". In all the investigated conditions, excluding conditions of dry-out, the tube appears to be covered by a layer of liquid that manifests its presence by a wavy surface. Unfortunately, it was not possible to determine the liquid film thickness around the tubes in the bundle boiling facility. A sequence of representative raw images, obtained by the experimental campaign, is given in Fig. (5.31) where the waves are clearly visible. One possibility, from the acquired images, is to compute the local void fraction based on the area occupied by the liquid and the vapor phases. In the presented case, the image is a two-dimensional representation of the flow; this can lead to misinterpretations since the two-phase flow normal to the observation plane is not known. Therefore, the images do not give a full representation of the inter-tube volume. The present images are a good starting point for flow identification, but future improvements of the developed techniques should provide a better view of the flow field.

Coming back to the power spectrum of the pressure signal, it is interesting now to compare the four identified modes with the visual results. For the mode defined previously as A, the high energy peaks at low frequency are most probably linked with the direct passage of bubbles or more generally gas structures. The passage of a gas structure leads to a variation in the pressure. This can explain the continuous shift of the low frequency peaks towards higher frequencies. For modes B and C it was not possible to find any link with the flow observations. Mode D, characteristic of chaotic motion, is representative of a flow that appears visually as a continuous structure of gas without liquid inclusions, and where a wavy surface indicates the presence of a liquid film. Therefore, it is possible to speculate that in this case the liquid is mainly present as a film. The wide range of higher frequencies characteristic of mode D could be an effect of the wavy film pattern.

The measurement campaign was carried out in a range of mass velocities between 4 and $40\,kg/sm^2$. The results did not show agreement with the maps of Noghrehkar et al. [16] and Ulbrich and Mewes [12]. This mismatch is also clear from the frictional pressure drop and the local heat transfer data. The lack of changes in behavior in the measured data could indicate that they were all taken in the same flow regime, and that no mode change occurred. This could suggest the validity of the map proposed by Xu et al. [14], [15], since all his points fall in the churn regime that is controlled by gravitational forces and characterized by chaotic motion and distorted bubble shapes. However, this is speculation since the experiments conducted by Xu et al. were for air-water flows. According to our identification campaign,

it was not feasible to propose a new flow pattern map, at least at this time, since the visual data indicate a gradual transition from one condition to another. It is of course possible to define different flow regimes according to bubble sizes, but since there is no direct effect on the measured local heat transfer or frictional pressure drops, this appears not to be important at this stage.

Flow pattern maps proposed in literature for tube bundles are based on their supposed correspondence to intube two-phase flows. However, the results of the present study do not lead to a validation of this duality. The observed discrepancies include:

- Due to the change in geometry within a tube bundle, the convected bubbles are subjected to cyclic compression and expansion as they pass across the tube vows.

- Unlike intube flows, the liquid film is no longer continuous but becomes interrupted from tube to tube.

- The bundles display secondary flow patterns absent in intube two-phase flow.

- The convected bubbles may coalesce with others when impacting against successive tubes in a bundle
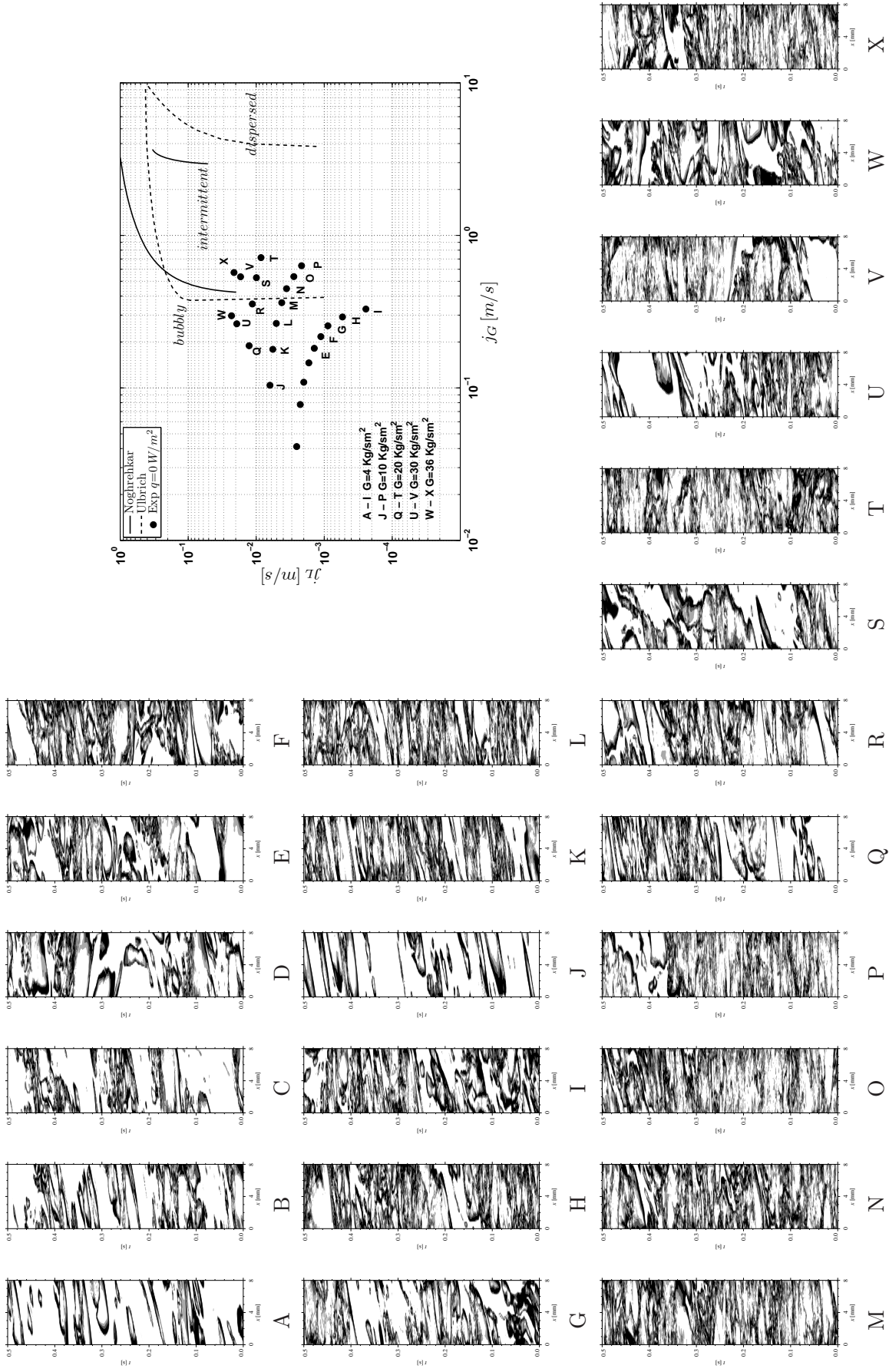
Figure 5.26: Flow visualization, adiabatic R236fa, $T_{sat}=10\,^{\circ}C$
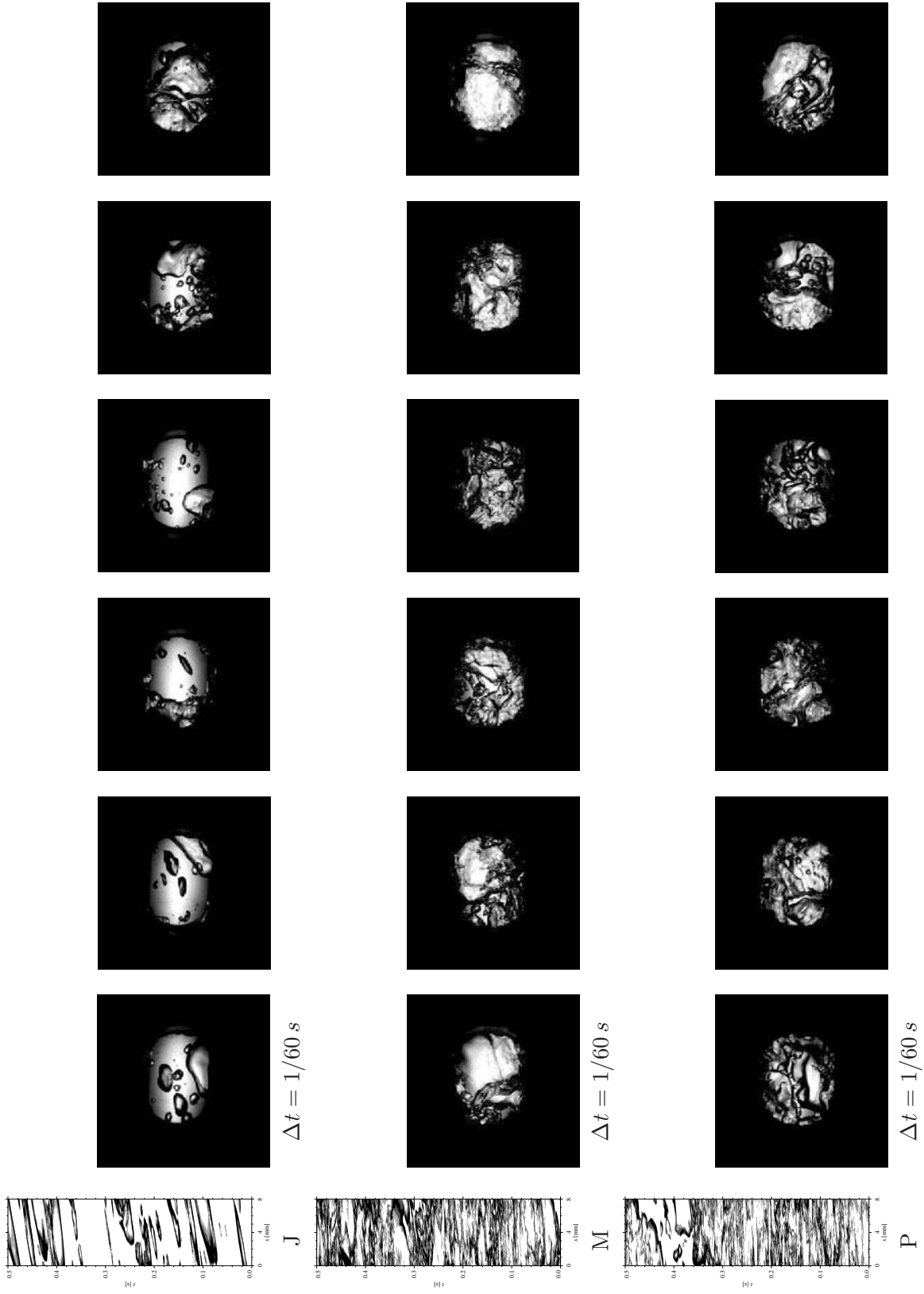
Figure 5.27: Flow visualization, image series, adiabatic R236fa, $T_{sat}=10\,°C$

$\Delta t = 1/60\,s$

J

$\Delta t = 1/60\,s$

M

$\Delta t = 1/60\,s$

P

Figure 5.28: Flow visualization, q=7000 $[W/m^2]$, R236fa, T_{sat}=10 °C
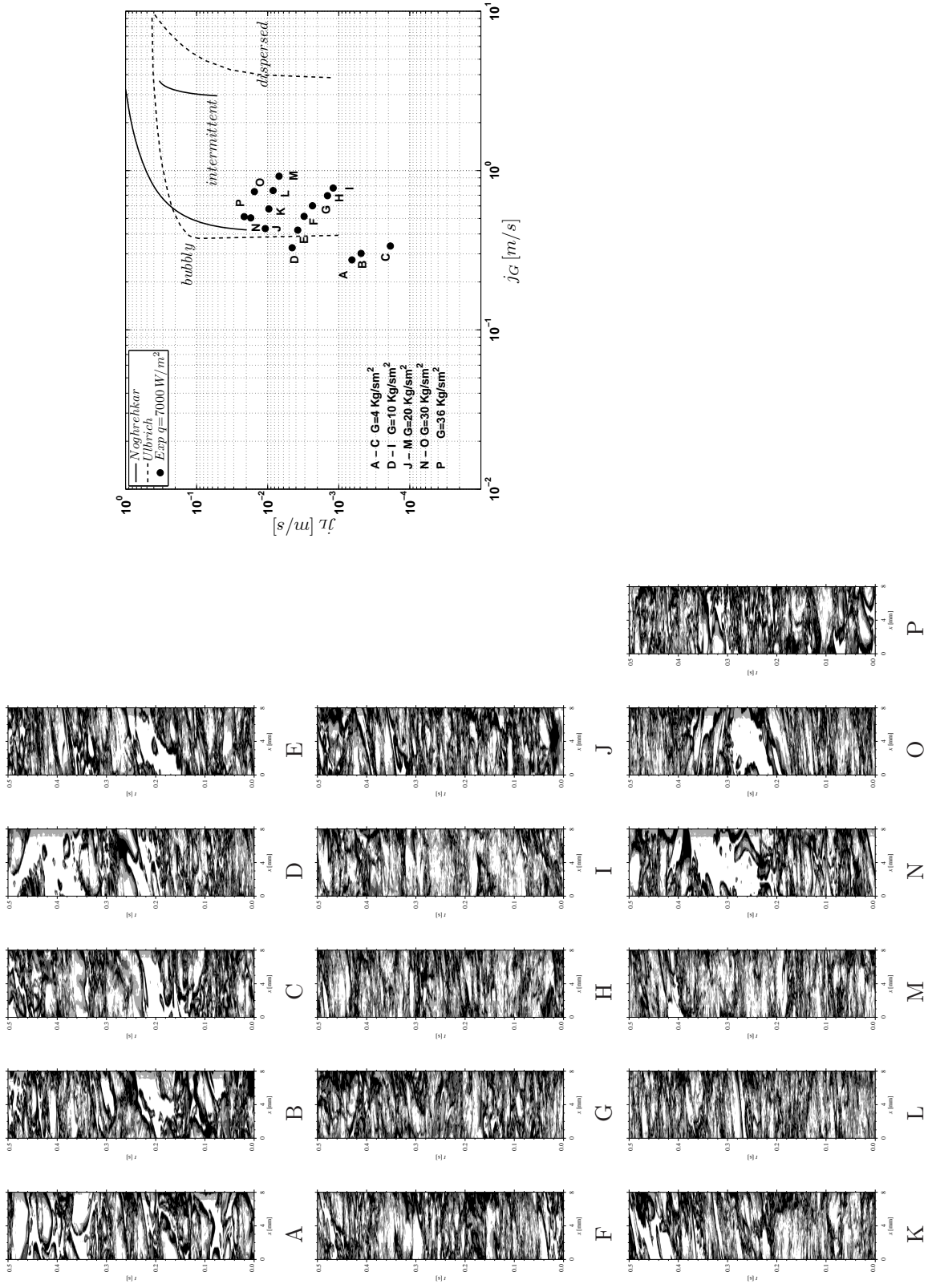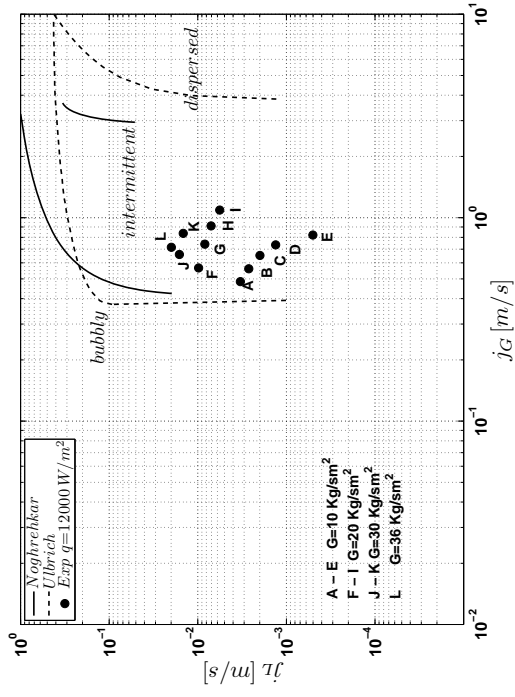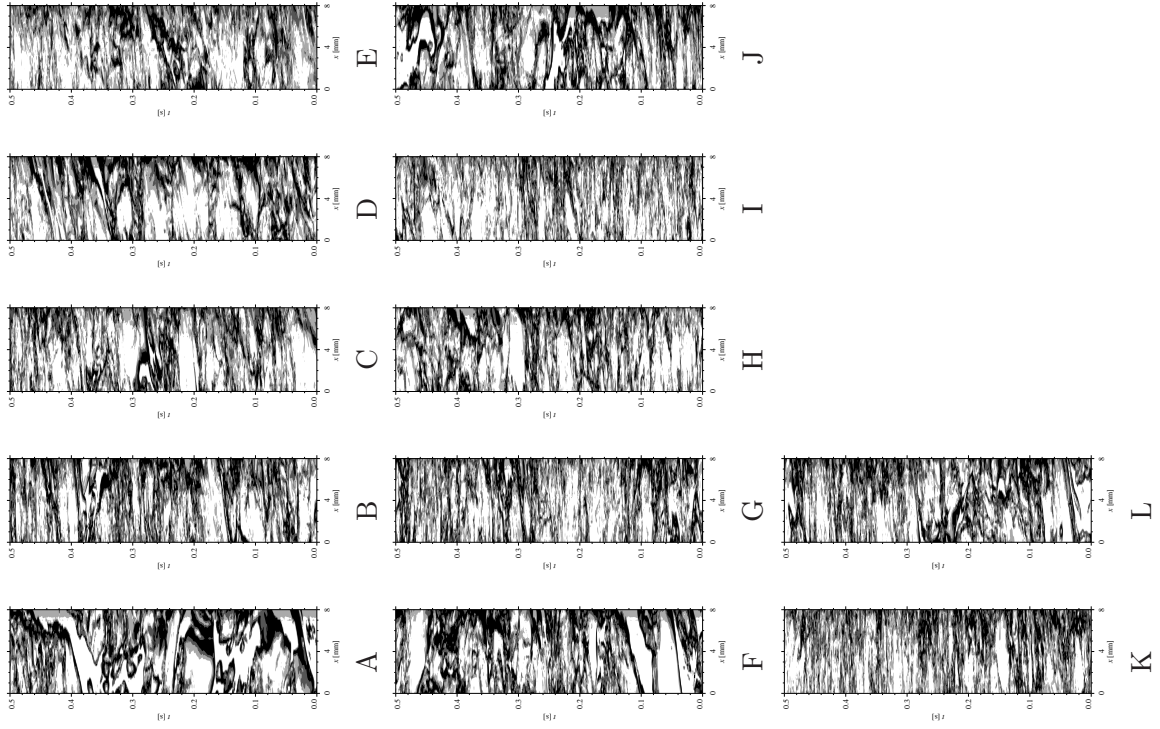
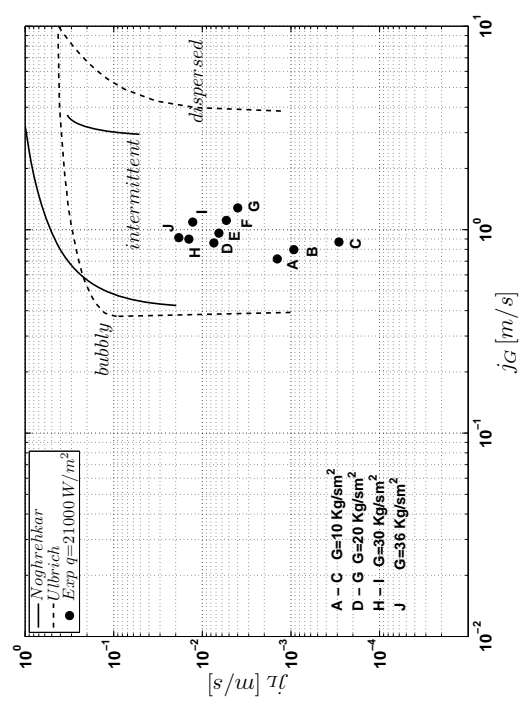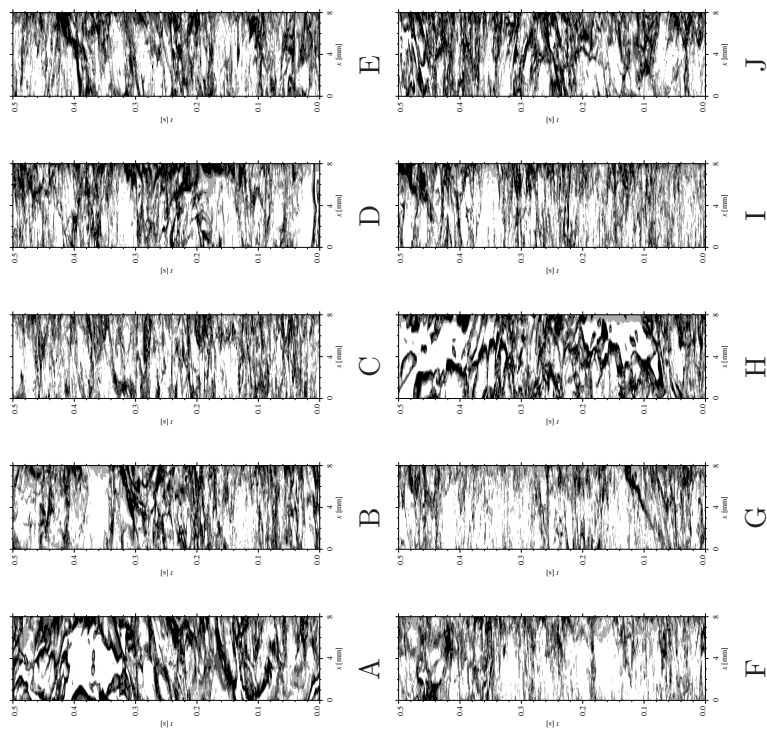Figure 5.29: Flow visualization, q=12000 $[W/m^2]$, R236fa, T_{sat}=10 °C

Figure 5.30: Flow visualization, q=21000 $[W/m^2]$, R236fa, T_{sat}=10 °C
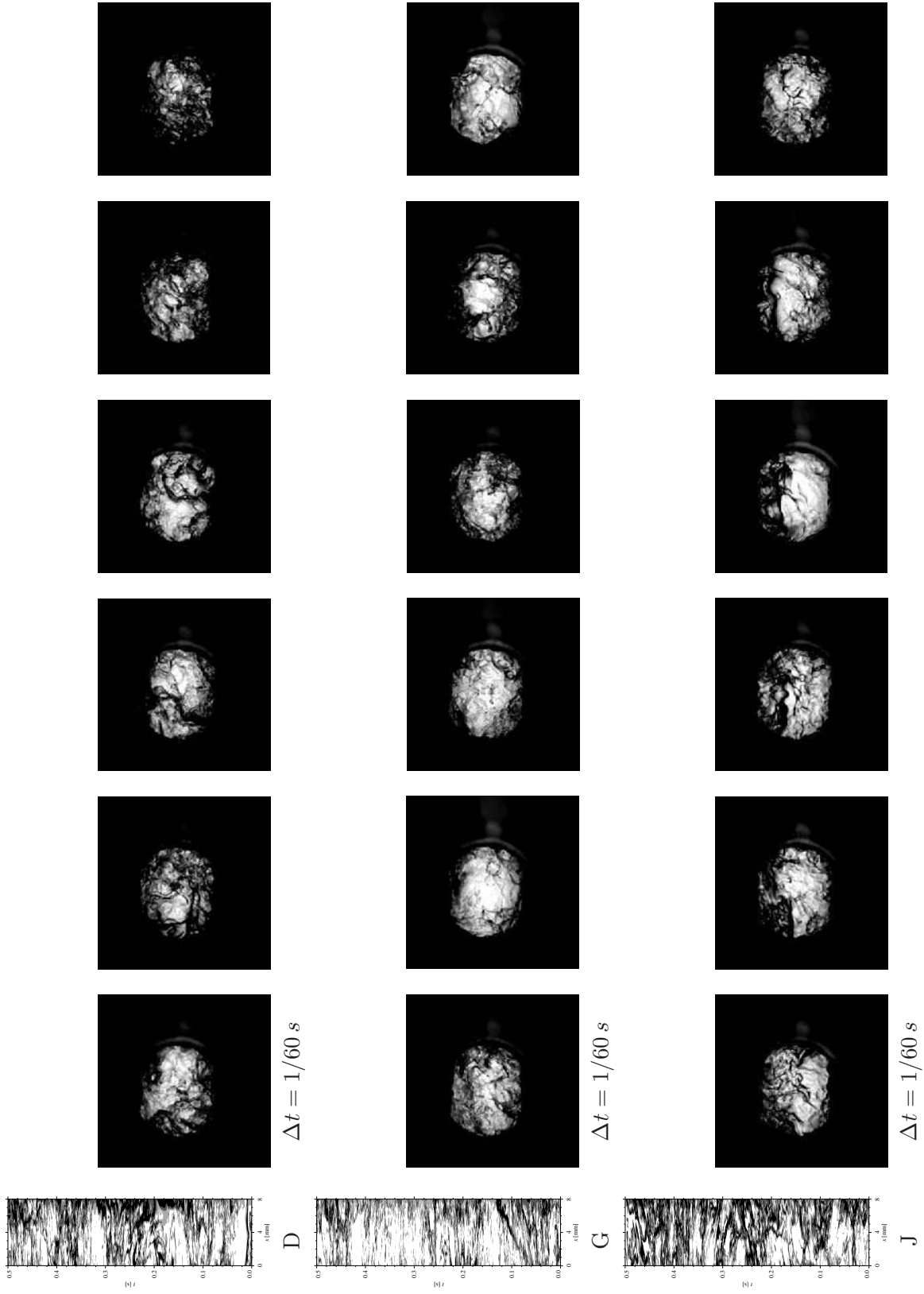
Figure 5.31: Flow visualization, image series, q=21000 $[W/m^2]$, R236fa, T_{sat}=10 °C

Chapter 6

Pressure Drop

In this chapter, the experimental results concerning pressure drop in tube bundles are discussed and compared to existing two-phase pressure drop correlations. An analysis of local frictional two-phase pressure drop and an update of the existing LTCM prediction method is proposed.

6.1 Single phase pressure drop results

A validation of the test-section in single-phase flow conditions was undertaken for tests with sub-cooled liquid $R134a$ flowing through the test section from bottom to top. The experimental test conditions are presented in Table 6.1.

Tubes	Smooth tubes (Table 6.2)
Test fluid	R134a
Saturation temperature	T_{sat}=14 °C
Mass flux	4-40 $[Kg/m^2 s]$

Table 6.1: Single phase test conditions

The liquid flow is driven through the test section at controlled conditions. When steady-state conditions were reached, the acquisition was performed. The differential pressure taps are located at the inlet and at the exit of the test section.

6.1.1 Geometry

The geometry arrangement of the tube bundle in non-dimensional form is represented as:

$$a = \frac{s_q}{D_o} = 1.178\,[-] \qquad b = \frac{s_l}{D_o} = 1.020\,[-] \qquad c = \frac{s_d}{D_o} = 1.178\,[-] \tag{6.1}$$

The equivalent diameter of the tube bundle was computed as described in 3.3.1, resulting in $d_{gb} = 9.98\,mm$.

D_o	18.87 $[mm]$
D_i	16.00 $[mm]$
Material	Alloy 12200
Layout	Staggered equilateral
s_q	22.22 $[mm]$
s_d	22.22 $[mm]$
s_l	22.22$\cdot \left(\sqrt{3}/2 \right)$ $[mm]$

Table 6.2: Tube geometry parameters

6.1.2 Experimental results

The following results are representative of the experimental conditions noted previously in Table 6.1. The Reynolds numbers covered were for Re from 340 to 3400. In Fig. (6.1) the total single phase pressure drop was measured and its gravitational component is plotted versus the mass flux. As expected, at low mass velocities in the investigated range, the gravitational component is the dominant one. Its values for an all liquid flow is 2040 Pa, two orders of magnitudes larger than the frictional component. Fig. (6.2) depicts the experimental frictional component versus those predicted from the Žukauskas and the Gnielinski methods presented in 3.3.1. As expected, the single phase frictional component is very small; this is due to the low Reynolds numbers imposed through the test section, according to the feasible operating range of the test facility. The two prediction methods agree well with each other but they do not predict the experimental data in a satisfactory way. Considering the accuracy of the differential pressure transducers employed that were sized for two-phase flow, the difference between the experimental and predicted components remains inside the uncertainty of the differential pressure transducer. Hence, is not possible to pre-validate the measurements with single-phase liquid tests, as their values are too low for the instrumentation chosen for the much larger two-phase pressure drops.
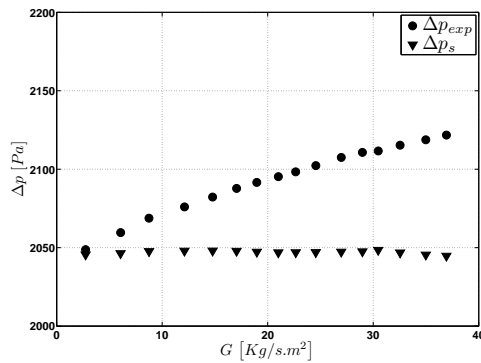
Figure 6.1: Experimental pressure drop

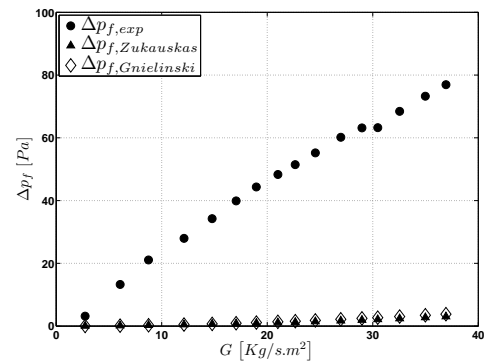Figure 6.2: Experimental frictional pressure drop versus predicted

6.2 Two-phase pressure drop results

Measurements of the two-phase pressure drop were carried out. Each measurement is comprised three components: gravitational, momentum and frictional pressure drop. According to the equations presented in 3.3.2, the gravitational and momentum components can be backed out from the measured test condi-

tions and from the evaluation of the void fraction by the application of the Feenstra et al. method [50] described in 3.2. The computation of the void fraction makes use of the computed values of the vapor quality through the tube bundle; this is possible through thermal balances across a discretized geometry of the tube bundle. The discretization of the tube bundle for the thermal balance and thus for the vapor quality and void fraction is depicted in Fig. (6.3): thermal balances are based on the control volumes indicated as $A1$ to $A7$ and identified with the coordinate z from $i0$ to $i7$, the corresponding values are shown in Table 6.3. Coming back to the original problem of the frictional pressure drop computation, once all the necessary quantities are calculated to determine the gravitational and momentum component, the frictional one is backed out from the measured total pressure drop. For the pressure drop computation, the discretization scheme is slightly different and the distance between two reference sections is now one pitch of the tube bundle and is indicated in Fig. (6.3) with letters from a to h. At this point, the values of the void fraction at the section of interest are computed through a linear interpolation between two values of the discretization scheme of the heat transfer. This is done, according to equations presented in 3.3.2, to account for variations of the thermal properties of the refrigerant for the calculation of the gravitational component.

Figure 6.3: Void fraction, vapor quality and pressure drop discretization schemes
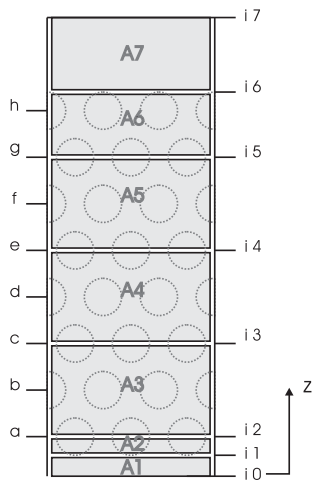
Position	Distance z [mm]
$i0$	0.00
$i1$	5.32
$i2$	14.75
$i3$	53.25
$i4$	91.75
$i5$	130.25
$i6$	159.00
$i7$	182.00

Table 6.3: Discretization geometric reference

Fig. (6.4) and Fig. (6.5) depict, for adiabatic $R134a$ and $R236fa$, the static and frictional pressure drop as a percentage on the total pressure drops. Each static pressure drop data is paired with a frictional one and vice-versa. The static and frictional pressure drop results are of the same order of magnitude. For diabatic tests, Fig. (6.6) and Fig. (6.7) additionally depict the momentum component. The static and frictional pressure drop results are of the same order of magnitude and the momentum pressure drop, that reflects the change in kinetic energy of the flow, is negligible.

The interpretation of the frictional pressure drop data results must consider that the uncertainty on the frictional pressure drop is strictly linked with the uncertainty on the prediction of the void fraction. The void fraction model, Feenstra et al. method [50], predicts values within $\pm 20\%$.

6.2.1 Local experimental pressure drop results

Adiabatic flow

Local plots of the pressure drop components across the tube bundle are presented here. The frictional pressure drop appears not to be sensitive to the saturation temperature in the investigated range T_{sat}=5-15 °C. In Fig. (6.8) and Fig. (6.9), plots of the frictional pressure drop for $R134a$ and $R236fa$ under adiabatic conditions at a mass velocity G=10 kg/sm^2 are presented. The increase in two-phase frictional pressure drop with vapor quality is also in line with expectations. No clear dependencies on saturation
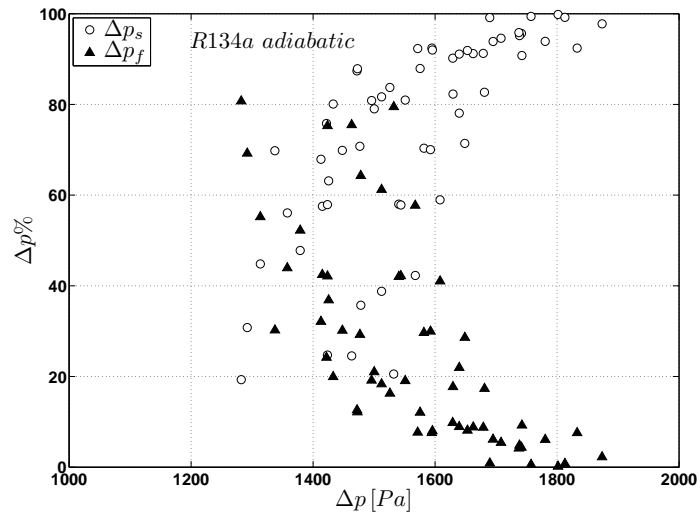
Figure 6.4: Comparison of the static and frictional pressure drops, R134a adiabatic
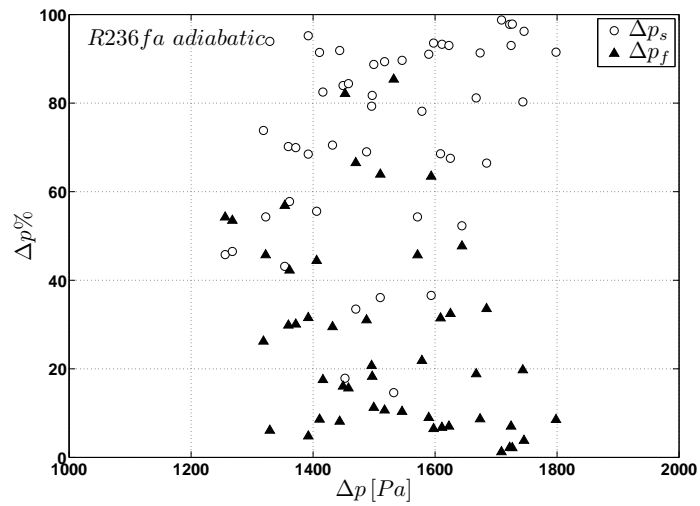

Figure 6.5: Comparison of the static and frictional pressure drops, R236fa adiabatic
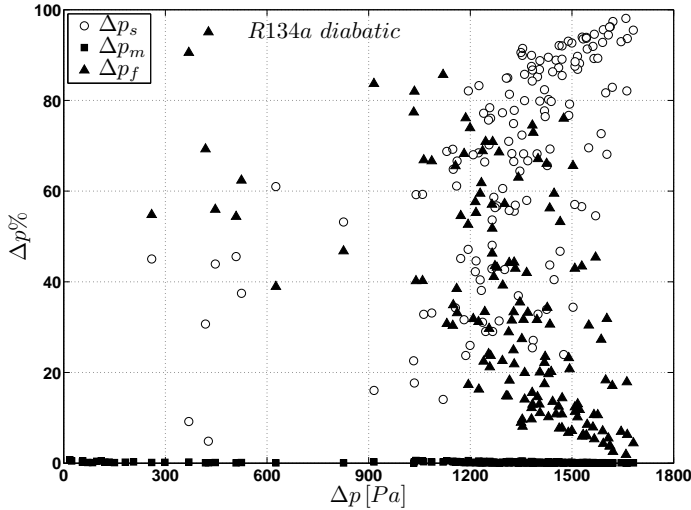
Figure 6.6: Comparison of the static, momentum and frictional pressure drops, R134a diabatic
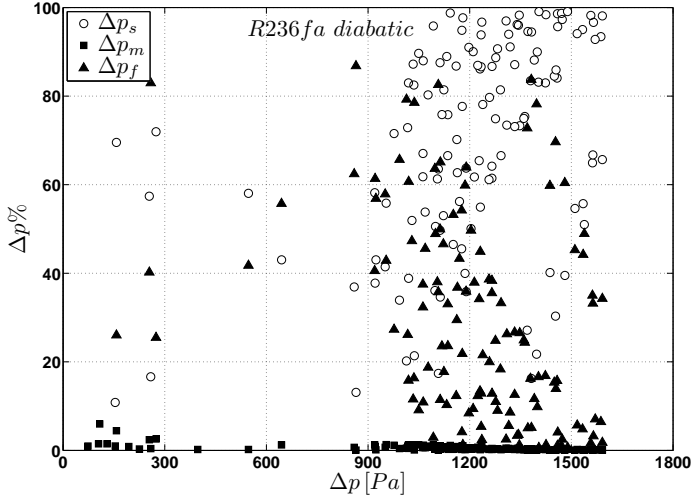

Figure 6.7: Comparison of the static, momentum and frictional pressure drops, R236fa diabatic

temperature are noticed. The same behavior appears for the wide range of mass velocities investigated. For this reason, only the results at the saturation temperature of 15 °C will be shown. Analyzing the frictional pressure drop data under adiabatic conditions, slightly negative values are obtained, this is due to the accuracy of the instrumentation and to the procedure used to back out this pressure drop component; a process which is affected by uncertainties in the heat balances and the void fraction model.
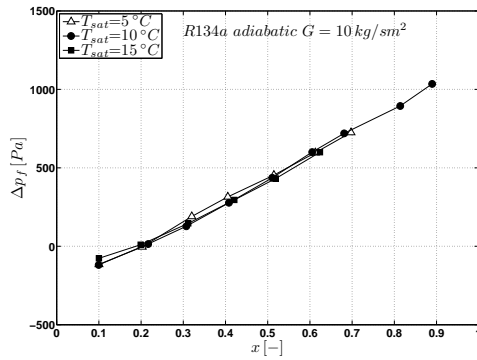

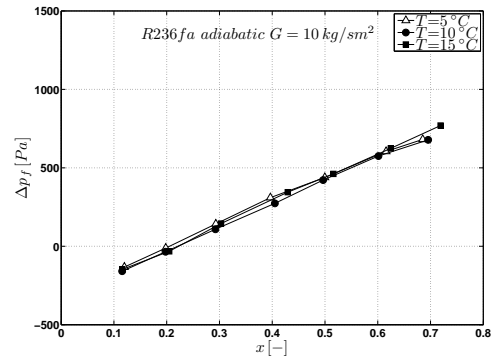Figure 6.8: R134a adiabatic, G=10 kg/sm^2, frictional pressure drop component

Figure 6.9: R236fa adiabatic, G=10 kg/sm^2, frictional pressure drop component

Concerning the adiabatic results for $R134a$ in Fig. (6.10), Fig. (6.11) and Fig. (6.12), the total pressure drop, the static and the frictional component are plotted as a function of the vapor quality according to the mass velocity that ranges between 4 and 40 kg/sm^2. At higher mass velocities, a wide range of vapor qualities could not be covered due to limitations of the experimental facility. Observing the total pressure drop Fig. (6.10) and the static one Fig. (6.11), there is a decrease of the pressure drop with increasing vapor quality for a fixed mass velocity. The measurements also depict lower total and static pressure drop values for lower mass velocities. This is visible also for $R236fa$ in Fig. (6.13) and Fig. (6.14).

These decreases with increasing vapor qualiy can be explained considering Fig. (6.16), where for a fixed temperature and vapor quality, the void fraction ε and the velocity ratio S are plotted as a function of the mass velocity G. The void fraction increases with the mass velocity at a fixed vapor quality, showing a factor of 3 between the lowest and the highest mass velocity (4-30 kg/sm^2). The velocity ratio, between the vapor and liquid phases, decreases by a factor of 5 for mass velocities ranging from 4 to 30. Considering now that the density used to compute the static pressure drop is a linear combination of vapor and liquid densities weighted respectively to ε and $(1 - \varepsilon)$, the behavior is directly linked to the fact that different void fractions are obtained for different mass velocities with the same vapor quality.

Analyzing now the frictional component, for $R134a$ and $R236fa$ depicted in Fig. (6.12) and Fig. (6.15), the frictional pressure drop, as expected, increases with the vapor quality for a fixed mass velocity over the investigated range (x=0 − 0.9). The adiabatic experiments reached a maximum vapor quality of 0.9 (limited by the pre-heater). A maximum of the pressure drop right before the dry-out would be expected but could not be reached experimentally. An increase of the mass velocity for the same vapor quality led to an increase of the frictional pressure drop, as expected. A plot of the void fraction and velocity ratio for a fixed mass velocity of 4 kg/sm^2 as a function of the vapor quality at adiabatic conditions for $R236fa$ at a saturation temperature of T_{sat}=15 °C is given in Fig. (6.17): the velocity ratio decreases slightly showing a limited dependency on the vapor quality.

No significant changes in trends of the pressure drop were observed, that would perhaps have indicated a change of the flow pattern in the investigated experimental range. Another possibility is that for the flow patterns covered with the present investigation, the flow patterns do not play a dominant role in the pressure drop behavior.
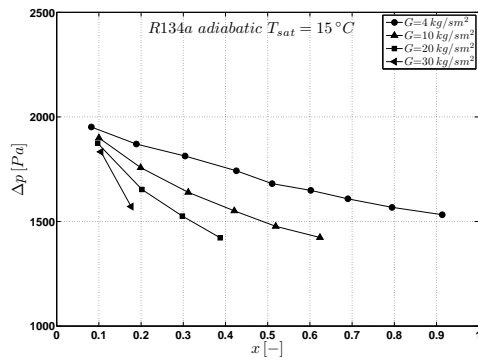
Figure 6.10: R134a adiabatic, T_{sat}=15 °C, total pressure drop

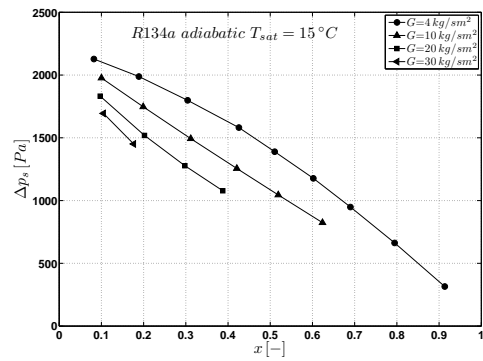Figure 6.11: R134a adiabatic, T_{sat}=15 °C, static pressure drop component

Figure 6.12: R134a adiabatic, T_{sat}=15 °C, frictional pressure drop component
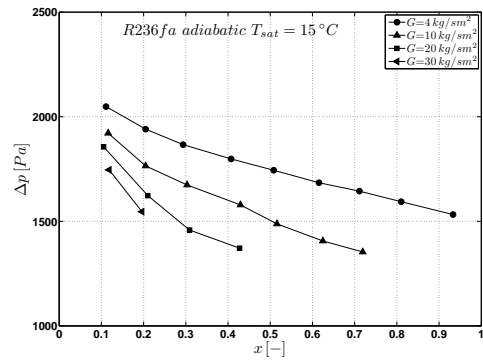
Figure 6.13: R236fa adiabatic, T_{sat}=15 °C, total pressure drop

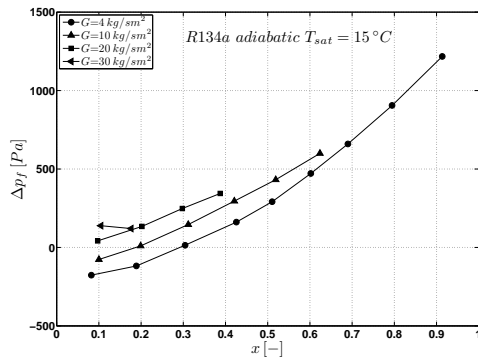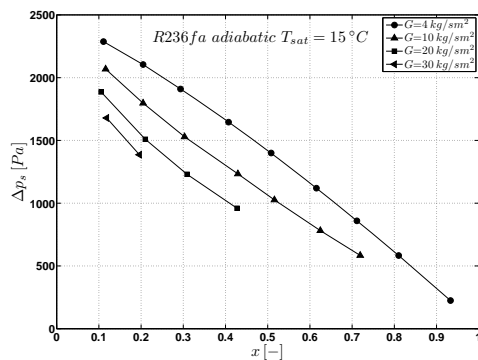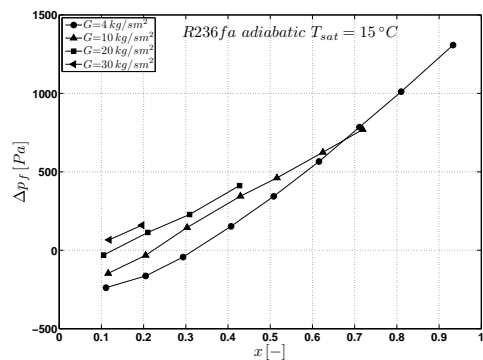Figure 6.14: R236fa adiabatic, T_{sat}=15 °C, static pressure drop component

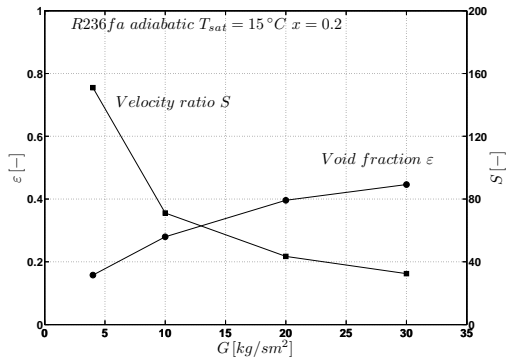Figure 6.15: R236fa adiabatic, T_{sat}=15 °C, frictional pressure drop component

Figure 6.16:   R236fa adiabatic, T_{sat}=15 °C, x=0.2 [−], void fraction and velocity ratio
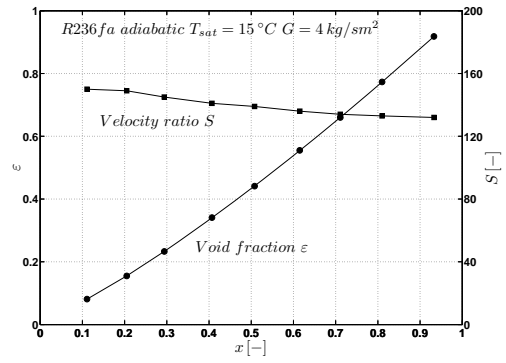

Figure 6.17:   R236fa adiabatic, T_{sat}=15 °C, G=4 [kg/sm^2], void fraction and velocity ratio

Diabatic flow

The results for frictional pressure drops for diabatic flow are presented here. The frictional pressure drop is plotted as a function of the mean vapor quality between the inlet and the outlet of the test section (the vapor quality changes across the tube bundle). $R134a$ and $R236fa$ were investigated and the results were grouped according to fluid type and heat flux, depicted from Fig. (6.18) to Fig. (6.23).

The frictional pressure drop in each case shows the classical trend: it increases with the vapor quality for a fixed mass velocity. When the conditions of the vapor quality equal to 1 are approached for the lowest mass velocity ($4 \, kg/sm^2$), there is a dramatic drop of the pressure drop. This is visible for example at a heat flux of $7000 \, W/m^2$ in Fig. (6.18), which approaches a vapor quality of 1 at the exit of the bundle facility is indicated with the circle. At a low mass velocity, dry-out suddenly covers most of the heat transfer area and for this reason a quick drop in the frictional pressure drop appears. The same behavior is visible for $R236fa$ at the same heat flux levels as in Fig. (6.21), where dry-out appears at earlier inlet vapor qualities for a fixed mass velocity. This difference between $R134a$ and $R236fa$ is linked to the thermophysical properties of the fluid and particularly to the latent heat of vaporization: for $R236fa$ at T_{sat}=15 °C, the latent heat is 19% smaller than for $R134a$. Earlier dry-out for $R236fa$ in respect to $R134a$ is visible for all levels of heat flux. Particularly, at low mass velocities, the frictional pressure drop indicates the dry-out as a sudden drop as in Fig. (6.18) to Fig. (6.23).

Figure   6.18:   R134a, q=7000 W/m^2, T_{sat}=15 °C, frictional pressure drop component

Figure   6.19:   R134a, q=12000 W/m^2, T_{sat}=15 °C, frictional pressure drop component

Figure 6.20: R134a, q=21000 W/m^2, T_{sat}=15 °C, frictional pressure drop component
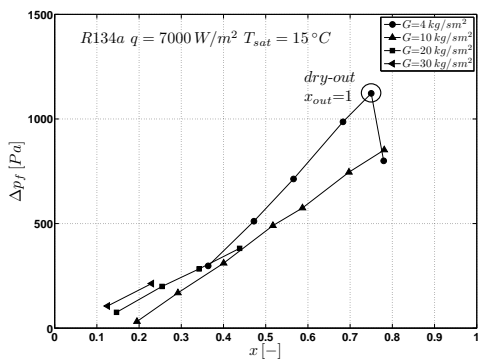

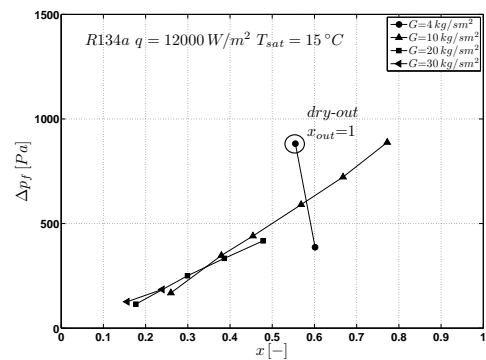Figure 6.21: R236fa, q=7000 W/m^2, T_{sat}=15 °C, frictional pressure drop component

Figure 6.22: R236fa, q=12000 W/m^2, T_{sat}=15 °C, frictional pressure drop component

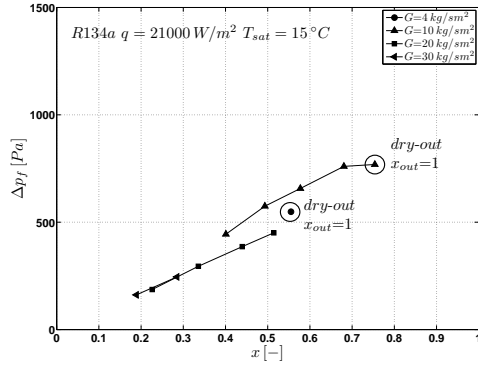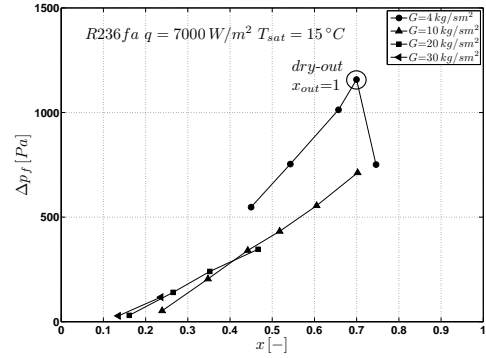Figure 6.23: R236fa, q=21000 W/m^2, T_{sat}=15 °C, frictional pressure drop component

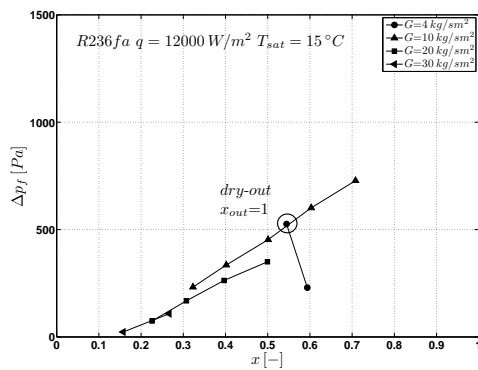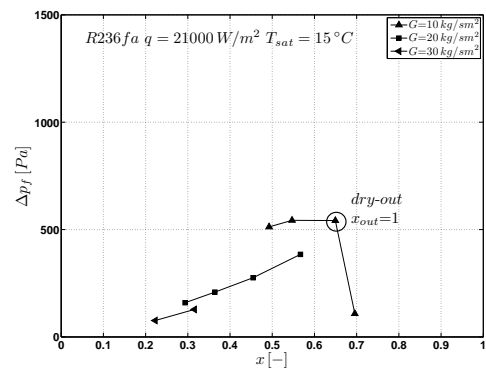### 6.2.2 Experimental results vs. prediction methods

Adiabatic flow

The experimental frictional pressure drop results for $R134a$ and $R236fa$ in adiabatic conditions were compared to the prediction methods of Ishihara et al. [58], Xu et al. [14] and Consolini et al. [51]. The basic idea was to select the adiabatic experimental results as reference for a comparison with the existing methods; they are more accurate as they account for the fact that during the measurements, the momentum component of the pressure drop is not present and the vapor quality (and thus the void fraction) are uniform in the bundle.

The method of Ishihara et al. and Xu et al. are correlations based on the Martinelli model to represent the two-phase friction multiplier. The two-phase multiplier accounts for the ratio between the two-phase pressure drop and the single phase liquid pressure drop:

$$\Phi_L = \frac{\Delta p_{2\phi}}{\Delta p_L} = 1 + \frac{C}{X_{tt}} + \frac{1}{X_{tt}^2} \tag{6.2}$$

Ishihara set the parameter C to a value of 8 (for the data reduction, the single phase pressure drop was predicted by the method of Žukauskas and Ulinska [52] presented in 3.3.1). Xu et al. instead of using a constant value of C as assumed by Ishihara, proposed an empirical equation for C based on the dimensionless superficial velocity and the vapor quality. The method of Ishihara Fig. (6.24) and Fig. (6.25), and the method of Xu Fig. (6.26) and Fig. (6.27) do not predict the experimental trends and values of the frictional pressure drop. This is due to a very poor prediction of the factor C that greatly differ from the experimental values. A plot of the two phase friction multiplier as a function of the Martinelli parameter is given in Fig. (6.28) for $R134a$ and in Fig. (6.29) for $R236fa$. The assumption of a constant C is hardly applicable, in tube bundle literature, as underlined by Ribatski [49], since the values of C seem to change according to the fluid, the tube bundle layout, the pitch to the diameter ratio and to the flow conditions. The method of Xu et al. was developed with a database covering mass velocities ranging for 40 to $700\,kg/sm^2$, so considering that the experimental campaign in the present work covered a range from 4 to $40\,kg/sm^2$, this could be a reason for the poor prediction of the factor C. The Ishihara et al. method was also developed for a range of mass velocities much larger than the low mass velocity conditions tested here; the present conditions are typical of actual operating conditions of such units.

Figure 6.24: R134a adiabatic, frictional pressure drop, experimental vs. predicted - Ishihara [58]
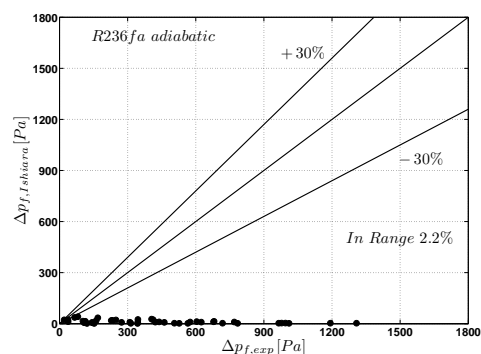
Figure 6.25: R236fa adiabatic, frictional pressure drop, experimental vs. predicted - Ishihara [58]

The results were then compared to the method developed at LTCM [51]; this method is described in 3.3.2 and is based on the prediction of the friction factor in respect to homogeneous flow. The comparison with
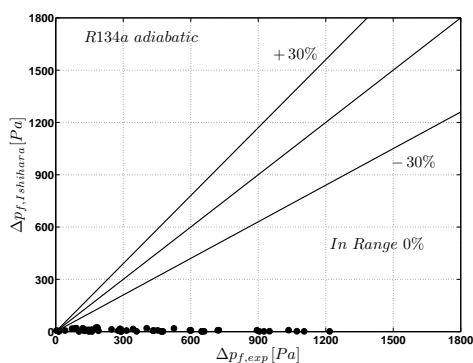
Figure 6.26: R134a adiabatic, frictional pressure drop experimental vs. predicted - Xu [14]

Figure 6.27: R236fa adiabatic, frictional pressure drop experimental vs. predicted - Xu [14]

Figure 6.28: R134a adiabatic, two-phase friction multiplier data with Martinelli parameter

Figure 6.29: R236fa adiabatic, two-phase friction multiplier data with Martinelli parameter

the experimental data for $R134a$ and $R236fa$ is depicted in Fig. (6.30) and Fig. (6.31). The method of Consolini et al. developed at LTCM only predicts 7.3% and 13.4%, respectively, of the data for $R134a$ and $R236fa$ within $\pm 30\%$.

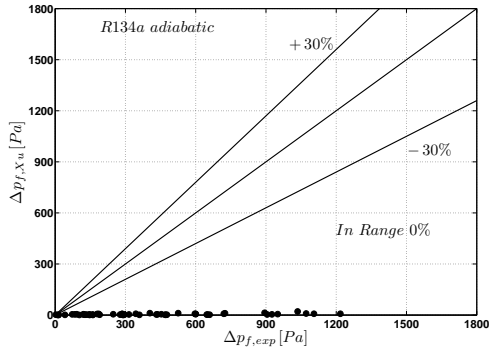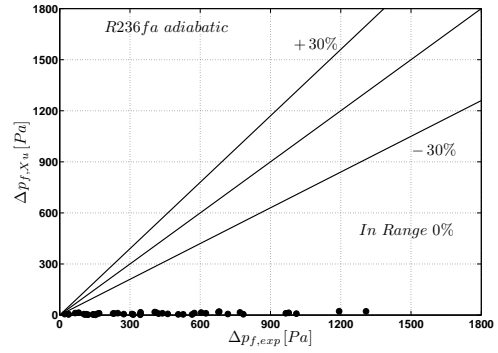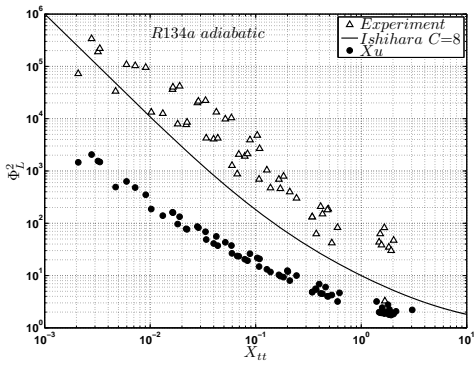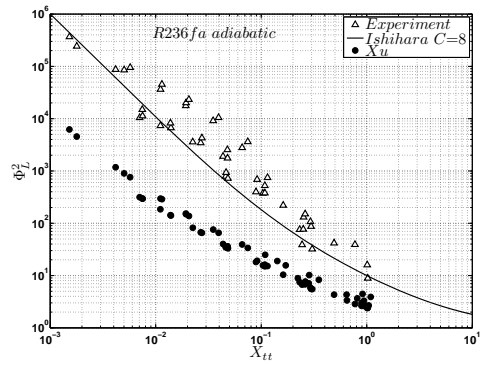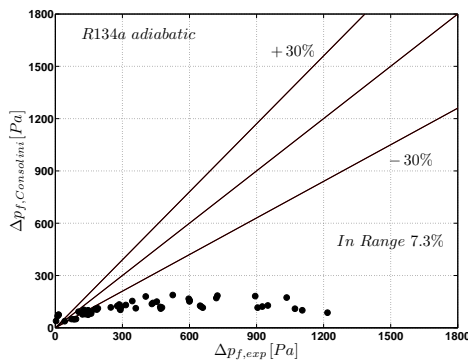Figure 6.30: R134a adiabatic, frictional pressure drop, experimental vs. predicted by the method of Consolini et al. [51]
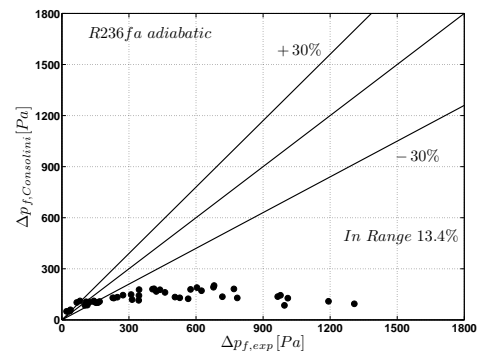
Figure 6.31: R236fa adiabatic, frictional pressure drop, experimental vs. predicted by the method of Consolini et al. [51]

The principle reason why the model developed at $LTCM$ does not predict in a satisfactory way the adiabatic experimental data is that it was based on diabatic data and because it accounts for different types of tube surfaces: smooth and enhanced. The possibility of using adiabatic data as validation for a model would give more reliability, accounting for the fact that adiabatic data are intrinsically more accurate than diabatic.

Going now through the method, it is based on the prediction of the ratio of the homegenous friction factor $f1$ to the two-phase factor $f2$. This ratio $\lambda = f2/f1$ is assumed to have a parabolic distribution with x and is parameterized with a non dimensional mass velocity. Assuming the parabolic distribution of λ proposed by Consolini et al. is like assuming a maximum difference between the homogeneous model and the real case at $x = 0.5$ for all the mass velocities. Considering now the experimental results in terms of λ at $G = 4\,kg/sm^2$ for $R134a$ and $R236fa$, they show a different behavior in respect to the prediction method proposed by Consolini et al. as depicted in Fig. (6.32). The parabolic distribution does not fit the data, secondly the maximum value in λ is not at $x = 0.5$ for all the mass velocities and thirdly the peak value is underestimated by a factor of 5. This means that the divergence from the homogeneous model does not have a maximum at $x = 0.5$.

As shown in Fig. (6.32), different fluids, with different thermophysical properties, show the same trends.

Fig. (6.33) depicts a plot of the experimental results for $R134a$ and $R236fa$ (grouped together) in terms of λ as a function of the vapor quality at various mass velocities. The parameter λ appears to be strongly dependent on the mass velocity. The distribution of λ as function of the vapor quality changes according to the mass velocity. Particularly, the peak in the distribution shifts from high vapor qualities for low mass velocities to lower values at higher mass velocities. Increasing the mass velocity, the curve gets flatter, showing that the frictional factor at higher mass velocities corresponds to a closer approximation to the homogeneous frictional factor. This agrees with the Feenstra et al. model [50] implemented for the void fraction prediction. In Fig. (6.34) the void fraction as a function of the vapor quality is plotted for the homogeneous model and for the Feenstra et al. method; the mass velocities range from 4 to $30\,kg/sm^2$ at a saturation temperature $T_{sat}=15\,°$C for $R134a$. The void fraction predicted, as expected, tends to approach the homogeneous one with increasing mass velocity.

Frictional pressure drop model update   An adjustment to the LTCM prediction method is proposed for adiabatic flows, the following new set of equations fit the experimental data well, as shown in Fig. (6.33).
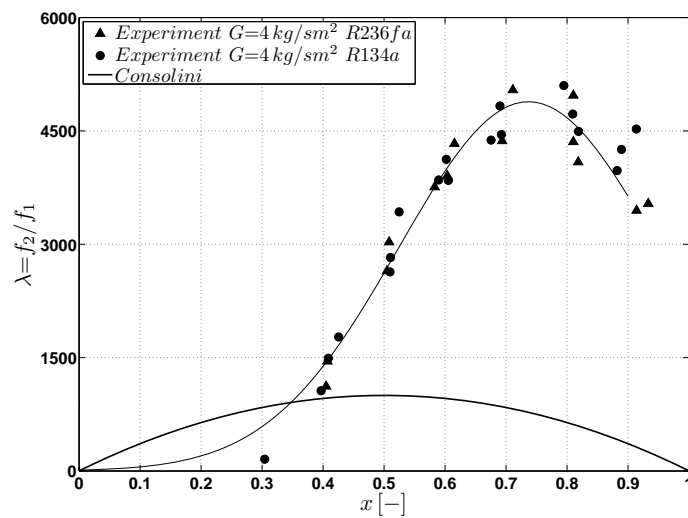
Figure 6.32: Friction factor multiplier λ, experimental vs. predicted by the method of Consolini et al. [51]
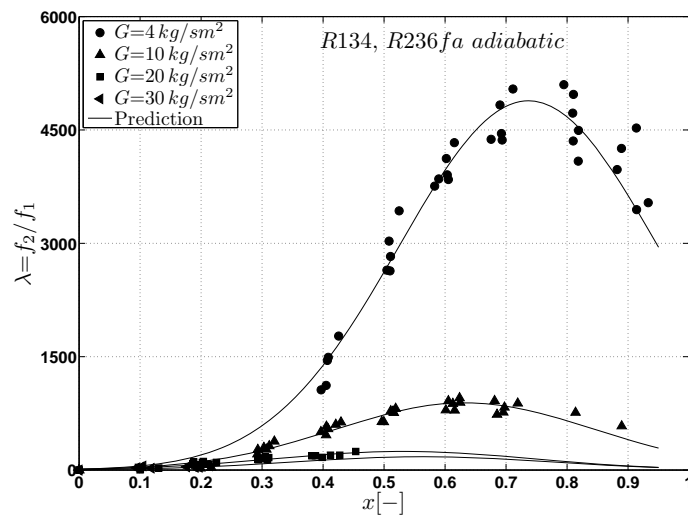
Figure 6.33: Friction factor multiplier λ, experimental vs. new prediction method
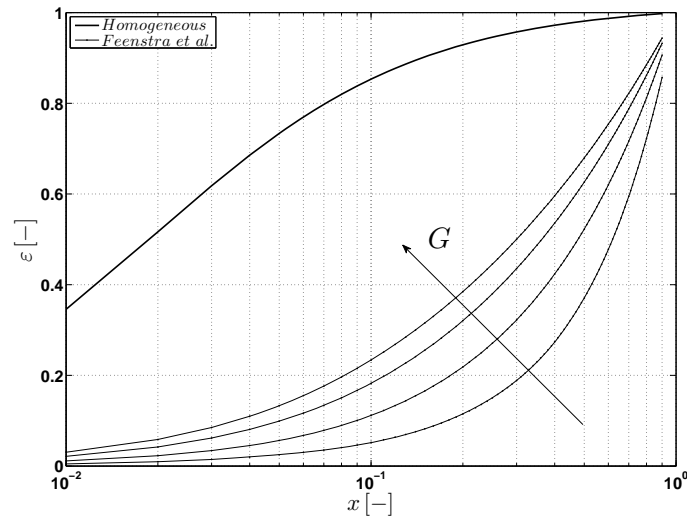
Figure 6.34: Void fraction with vapor quality, Feenstra et al. vs. homogeneous model, $R134a$, T_{sat}=15 °C

$$\lambda = \frac{f_2}{f_1} \quad = \quad exp\left[-\left(\frac{(x-C2)}{0.3}\right)^2 + C1\right] \tag{6.3}$$

$$C1 \quad = \quad -25.015\Lambda + 24.193 \tag{6.4}$$

$$C2 \quad = \quad -1.168\Lambda + 1.4521 \tag{6.5}$$

$$\Lambda \quad = \quad \left(\frac{G}{G_{ref}}\right)^{0.1} \tag{6.6}$$

This new set of equations is substituted for the ones proposed by Consolini et al. [51] and appears to be more representative of the two-phase flow conditions. The new prediction method allows a satisfying prediction of the adiabatic frictional pressure drop data. For $R134a$, the new method predicts 63.8% of the data within $\pm30\%$ and 81.3% within $\pm30\%$ for $R236fa$. The results are depicted in Fig. (6.35) and Fig. (6.36).
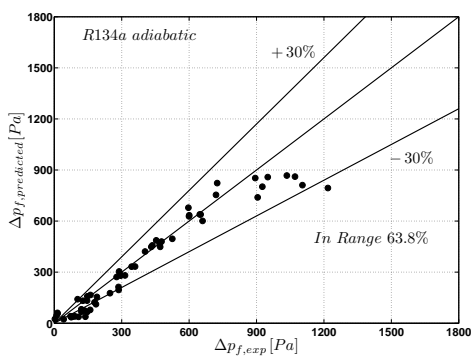
Figure 6.35: R134a adiabatic, frictional pressure drop experimental vs. new prediction method
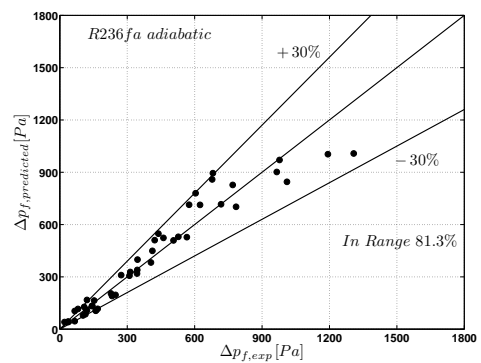
Figure 6.36: R236fa adiabatic, frictional pressure drop experimental vs. new prediction method

Diabatic flow

Existing methods, available in literature, were also employed to evaluate the prediction of the diabatic frictional pressure drop data described earlier. The models of Ishihara et al. [58] and Xu et al. [14] did not predict the experimental frictional pressure drop data satisfactory for diabatic tests with $R134a$ and $R236fa$, with 0% of the data within $\pm30\%$. The method proposed by Aprin [57], whose method accounts for the heat flux influence through the Boiling number introduced in the expression for the friction factor, was also tried here. Since that the bundle boiling facility is half adiabatic and half diabatic, the method was implemented for the diabatic part but did not capture any trend for $R134a$ and $R236fa$.

In Fig. (6.38) a comparison with the LTCM method is shown. The method of Consolini et al. [51] applied to the diabatic frictional pressure drop data, predicted 18.6% of the data within $\pm30\%$ for R134a and 18.5% of the data within $\pm30\%$ for $R236fa$, Fig. (6.37) and Fig. (6.38). The resulting predictions are poor and underpredict the data, also the trends are not respected.
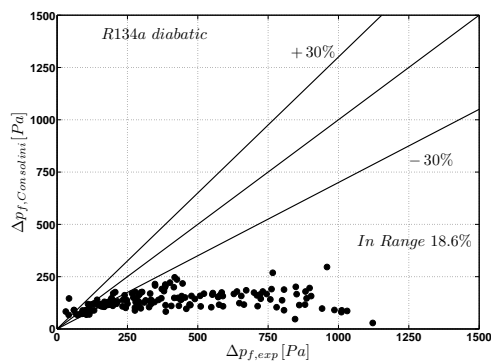
Figure 6.37: R134a diabatic, Frictional pressure drop experimental vs. predicted by the method of Consolini et al. [51]
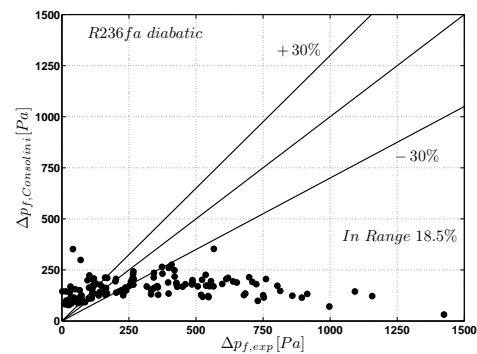
Figure 6.38: R236fa diabatic, frictional pressure drop experimental vs. predicted by the method of Consolini et al. [51]

The new model proposed for the adiabatic two-phase frictional pressure drop will now be applied for diabatic tests. In this case, the computation is performed over a discretized tube bundle domain, which accounts for the variation of the thermophysical quantities, vapor quality and void fraction across the test section during evaporation. The diabatic frictional pressure drop data were predicted well with 75.4% of the data within $\pm30\%$ for $R134a$. This is not the case for $R236fa$, where only 12.3% of the data were within $\pm30\%$. Results are depicted in Fig. (6.39) and in Fig. (6.40). While better than the previous methods, the present method still requires further improvement, with more fluids added to the database.

Figure 6.39: R134a diabatic, frictional pressure drop, experimental vs. new prediction method

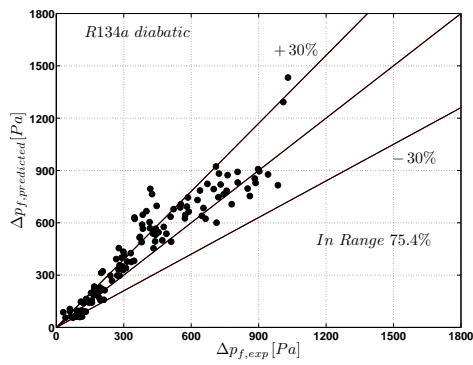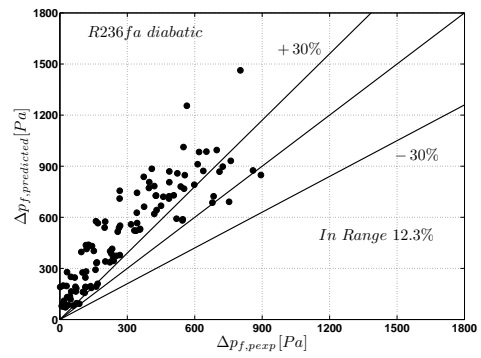Figure 6.40: R236fa diabatic, frictional pressure drop, experimental vs. new prediction method

Chapter 7

Heat Transfer

An analysis of the local heat transfer data is presented and compared with the existing prediction methods.

7.1 Heat transfer coefficient

The enthalpy profile method is employed to obtain the local heat flux. The experimental methodology is such that the water supplies the amount of heat necessary to evaporate the refrigerant. Water flows through tubes whose circuits are highly instrumented. Measurements of temperature at fixed locations along the developing water circuits are made. A second order polynomial fit of the temperature profile is made, this provides an optimal estimation of the water temperature variation along the circuit. From this information, the local heat flux is computed and employed to evaluate the local heat transfer coefficient on the outside of the tube. The local external heat transfer coefficient may be expressed as:

$$\alpha_o = \frac{q_o}{T_{wall,o} - T_{sat}} \tag{7.1}$$

This technique does not provide wall temperature measurements; it makes use of the water temperature. In such a case, the axial conduction along the axis of the tube is negligible and thus neglected. Knowing the temperature profile $T_{wat} = T_{wat}(s)$, where s is the curvilinear coordinate through the water circuit, we can state:

$$\delta Q = \dot{m} c_{p,wat} \delta T_{wat} \tag{7.2}$$

Considering that

$$dA_o = \pi D_o ds \tag{7.3}$$

we obtain the local external heat flux to be:

$$q_o = \frac{\dot{m} c_{p,wat}}{\pi D_o} \frac{dT_{wat}}{ds} \tag{7.4}$$

The heat transfer phenomena can be analyzed through a thermal resistance model. The overall resistance is the sum of the external, wall, and internal resistances. In a flooded evaporator, the external resistance refers to the evaporating fluid, the internal one to the fluid that supplies the heat necessary to the phase change, and the wall resistance to the physical barrier between the two fluids (metallic tube wall). Thus,

$$R_{ov} = R_o + \tilde{R}_{wall} + R_i \tag{7.5}$$

$$R_{wall} = \tilde{R}_{wall} dA_o = \frac{D_o}{2\lambda_{wall}} ln\left(\frac{D_{or}}{D_i}\right) \tag{7.6}$$

Furthermore,

$$\frac{1}{U_o dA_o} = \frac{1}{\alpha_o dA_o} + \frac{1}{\alpha_i dA_i} + \tilde{R}_{wall} \tag{7.7}$$

$$\hookrightarrow \frac{1}{U_o} = \frac{1}{\alpha_o} + \frac{1}{\alpha_i}\frac{D_o}{D_i} + R_{wall} \tag{7.8}$$

In general terms:

$$q_o = U_o(T_{wat} - T_{sat}) \tag{7.9}$$

Using water and refrigerant thermocouple readings and through equations Eq. (7.4) to Eq. (7.9), U_o is computed. U_o represents the global heat transfer coefficient in respect to the reference heat transfer area A_o. To compute the external heat transfer coefficient α_0, the relationship Eq. (7.8) is employed. The internal heat transfer coefficient is estimated by the Gnielinski correlation [59], corrected through a multiplier C_i determined using the Modified Wilson Plot Method:

$$\alpha_i = C_i \alpha_{Gn,i} \tag{7.10}$$

The formulation of $\alpha_{Gn,i}$ and of the friction factor f, defined by Petukov [60] are:

$$\alpha_{Gn,i} = \frac{(f/8)(Re_{D_h} - 1000)Pr}{1 + 12.7(f/8)^{1/2}(Pr^{2/3} - 1)}\frac{\lambda}{D_h} \tag{7.11}$$

$$f = (0.79ln(Re_{D_h}) - 1.64)^{-2} \tag{7.12}$$

This correlation is suitable for Reynolds numbers corresponding to the transition region ($2300 \lesssim Re_{D_h} \lesssim 10000$) as well as for the fully turbulent regime up to $Re_{D_h} = 10^6$. The hydraulic diameter D_h is the geometric parameter employed in the Reynolds number definition and is calculated as follow:

$$D_h = \frac{4(Cross\ section)}{Wetted\ perimeter} \tag{7.13}$$

7.2 Evaluation of physical properties

The procedure for physical properties evaluation described in Gstöhl [61] has been employed. The physical properties of water were evaluated by the software Engineering Equation Solver: EES. For the refrigerants, $REFPROP$ 8.0, developed at NIST, was used. The saturation properties were based on temperature values: they turned out to be the most accurate. The same procedure can be carried out from the pressure measurements of the refrigerants but leads to less accurate values.

7.3 Wilson plot results

The Wilson Plot experimental campaign lead to the determination of the coefficient C_i. By accounting for the internal heat transfer enhancement of the tube due to the annulus and the helical rib wrapped around the inner tube to increase mixing, this yielded a more accurate value for the local water temperature. This coefficient is independent from the external fluid and from its saturation temperature. Thus $R134a$ at a saturation temperature T_{sat}=20 °C was selected as the external conditions. The experimental test conditions are presented in Table 7.1.

Tubes	Smooth tubes (Table 6.2)
Test fluid	R134a
Saturation temperature	T_{sat}=20 $[°C]$
Heat flux	q_{ref}=24000 $[W/m^2]$
Water Reynolds number	Re_{water}=8000-16000 $[-]$
Pool boiling exponent	n=0.667 $[-]$

Table 7.1: Wilson Plot - Experimental conditions

In Figure Fig. (7.1) the Modified Wilson Plot, applying the LTCM method, is presented. The slope of the interpolating curve allows the computation of the C_i.
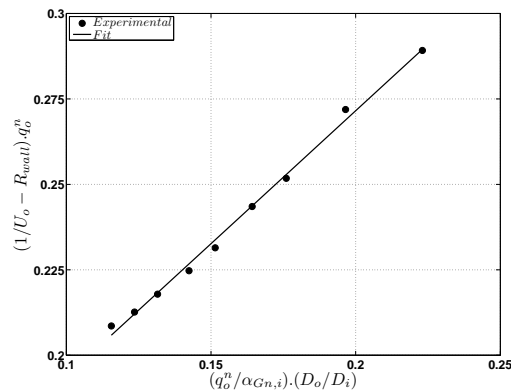
Figure 7.1: Tube geometry

Starting from the same raw experimental data, four different methods described in appendix B were implemented. The different values are reported in Table 7.2. No mean on the obtained values is proposed, and each one of them represents the parameter C_i as a result of different approaches. It is the freedom of the experimenter to choose the one he considers as the most representative. The Jacobi approach, here applied respectively to LTCM and Rose's methods, assumes constant uncertainties on the abscissa and ordinate: this hypothesis is not respected for the present investigation. For this reason, the resulting uncertainties are not reported here. The implementation of the complete method presented by Styrylska [62] is left to future experimenters.

The parameter C_i is assumed to be 1.2856. The value of the coefficient agrees well with the experimental results for plain tubes obtained from Gstöhl [61] ($C_i = 1.27$). It differs from the value measured by Robinson [63] ($C_i = 1$) but in that case the inner tubes were not yet equipped with a helicoidal rib for heat transfer augmentation.

	LTCM	Rose	Jacobi - LTCM	Jacobi - Rose
C_i $[-]$	1.2856	1.2854	1.3196	1.2806

Table 7.2: Gnielinski multiplier - C_i

7.4 Convective boiling

In convective boiling, a controlled amount of refrigerant flows through the test section. The water side heat transfer coefficient can now be computed through the Gnielinski correlation corrected with the multiplier obtained by the Modified Wilson Plot method. From the measured water temperature profile and applying Eq. (7.4), the local heat flux is computed. Through Eq. (7.9) and Eq. (7.8), the outside heat transfer coefficient (shell side) α_o is finally obtained.

7.5 Pool boiling

The same data-reduction procedure described in 7.4 is employed for pool boiling experiments. In this case there is no refrigerant flowing and experiments are run at constant saturation temperature (water from a cooling source is circulated through an upper tube to condense the vapor generated and thus to maintain the thermal equilibrium). A correlation like Eq. (B.12) fits the pool boiling data well. Applying a logarithmic function we get:

$$ln(\alpha_o) = ln(C_o) + n\,ln(q_o) \tag{7.14}$$

Performing a linear fit with the variables $ln(q_o), ln(\alpha_o)$, the values of the exponent n and the constant $ln(C_o)$ are obtained. The pool boiling heat transfer coefficient will be referred to $\alpha_{o,pb}$.

To compute the Gnielinsky correction multiplier C_i, a value of the exponent n is required. Contrary, the multiplier C_i is necessary to compute the value of n. To overcome this problem, an iterative procedure is mandatory: a guessed value of n is imposed, the multiplier C_i is computed and pool boiling experiments were run and n is recalculated.

7.5.1 Smooth tubes

Pool boiling results

The experimental conditions and results are reported in Table 7.3. The pool boiling curves for $R134a$, varying the saturation temperature, are depicted in Fig. (7.2), Fig. (7.3) and Fig. (7.4) and for $R236fa$ in Fig. (7.5), Fig. (7.6) and Fig. (7.7). With the given fluids and the bundle boiling facility it was not possible to perform tests at $5\,°C$ at pool boiling conditions on a single tube.

The experimental results are compared to the pool boiling correlation proposed by Cooper [64] as reported in Eq. (7.15).

$$\alpha_{o,pb} = 55 p_r^{(0.12-0.08686ln(R_p))} \left(-0.4343ln(p_r)\right)^{-0.55} M^{-0.5} q_o^{0.67} \tag{7.15}$$

where p_r is the reduced pressure, M is the molecular weight of the investigated fluid and R_p is the roughness parameter of the tube measured in μm (DIN 4762). The roughness of the smooth tubes was

Fluid	T_{sat} [°C]	Re [−]	C_i [−]	C_o $\left[K.(\frac{W}{m^2})^{(1-n)}\right]$	n [−]
R134a	10	8500	1.2856	5.116	0.7074
	15	8500	1.2856	5.088	0.7211
	20	8500	1.2856	34.590	0.5559
R236fa	10	9000	1.2856	6.298	0.6418
	15	9000	1.2856	6.676	0.6541
	20	9000	1.2856	16.725	0.5809

Table 7.3: Pool boiling - experimental conditions

measured by means of a laser profilometer; several samples were measured and the resulting roughness was R_p=2.30 [μm]. The Cooper correlation, as visible from Fig. (7.2) to Fig. (7.7), underpredicts the pool boiling experimental data. The approximate deviation are as follows: 35% in Fig. (7.2), 38% in Fig. (7.3), 48% in Fig. (7.4), 22% in Fig. (7.5), 28% in Fig. (7.6) and 35% in Fig. (7.7).
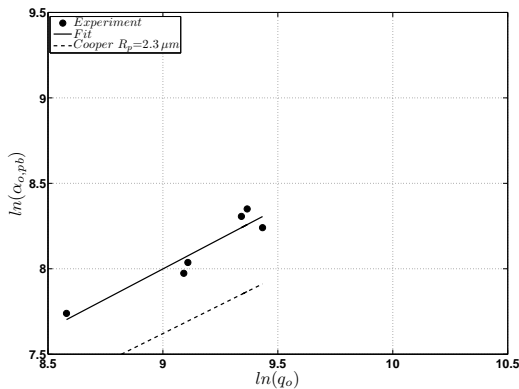
Figure 7.2: Pool boiling R134a, T_{sat}=10 °C
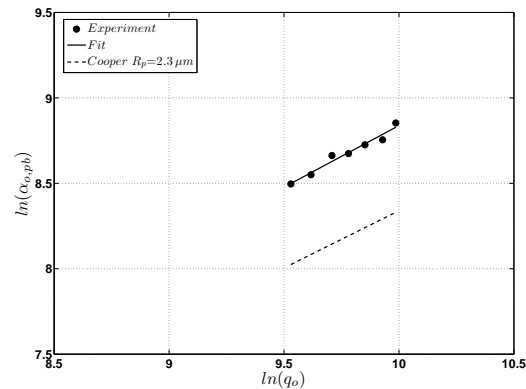
Figure 7.3: Pool boiling R134a, T_{sat}=15 °C

Bundle boiling results

The local bundle results are now calculated and presented for fluid $R134a$, the values are depicted in Fig. (7.8) to Fig. (7.37) and for fluid $R236fa$ the values in Fig. (7.38) to Fig. (7.67). The data are segregated according to the mass flux that ranges from 4 to $36\,kg/sm^2$, to the saturation temperature that varies from 5 to 15 °C and the heat flux that was varied from 7000 to $21000\,W/m^2$.

The experimental results for fluid $R134a$ exhibit an increase of the heat transfer coefficient with the heat flux. Considering now that local measurements of the heat transfer coefficient were performed at rows number 1 and 3, the results show a dependence on the vertical position. The local heat transfer coefficient slightly decreases, going from row 1 to row 3. This is due to the nature of the experiments where the heat flux is not constant along the developing water circuit. Considering the fact that the water temperature follows a quadratic distribution, the heat flux will decrease linearly across the tube bundle. The results are independent for the saturation temperature and almost independent of the vapor quality. The independency of the heat transfer coefficient from the vapor quality is different from the general trend observed in an in-tube convective boiling, where the heat transfer usually increases as the vapor quality increases up to x=0.8-0.9 due to the thinning of the annular film on the tube wall. No de-
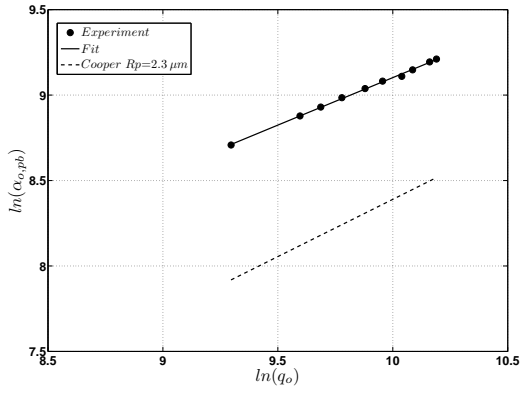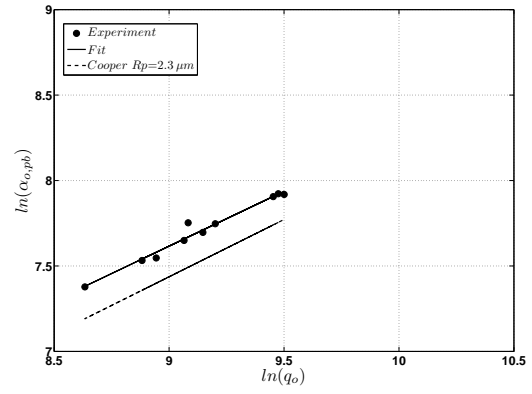
Figure 7.4: Pool boiling R134a, T_{sat}=20 °C

Figure 7.5: Pool boiling R236fa, T_{sat}=10 °C
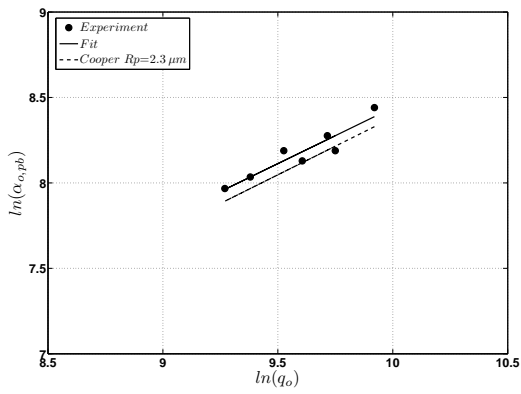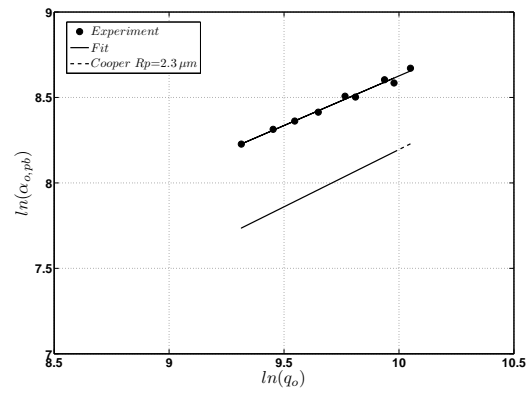

Figure 7.6: Pool boiling R236fa, T_{sat}=15 °C

Figure 7.7: Pool boiling R236fa, T_{sat}=20 °C

pendance on G was evident. According to the flow maps discussed in the literature review, chapter 3, the experimental data fall in the bubbly and intermittent regions. No annular flow conditions were covered. The local heat transfer coefficient trends fully agree with the results of Kim et al. [65]. As underlined by Kim et al., the independency of the heat transfer coefficient on the vapor quality is believed to be related to the flow pattern in the tube bundle; the mass velocity effect is known to be significant only at low heat flux combined with a high mass velocity. For fluid $R236fa$, the dependance on the heat flux exhibits the same behavior as for fluid $R134a$. The dependance on the row number is limited for this fluid and reduced to the minimum: the values are almost the same. There is a slight increase of the local heat transfer coefficient with increasing saturation temperature. Also, in this case, the results are almost independent of the vapor quality.

Heat transfer prediction: experimental data vs. Shah model [55]

The present heat transfer results were compared with the recent empirical model of Shah [55]. This model accounts of three possible heat transfer regimes: *intense boiling, convective boiling*, and *convection regimes*. The experimental data collected with the bundle boiling facility falls in the first two regimes according to the Shah classification. The presented data are grouped according to the fluid type and the saturation temperature. In Fig. (7.68), Fig. (7.69) and Fig. (7.70) experimental vs. predicted data for $R134a$ are presented. The model makes use of the experimental pool boiling curves; since the curve for the saturation temperature of $5\,^\circ$C was not measured, the curve measured from Robinson [63] was employed. For $R134a$, the model predicts 88.7% of the data within $\pm30\%$ at a saturation temperature of $5\,^\circ$C. For temperatures of 10 and $15\,^\circ$C, the model underpredicts the experimental data. Concerning the results for fluid $R236fa$, the Shah model predicts 100% of the data within $\pm30\%$ for saturation temperatures of 5 and $10\,^\circ$C and 98.7% for $15\,^\circ$C. Thus the Shah method predicts the experimental data well for $R236fa$. The reason for its weakness concerning $R134a$ is not evident. In general, the Shah method underpredicts the data. Implementing a correction factor of 1.194 to his method, now the 77.4% of all the data are predicted within $\pm20\%$, see Fig. (7.74). The reason to this larger increase relative to pool boiling values may be the tight tube pitch tested here.

The Shah model, implemented as a comparison to the obtained experimental data, defines a parameter able to identify the heat transfer regime. It is now interesting to examine the flow map depicted in Fig. (7.75) and Fig. (7.76) for fluid $R134a$ and $R236fa$ respectively. In figures Fig. (7.75) and Fig. (7.76), the acquired experimental data points are grouped according to the heat transfer flow pattern map defined by Shah. In particular, the circles refer to the intensive boiling regime and the triangles to the convective boiling regime. This plot shows an immediate and clear discrepancy between the fluid structure to be considered as a reciprocal disposition of the two phases in the fluid and the results in the heat transfer. At this point, it seems that the prediction proposed by Shah for heat transfer on plain tube bundles is not coupled with the flow regime, at least if we consider a classification based on the superficial velocities of the maps by Noghrehkar et al. [16] and Ulbrich and Mewes [12].
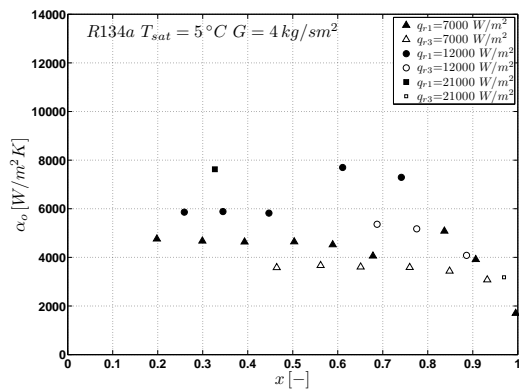
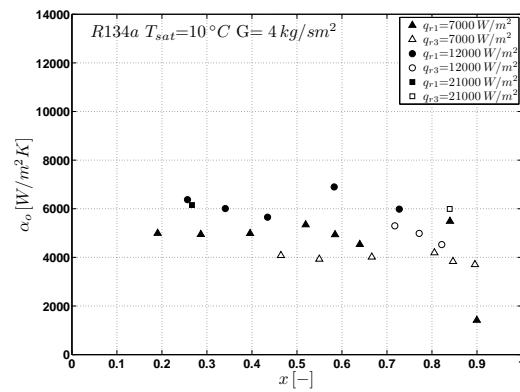Figure 7.8: Local bundle heat transfer coefficient, R134a, T_{sat}=5 °C, G=4 kg/sm^2

Figure 7.9: Local bundle heat transfer coefficient, R134a, T_{sat}=10 °C, G=4 kg/sm^2

Figure 7.10: Local bundle heat transfer coefficient, R134a, T_{sat}=15 °C, G=4 kg/sm^2

Figure 7.11: Local bundle heat transfer coefficient, R134a, q=7000 W/m^2, G=4 kg/sm^2

Figure 7.12: Local bundle heat transfer coefficient, R134a, q=12000 W/m^2, G=4 kg/sm^2

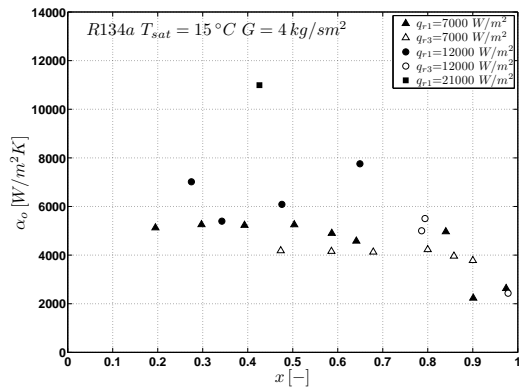Figure 7.13: Local bundle heat transfer coefficient, R134a, q=21000 W/m^2, G=4 kg/sm^2

Figure 7.14: Local bundle heat transfer coefficient, R134a, T_{sat}=5 °C, G=10 kg/sm^2

Figure 7.15: Local bundle heat transfer coefficient, R134a, T_{sat}=10 °C, G=10 kg/sm^2

Figure 7.16: Local bundle heat transfer coefficient, R134a, T_{sat}=15 °C, G=10 kg/sm^2

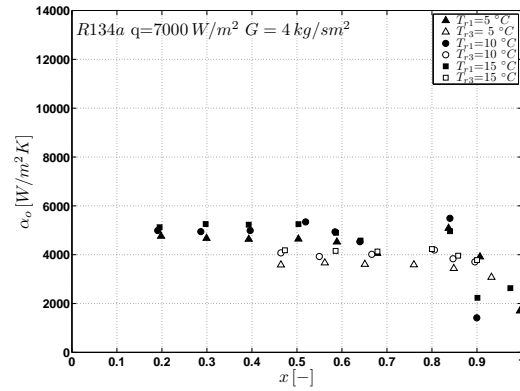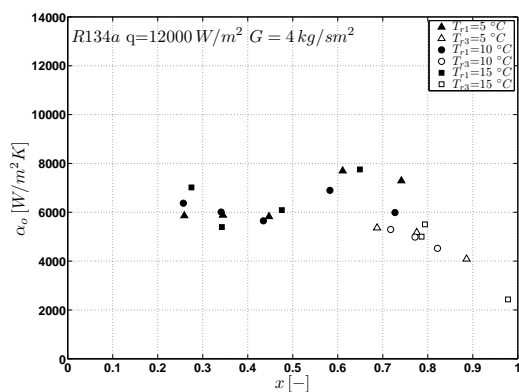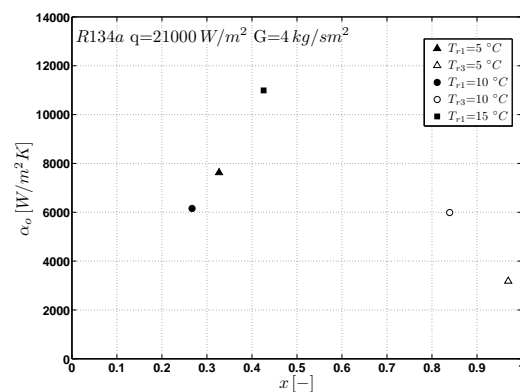Figure 7.17: Local bundle heat transfer coefficient, R134a, q=7000 W/m^2, G=10 kg/sm^2

Figure 7.18: Local bundle heat transfer coefficient, R134a, q=12000 W/m^2, G=10 kg/sm^2

Figure 7.19: Local bundle heat transfer coefficient, R134a, q=21000 W/m^2, G=10 kg/sm^2
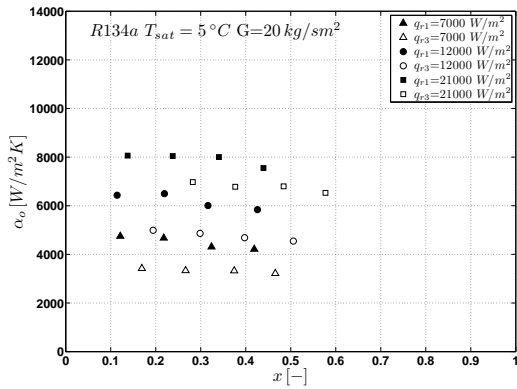
Figure 7.20: Local bundle heat transfer coefficient, R134a, T_{sat}=5 °C, G=20 kg/sm^2
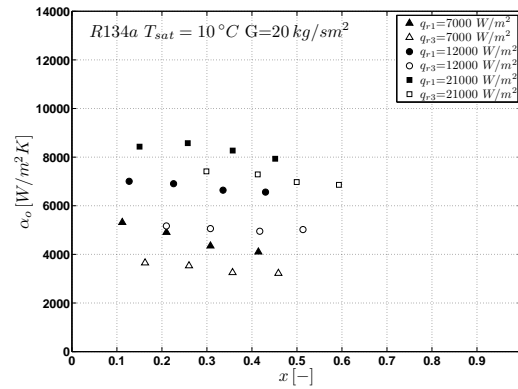
Figure 7.21: Local bundle heat transfer coefficient, R134a, T_{sat}=10 °C, G=20 kg/sm^2
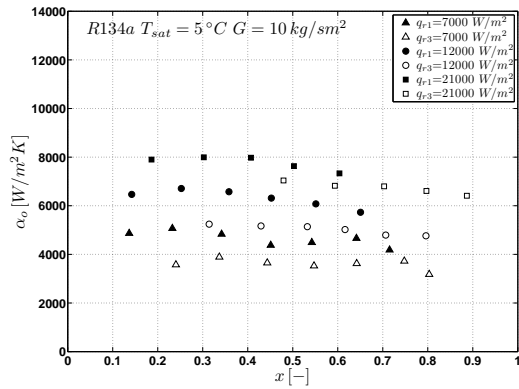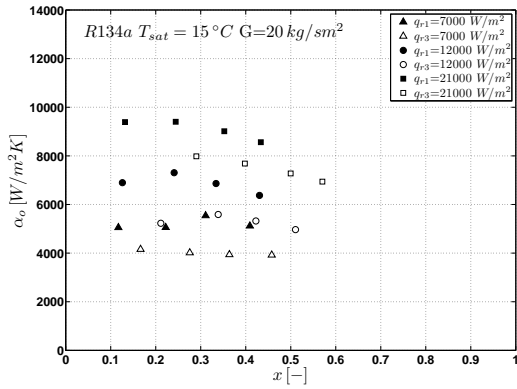

Figure 7.22: Local bundle heat transfer coefficient, R134a, T_{sat}=15 °C, G=20 kg/sm^2

Figure 7.23: Local bundle heat transfer coefficient, R134a, q=7000 W/m^2, G=20 kg/sm^2

Figure 7.24: Local bundle heat transfer coefficient, R134a, q=12000 W/m^2, G=20 kg/sm^2

Figure 7.25: Local bundle heat transfer coefficient, R134a, q=21000 W/m^2, G=20 kg/sm^2

Figure 7.26: Local bundle heat transfer coefficient, R134a, T_{sat}=5 °C, G=30 kg/sm^2

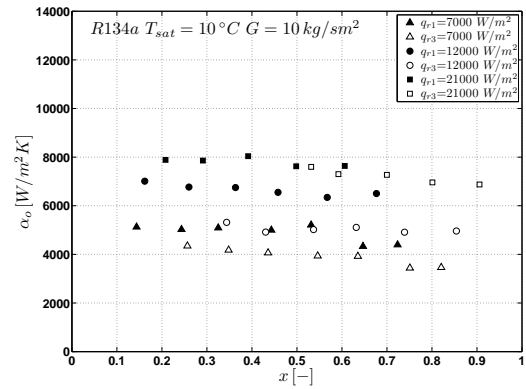Figure 7.27: Local bundle heat transfer coefficient, R134a, T_{sat}=10 °C, G=30 kg/sm^2
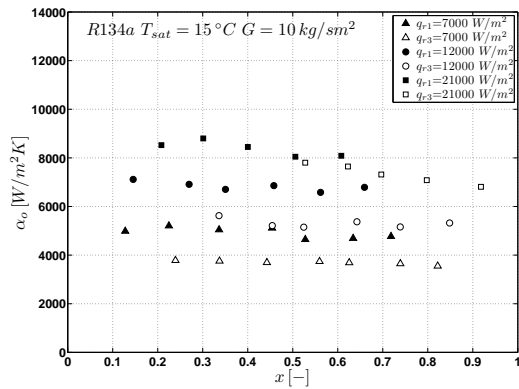

Figure 7.28: Local bundle heat transfer coefficient, R134a, T_{sat}=15 °C, G=30 kg/sm^2

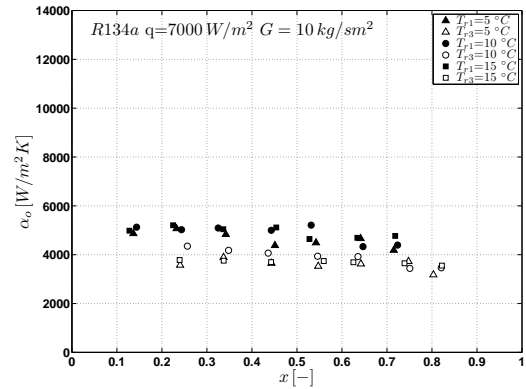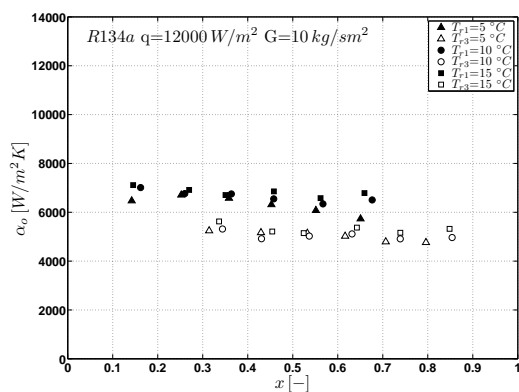Figure 7.29: Local bundle heat transfer coefficient, R134a, q=7000 W/m^2, G=30 kg/sm^2

Figure 7.30: Local bundle heat transfer coefficient, R134a, q=12000 W/m^2, G=30 kg/sm^2

Figure 7.31: Local bundle heat transfer coefficient, R134a, q=21000 W/m^2, G=30 kg/sm^2

Figure 7.32: Local bundle heat transfer coefficient, R134a, T_{sat}=5 °C, G=36 kg/sm^2

Figure 7.33: Local bundle heat transfer coefficient, R134a, T_{sat}=10 °C, G=36 kg/sm^2

Figure 7.34: Local bundle heat transfer coefficient, R134a, T_{sat}=15 °C, G=36 kg/sm^2

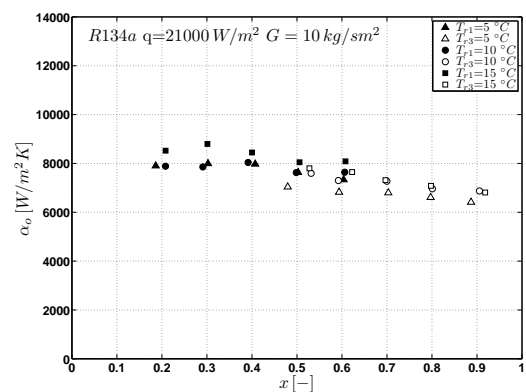Figure 7.35: Local bundle heat transfer coefficient, R134a, q=7000 W/m^2, G=36 kg/sm^2

Figure 7.36: Local bundle heat transfer coefficient, R134a, q=12000 W/m^2, G=36 kg/sm^2
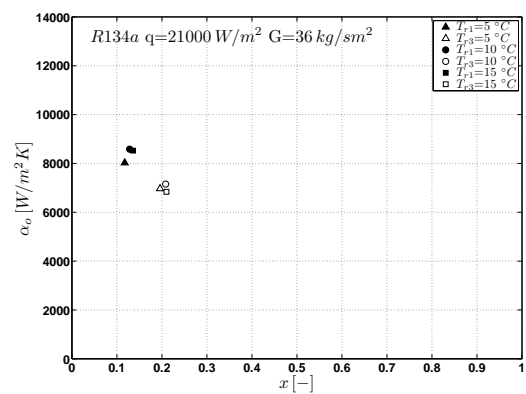
Figure 7.37: Local bundle heat transfer coefficient, R134a, q=21000 W/m^2, G=36 kg/sm^2
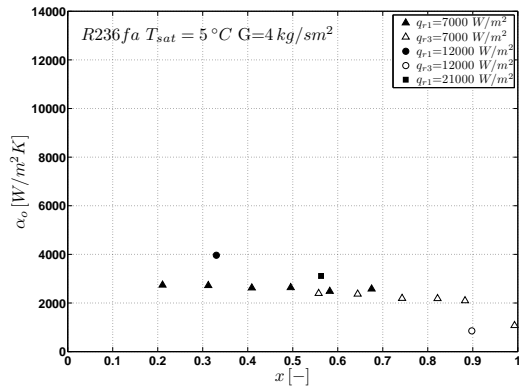
Figure 7.38: Local bundle heat transfer coefficient, R236fa, T_{sat}=5 °C, G=4 kg/sm^2
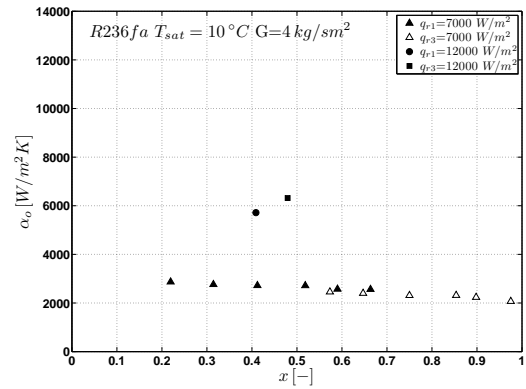
Figure 7.39: Local bundle heat transfer coefficient, R236fa, T_{sat}=10 °C, G=4 kg/sm^2
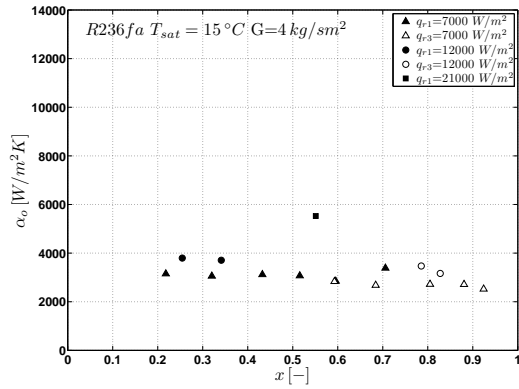
Figure 7.40: Local bundle heat transfer coefficient, R236fa, T_{sat}=15 °C, G=4 kg/sm^2
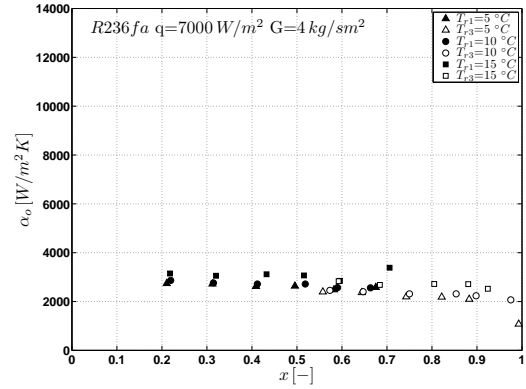
Figure 7.41: Local bundle heat transfer coefficient, R236fa, q=7000 W/m^2, G=4 kg/sm^2
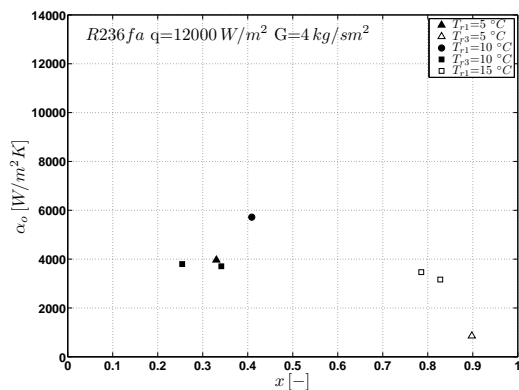
Figure 7.42: Local bundle heat transfer coefficient, R236fa, q=12000 W/m^2, G=4 kg/sm^2
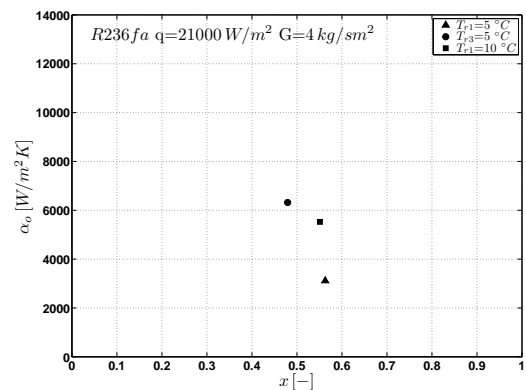
Figure 7.43: Local bundle heat transfer coefficient, R236fa, q=21000 W/m^2, G=4 kg/sm^2
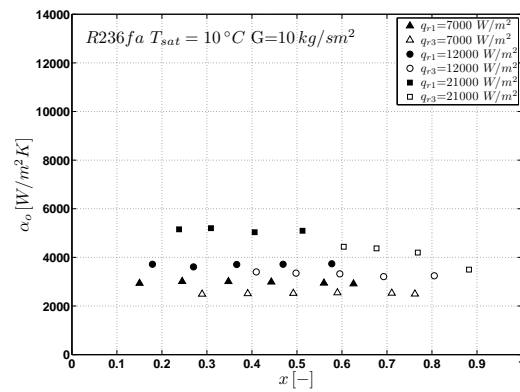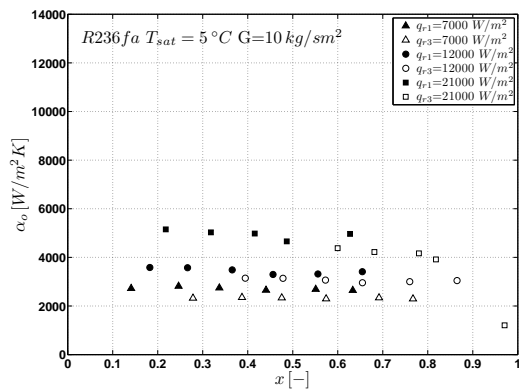
Figure 7.44: Local bundle heat transfer coefficient, R236fa, T_{sat}=5 °C, G=10 kg/sm^2

Figure 7.45: Local bundle heat transfer coefficient, R236fa, T_{sat}=10 °C, G=10 kg/sm^2
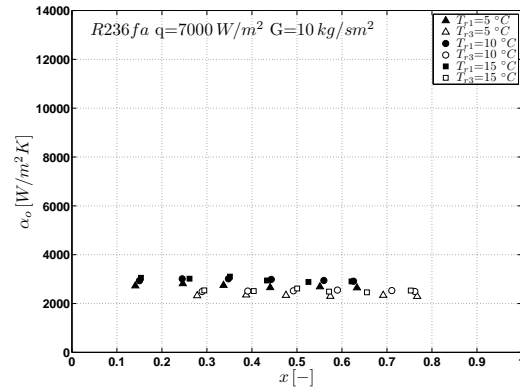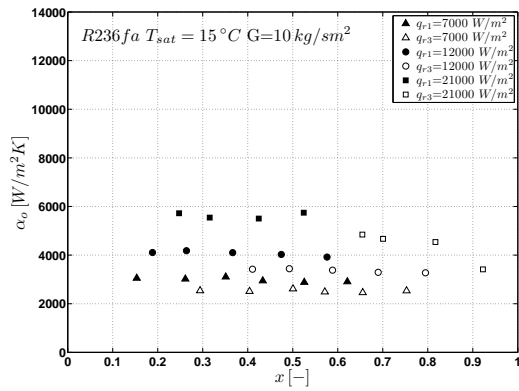
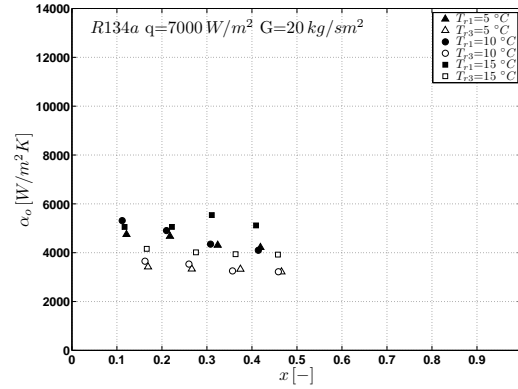Figure 7.46: Local bundle heat transfer coefficient, R236fa, T_{sat}=15 °C, G=10 kg/sm^2

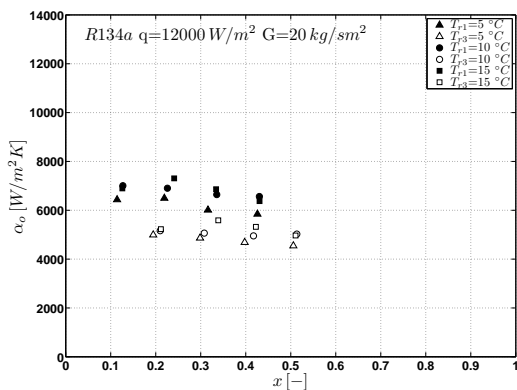

Figure 7.47: Local bundle heat transfer coefficient, R236fa, q=7000 W/m^2, G=10 kg/sm^2
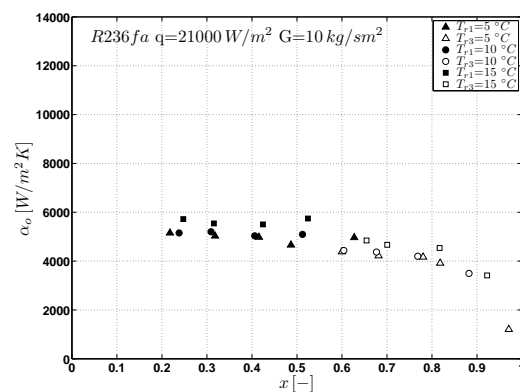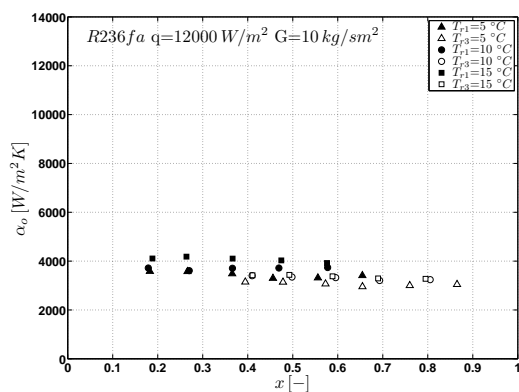
Figure 7.48: Local bundle heat transfer coefficient, R236fa, q=12000 W/m^2, G=10 kg/sm^2
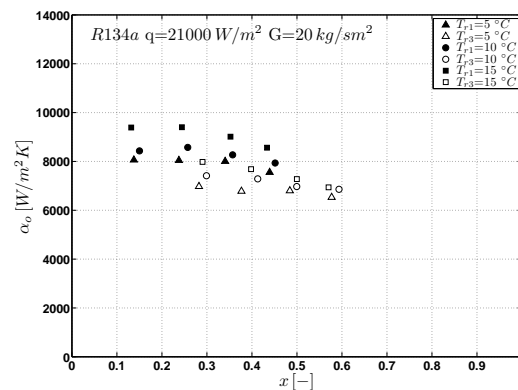

Figure 7.49: Local bundle heat transfer coefficient, R236fa, q=21000 W/m^2, G=10 kg/sm^2
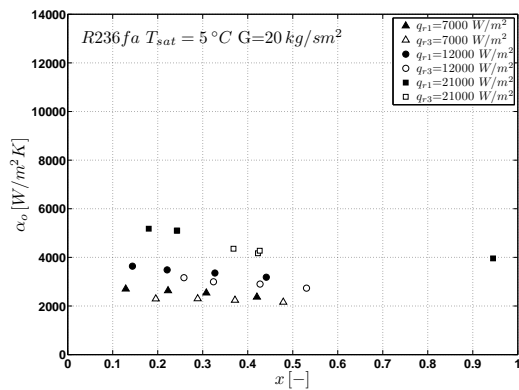
Figure 7.50: Local bundle heat transfer coefficient, R236fa, T_{sat}=5 °C, G=20 kg/sm^2
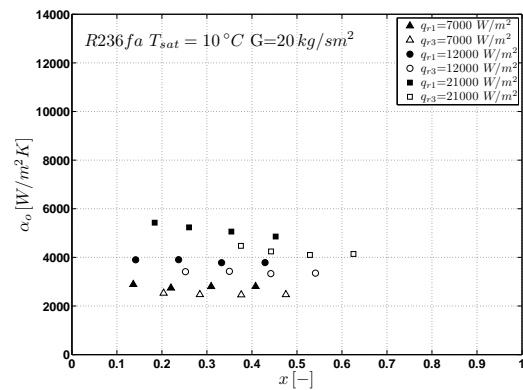
Figure 7.51: Local bundle heat transfer coefficient, R236fa, T_{sat}=10 °C, G=20 kg/sm^2
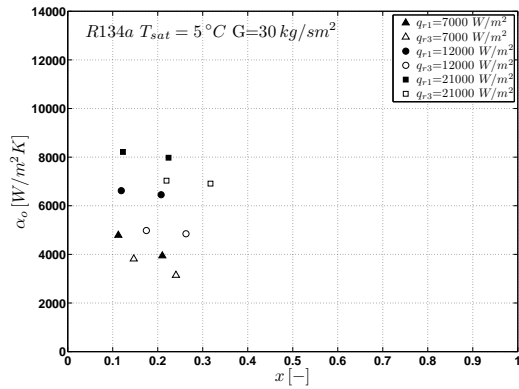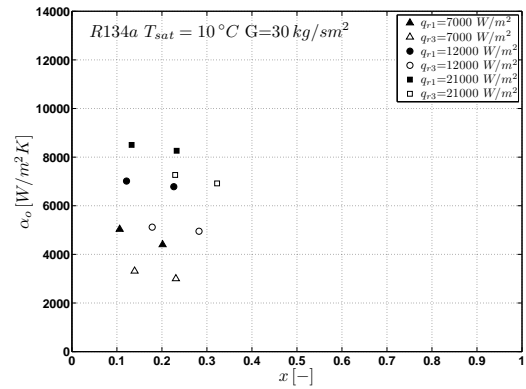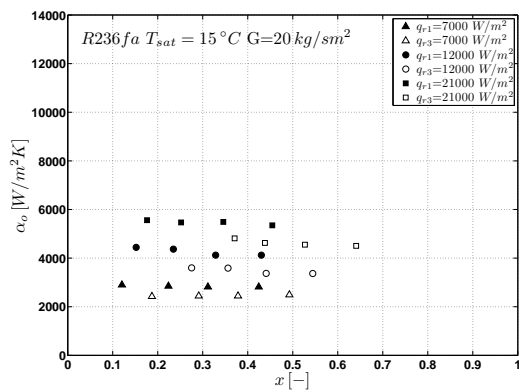

Figure 7.52: Local bundle heat transfer coefficient, R236fa, T_{sat}=15 °C, G=20 kg/sm^2
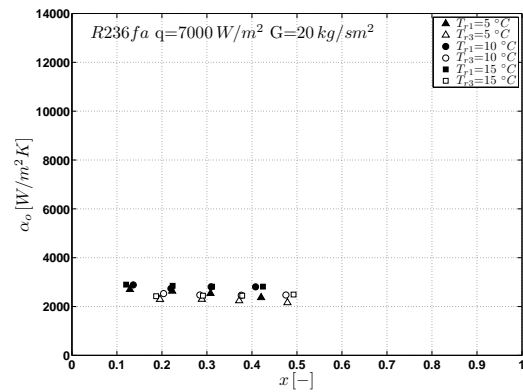
Figure 7.53: Local bundle heat transfer coefficient, R236fa, q=7000 W/m^2, G=20 kg/sm^2
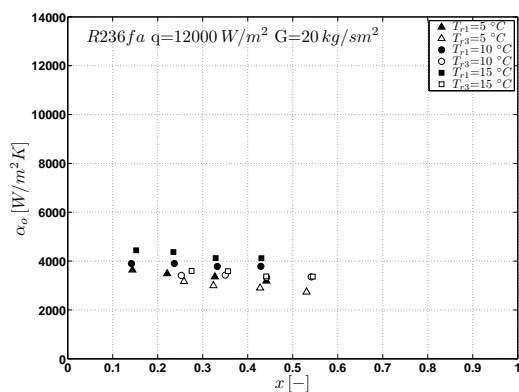
Figure 7.54: Local bundle heat transfer coefficient, R236fa, q=12000 W/m^2, G=20 kg/sm^2
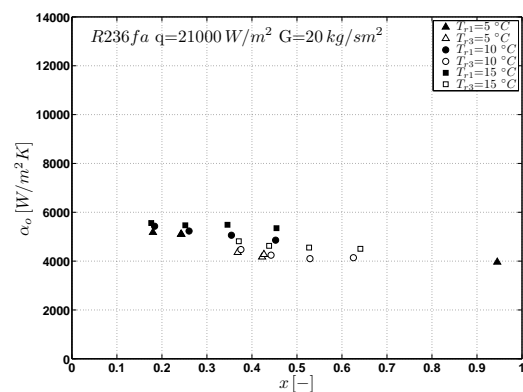
Figure 7.55: Local bundle heat transfer coefficient, R236fa, q=21000 W/m^2, G=20 kg/sm^2
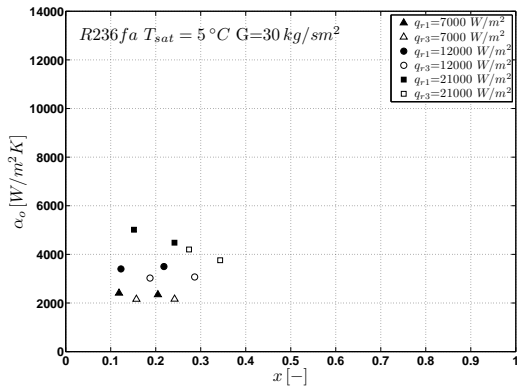
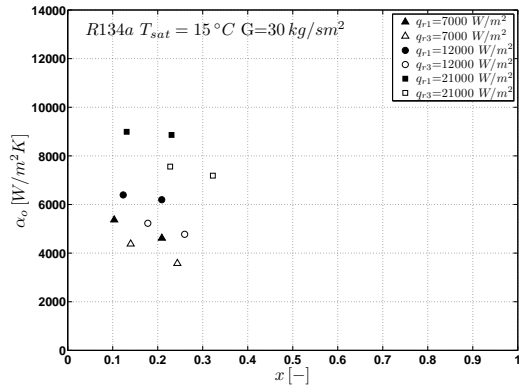Figure 7.56: Local bundle heat transfer coefficient, R236fa, T_{sat}=5 °C, G=30 kg/sm^2
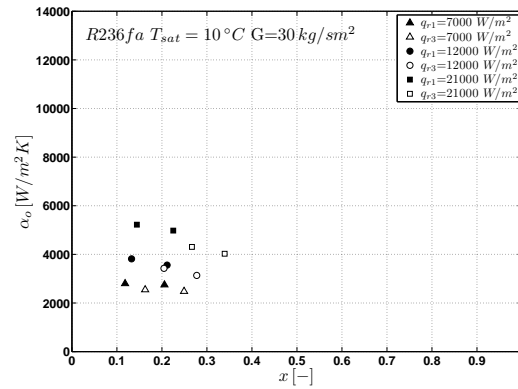
Figure 7.57: Local bundle heat transfer coefficient, R236fa, T_{sat}=10 °C, G=30 kg/sm^2
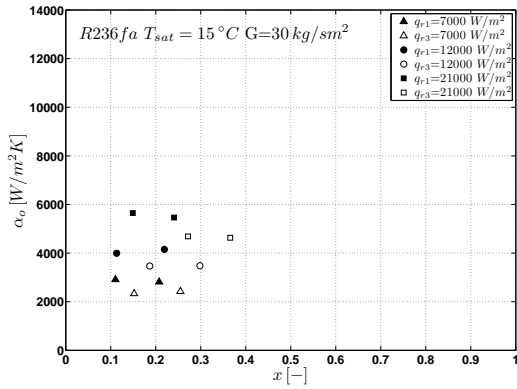
Figure 7.58: Local bundle heat transfer coefficient, R236fa, T_{sat}=15 °C, G=30 kg/sm^2
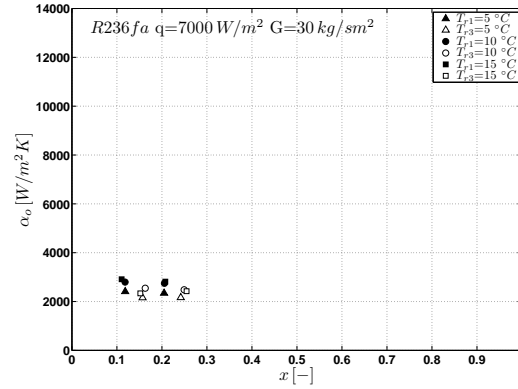
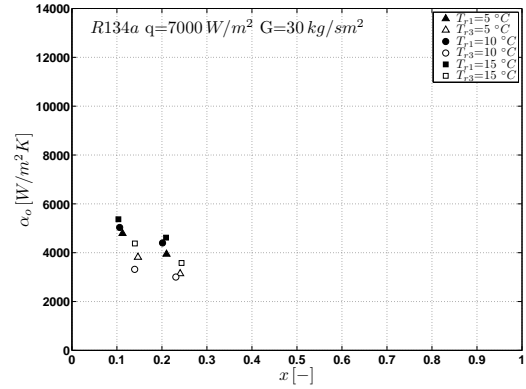

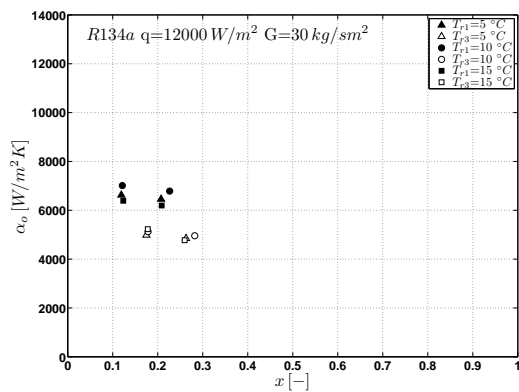Figure 7.59: Local bundle heat transfer coefficient, R236fa, q=7000 W/m^2, G=30 kg/sm^2
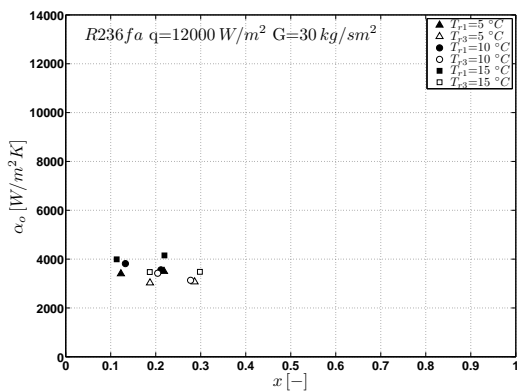
Figure 7.60: Local bundle heat transfer coefficient, R236fa, q=12000 W/m^2, G=30 kg/sm^2
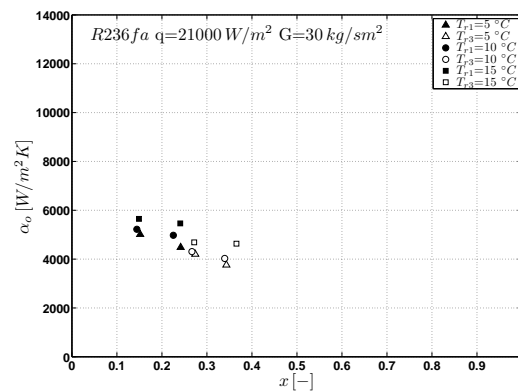
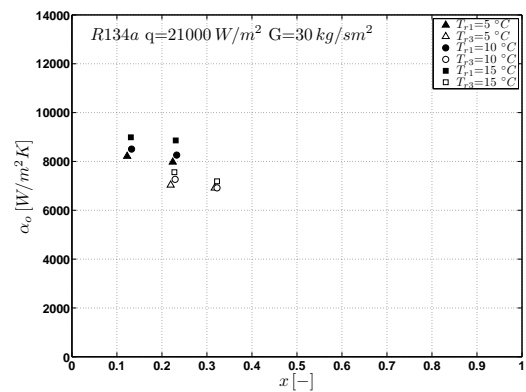
Figure 7.61: Local bundle heat transfer coefficient, R236fa, q=21000 W/m^2, G=30 kg/sm^2
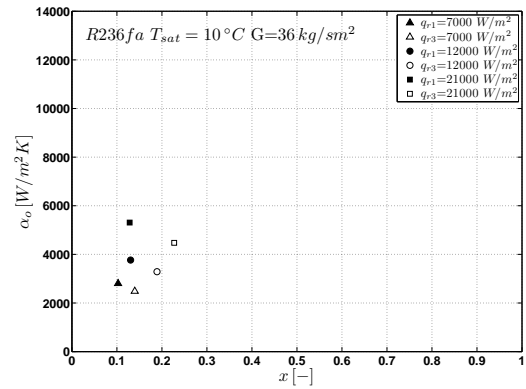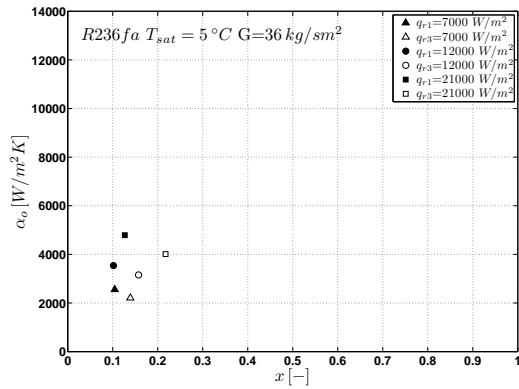
Figure 7.62: Local bundle heat transfer coefficient, R236fa, T_{sat}=5 °C, G=36 kg/sm^2

Figure 7.63: Local bundle heat transfer coefficient, R236fa, T_{sat}=10 °C, G=36 kg/sm^2
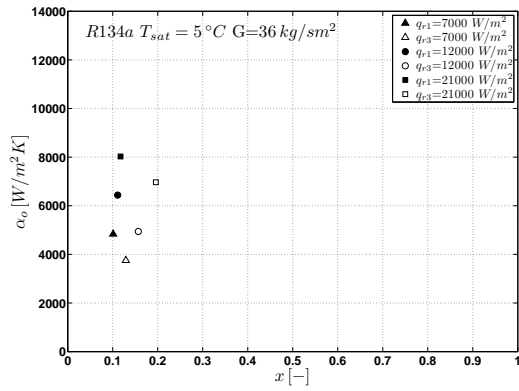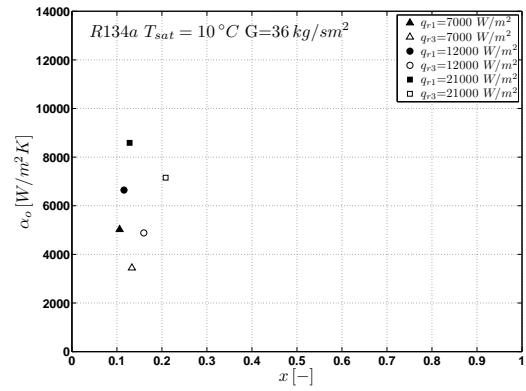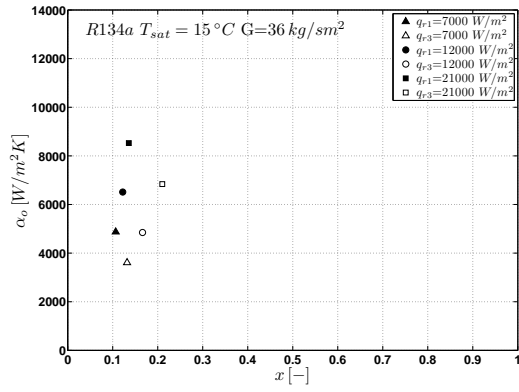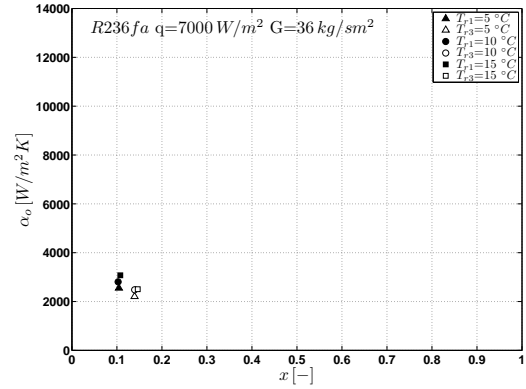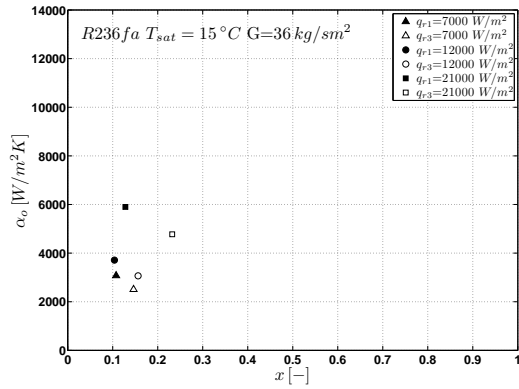

Figure 7.64: Local bundle heat transfer coefficient, R236fa, T_{sat}=15 °C, G=36 kg/sm^2

Figure 7.65: Local bundle heat transfer coefficient, R236fa, q=7000 W/m^2, G=36 kg/sm^2
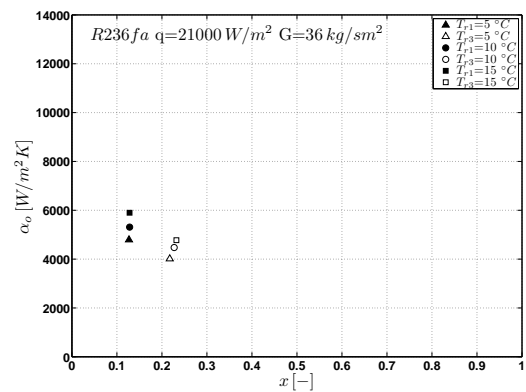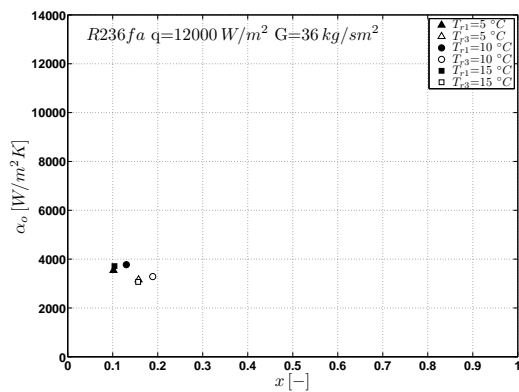
Figure 7.66: Local bundle heat transfer coefficient, R236fa, q=12000 W/m^2, G=36 kg/sm^2

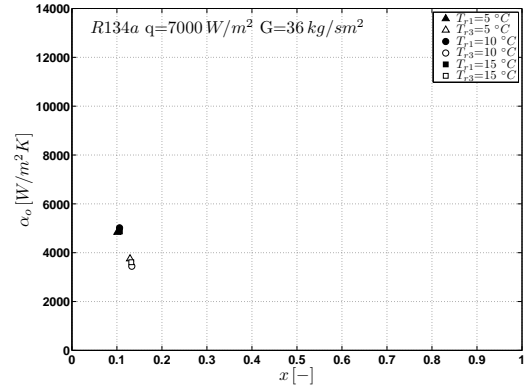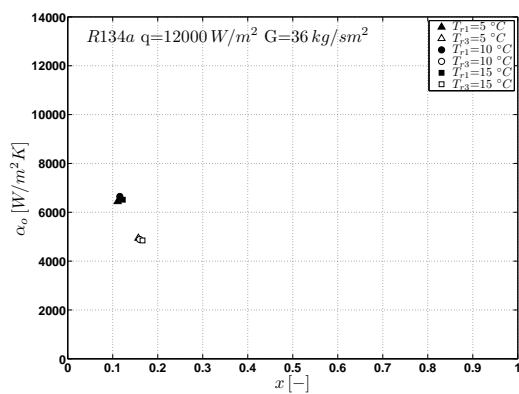
Figure 7.67: Local bundle heat transfer coefficient, R236fa, q=21000 W/m^2, G=36 kg/sm^2
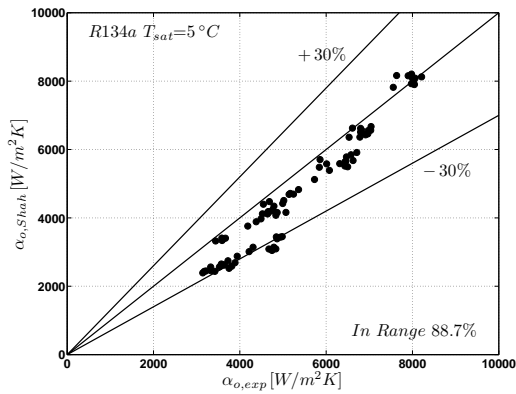
Figure 7.68: Local bundle heat transfer coefficients, experimental vs. predicted, R134a, $T_{sat} = 5\,°C$
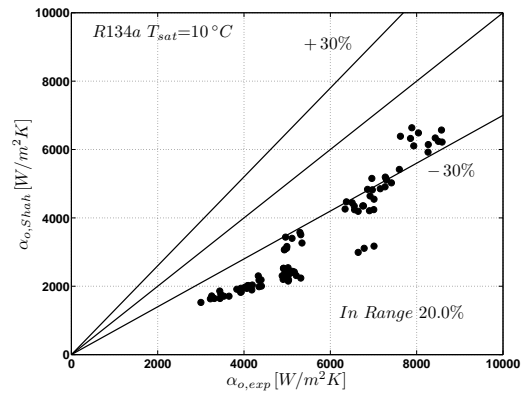
Figure 7.69: Local bundle heat transfer coefficients, experimental vs. predicted, R134a, $T_{sat} = 10\,°C$
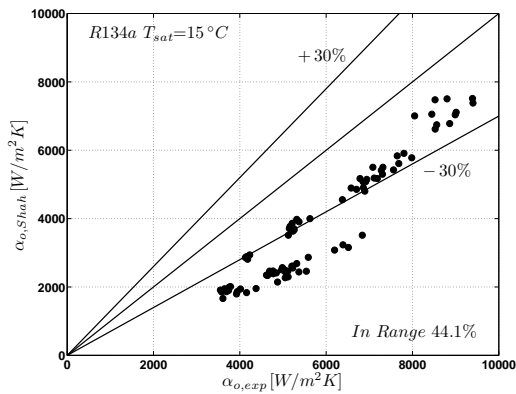
Figure 7.70: Local bundle heat transfer coefficients, experimental vs. predicted, R134a, $T_{sat} = 15\,°C$
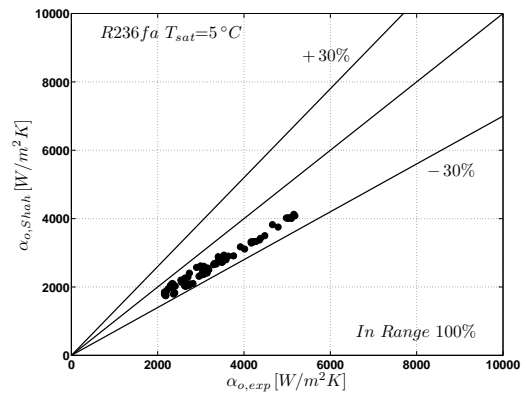
Figure 7.71: Local bundle heat transfer coefficients, experimental vs. predicted, R236fa, $T_{sat} = 5\,°C$
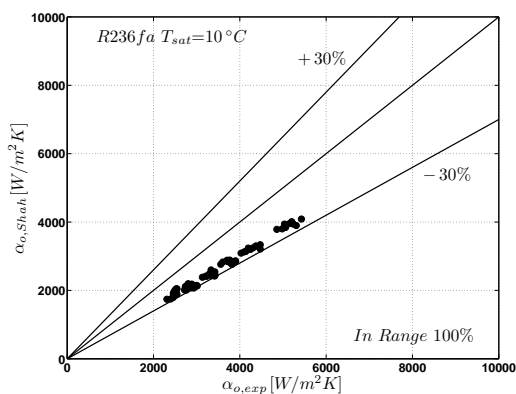
Figure 7.72: Local bundle heat transfer coefficients, experimental vs. predicted, R236fa, $T_{sat} = 10\,°C$
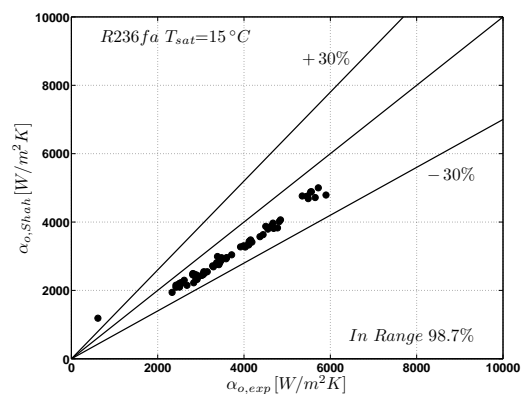
Figure 7.73: Local bundle heat transfer coefficients, experimental vs. predicted, R236fa, $T_{sat} = 15\,°C$
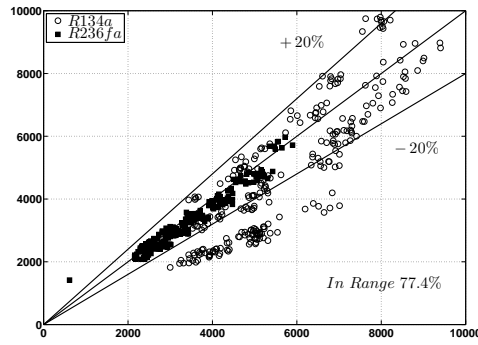
Figure 7.74: Local bundle heat transfer coefficients, experimental vs. predicted (corrected), R134a, R236fa
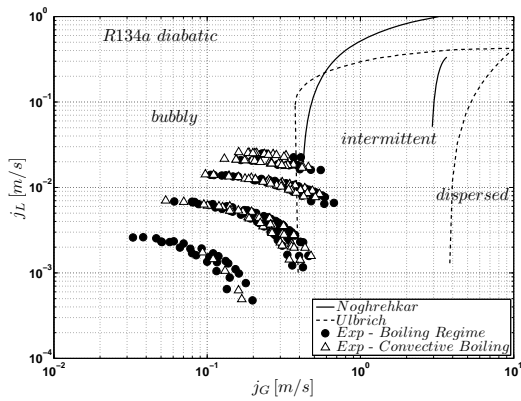
Figure 7.75: R134a, boiling regimes at their test conditions vs. two flow pattern maps
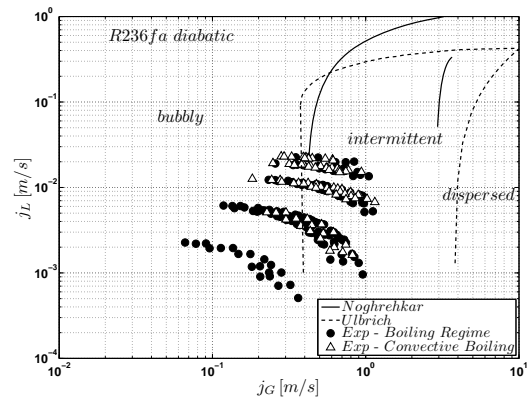
Figure 7.76: R236fa, boiling regimes at their test conditions vs. two flow pattern maps

In summary, a large experimental database for $R134a$ and $R236fa$ has been obtained for a plain tube bundle at three saturation temperatures. The Shah [55] bundle boiling method is only partially successful in predicting these data. By including an empirical adjustment factor of 1.45 to his method, to account for the tight tube pitch tested here, the method now captures 77.4% of all the data to within $\pm 20\%$.

Chapter 8

Conclusions

The present study involved an experimental investigation of two-phase flow and heat transfer in tube bundles. Boiling refrigerants were tested in an operability range comparable with that of an industrial shell-side bundle boiling evaporator. Local flow measurements were taken to characterize the two-phase flow structure and improve understanding the physical phenomena taking place. These flow structure observations and measurements were made with a laser-photodiode setup, a piezo-electric pressure transducer and a high speed video flow visualization system. The designed instrumentation, for the first time, allowed a visualization of two-phase structures in the core of a tube bundle. The conclusions drawn from this work are summarized below:

- The laser attenuation technique lead to the development a precise method for identifying the onset of dry-out. A dry-out line was then identified on a flow pattern map, thus allowing the clear identification of a dry-out zone and the much higher heat transfer in the wetted zone. These zones were shown to be the same for R134a and R236fa fluids. The definition of the dry-out zone constitutes an important achievement in the field of bundle boiling evaporation because it enables one to identify conditions of low thermal efficiency.

- The analysis of the pressure fluctuation power spectrum and the flow visualization results gave a better view of the two-phase flow inside tube bundle. No significant flow pattern effects on two-phase pressure drop and heat transfer data were evident from pressure fluctuations in the investigated experimental range. From the visualization of the flow, it was found that changes in experimental conditions lead to continuous and smooth changes in the relative distribution of gas and liquid phases. Therefore, no classification was possible since the flow did not highlight characteristics that could indicate a change in flow pattern. No bubbly flow, as is usually defined in literature, was found at low vapor qualities. Notably, the size of the bubbles at low gas velocity conditions was much bigger than the tube gap and became elongated when passing between the tubes. At higher vapor qualities, the gas structures merged to cover all the visual area. In the condition of non dry-out and high vapor quality, a film of liquid appears to be present around the tube; this can be identified from the visual observation as a pattern of waves over the tube surface.

- The experimental database, based on smooth tubes, allowed the refinement of frictional pressure drop models previously developed at LTCM. Particularly, the adiabatic data set was employed to give a better prediction of the frictional multiplier that accounts for the difference between the homogeneous model and reality. The parameter was found to be dependent on the mass velocity. The magnitude of the peak decreased with mass velocity and shifted to lower vapor qualities with increasing mass velocities. The new two-phase multiplier was found not to be dependent on the fluid type. No particular trends of the frictional pressure drop were highlighted when changing the experimental conditions; this indicates a negligible effect of the flow pattern on this measured parameter. No effects of the saturation temperature were found for the frictional pressure drop in the narrow range tested. The measured decrease in the total pressure drop with increasing vapor quality was explainable by the decrease in the static head component. The new model provided a

good prediction of the adiabatic data and a satisfactory prediction for the diabatic data.

- The local heat transfer data highlighted the dependency of the heat transfer coefficient on the heat flux. The heat transfer values for the tube bundle were found to be independent of the saturation temperature over the range tested and were almost independent of the vapor quality. Some what surprisingly, no dependency on mass velocity was found. As for the frictional pressure drop, no clear trends that could indicate an influence of flow pattern on the heat transfer behavior were found. Once a correction factor was introduced to account for the tighter tube pitch used in the present investigation. Current methods available in literature satisfactory predicted the data.

- The present study aimed to provide further insights into two-phase bundle boiling flow through the development of new instrumentation. However, a new flow pattern map could not be proposed since no flow pattern effects were identified in the investigated range at the measurement location. Furthermore, no direct effects of flow distribution on the local heat transfer and the pressure drop were found. It is left to future investigations to refine the developed measurement techniques. Due to local variations in the flow over the bundle, and a secondary flow effect, such further development should include multipoint measurements.

Appendix A

Statistics of Signal Processing: Fundamentals and Tips

Definitions: Let $x(t)$ be a time trace representative of a physical quantity. Let $(x_1, ..., x_n)$ be measured values: sampled discrete signals (at equal increment of time). Let $\bar{x}$ be the most probable value.

A.1 Statistical moments

A.1.1 Variance

The Variance is the square of the Standard Deviation (SD). The standard deviation is the Root Mean Square (RMS) deviation of the individual measurements about the universe average. There is a substantial difference between the root mean square and the variance. *The RMS does not have the widest possible significance because it indicates only how a particular set of N values deviate from their average. We do not know whether or not this quantity depends systematically upon the number of values N in the set. Furthermore, the errors we are now considering are completely random, so that a second set of N measurements generally does not yield an average value identical with the first, nor an identical set of deviations because of what are called statistical fluctuations. To establish a quantity which has greater significance, we employ the concept that such sets of N measurements are two samples of the entire universe of measurements which might be made, the number of the measurements in the universe being infinite [26].*

$$\sigma(x_1, ..., x_n) = \frac{1}{N-1} \sum_{j=1}^{N} (x_j - \overline{x})^2 \tag{A.1}$$

A.1.2 Skewness

The Skewness or third moment, characterizes the degree of asymmetry of a distribution around its mean. The skewness is defined in such a way to be non-dimensional. It is a pure number that characterizes only the shape of the distribution. A positive value of the skewness signifies a distribution with an asymmetric tail extending out toward more positive values of x; a negative value will be representative of a tail extending toward negative values of x.

$$Skew(x_1, ..., x_n) = \frac{1}{N} \sum_{j=1}^{N} \left[\frac{x_j - \overline{x}}{\sigma} \right]^3 \tag{A.2}$$

A.1.3 Kurtosis

Kurtosis it is a non dimensional quantity. It measures the relative peakedness or flatness of a distribution relative to a normal distribution. A distribution with a positive Kurtosis is defined as Leptokurtic while a negative distribution is Platykurtic (this last one will be the flatter one).

$$Kurt(x_1, ..., x_n) = \left\{ \frac{1}{N} \sum_{j=1}^{N} \left[\frac{x_j - \overline{x}}{\sigma} \right]^4 \right\} - 3 \tag{A.3}$$

(The -3 term makes the value zero for a normal distribution. This term is a pure convention. It may be omitted.)

A.2 Probability Density Function (PDF)

The PDF is a widely used statistical tool for the *linear analysis of experimental time series*: it represents the probability that the value of a given time series falls into an infinitesimal interval of the time series co-domain, so that the PDF integration over the whole co-domain equals one, and the integral of the PDF-weighted co-domain yields the time series mean value. Let's assume the following quantities:

$$x \quad \text{signal trace} \tag{A.4}$$

$$P(x) \quad \text{probability that the signal } x \text{ is below some specific value} \tag{A.5}$$

$$\frac{dP(x)}{dx} = p(x) \quad \begin{array}{l} \text{probability per unit void fraction that the void fraction lies in the} \\ \text{interval } [x, x + dx] \end{array} \tag{A.6}$$

Consider a time-signal trace record where the signal scale is broken into equal increments Δx_i and the time scale broken into equal increments is Δt_j. If, during the total time interval T, the signal is seen to be in Δx_i a total of n_i times, then:

$$\frac{n_i/N}{\Delta x_i} = \frac{1}{\Delta x_i} \sum_{j=1}^{n} \frac{\Delta t_j}{T} \tag{A.7}$$

Since the ratio $\sum_{j=1}^{n} \frac{\Delta t_j}{T}$ is the probability that the void fraction lies within the given interval Δx_i, it can be seen that:

$$\lim_{\Delta x_i \to 0} = \frac{1}{T \Delta x_i} \sum_{j=1}^{n} \Delta t_j \to p(x) \tag{A.8}$$

The previous equation represents the *probability density function* of the particular record examined. If a number of these records is obtained and the PDF results are averaged, the result is:

$$\overline{p(x)} = \frac{1}{K} \sum_{k=1}^{K} p^k(x) \tag{A.9}$$

If sufficient records are used for a statistically stationary process to cover a time interval that is large compared with the longest significant period of fluctuation, the PDF itself becomes becomes relatively constant. In fact, the result becomes essentially identical to a single PDF taken over a total period of time representing the one used for all K records.

A.3 Spectral methods

A physical process can be described either in the time domain, by the value of a quantity x as a function of time t, e.g. $x(t)$, or else in the frequency domain, where the process is specified by giving the amplitude X (generally a complex number indicating also the phase) as a function of frequency f, that is $X(f)$. For many purposes it useful to think of $x(t)$ and $X(f)$ as being two different representations of the same function. The Fourier transform provides the mathematical basis for frequency-domain analysis. Introducing the Fourier equations for a continuous signal:

$$X(f) = \int_{-\infty}^{\infty} x(t)e^{2\pi ift}dt \tag{A.10}$$

$$x(f) = \int_{-\infty}^{\infty} X(f)e^{-2\pi ift}df \tag{A.11}$$

$$\tag{A.12}$$

The Fourier transform is a linear operation.

A.3.1 Convolution

Let $x(t)$ and $y(t)$ be two functions and $X(f)$ and $Y(f)$ their corresponding Fourier transforms. The convolution is defined as:

$$x * y = \int_{-\infty}^{\infty} x(\tau)y(t-\tau)d\tau \tag{A.13}$$

The Convolution theorem says that:

$$x * y \Leftrightarrow X(f)Y(f) \tag{A.14}$$

A.3.2 Correlation

We define *correlation* as follows:

$$Corr(x,y) = R_{xy} = \int_{-\infty}^{\infty} x(\tau+t)y(\tau)d\tau \tag{A.15}$$

The Correlation theorem:

$$Corr(x,y) \Leftrightarrow X(f)Y(f) \tag{A.16}$$

The Correlation is a function of t, which is called the *lag*. It therefore lies in the time domain. The time lag is fixed for each integration, so the correlation is dependent on that time lag. The correlation is also known as the cross correlation. It is a standard method of estimating the degree at which two series are correlated. The correlation of a function with itself is called the *autocorrelation*:

$$Corr(x,x) = R_{xx} = \int_{-\infty}^{\infty} x(\tau+t)x(\tau)d\tau \tag{A.17}$$

$$Corr(x,x) \Leftrightarrow X(f)X(f) = X(f)^2 \tag{A.18}$$

In other words we speak about autocorrelation when the correlation is calculated between a series and a lagged version of the latter. In this case, a high correlation is likely to indicate a periodicity in the signal of the corresponding time duration. This quantity is a powerful tool to detect non-randomness in data and to identify an appropriate time series model if the data is not random.

A.3.3   Power spectrum

The total power in a signal is the same whether we compute it in the time domain or in the frequency domain:

$$\text{Total Power} = \int_{-\infty}^{\infty} |x(t)|^2 dt = \int_{-\infty}^{\infty} |X(f)|^2 df \tag{A.19}$$

Frequently one wants to know "how much power" is contained in the frequency interval between f and $f + df$. In such cases, one defines the one-side power spectral density PSD of the function x as:

$$P_x(f) = |X(f)|^2 + |X(-f)|^2 \tag{A.20}$$

When the function $x(t)$ is real (not complex):

$$P_x(f) = 2|X(f)|^2 \tag{A.21}$$

If the function $y(t)$ goes endlessly from $-\infty < t < \infty$, then its total power and power spectral density will, in general, be infinite. It is common to define the power spectral density per unit time. This is computed by taking a long, but finite, interval of the function $y(t)$, computing its PSD (that is, the PSD of a function that equals $y(t)$ in the finite interval but is zero everywhere else), and dividing the resulting PSD by the length of the interval used. Taking an interval of the function $y(t)$ over a time T, the PSD per unit time will assume the following form:

$$P_x(f) = \frac{1}{T} \left(2|X(f)|^2 \right) \tag{A.22}$$

(Occasionally the previous quantity is defined without the factor two. Strictly speaking, they are called two-sided spectral densities). What is previously described in terms of signal analysis, refers to continuous signals $y(t)$. In the general case of a sampled signal at evenly spaced intervals of time, we must deal with discretely sampled data. In such a case, the previous relationships can be rewritten to answer to the new requirements. Conceptually the two cases are similar.
An analysis of the previous quantities will provide information about the possible periodicity in the signal.

A.3.4   Fast Fourier Transform (FFT)

In terms of computation, it is important to consider the Fast Fourier Transform FFT. The discrete Fourier transform appears to be an $O(N^2)$ process. The discrete Fourier transform can, in fact, be computed in $O(N \log_2 N)$ with the algorithm called FFT. Limitations are introduced by the use of the FFT algorithm. We defer here to specialized texts and basic considerations are available in [48].

Appendix B

Wilson Plot: a Critical Historical Review

Historically, the Wilson plot technique was developed by Wilson [66] in 1915. Wilson devised a method to determine individual resistances from an overall resistance. this method is useful when the thermal resistance of the test fluid is the same order of magnitude as that of the other side and the other side is also unknown. Wilson expressed the tube-side resistance in terms of a reduced velocity v_r including the effects of property variations with temperature and tube diameter. In discussing this paper, Buckingham, father of the dimensional analysis [70], showed that the reduced velocity was the dimensionless quantity $D.u.\rho/\mu$. Buckingham call this parameter the *turbulence variable*, known today as the Reynolds number. Wilson modified equation (Eq. (7.7)) introducing the reduced velocity v_r (the original formulation consider a global area of exchange and does not consider a differential one as latter introduced).

Rewriting equation (Eq. (7.7)):

$$\frac{1}{UA} = \frac{1}{\alpha_o A_o} + \frac{1}{\alpha_i A_i} + \tilde{R}_{wall} \tag{B.1}$$

The out side resistance is kept fixed and provided by condensing steam, the tube-side Nusselt number for turbulent flow was assumed to be:

$$Nu = CRe^a Pr^{0.4} \tag{B.2}$$

The exponent a was chosen such that the resulting fit was the 'best' linear fit to the data points. This was done using the available data by a trial-and-error procedure. a was assumed to be 0.82. The value of a is close to $4/5$, the value used in the Dittus-Boelter equation [69] as exponent of the Reynolds number ($Re_{D_h} \gtrsim 10000$). From the resistance balance and from the previous assumptions:

$$\underbrace{\frac{1}{UA}}_{y} = C \underbrace{\frac{1}{(v_r)^{0.82}}}_{x} + R \tag{B.3}$$

Equation (Eq. (B.3)) takes the form of a straight line. C is a constant, R is the sum of the wall and shell-side resistances, A has to be intended as the reference heat transfer area and U the overall heat transfer coefficient referred to the mentioned area. It is important to underline that in the experimental campaign carried out from Wilson, the heat flux was not the same for all data points, which meant a shell-side resistance not constant.

Shah [74], underline several limitations regarding to this method because generally it requires:

    ◇ stable log-mean average temperatures of fluids and mass flow rates in both circuits

    ◇ known exponents of the Reynolds (reduced velocity) and Prandtl numbers

    ◇ the same order of magnitude of thermal resistances on both sides of separating barrier

    ◇ all the test data for the Wilson plot technique must be in one flow regime for the test fluid.

Going further in the development of this technique, Nobbs and Mayhew [73] modified the original approach of Wilson. They conducted experiments where the objective was to investigate variations in the steam-side resistance. For this reason, the Wilson plot method, where the steam-side resistance was assumed to be constant, could not be used. They proposed a modification in which relations were assumed for both condensing steam (shell-side) and cooling water (tube-side) heat transfer coefficients.

B.1 Modified Wilson Plot Method

Historically, the second important step in the development of this methodology is found in the work of Briggs and Young [72], fathers of the so called Modified Wilson Plot. The starting point is provided from Young and Wall (see [71]); they proposed heat transfer correlation for both the external and internal flows.

B.1.1 Young and Wall

In the case of single phase flow they assumed valid the correlation (Eq. (B.2)) for the external and internal flows. Imposing the same value for each side of a, equal to 0.8 (Dittus-Boelter, turbulent flow), and rewriting the resistance balance:

$$\underbrace{\frac{1}{UA} - \tilde{R}_{wall}}_{y} = \frac{1}{C_t} \underbrace{\frac{1}{[Re^{0.8}Pr^{0.4}A\lambda/D]_t}}_{x} + \frac{1}{C_s} \frac{1}{[Re^{0.8}Pr^{0.4}A\lambda/D]_s} \tag{B.4}$$

The parameters C_s and C_t can be determined from the linear fitting respectively from the slope and from the intercept. In this case, the quantity $[Re^{0.8}.Pr^{0.4}.A.\lambda/D]_s$ has to be kept constant in order to fit a linear line. This requires that the external fluid velocity and average temperature have to be kept constant.

B.1.2 Briggs and Young

Briggs and Young relaxed the requirement that the out-side Reynolds number exponent had to be know in advance. In this case, equation (Eq. (B.4)) assumes the form:

$$\frac{1}{UA} - \tilde{R}_{wall} = \frac{1}{C_t} \frac{1}{[Re^{0.8}Pr^{0.4}A\lambda/D]_t} + \frac{1}{C_s} \frac{1}{[Re^{d}Pr^{0.4}A\lambda/D]_s} \tag{B.5}$$

In this case the unknowns are C_s,C_t and d. The wall resistance is assumed to be known. If d is known, as in equation (Eq. (B.4)), equation (Eq. (B.5)) can be written in the form of a straight line form and then C_t and C_s can be computed separately. But the same equation cannot be used to calculate all three unknowns by imposing a linear fit. The authors overcame this issue by using two successive linear regressions in an iterative scheme. Rearranging:

$$\underbrace{\left(\frac{1}{UA} - \tilde{R}_{wall}\right)\left[Re^d Pr^{0.4} A\lambda/D\right]_s}_{y} = \frac{1}{C_t}\underbrace{\frac{\left[Re^d Pr^{0.4} A\lambda/D\right]_s}{\left[Re^{0.80} Pr^{0.4} A\lambda/D\right]_t}}_{x} + \frac{1}{C_s} \tag{B.6}$$

If the Reynolds number exponent d is known, then the parameters C_t and C_s can be determined through a linear fit.

If the internal fluid correlation is known, the out-side parameters C_s and d can be determined by subtracting the wall resistance and the internal side resistance from the overall measured resistance. Rearranging equation Eq. (B.5):

$$\frac{1}{UA} - \tilde{R}_{wall} - \frac{1}{C_t}\frac{1}{\left[Re^{0.8} Pr^{0.4} A\lambda/D\right]_t} = \frac{1}{C_s}\frac{1}{\left[Re^d Pr^{0.4} A\lambda/D\right]_s} \tag{B.7}$$

In this case C_t is assumed to be known, from equation (Eq. (B.7)):

$$\underbrace{\frac{1}{UA} - \tilde{R}_{wall} - \frac{1}{C_t}\frac{1}{\left[Re^{0.8} Pr^{0.4} A\lambda/D\right]_t}\left[Pr^{0.4} A\lambda/D\right]_s}_{y} = \frac{1}{C_s\left(Re^d\right)} \tag{B.8}$$

Rewriting:

$$\frac{1}{y} = C_s\left(Re^d\right) \tag{B.9}$$

Assuming single phase flow also for the out-side, from equation (Eq. (B.2)) we know also that:

$$y = (Pr_s)^{0.4}/Nu_s \tag{B.10}$$

From equation (Eq. (B.9)):

$$\underbrace{ln\left(\frac{1}{y}\right)}_{Y} = ln\left(C_s\right) + d\underbrace{ln\left(Re_s\right)}_{X} \tag{B.11}$$

New values of C_s and d can now be determined with a linear fit according to equation (Eq. (B.11)).

The procedure may be summarized as follow: *a value of d is assumed. The parameters C_t and C_s are calculated from the first linear fit; the values of C_s and d are recomputed through a second linear fit closing the iterative loop. d is the parameter of convergence.*

Shah [74], analyzing this method made the following considerations:

◇ a complete out-side and internal-side range should be covered applying this method (equation (Eq. (B.11)) represents a out-side modified Wilson plot, (Eq. (B.6)) represents an internal-side modified Wilson plot)

◇ the wall resistance must be kept considerably lower than the global resistance for all data points

◇ for the internal-side modified Wilson plot, (Eq. (B.6)), both terms on the right hand side should be of the same order of magnitude

⋄ for the out-side modified Wilson plot, (Eq. (B.11)), the out-side thermal resistance must be dominant for all the test points

⋄ if the out-side resistance is dominant, C_s will not converge in the iteration and the method of Briggs and Young will not yield a reasonably accurate correlation on the out-side.

Khartabil, Christensen and Richards [71] pointed out that the previous methods, here presented, can be applied to limited types of heat exchangers for which some information about both heat transfer and wall resistance have to be known in advance. They point out that there are situations, where neither heat transfer correlations, nor wall resistance expressions are available. A new method, with a modified Wilson plot scheme was proposed: it allows for determining all three resistances (tube, shell and wall) from overall resistance measurements and up to five parameters. The authors in this case underline the importance of the method accuracy and its management. For this method, the value of each resistance can be obtained by subtracting the two remaining resistances from the overall resistance. The uncertainty in each resistance is therefore determined by how large that resistance is when compared with the two remaining. From this point of view, the relative resistances have a significative effect on the accuracy of the resulting correlations. Also for this case, Shah [74], point out the limitation that all the test data on one fluid side must be in one flow regime only (e.g. turbulent regime).

The more recent developments of this technique and examples of its implementations will now be presented.

B.1.3   LTCM approach [61]

The conceptual basis of the LTCM approach is the method developed from Briggs and Young. In this approach, currently used at LTCM, initially pool boiling tests are performed on the outside of the tube, taking advantage of their large values to characterize the internal correlation. For a fixed saturation temperature, the outside pool boiling heat transfer coefficient can be correlated according to the following expression:

$$\alpha_o = C_o q_o^n \tag{B.12}$$

From (Eq. (7.10)),(Eq. (B.12)) and rearranging (Eq. (7.8)):

$$\left[\frac{1}{U_o} - R_{wall} \right] q_o^n = \frac{1}{C_o} + \frac{1}{C_i} \left[\frac{q_o^n}{\alpha_{Gn,i}} (D_o/D_i) \right] \tag{B.13}$$

Plotting $[\frac{1}{U_o} - R_{wall}].q_o^n$ versus $[\frac{q_o^n}{\alpha_{Gn,i}}.(D_o/D_i)]$, $\frac{1}{C_i}$ will be the slope of the line fitted through the experimental data points. The 'best' straight line by linear regression minimizes S, the sum of squares of residuals of $[\frac{1}{U_o} - R_{wall}].q_o^n$:

$$
\begin{aligned}
S &= \sum \left\{ \left[\left(\frac{1}{U_o} - R_{wall} \right) q_o^n \right]_{calc} - \left[\left(\frac{1}{U_o} - R_{wall} \right) q_o^n \right]_{exp} \right\}^2 \\
&= \sum \left\{ \frac{1}{C_o} + \frac{1}{C_i} \left[\frac{q_o^n}{\alpha_{Gn,i}} (D_o/D_i) \right] - \left[\left(\frac{1}{U_o} - R_{wall} \right) q_o^n \right]_{exp} \right\}^2 \tag{B.14}
\end{aligned}
$$

For minimum S:

$$\frac{\partial S}{\partial (1/C_o)} = 0 \qquad \frac{\partial S}{\partial (1/C_i)} = 0 \tag{B.15}$$

These two equations will yield a linear algebraic system that may be solved for C_o and C_i. To obtain the data points, the internal heat transfer coefficient is varied. This is obtained by varying the water mass flow rate and thus the Reynolds number. During this procedure the external heat transfer coefficient must be kept constant. The imposed inlet water temperature is varied to maintain the mean heat flux constant. This means that the heat per unit time discharged to the refrigerant is constant. Remembering that the temperature profile was fitted with a second order polynomial, this is equivalent to maintaining the same heat flux at the center of the tube. The multiplier C_i accounts for the internal enhancement provided from the internal fins of the tube.

In this procedure, equal weight is given to all the data points. This means that the same uncertainty, for a given confidence interval, is postulated for the quantities whose residuals will be minimized during the fitting. As pointed out by Rose [67], more accurate parameters, with the presented approach, would be obtained by using appropriate weighting factors for the points in the minimization (linear regression) procedure.

B.1.4   Rose [67]

The method presented in B.1.3 is based on the concept of the thermal resistance, a ratio between temperature difference and heat flux. Instead, Rose's method considers directly the temperature differences. The overall temperature difference is written as:

$$\Delta T_{ov} = \Delta T_o + \Delta T_{wall} + \Delta T_i \tag{B.16}$$

Without axial conduction, the following thermal balance may be written:

$$\delta Q = \pi D_i \delta s q_i = \pi D_o \delta s q_o \tag{B.17}$$
$$\hookrightarrow q_i = q_o \frac{D_o}{D_i} \tag{B.18}$$

Considering that:

$$\Delta T_i = \frac{q_i}{\alpha_i} \qquad \Delta T_o = \frac{q_o}{\alpha_o} \qquad \Delta T_{wall} = q_o R_{wall} \tag{B.19}$$

Applying Eq. (7.10), Eq. (B.12) we obtain:

$$\Delta T_{ov} = \underbrace{\frac{1}{C_o}}_{a} \cdot \underbrace{\left(q_o^{1-n}\right)}_{x} + \underbrace{\left[q_o \frac{D_o}{2\lambda_{wall}} ln \frac{D_{or}}{D_i}\right]}_{y} + \underbrace{\frac{1}{C_i}}_{b} \underbrace{\left(\frac{q_o}{\alpha_{Gn,i}} \frac{D_o}{D_i}\right)}_{z} \tag{B.20}$$

Rearranging Eq. (B.20):

$$\Delta T_{ov} = ax + y + bz \tag{B.21}$$

In Eq. (B.21) the parameters a, b are unknown. They can be estimated minimizing the residuals S defined as follows:

$$S = \sum \left(\Delta T_{ov,calc} - \Delta T_{ov,exp}\right)^2 \tag{B.22}$$

Imposing a minimum

$$\frac{\partial S}{\partial a} = 0 \qquad \frac{\partial S}{\partial b} = 0 \tag{B.23}$$

The following expressions are obtained:

$$a = \frac{\sum xz \sum yz - \sum z^2 \sum xy + \sum z^2 \sum x\Delta T_o - \sum xz \sum z\Delta T_o}{\sum z^2 \sum x^2 - \sum xz \sum xz} \tag{B.24}$$

$$b = \frac{\sum xz \sum xy - \sum x^2 \sum yz + \sum x^2 \sum z\Delta T_o - \sum xz \sum x\Delta T_o}{\sum z^2 \sum x^2 - \sum xz \sum xz} \tag{B.25}$$

The LTCM approach in B.1.3 is an indirect approach: the minimized quantities are not direct measurements. Instead, Rose's approach is a direct one. The quantities that are minimized are the differences of temperature. A particular advantage of this method is that the error in the quantities whose residuals are minimized is generally expected to be approximately constant for each data point. So the assumption of a constant uncertainty for each point is more visible.

B.1.5   El Sherbini, Joardar, Jacobi [68]

Their method is based on the fact that measurement uncertainties in the measured quantities have a direct impact on the slope and the ordinate intercept of the Wilson Plot. Moreover, the magnitude and the relative distribution of each point on the Wilson plot also affects the uncertainty in the ordinate intercept. In general terms, these authors point out that in all the Wilson plot methods the accuracy depends on:

◇ Number of data points for each Wilson line

◇ Range and spatial separation between each data point (abscissa)

◇ The single-sample uncertainty for each data point and the distribution of uncertainty

◇ Validity and accuracy of the Nusselt correlation used for one or both fluids

◇ Number of constants to be determined.

This method could be generally applied to the LTCM and Rose approaches since it focuses on the fitting procedure.

For a *last-squared fitting* (the residual sum of squares of the quantity in the ordinate are minimized) the major disadvantage is that the same weight is assigned to all data points and the single uncertainties are neglected. El Sherbini et al. overcame this problem using a weighted *least square or χ^2-fitting*. It is a quantitative measure of how well the data fit the model (agreement between model and data set) and whether the fit is reasonable or out right wrong. If the measurement errors are normally distributed and the fitting equation is of the form:

$$y_i = a + bx_i \tag{B.26}$$

The χ^2 merit function is defined as:

$$\chi^2(a, b) = \sum_{i=1}^{n} \left(\frac{y_i - a - bx_i}{\sigma_i} \right)^2 \tag{B.27}$$

It will give the maximum likelihood parameter estimation of a, b as:

$$a = \frac{S_{xx}S_y - S_xS_{xy}}{\Delta} \qquad b = \frac{SS_{xy} - S_xS_y}{\Delta} \tag{B.28}$$

where:

$$S = \sum_{i=1}^{n}\frac{1}{\sigma_i^2} \qquad S_x = \sum_{i=1}^{n}\frac{x_i}{\sigma_i^2} \qquad S_{yy} = \sum_{i=1}^{n}\frac{y_i}{\sigma_i^2}$$

$$S_{xx} = \sum_{i=1}^{n}\frac{x_i^2}{\sigma_i^2} \qquad S_{xy} = \sum_{i=1}^{n}\frac{x_iy_i}{\sigma_i^2} \qquad \Delta = SS_{xx} - (S_x)^2 \tag{B.29}$$

The method allows for an uncertainty computation to be made on the resulting estimated parameter and it provides an estimation of the goodness of fit (GOF):

$$GOF = Q\left(\frac{N-2}{2}, \frac{\chi^2}{2}\right) \tag{B.30}$$

where Q is the incomplete gamma function and N are the number of data points. Details are also available from [48].

From a theorical point of view, this is the best method because an approach to fitting data statistically gives the right importance to the uncertainty terms. The previous equations are valid only when the uncertainty is associated to the y_i variable and the values of x_i are considered to be exactly known and this is not generally true.

The method presented by Styrylska [62], known as the unified Wilson plot method, overcame all the problems shown previously. The data reduction employed is based on constrained optimization methods. The method involves to complex matrix/iterative computations. So from this point of view of the experimenter, in terms of computational costs, its application is appropriate only when the other methodologies do not. Several critics of the Wilson plot technique and the modified Wilson plot technique have been advanced. Shah [74] underlined some of the limitations in the different presented techniques. Wójs and Tietze [75] showed that the stability of temperature within a test section investigated with the Wilson plot technique affects measured values of the heat transfer coefficient. This investigation lead to the evaluation of the effects of temperature uncertainty on the calculated heat transfer coefficient through the modified Wilson plot method. The results indicate that the Wilson plot technique of determining the heat transfer coefficient is sensitive to temperature interference. For the analyzed case, they showed that a root-mean-square deviation of $0.1\,K$ in temperature measurements (representative of the uncertainty for high accuracy thermometers) lead to an error of $\simeq 20\%$ in the heat transfer coefficient. Their simulations also showed that a deviation of $1\,K$ can lead to physically un-reasonable results. Kumar et al. [76] experimentally found that the modified Wilson plot technique under-predicts the condensing side heat transfer coefficient by $7.5 - 25\%$ for different fluid, but no uncertainty analysis was presented.

B.1.6 Roetzel and Spang

Roetzel and Spang [78] presented a new steady state method for determining heat transfer coefficients on both sides of a heat exchanger from measuring the overall heat transfer coefficients. The method overcomes the limitations previously exposed in the description of the Wilson plot techniques. It is based on measurements with two fluids of different thermal conductivity under the same conditions.

The basic idea of the method is to carry out two independent measurements, I and II, using fluids of different thermal conductivity. This means that in the first experimental session a first fluid is used; in the second session a fluid with different thermal conductivity will substitute the first one. Experimental conditions have to be done such that:

$$
\begin{aligned}
Nu_{o,I} &= Nu_{o,II} = Nu_o & \text{(B.31)} \\
Nu_{i,I} &= Nu_{i,II} = Nu_i & \text{(B.32)}
\end{aligned}
$$

Using L_{ci}, L_{co} as the characteristic lengths, from equation (Eq. (B.1)):

$$
\begin{aligned}
\frac{1}{(U.A)_I} &= \frac{L_{co}}{\lambda_{o,I} Nu_o A_o} + \tilde{R}_{wall} + \frac{L_{ci}}{\lambda_{i,I} Nu_i A_i} & \text{(B.33)} \\
\frac{1}{(U.A)_{II}} &= \frac{L_{co}}{\lambda_{o,II} Nu_o A_o} + \tilde{R}_{wall} + \frac{L_{ci}}{\lambda_{i,II} Nu_i A_i} & \text{(B.34)}
\end{aligned}
$$

Measuring $(UA)_I$ and $(UA)_{II}$ and knowing the geometrical parameters and thermo-physical properties, the Nusselt numbers can be determined from equations (Eq. (B.33)) and (Eq. (B.34)):

$$
\begin{aligned}
\frac{1}{Nu_o} &= \left[\frac{\lambda_{i,I}}{(U.A)_I} - \frac{\lambda_{i,II}}{(UA)_{II}} - \tilde{R}_{wall}(\lambda_{i,I} - \lambda_{i,II}) \right] \left[\frac{L_{co}}{A_o} \left(\frac{\lambda_{i,I}}{\lambda_{o,I}} - \frac{\lambda_{i,II}}{\lambda_{o,II}} \right) \right]^{-1} & \text{(B.35)} \\
\frac{1}{Nu_i} &= \left[\frac{\lambda_{o,I}}{(UA)_{II}} - \frac{\lambda_{o,II}}{(UA)_I} - \tilde{R}_{wall}(\lambda_{o,II} - \lambda_{o,I}) \right] \left[\frac{L_{ci}}{A_i} \left(\frac{\lambda_{o,II}}{\lambda_{i,II}} - \frac{\lambda_{o,I}}{\lambda_{i,I}} \right) \right]^{-1} & \text{(B.36)}
\end{aligned}
$$

The authors suggest that the method can also be applied using fluids of different thermal conductivity only on one side and working with the same fluid during both measurements on the other side. With an arbitrarily chosen thermal conductivity $\lambda_{i,I} = \lambda_{i,II} = \lambda_i$, from equations (Eq. (B.35)) and (Eq. (B.36)):

$$
\begin{aligned}
\frac{1}{Nu_o} &= \left[\frac{1}{(UA)_I} - \frac{1}{(UA)_{II}} \right] \left[\frac{L_{co}}{A_o} \left(\frac{1}{\lambda_{o,I}} - \frac{1}{\lambda_{o,II}} \right) \right]^{-1} & \text{(B.37)} \\
\frac{1}{Nu_i} &= \left[\frac{1}{(UA)_{II}} - \frac{1}{(U.A)_I} \right] \left[\frac{L_{ci}}{A_i} \left(\frac{1}{\lambda_{i,II}} - \frac{1}{\lambda_{i,I}} \right) \right]^{-1} & \text{(B.38)}
\end{aligned}
$$

In implementing this method experimentally, in order to have the same Nusselt number during both measurements, besides the geometrical dimensions, the Reynolds numbers, Prandl number and viscosity ratios at the wall temperature and bulk mean temperature must be approximatively constant. If this cannot be ensured, the dependency of the Nusselt number on this parameter must be known. The authors point out that, in general, the application of the methods require fluids with high thermal conductivities but nearly the same Prandtl numbers. The method presented has the advantage, compared with the Wilson plot techniques, that no assumptions about the heat transfer characteristics are made. On the other hand, the experimental implementation of the method may be problematic in terms of testing and fluid handling.

In the successive work of Roetzel and Na Ranong [77], the authors consider a few simple but realistic calculated "experiments" and their evaluation according to the Wilson plot methodology. They showed that despite good results of the data regression, undesirable systematic errors in the obtained heat transfer coefficients may occur. The authors made the following recommendations to avoid undesirable systematic errors when applying the Wilson Plot Technique:

⋄ when the heat transfer coefficient on one of the two fluid sides is kept at a constant value, the thermal conductivity of the fluid with changing flow rate has to be varied in the experiments

⋄ when both mass and flow rates are varied, the ratio of the thermal conductivities of the fluids in both channels has to be varied in the experiments

⋄ the total range of Re and Pr or other dimensionless variables should be subdivided into subranges, for which simple correlations, can be used. When the ranges shrink to a single point, the method described previously may be employed

⋄ the change of thermal conductivity ratio could be realized by interchanging the fluids of both channels. One could arrange two identical heat exchangers in series to exchange the fluids in one experimental run. If gases are employed, one can make use of the temperature dependance of the thermal conductivity and merely change the mean gas temperature on one or both sides.

B.1.7 Additional considerations

A problem linked with the application of the Modified Wilson Plot Method its extreme sensitivity to the temperature measurement accuracy; see Wójs and Tietze [75]. Conceptually, this issue reflects the need to know more about the *robustness of the estimator*.

In order to check the sensitivity of the presented method, white noise is added to the current values of the measured temperature. A random normal distribution is employed to simulate the white noise. Different cases are investigated, considering different values of the standard deviation as in Table B.1.

	σ [°C]
a	0.0125
b	0.0250
c	0.0500
d	0.5000
e	1.0000

Table B.1: Added noise: standard deviations

What was found it is that for values of the standard deviation larger than 0.5 °C, physically unrealistic results are obtained: negative heat transfer coefficients and negative heat fluxes that do not correspond to the investigated physical phenomena, see [79]. This tells us that the method is very sensitive with respect to the uncertainty associated to the temperature measurements, and it fails when the instrumentation is not able to provide a value with an acceptable uncertainty.

Appendix C

Air-Water Tests

Prior to their use to the bundle boiling facility, the instrumentation was selected, designed and test through a series of air-water experiments carried out in a horizontal tube. This appendix describes the development of the piezo-electric transducer, laser photodiode and high speed flow visualization systems. It also presents the results of the their application in determining the flow regimes of the air-water flow.

C.1   Bubble frequency

An estimation of the bubble frequency was made in order to guide the selection of the instrumentation. Two different cases were considered:

a. Frequency of departure, a process linked with the boiling at the wall.
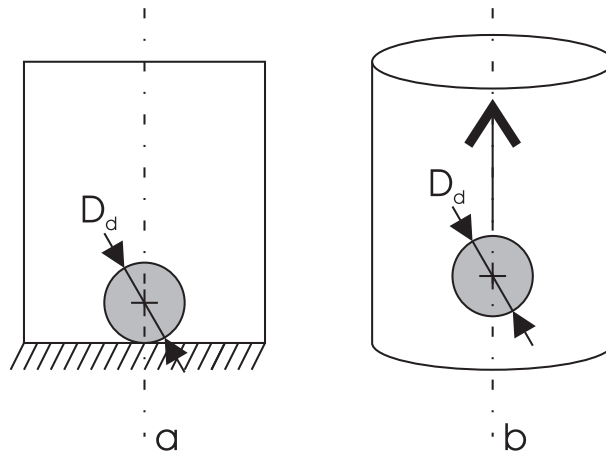
b. Bubble frequency due to forced convection.

Figure C.1: Bubble frequency: a. departure; b. forced convection

C.1.1   Bubble departure diameter and frequency of bubble release

From bubble growth analysis, the departure diameter and the release frequency appear to be related. The inverse of the frequency, $T = 1/f$, which is the time period associated with the growth of each bubble,

must equal the sum of the waiting period and the time required for the bubble to grow to its departure diameter D_d. The frequency of bubble release depends directly on how large the bubble must become before a release can occur, and, as consequence, on the rate at which the bubble can grow to this size. The bubble diameter at release is primarily determined by the net effect of forces acting on the bubble as it grows on the surface. Interfacial tension acting along the contact line invariably acts to hold the bubble in place on the surface. Buoyancy is often a major player in the force balance. If the bubble grows very rapidly, the inertia associated with the induced liquid flow field around the bubble may also tend to pull the bubble away from the surface. When the liquid adjacent to the surface has a bulk motion associated with it, drag and lift forces on the growing bubble may also act to detach the bubble from the surface.

Many correlations make use of the Bond number (or Eotvos number), representing the ratio between buoyancy forces and surface tension forces, to predict the departure diameter of bubbles during nucleate boiling:

$$Bo = \frac{g(\rho_L - \rho_G)D_d^2}{\sigma} \tag{C.1}$$

According to Cole [82], the Bond number can be expressed in terms of the Jacob number; it represents a ratio between sensible heat of superheating the liquid and latent heat of vaporization:

$$Ja = \frac{(T_w - T_{sat})c_{pL}\rho_L}{\rho_G h_{LV}} \tag{C.2}$$

$$Bo^{1/2} = 0.04 Ja \tag{C.3}$$

Once the Jacob number, and successively also the Bond number, are evaluated, the departure diameter can be computed from the definition of the Bond number:

$$D_d = \left[\frac{\sigma Bo}{g(\rho_L - \rho_V)}\right]^{1/2} \tag{C.4}$$

Based on the analogy between the bubble release process and natural convection, Zuber [83] suggested the following relation:

$$f_d D_d = 0.59 \left[\frac{\sigma g(\rho_L - \rho_V)}{\rho_L^2}\right]^{1/4} \tag{C.5}$$

The departure frequency can now be evaluated.

C.1.2 Forced convection

Let us consider the gas velocity:

$$u_G = \frac{Gx}{\rho_G \alpha} \sim \frac{\text{length scale}}{\text{time scale}} \tag{C.6}$$

where u_G represents the characteristic velocity of the gas phase; it represents a ratio between length and time scales.

Knowing experimentally the values of the mass flux G, the vapor quality x, the void fraction α and the thermo-physical properties of the fluid, the gas velocity can be computed. Assuming the length scale to be approximated by of the bubble departure diameter, the characteristic time scale can be evaluated. This assumption considers the fact that the minimum scale length is relative to the bubble at the condition of departure. The associated frequency will be its inverse value f_c.

From the experimental conditions reported in Table C.1, the frequencies previously discussed have been computed and the following result have been obtained:

⋄ $f_d = 220.7\,Hz$

⋄ $f_c = 4287.0\,Hz$

The selection of the instrumentation was based on the computed frequencies.

Label	Value	Unity
T_{sat}	4.6	[°C]
T_w	11.9	[°C]
$c_{p,L}$	1354	$[J/kg.K]$
ρ_L	1279.4	$[kg/m^3]$
ρ_G	16.9	$[kg/m^3]$
h_{LG}	195050	$[J/kg]$
σ	0.010901	$[N/m]$
G	18.06	$[kg/s.m^2]$
x	0.2408	$[-]$
$\varepsilon\,(^*)$	0.4195	$[-]$
Ja	3.83	$[-]$
Bo	0.023	$[-]$
D_d	$1.43.10^{-4}$	$[m]$
u_G	0.613	$[m/s]$

Table C.1: Bubble frequency evaluation ($R134a$): experimental conditions ((*) Computed using the Feenstra et al. [50] void fraction model)

C.2   Instrumentation test

Once the laser-photodiode and the piezo-electric pressure systems were selected, we investigated their capability to characterize the two-phase flows with a simplified experiment. Tests were conducted in an horizontal tube such that the diameter was comparable with the interspace between two tubes d^* in the bundle boiling facility, as represented in Fig. (C.3). For the LTCM bundle boiling facility $d^* = 3.35\,mm$ therefore, a glass tube with an internal diameter of $3\,mm$ was selected. An experimental campaign was then carried out [85]. A sketch of the facility is given in Fig. (C.2). Three independent parts are highlighted:

   A. *Test section*: It is composed of a system for injection air into the water stream, a static mixer and the horizontal glass tube.

B Air circuit: This provides dry air at controlled conditions to the mixer.

C Water circuit: This was composed of two systems connected in parallel; the first one works with a variable speed pump and a water tank for high flow rates, the second one is designed for lower flow rates and works with a bottle of water pressurized with nitrogen.
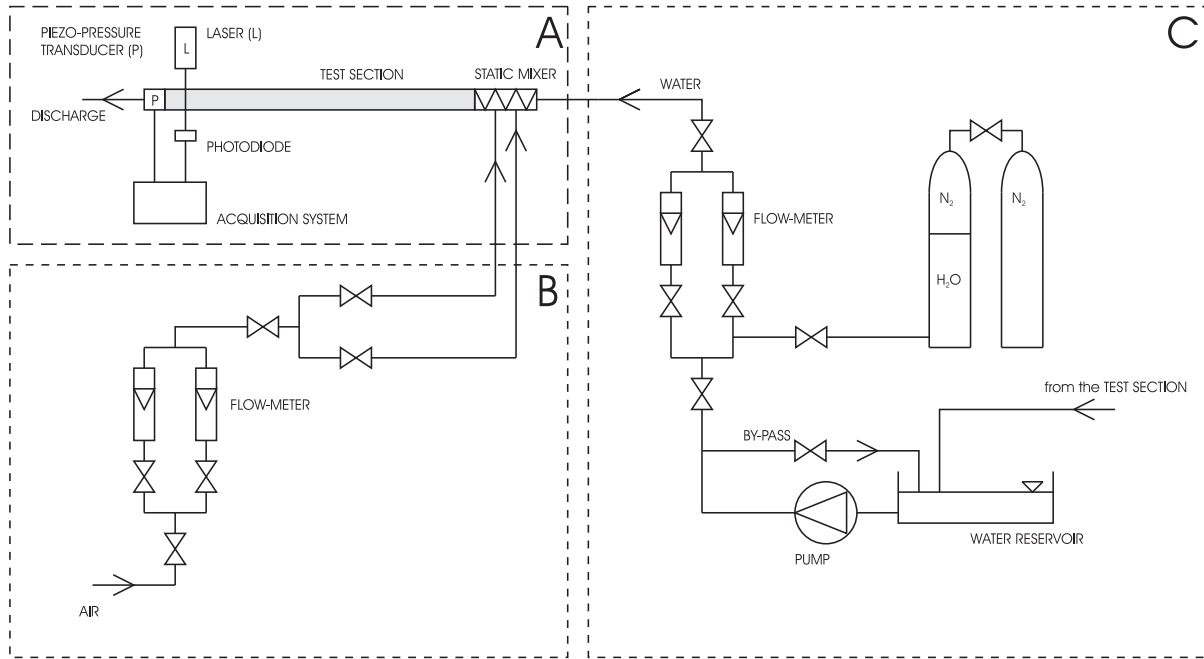

Figure C.2: Air-water facility: horizontal tube test circuit (A. test section; B. air circuit; C. water circuit)

The instrumentation was installed at the exit of the horizontal tube at a suitable distance from the mixer. The position of the measurement from the mixer discharge is reported in Table C.2. At this distance the flow can be considered fully developed and independent from the injection mechanism of the two fluids, see Fossa and Guglielmini [84]. For the $3\,mm$ tube diameter, the results are reported here. A further step was to install the instrumentation in a simplified tube bundle, comprised a single row of tubes, to verify the optical alignment of the laser components and the piezo-pressure capability. A schematic is given in Fig. (C.4). The two tubes were placed in a metallic box filled with distilled water, the air injectors were connected to the air system shown as B in figure Fig. (C.2). Two types of injectors were employed, as represented in Fig. (C.5).
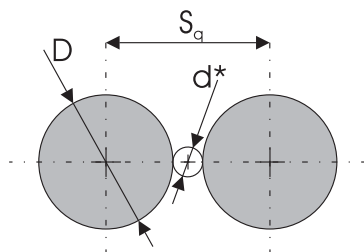

Figure C.3: Intertube spacing

D_i [mm]	D_o [mm]	L [mm]	L/D_i [−]
0.50	0.70	100	200
1.00	1.20	100	100
3.00	4.00	400	133
6.00	8.00	400	67

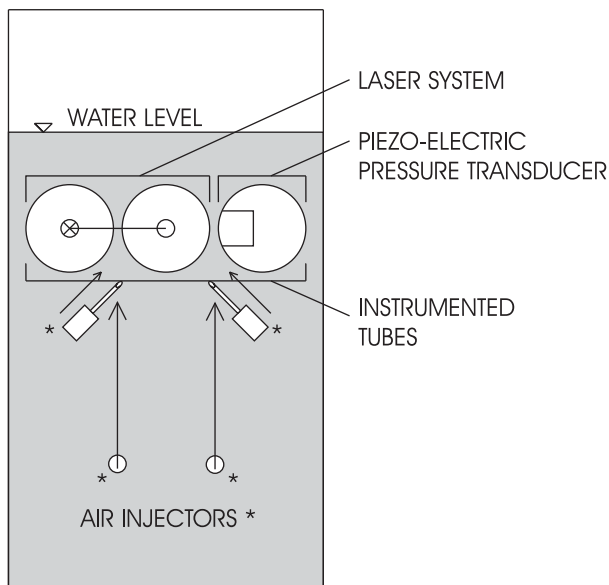Table C.2: Air-water, horizontal tubes tests
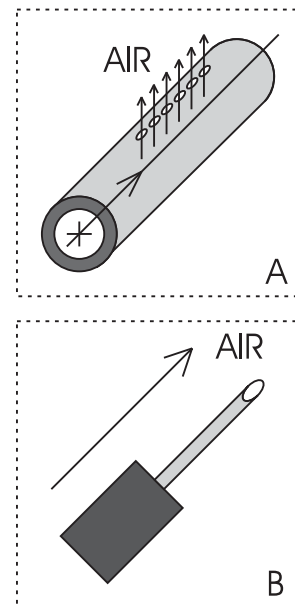
Figure C.4: Intertube spacing and setup

Figure C.5: Air injectors: A. Tube with holes; B. Tubular jet

C.2.1   Results

A few representative results for $D_i = 3\,mm$ are presented here. The five points plotted, see Fig. (C.6), on the Barnea map [86], are classified as follows:

⬦ *Bubbly flow*: The flowing water phase is continuous and contains bubbles of various sizes with diameters lower than the internal diameter Fig. (C.7).

⬦ *Intermittent*: Air bubbles are present with diameters comparable to the internal diameter. They assume an elongated shape. Bubbles are separated by water slugs. A thin film of water coats the tube wall Fig. (C.8).

⬦ *Slug*: Taking as reference the elongated flow regime, with increasing air velocity, the shape of the bubbles changes; starting at the tail and evolving to a more irregular bubble shape. Bubbles are separated by water bridges containing a dispersion of small bubbles Fig. (C.9).

⬦ *Churn*: Starting from slug flow with increasing water and air velocities, the air structures are broken down which leads to oscillatory motion of the water. The main phenomena are the instability of the bubbles near their trailing edges and periodical flooding waves Fig. (C.10).

⬦ *Annular*: This pattern is characteristic for low water velocity and high air velocity. The core of the tube will be occupied by air; a water film will cover the internal perimiter of the tube. Due to gravity, the thickness of the film is usually different between the bottom and top part of the tube Fig. (C.11).

The laser and the piezo-electric pressure transducer measurement were done at different axial locations. The two signals were normalized and plotted in the time domain with the shift determined by the cross correlation Fig. (C.12)- Fig. (C.16). Due to the computation of the cross correlation between the two signals, it was possible to determine the time shift of the two signals relative to the same gas structure. This appeared as a peak in the cross correlation plot Fig. (C.27). We could clearly identify a peak in the cross correlation of the laser signal and of the piezoelectric pressure signal for bubbly, intermittent, slug and churn flow.

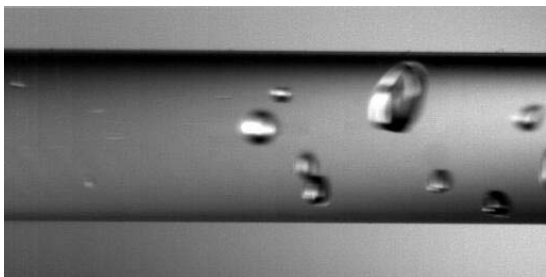| Regime	j_G [m/s]	j_L [m/s]
Bubbly	0.1965	3.9298
Intermittent	0.3930	0.3930
Slug	1.1789	1.9649
Churn	3.1438	1.3754
Annular	15.7190	0.2358

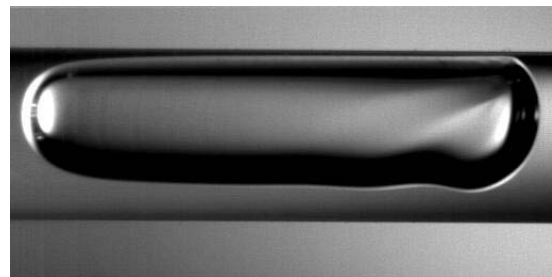Table C.3: Test conditions, $D_i = 3\,mm$
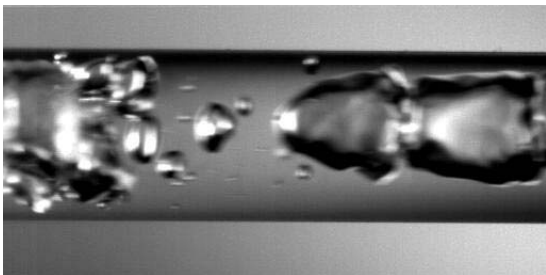

Figure C.7: Bubbly (B)

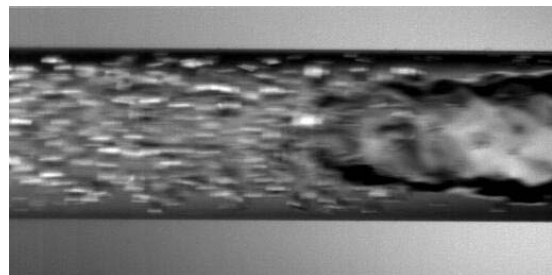Figure C.8: Intermittent (I)
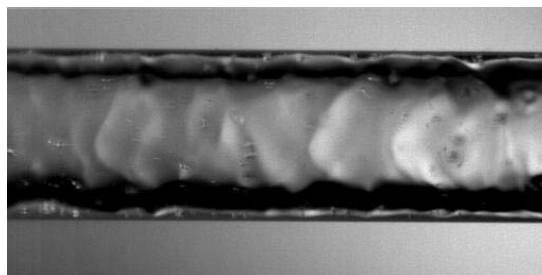

Figure C.9: Slug (S)

Figure C.10: Churn (C)
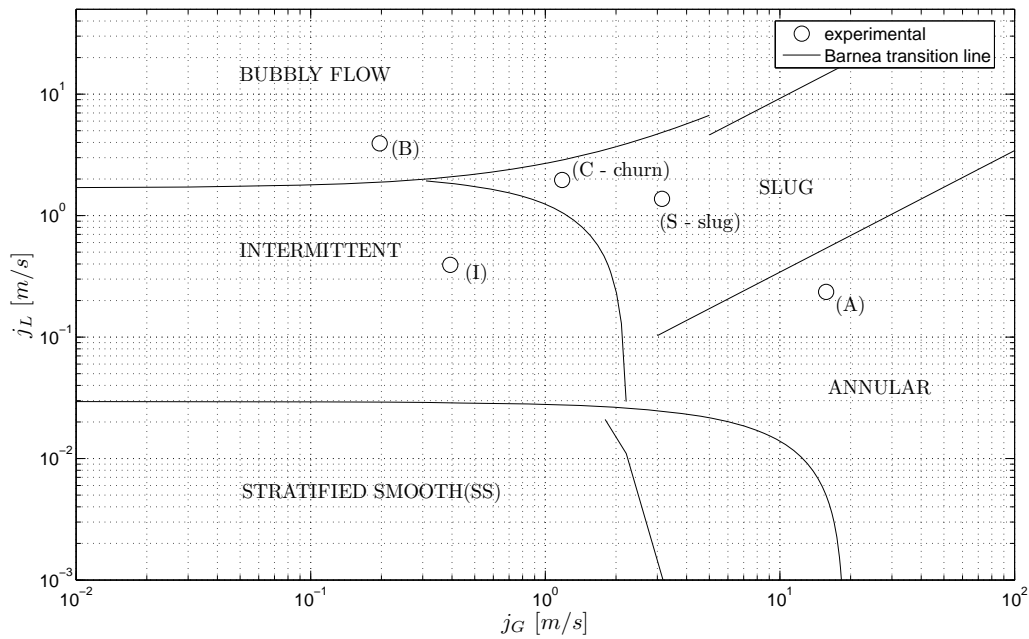

Figure C.11: Annular (A)

Figure C.6: Barnea map, $3\,mm$ tube

From the amplitude plot of the laser signal, the gas structure passage appears as sharp variations for bubbly, intermittent and slug flows. For intermittent and slug flows, directly from the analysis of the signal path, it is possible to underline a link between the laser signal and the pressure signal. This is present but less evident for bubbly and churn flows, where a single bubble is not passing but a family with different shapes, diameters and lengths. The plotted signals were normalized between 0 and 1. Concerning the laser diode system: a value close to 1 means gas phase whilst a value close to 0 implies the presence of the liquid phase. The frequency of acquisition was fixed to $f_{acq} = 10000\,Hz$ over a time of $1\,s$. The time scales change according to the flow regime: the signal abscissa representing time are modified accordingly.

In the state of the art review chapter, PDF analysis was underlined as a powerful tool to detect flow regimes. Considering the acquired signals, it was possible to assume a direct link between the void fraction and the laser signal. Analyzing the PDF plots shown in Fig. (C.17)- Fig. (C.21), we can see that the PDF is single peaked at a low normalized amplitude for bubbly flow, and double peaked for intermittent flow. The PDF peak amplitude at low void fraction decreases for slug flow until it disappears for churn and annular flows. These are characterized by a single peaked PDF at high void fraction whose intensity slightly decreases in amplitude for annular flow. These data match well with comparable data available in literature.

The analysis of the PDF of the pressure signal did not provide such clear results as for the photo-diode signal, see Fig. (C.22)- Fig. (C.26). Different distributions according to the flow regime were obtained. To give a full characterization, the Skewness and the Kurtosis were computed and reported in Table C.4.

To complete the signal analysis, the power spectrums of the signals for the different conditions were computed. For intermittent flow the power spectrums of the laser signals are reported in Fig. (C.28). Four different peaks are visible, the main one at a frequency of $\widetilde{f} = 23.8\,Hz$ represents the passage of the main gas structures.
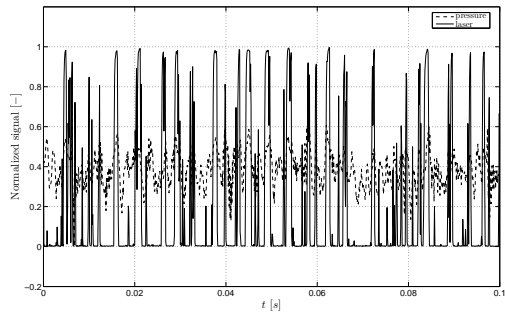
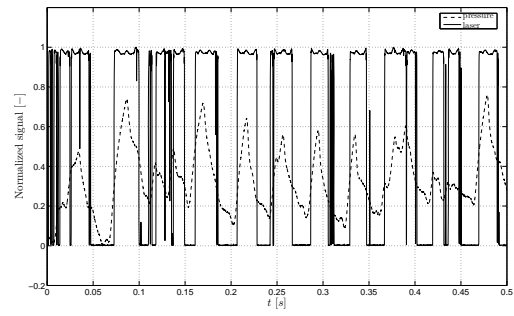Figure C.12: Bubbly (B), Normalized signal

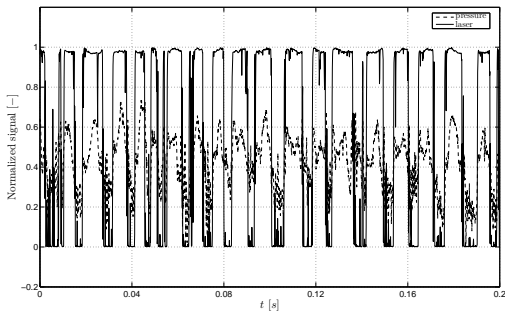Figure C.13: Intermittent (I), Normalized signal
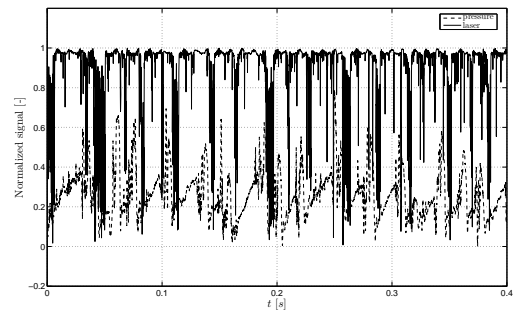

Figure C.14: Slug (S), Normalized signal

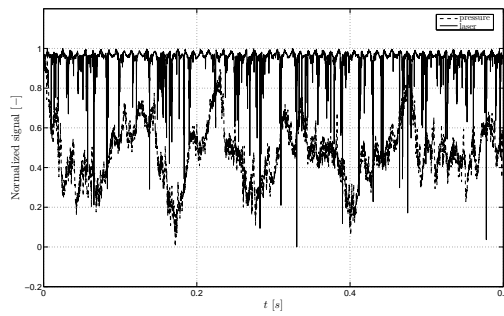Figure C.15: Churn (C), Normalized signal

Figure C.16: Annular (A), Normalized signal
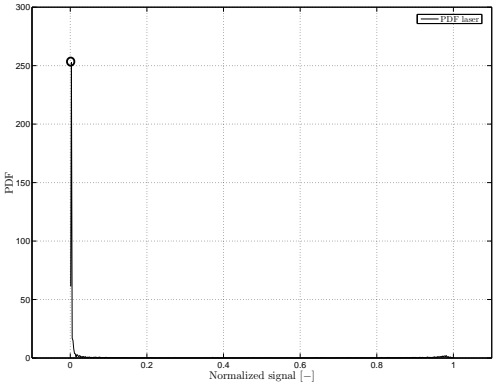
Figure C.17: Bubbly (B), PDF laser signal
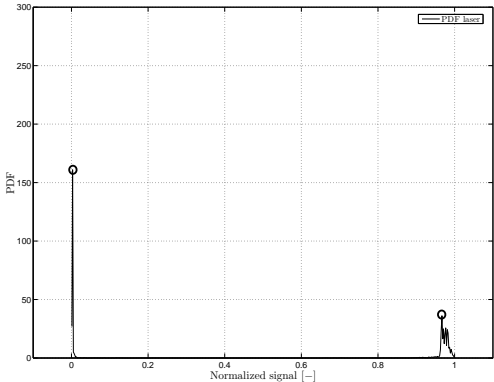
Figure C.18: Intermittent (I), PDF laser signal
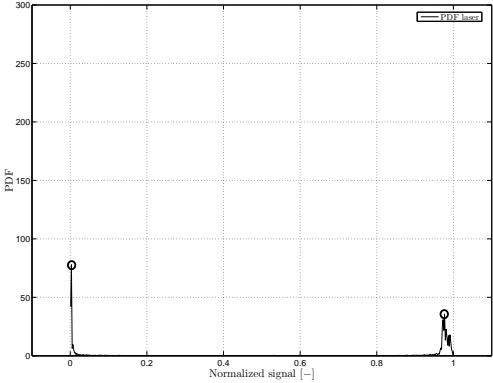
Figure C.19: Slug (S), PDF laser signal
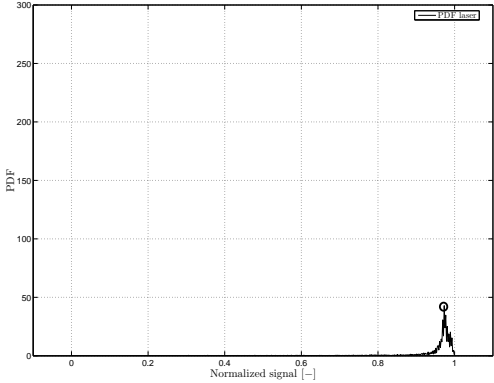
Figure C.20: Churn (C), PDF laser signal
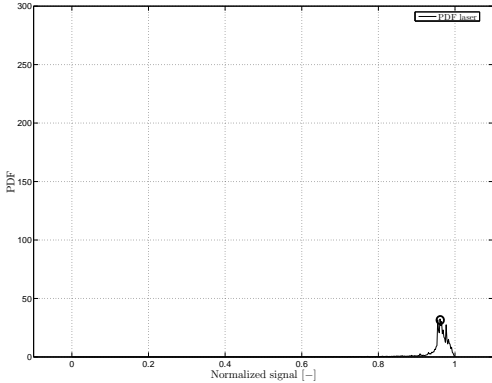
Figure C.21: Annular (A), PDF laser signal
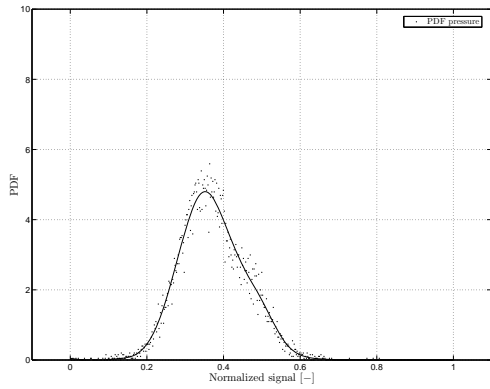
Figure C.22: Bubbly (B), PDF pressure signal
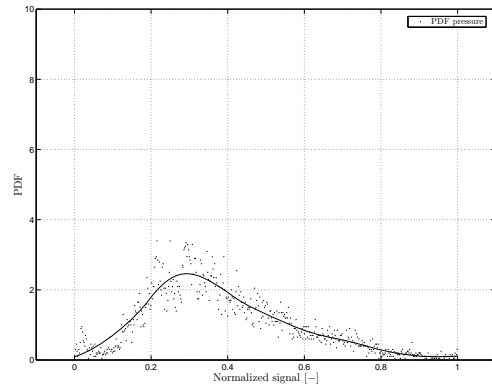
Figure C.23: Intermittent (I), PDF pressure signal
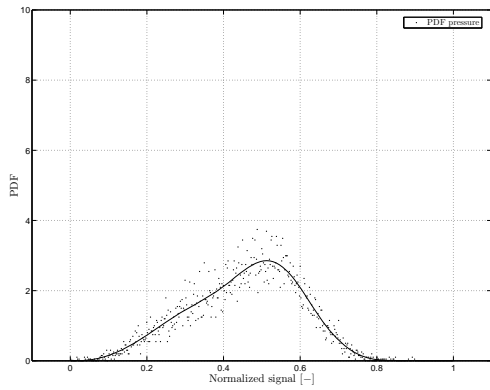
Figure C.24: Slug (S), PDF pressure signal
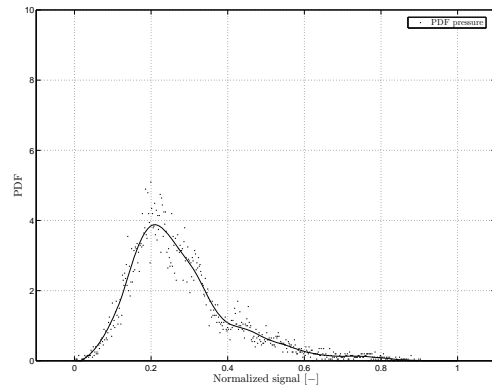
Figure C.25: Churn (C), PDF pressure signal
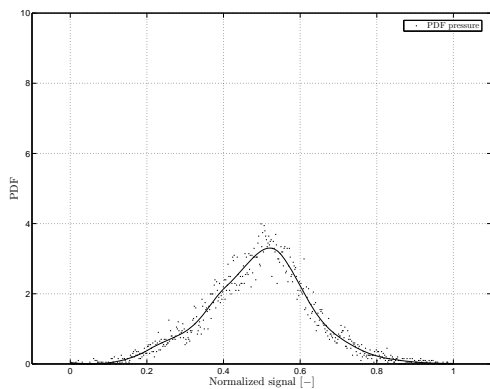
Figure C.26: Annular (A), PDF pressure signal

Regime	Skewness	Kurtosis
Bubbly	0.2325	0.5030
Intermittent	0.6437	0.1557
Slug	−0.2787	−0.3799
Churn	1.2354	1.9059
Annular	−0.0281	0.3045

Table C.4: Skewness and Kurtosis of the PDF pressure signal

Alter demonstrating the quality of the instrumentation and its capability in identifying the flow patterns for air-water flows, the next step was to implement the same system in the tube bundle. In passing to a bundle configuration with refrigerant, it was necessary to design a proper system for the installation of the laser photodiode, the piezo-electric pressure transducer and the flow visualization system. Once the design was completed, the instrumentation was re-tested in bundle conditions to verify the correct alignment of the laser; two different piezo-electric pressure transducer installations were tested, allowing the selection of the most suitable one.
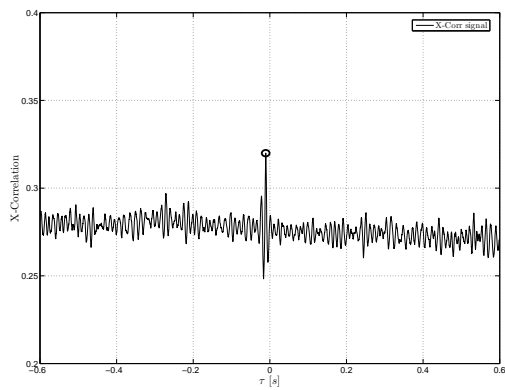
Figure C.27: Slug (S), Cross-Correlation laser-pressure ($\widetilde{\tau} = -0.0106$ $[s]$)
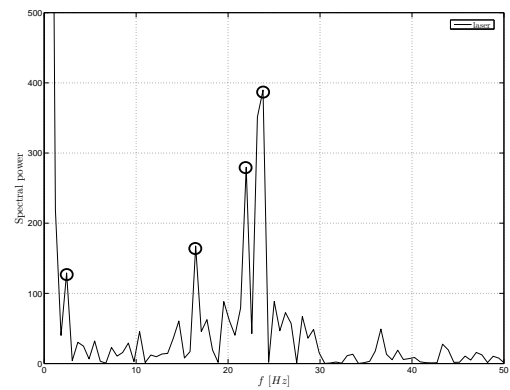
Figure C.28: Bubbly (B), Spectral density

C.3 Light transmission: reflection

The lighting and camera system were tested to obtain high quality flow visualizations. Big effort was put into the design of the system to obtain a uniform distribution of the background light. This section is dedicated to the design of reflection free lighting system that carries light along the tube axis. As described by Lion and Renotte [81], based on the earlier work of Cohen and Potts [80]: if a point source of coherent light is observed through a cylindrical tube with reflective inner walls, a series of definite light rings can be observed. These rings are caused by multiple reflections of the incident beam on the inner walls.

The present system was composed of a cold light source and an optical fiber. The optical fiber was necessary to bring light from the source to an elliptical mirror installed inside a copper tube at a distance of $500\,mm$ from its entrance, refer to chapter 4 for more details. The optical fiber reduces the physical distance between source and mirror. The adopted scheme reduces the number of reflections but does not ensure a free-reflection system. In Fig. (C.29) a schematic, as in Lion and Renotte [81], is given.
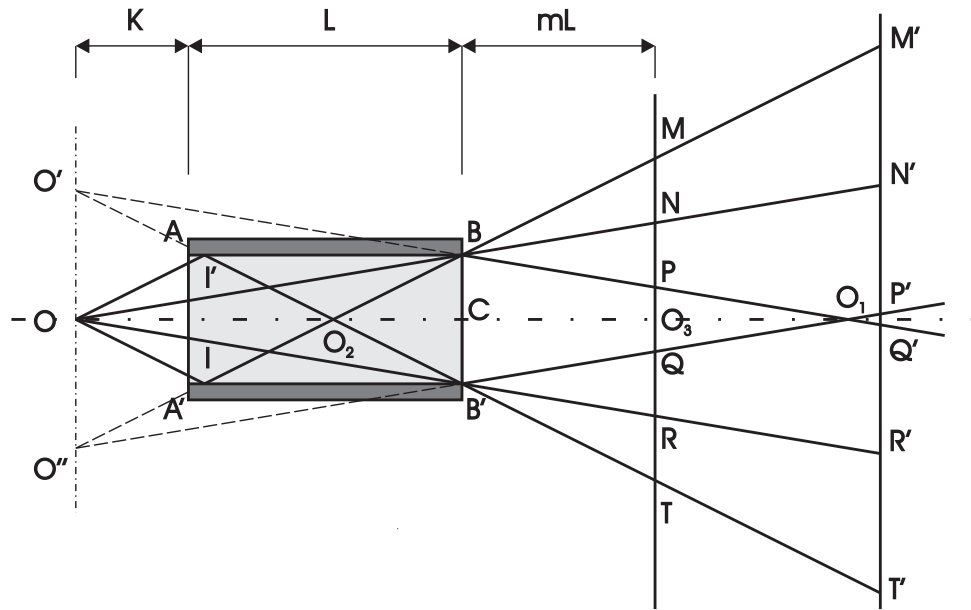
Figure C.29: In-tube reflection phenomena

For a simple explanation of the phenomenon a point source is considered, however in reality we have to deal with an illuminating area source. The geometry is a cross section of a tube of internal diameter D_i and length L. The light source is positioned at a distance K from the tube front, and the screen at a distance mL from the end of the tube itself. It is interesting to note that if the source of light is incoherent, the beams reaching the screen S directly, without reflection, will form a circle of diameter $\widetilde{D}_{NR}$:

$$\widetilde{D}_{NR} = D\left(1 + \frac{mL}{K+L}\right) \tag{C.7}$$

After reflection, the light beams form a cone whose vertex is at O_2 on the axis of the tube at a distance $\overline{OO_2} = 2(K+L)/3$; on the screen S, this will yield an illuminated area of diameter $\widetilde{D}_{MT}$:

$$\widetilde{D}_{MT} = D\left(1 + \frac{3mL}{K+L}\right) \tag{C.8}$$

The beams reflecting at B and B', intercept in O_1, $\overline{OO_1} = 2(K + L)$, will form a circle on the screen S of diameter $\widetilde{D}_{PQ}$

$$\widetilde{D}_{PQ} = D \left(1 - \frac{mL}{K + L} \right) \tag{C.9}$$

As visible in Fig. (C.29), the pattern will change according to the position of the screen S and its relative position from the source O. It is interesting to note that the number of possible reflections in the tube is given by:

$$N = int \left(1 + \frac{L}{2K} \right) \tag{C.10}$$

The reflection issue represented an obstacle to the successful illumination of the measurement volume. An experimental set-up was installed to verify the feasible solutions to this issue as reported in Fig. (C.30). The source light is coming from the optical fiber and is represented as a point source for simplicity.
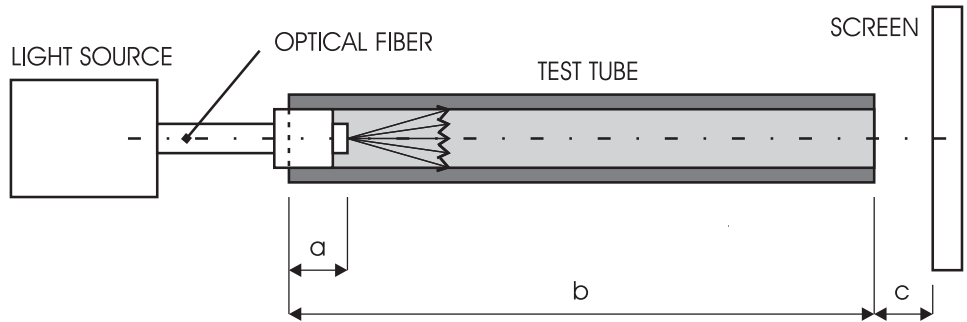
Figure C.30: Light reflection: test stand layout(a=40 mm; b=500 mm; c=60 mm)

The reflection issue for a non-treated tube is depicted in Fig. (C.31). Analyzing the picture relative to the reflection in a plain tube and post processing it, Fig. (C.32) is obtained. From the obtained results, the pattern described in Fig. (C.29) is easily identifiable.

The requirement was to design a system that avoided reflections without a reduction of the internal diameter of the tube. A first solution to the reflection issue was to wrap the internal diameter with black paper. This solution appeared to be optimal in terms of uniformity of the light but not applicable: since, in the main facility, the tube is installed such that the external part is in contact with refrigerant at a temperature lower than the atmospheric one and the internal part is in contact with air at atmospheric conditions, thus leading to condensation and deterioration of the "anti-reflecting" paper.

A normal black paint treatment and a black chrome surface treatment were tested as shown in Fig. (C.33) and Fig. (C.34) without solving the problem. The only solution was to increase the surface roughness in such a way as to trap the reflected light. Therefore, an internally enhanced tube Fig. (C.36) was employed. This resulted in a completely reflection-free system Fig. (C.35), and so provided an optimal solution to our problem.
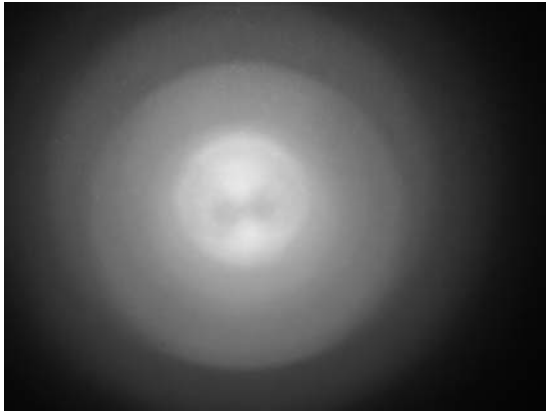
Figure C.31: Plain copper tube

Figure C.32: Reflection pattern identification, plain tube

Figure C.33: Black painted surface
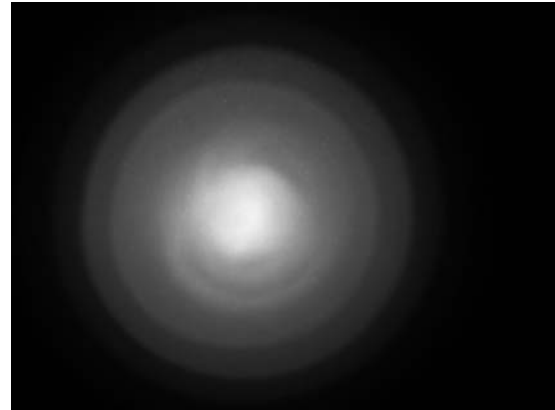
Figure C.34: Black chrome surface treatment

Figure C.35: Enhanced tube structure

Figure C.36: Enhanced surface

Appendix D

Flow visualization data

In this appendix the visualization data for R236fa at T_{sat}=5, 15 °C and for R134a at T_{sat}=5, 10, 15 °C will be presented.
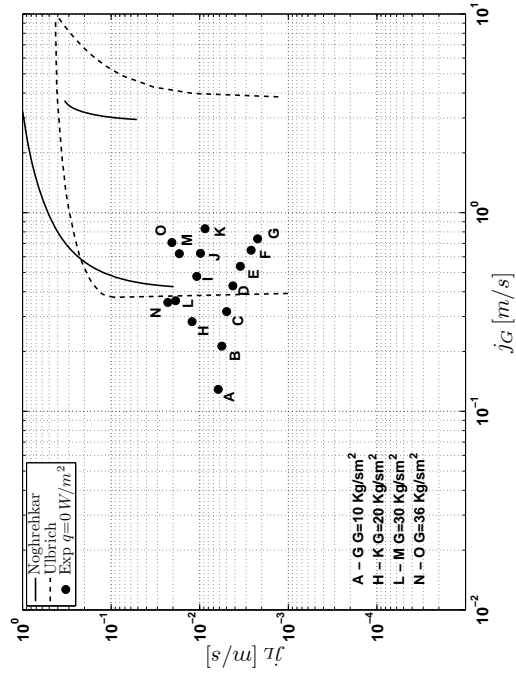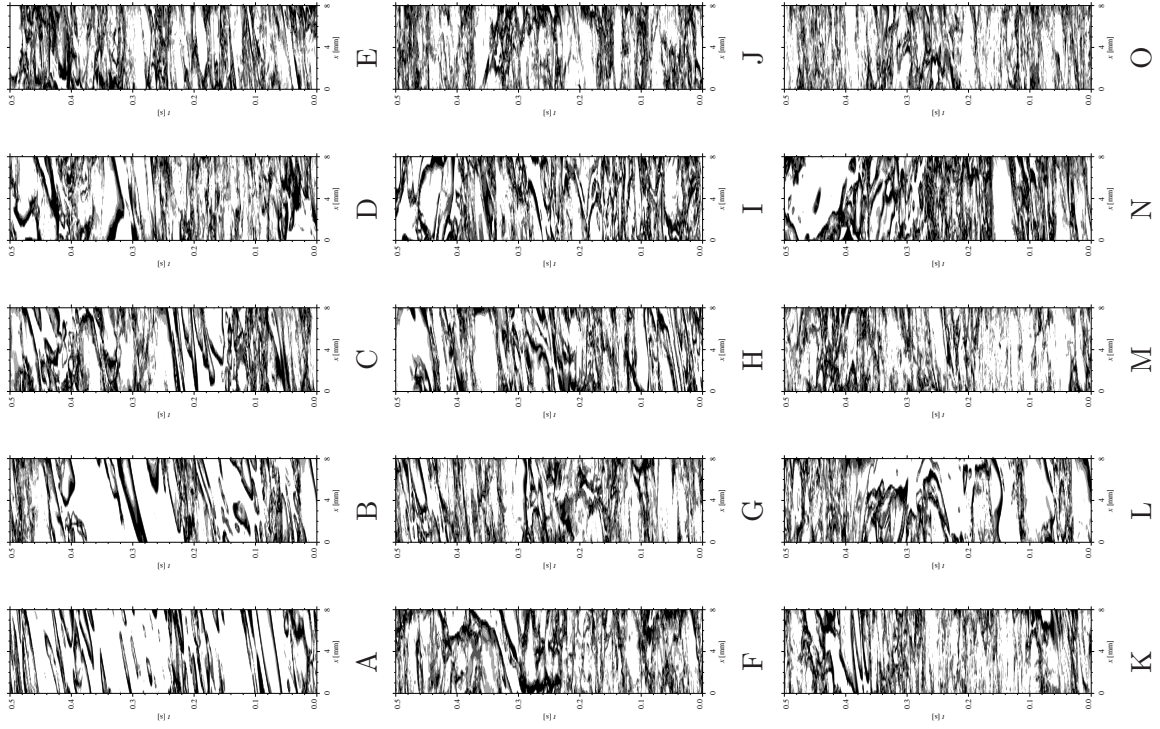
Figure D.1: Flow visualization, adiabatic R236fa, T_{sat}=5 °C
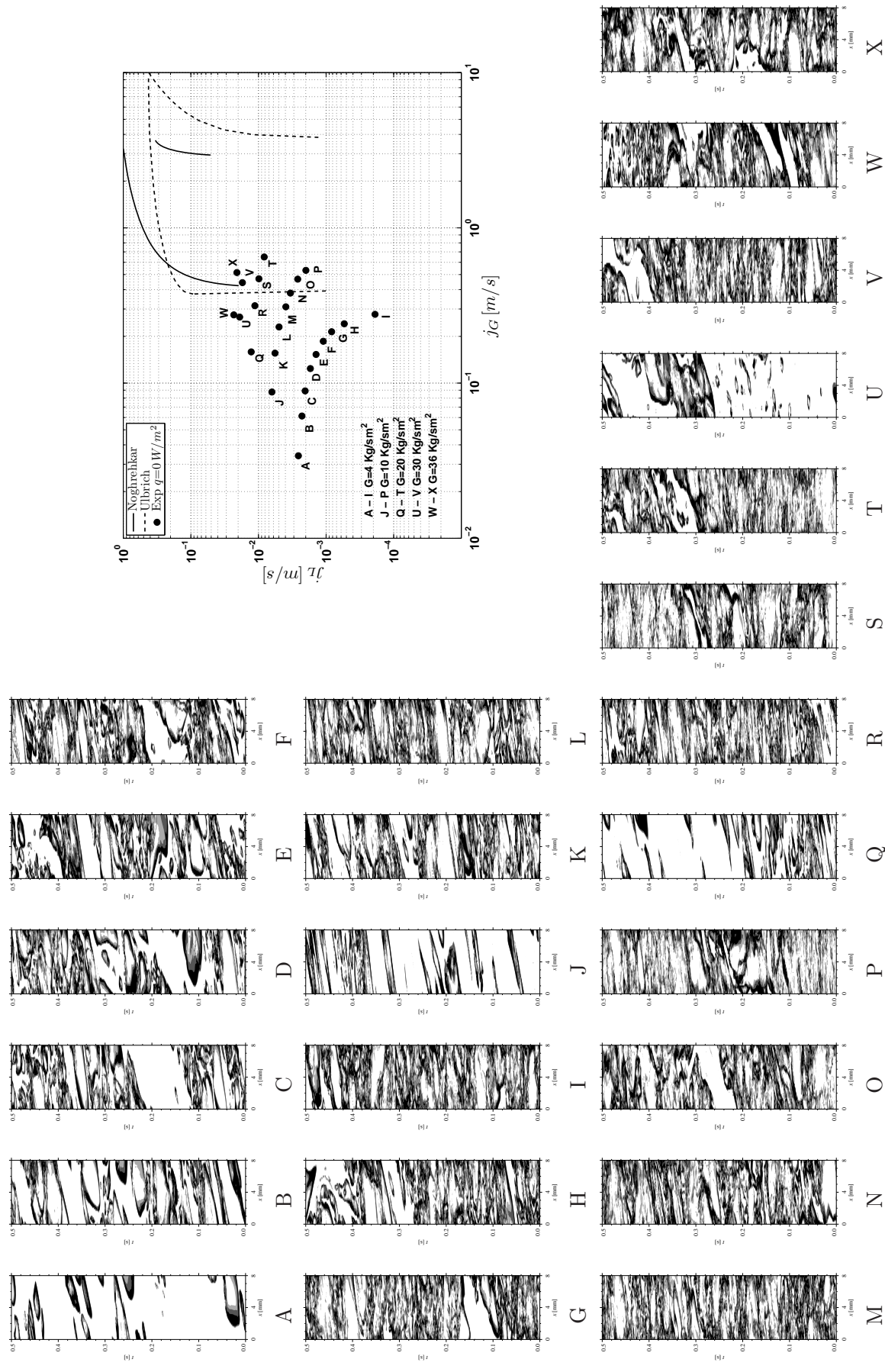
Figure D.2: Flow visualization, adiabatic R236fa, T_{sat}=15 °C
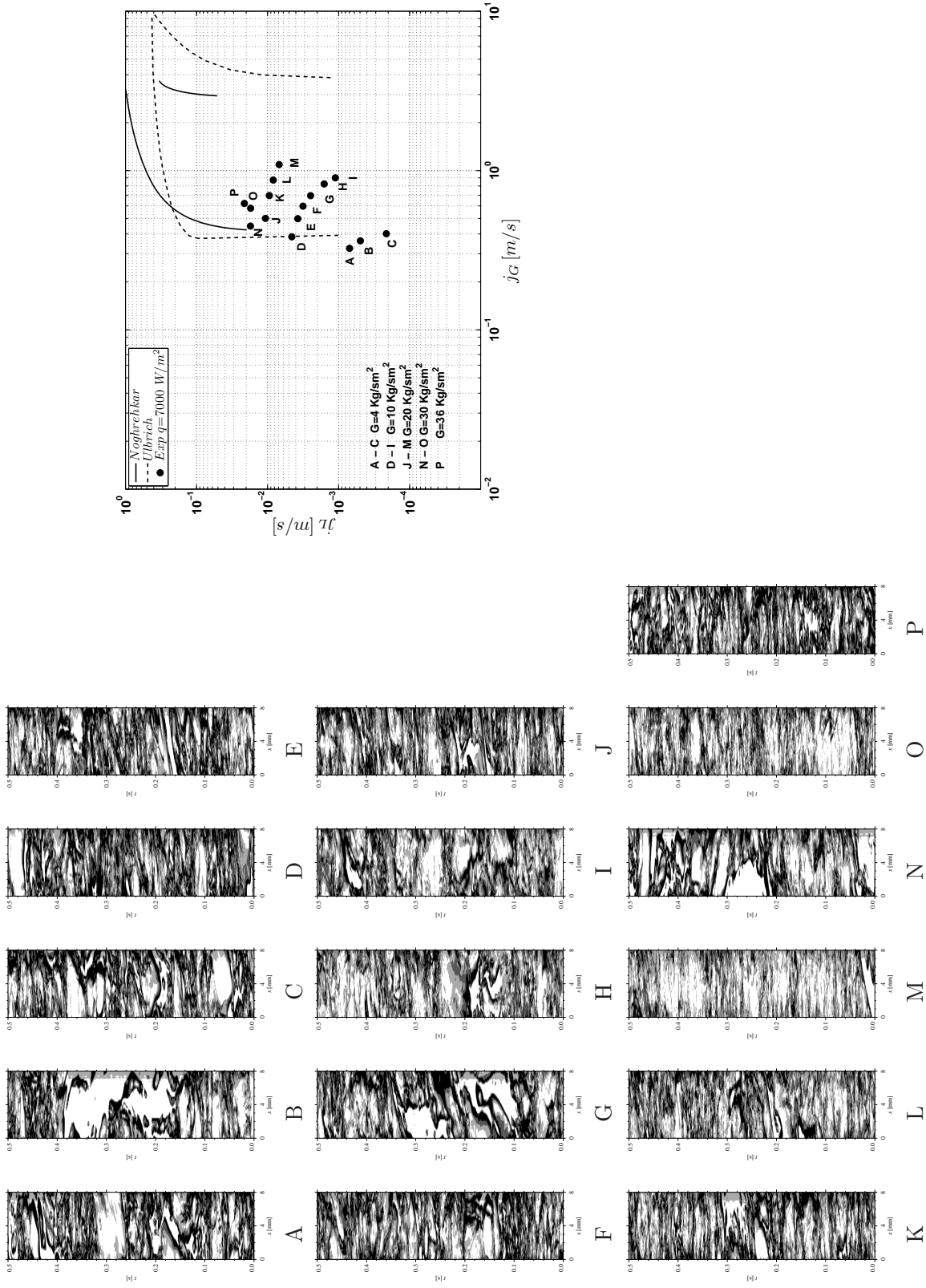
Figure D.3: Flow visualization, $q=7000\,[W/m^2]$, R236fa, $T_{sat}=5\,°C$
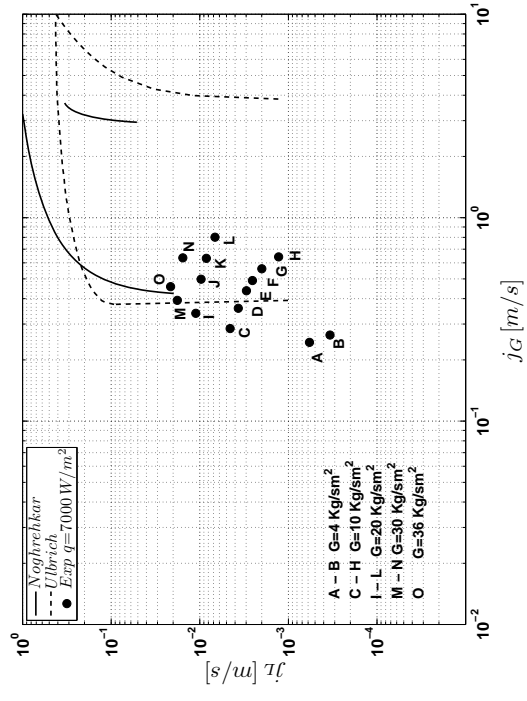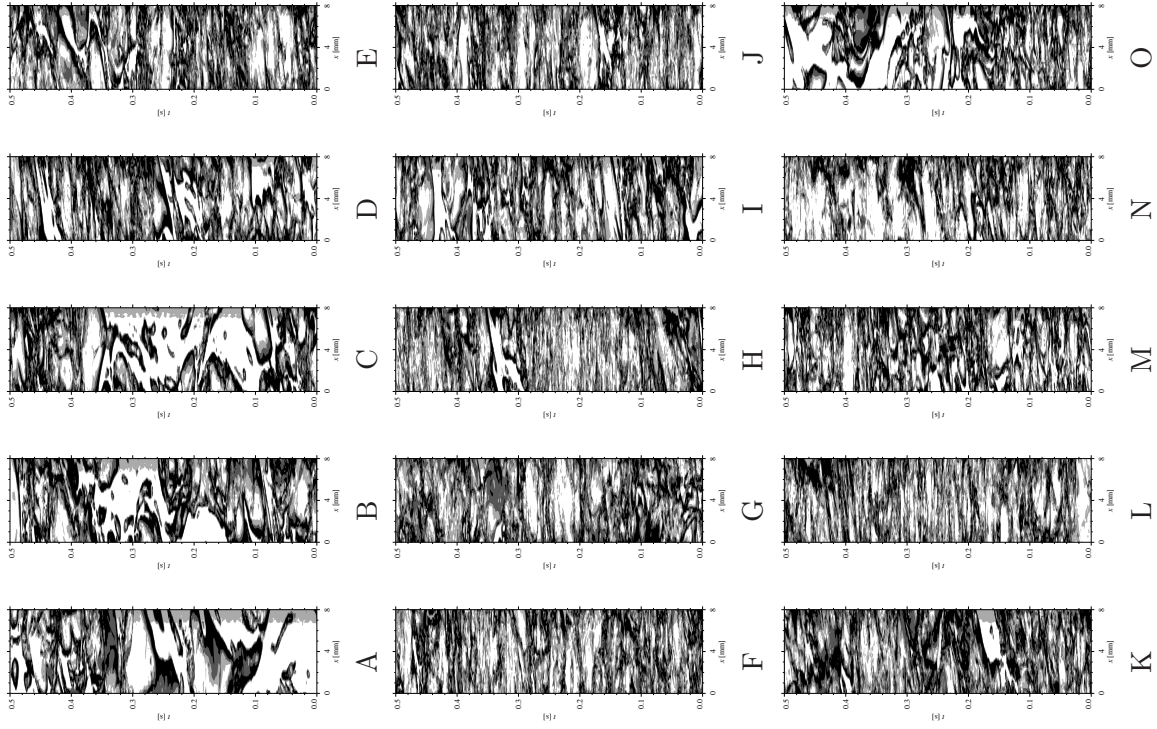
Figure D.4: Flow visualization, q=7000 $[W/m^2]$, R236fa, T_{sat}=15 °C
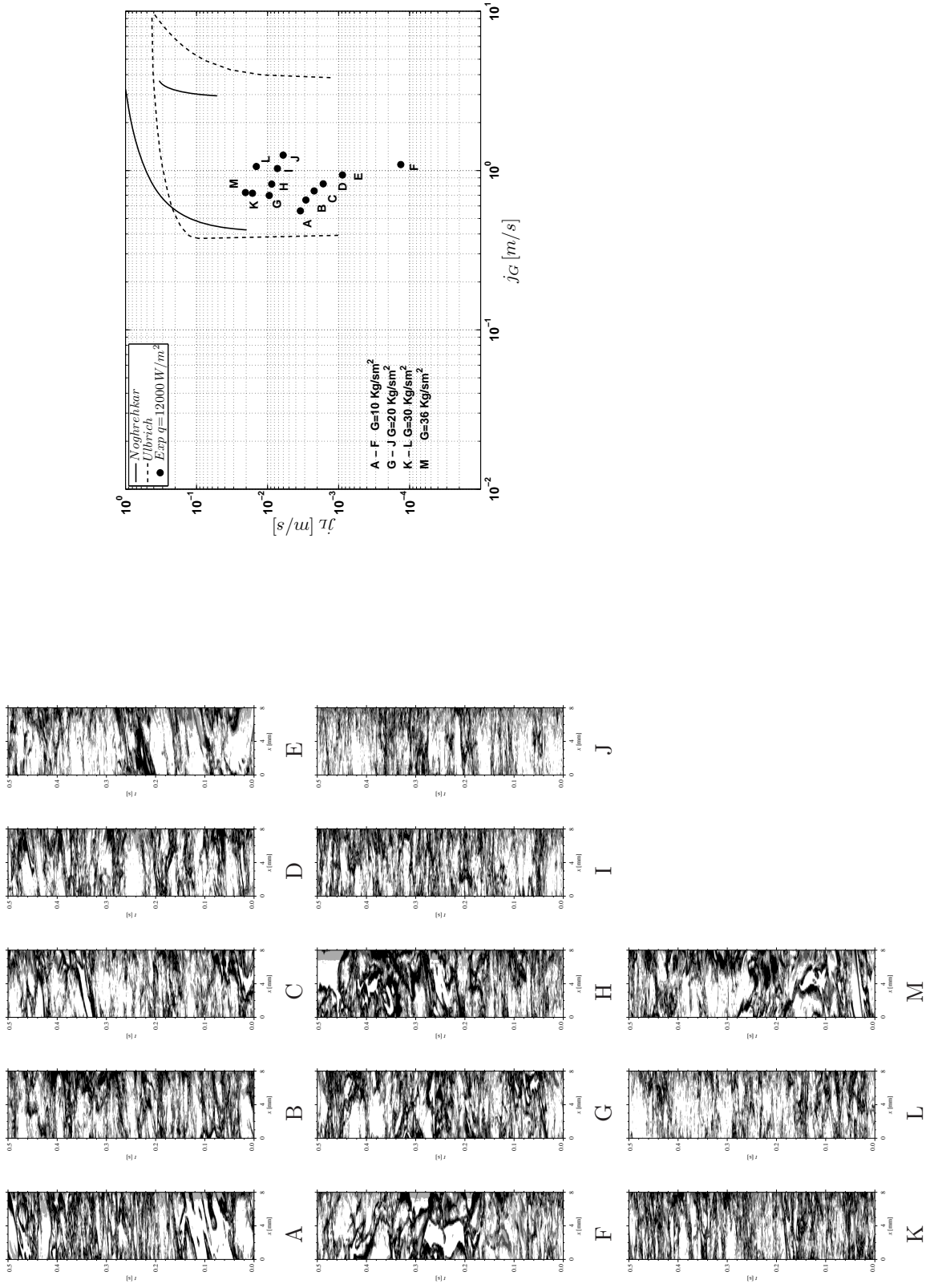
Figure D.5: Flow visualization, $q=12000\,[W/m^2]$, R236fa, $T_{sat}=5\,°C$
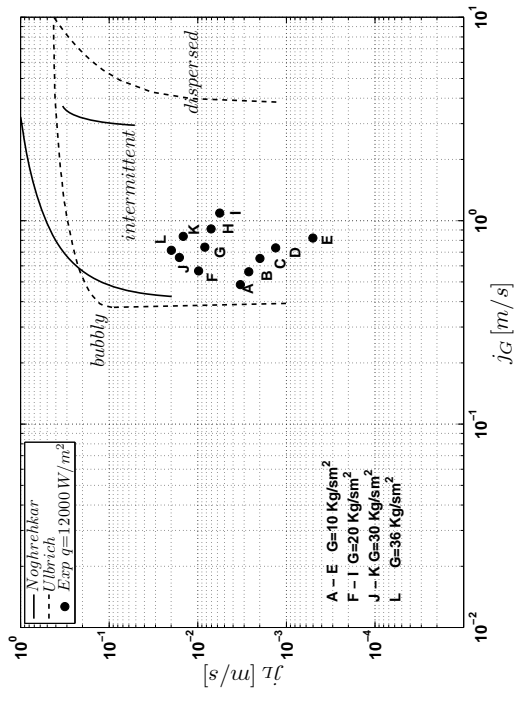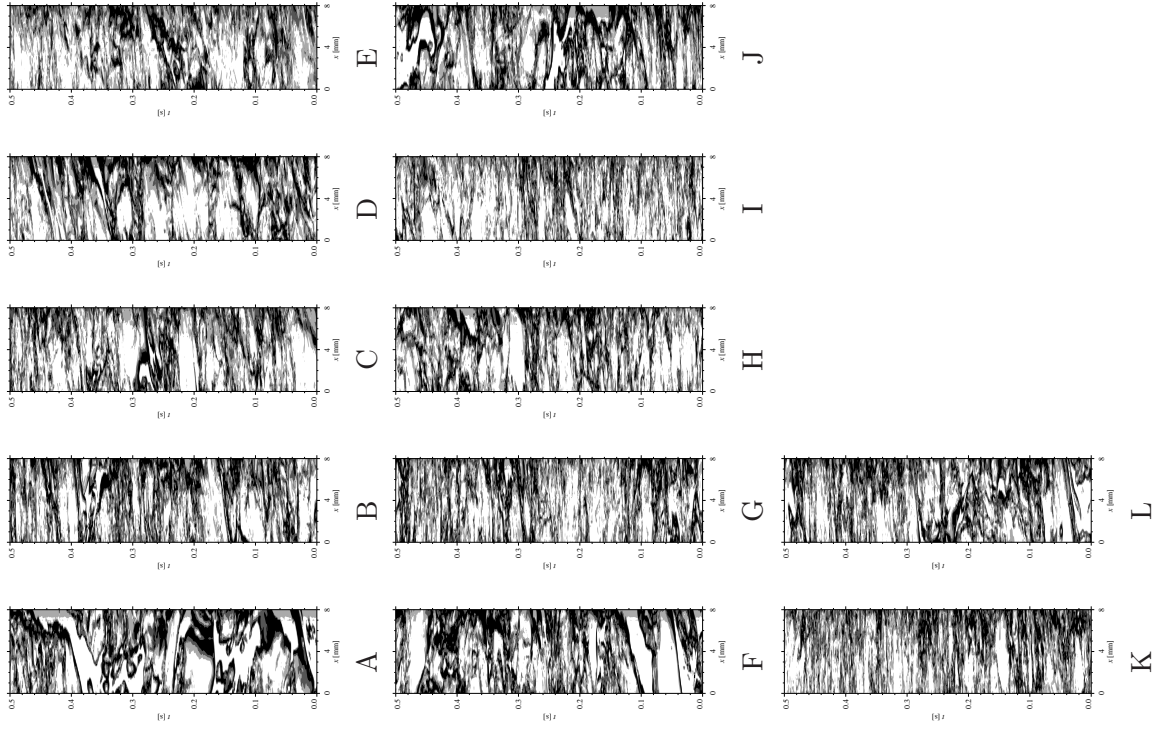
Figure D.6: Flow visualization, q=12000 $[W/m^2]$, R236fa, T_{sat}=10 °C
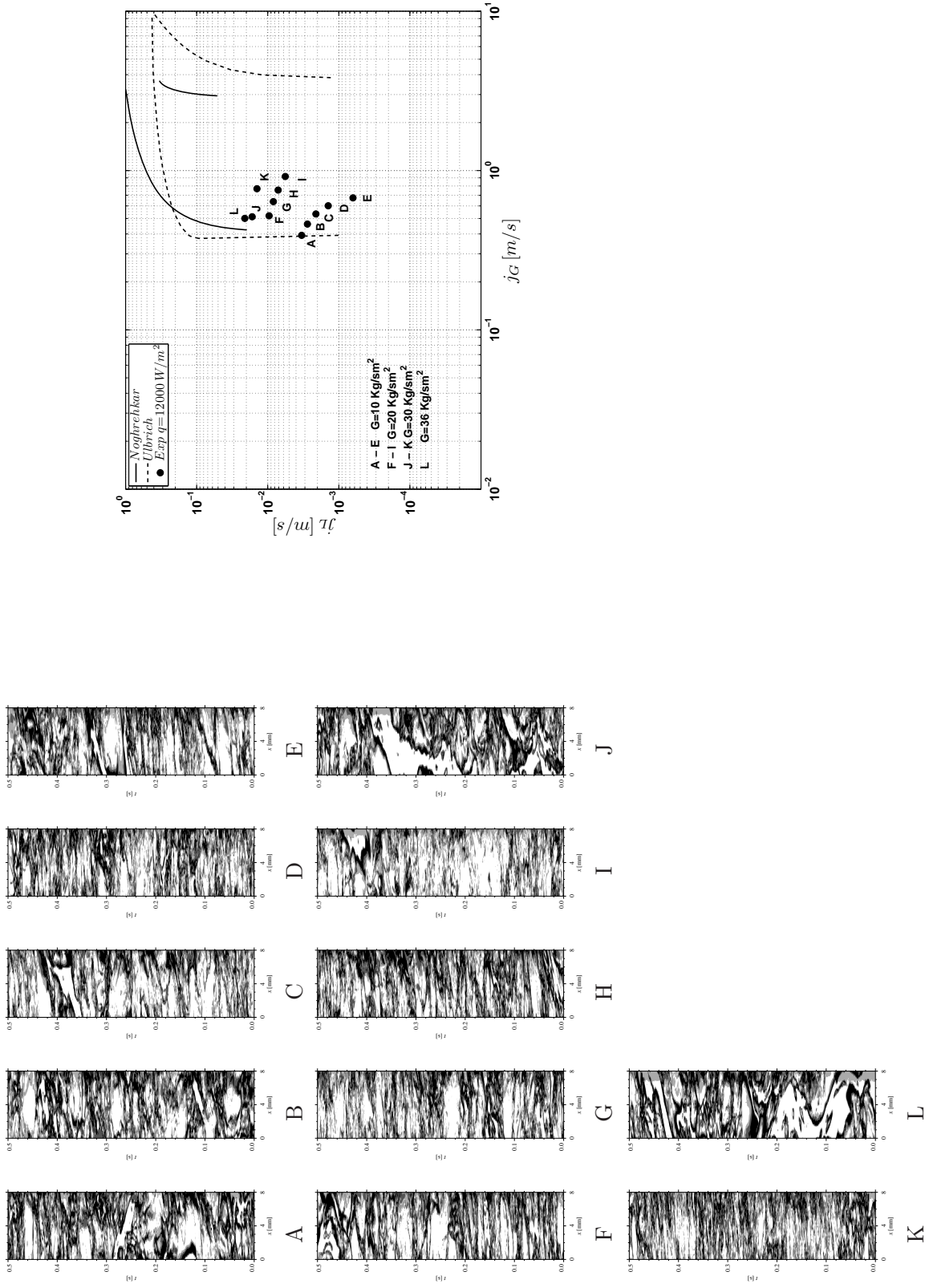
Figure D.7: Flow visualization, q=12000 $[W/m^2]$, R236fa, T_{sat}=10 °C
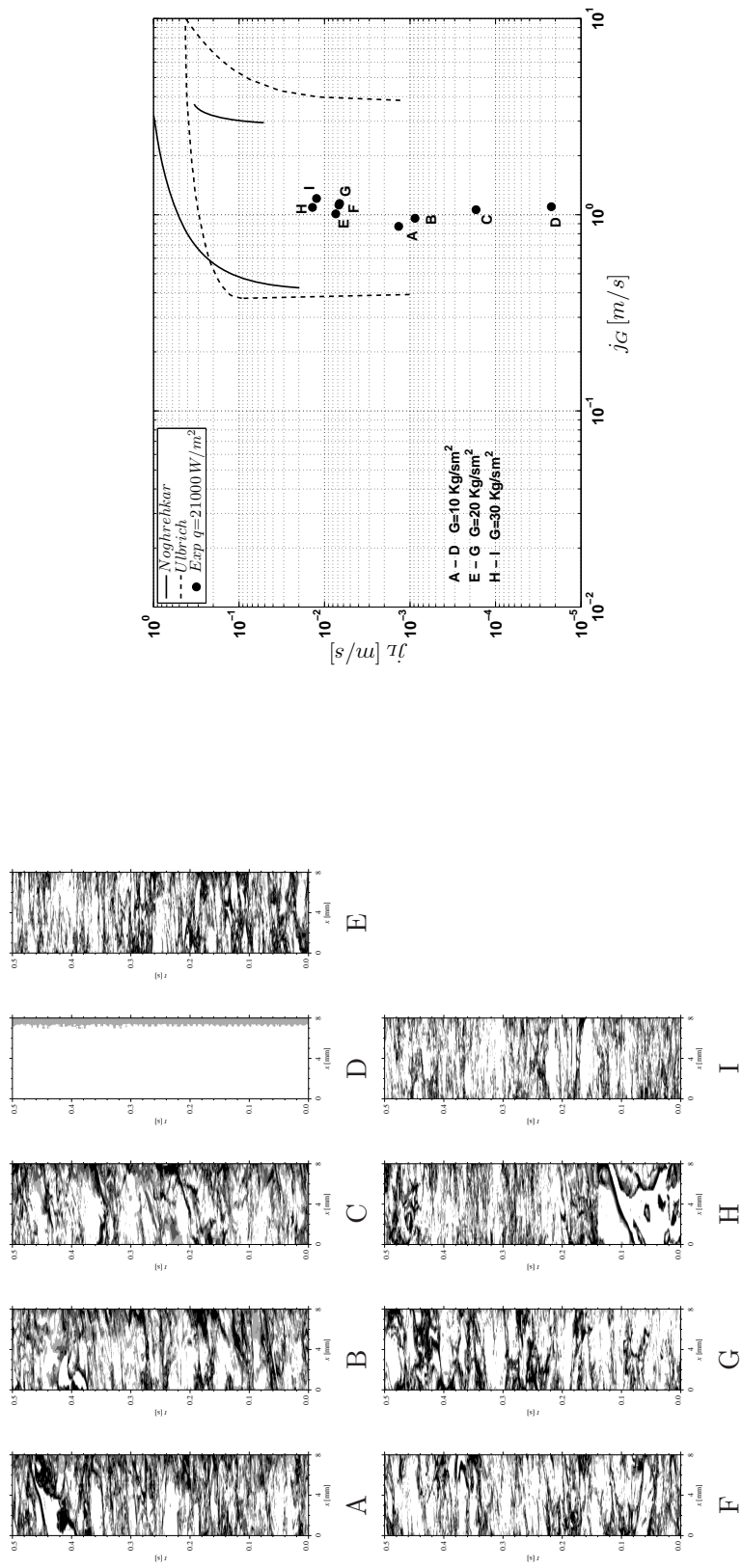
Figure D.8: Flow visualization, $q=21000\,[W/m^2]$, R236fa, $T_{sat}=5\,^{\circ}\mathrm{C}$
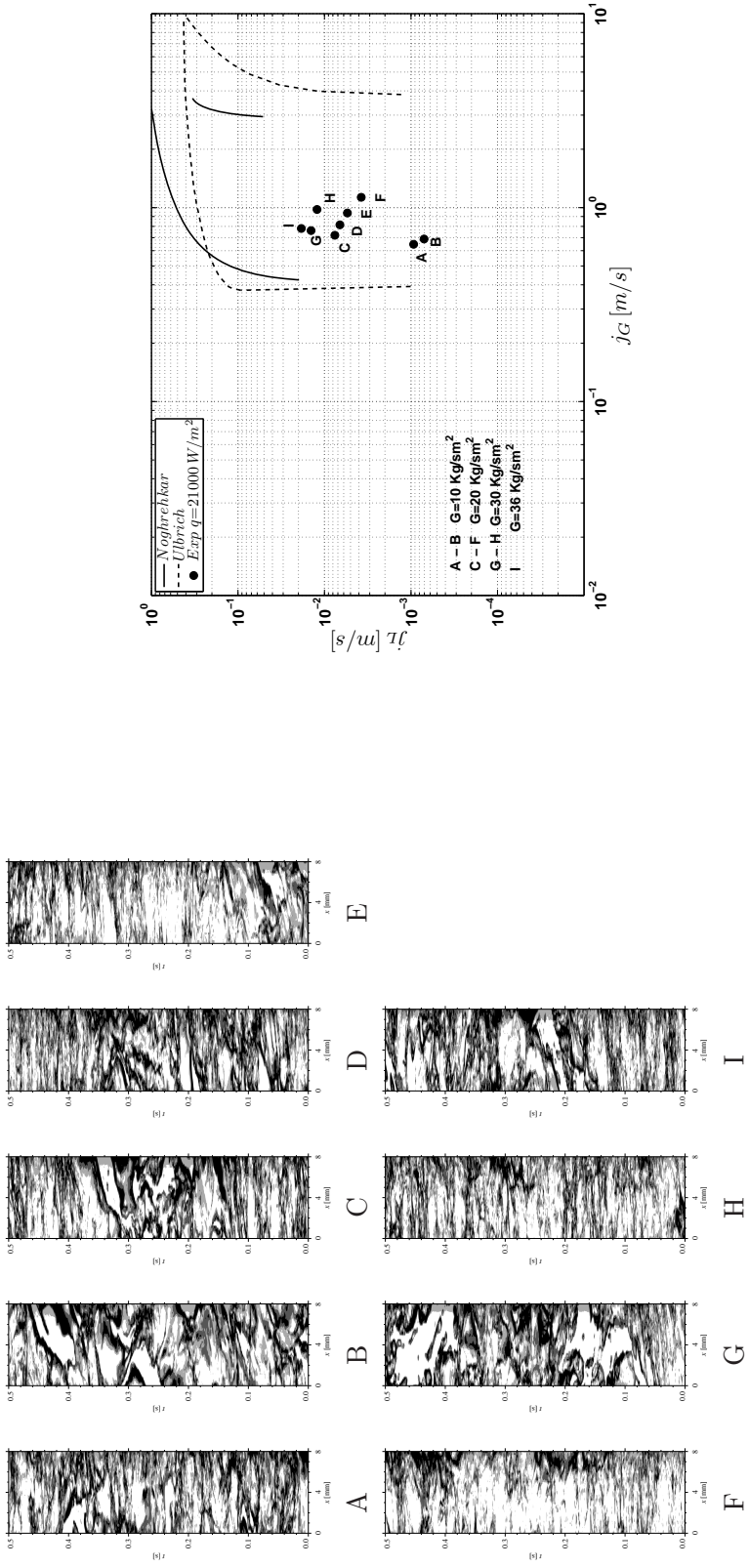
Figure D.9: Flow visualization, q=21000 [W/m^2], R236fa, T_{sat}=15 °C
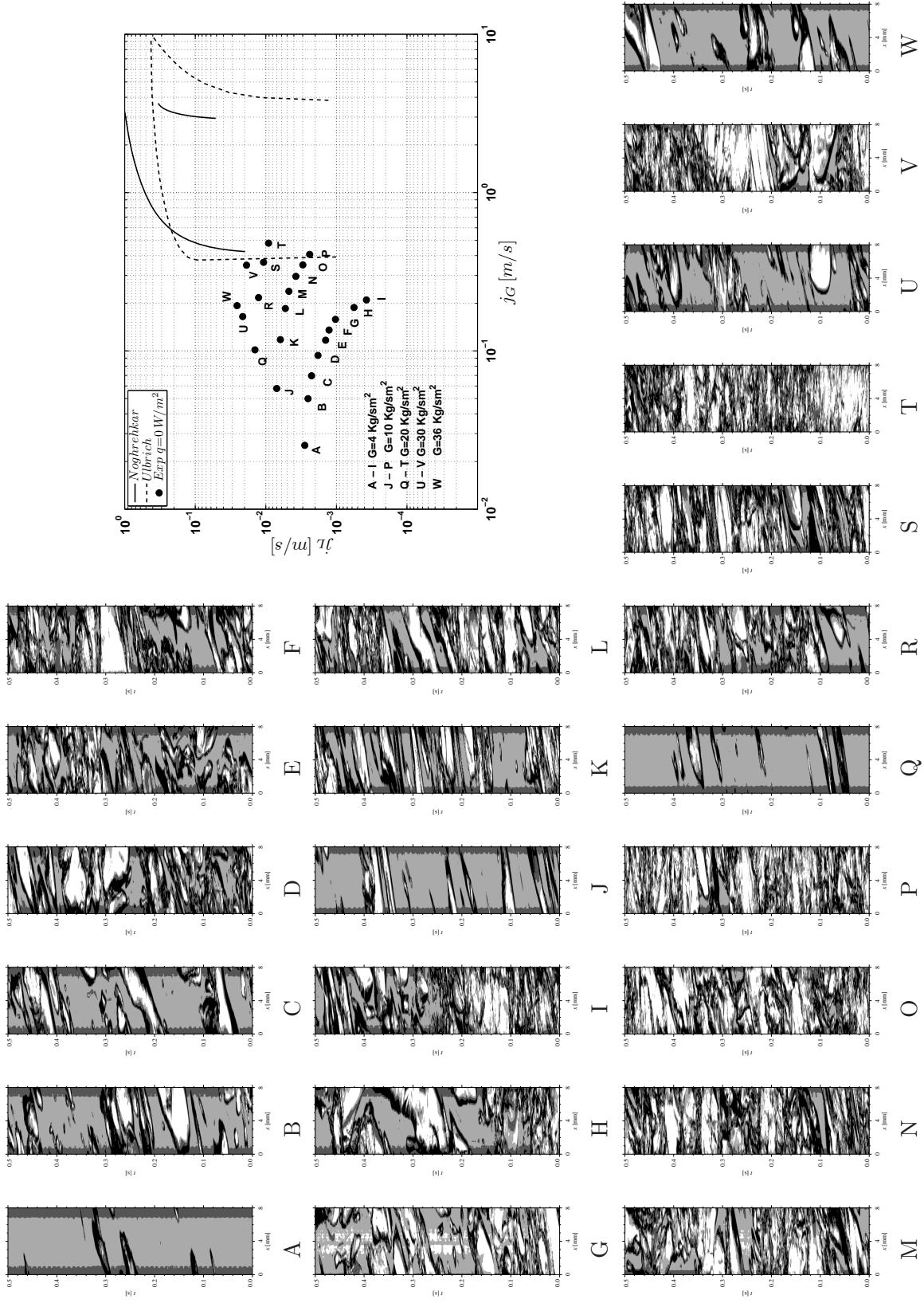
Figure D.10: Flow visualization, adiabatic R134a, T_{sat}=5 °C
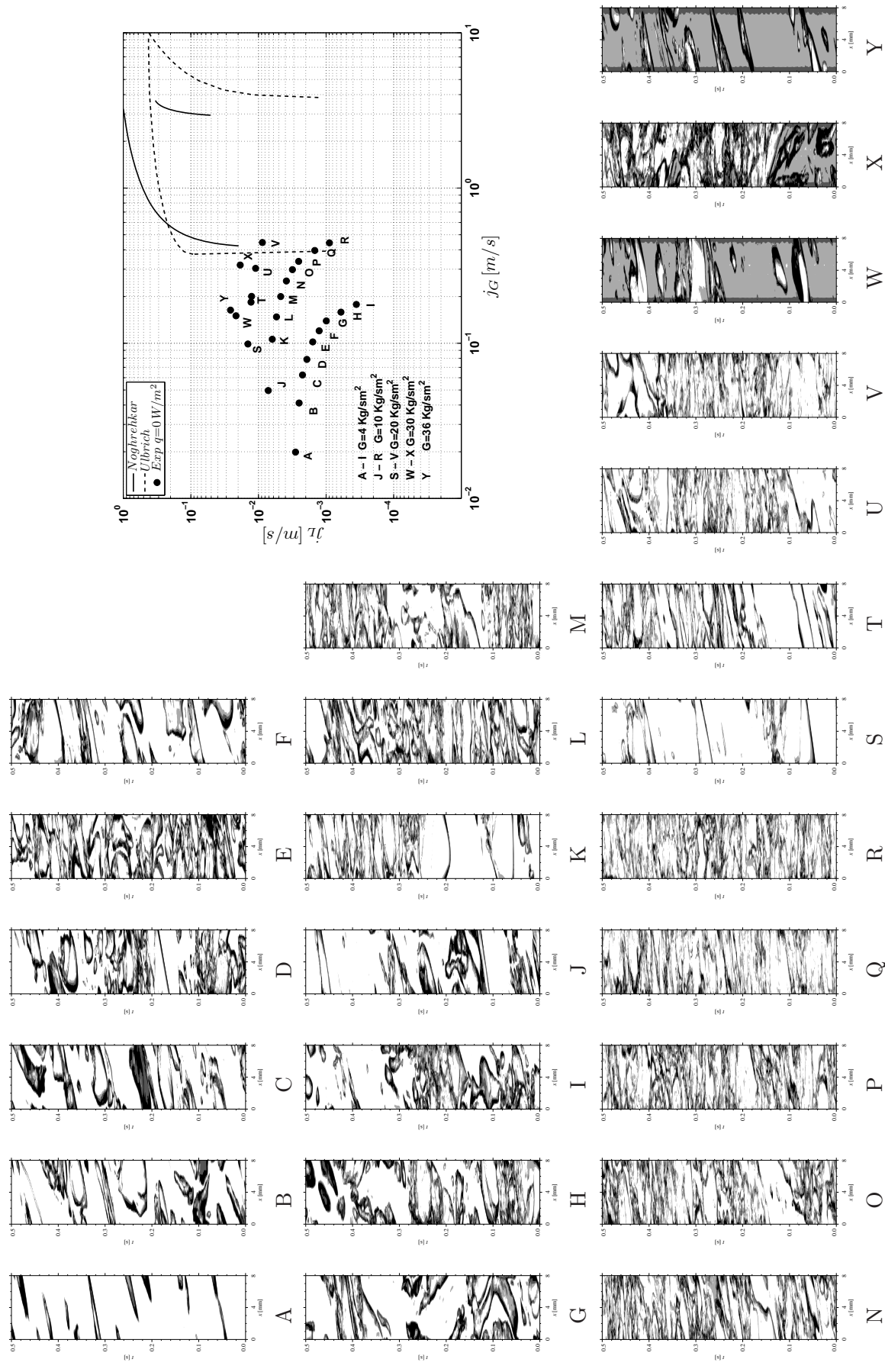
Figure D.11: Flow visualization, adiabatic R134a, T_{sat}=10 °C
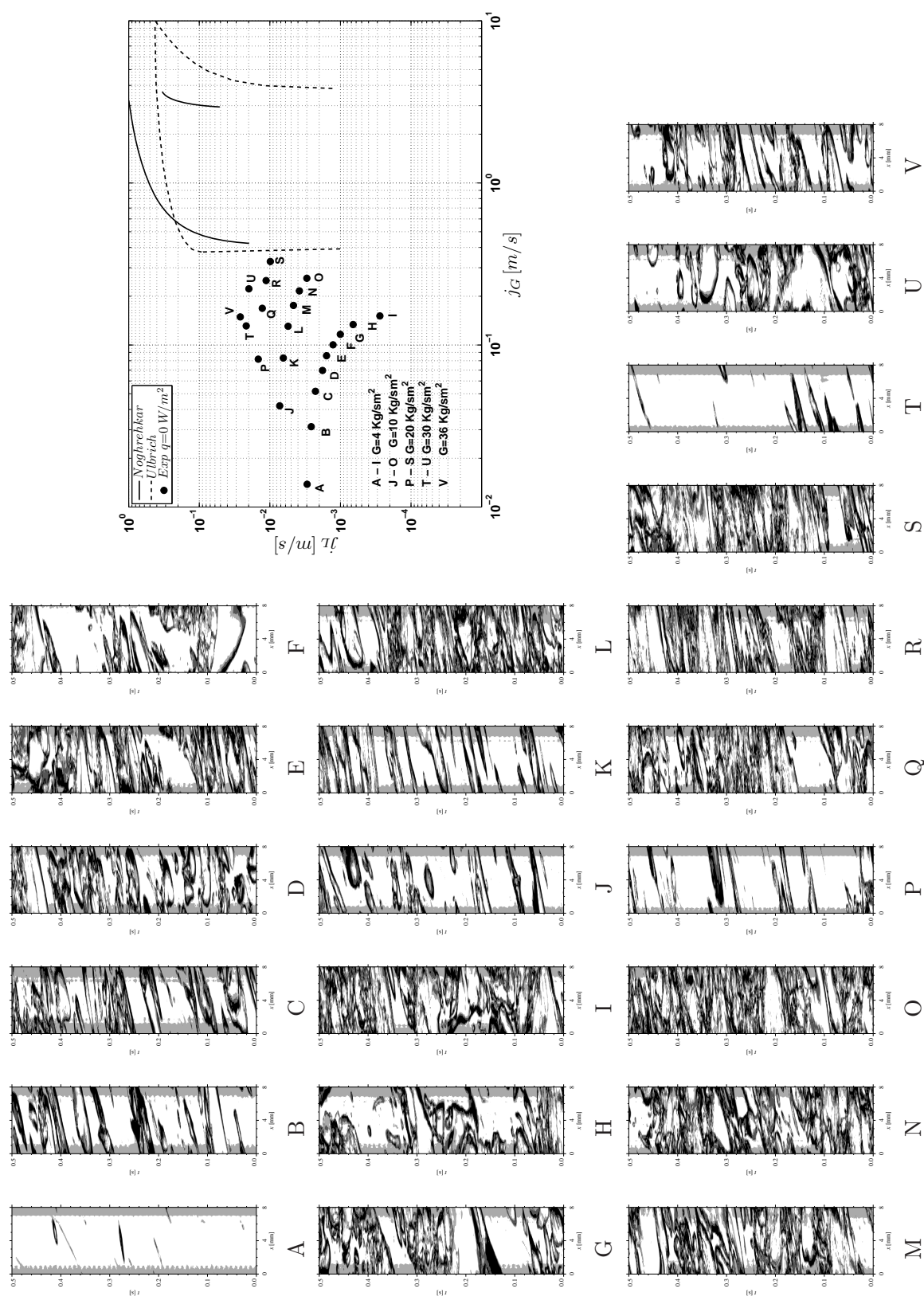
Figure D.12: Flow visualization, adiabatic R134a, T_{sat}=15 °C
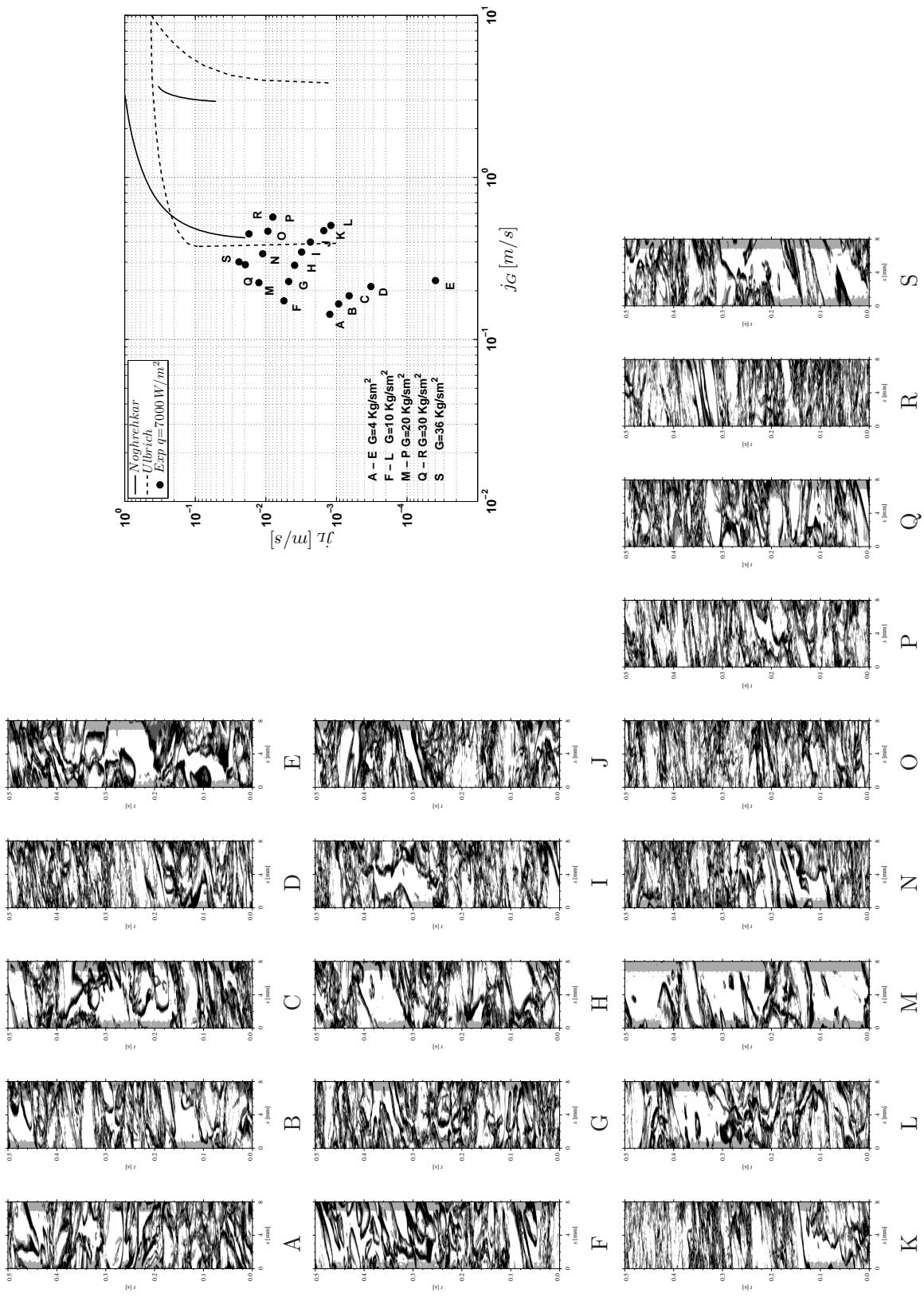
Figure D.13: Flow visualization, q=7000 [W/m^2], R134a, T_{sat}=5 °C
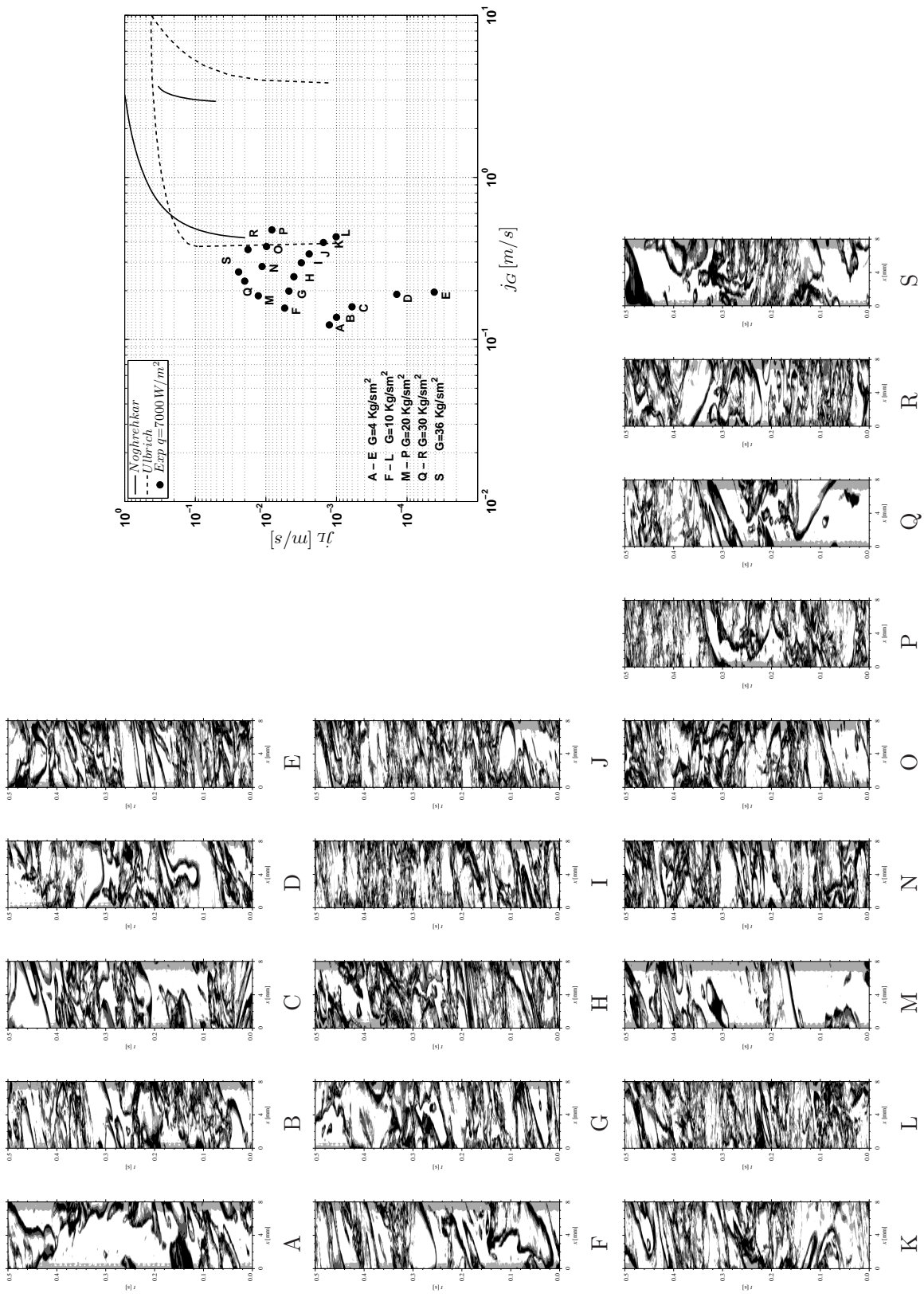
Figure D.14: Flow visualization, q=7000 $[W/m^2]$, R134a, T_{sat}=10 °C
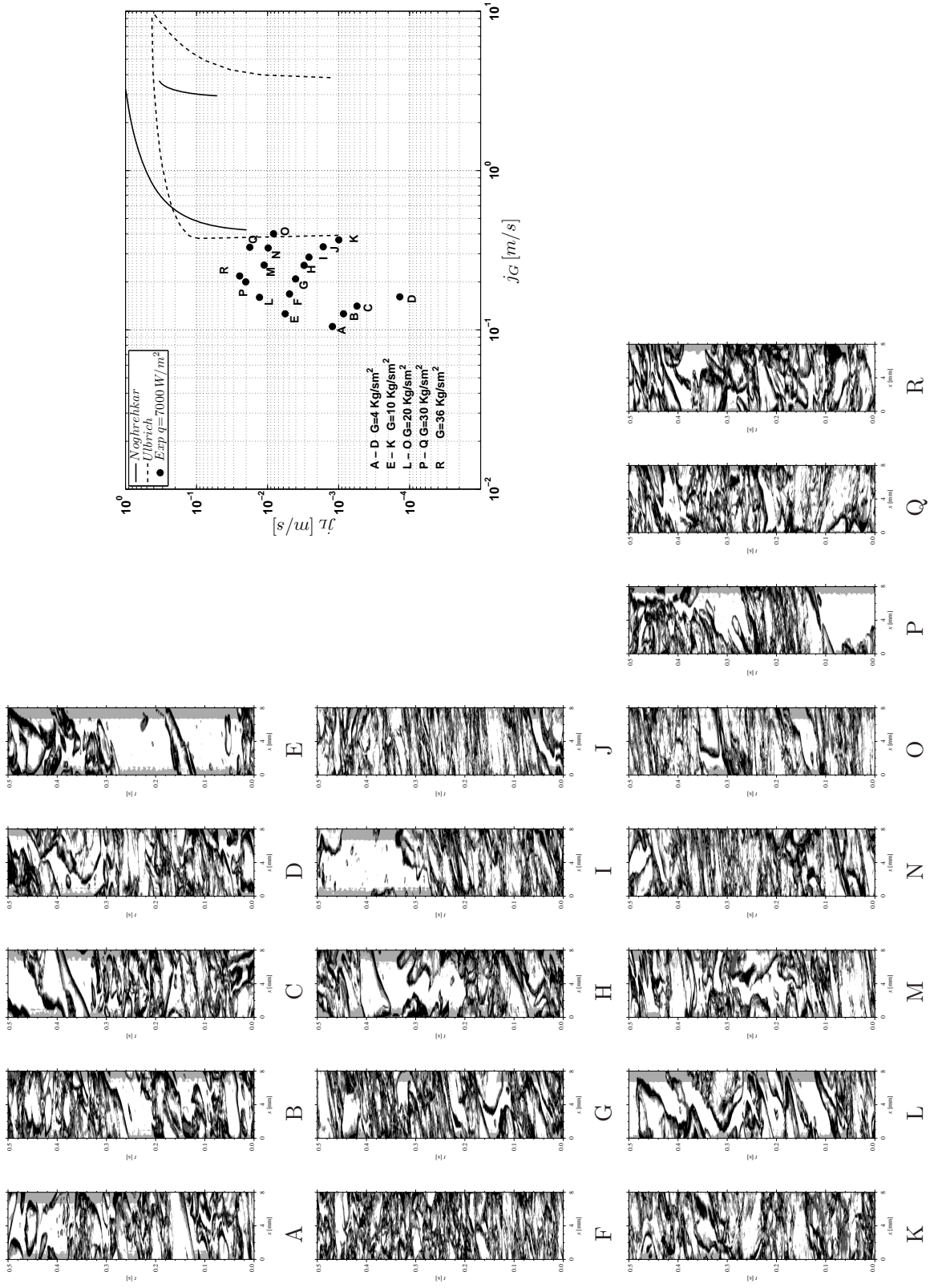
Figure D.15: Flow visualization, q=7000 [W/m^2], R134a, T_{sat}=15 °C
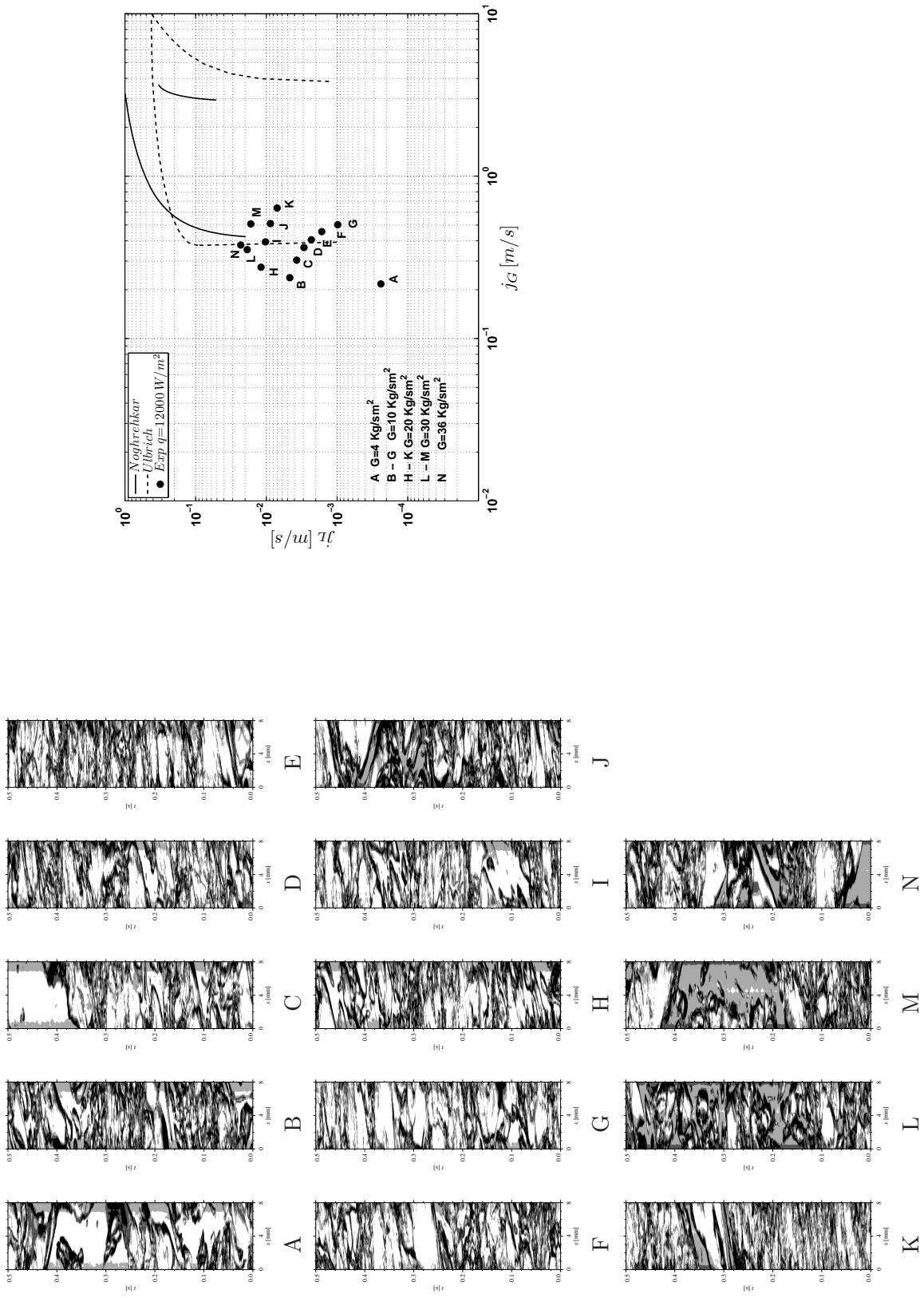
Figure D.16: Flow visualization, $q=12000\,[W/m^2]$, R134a, $T_{sat}=5\,°C$
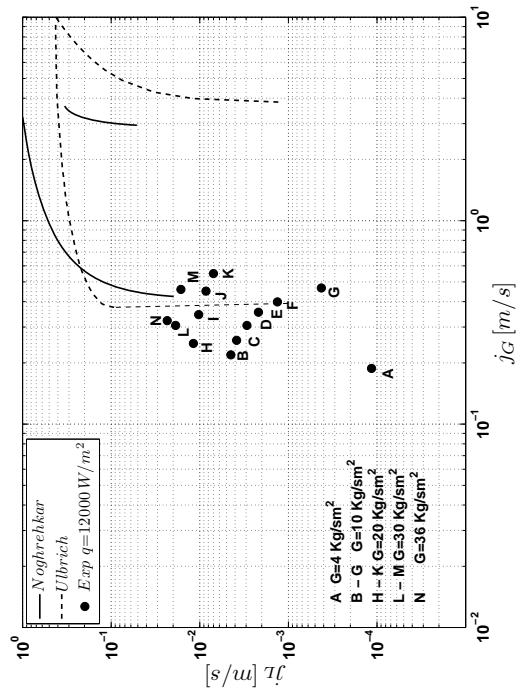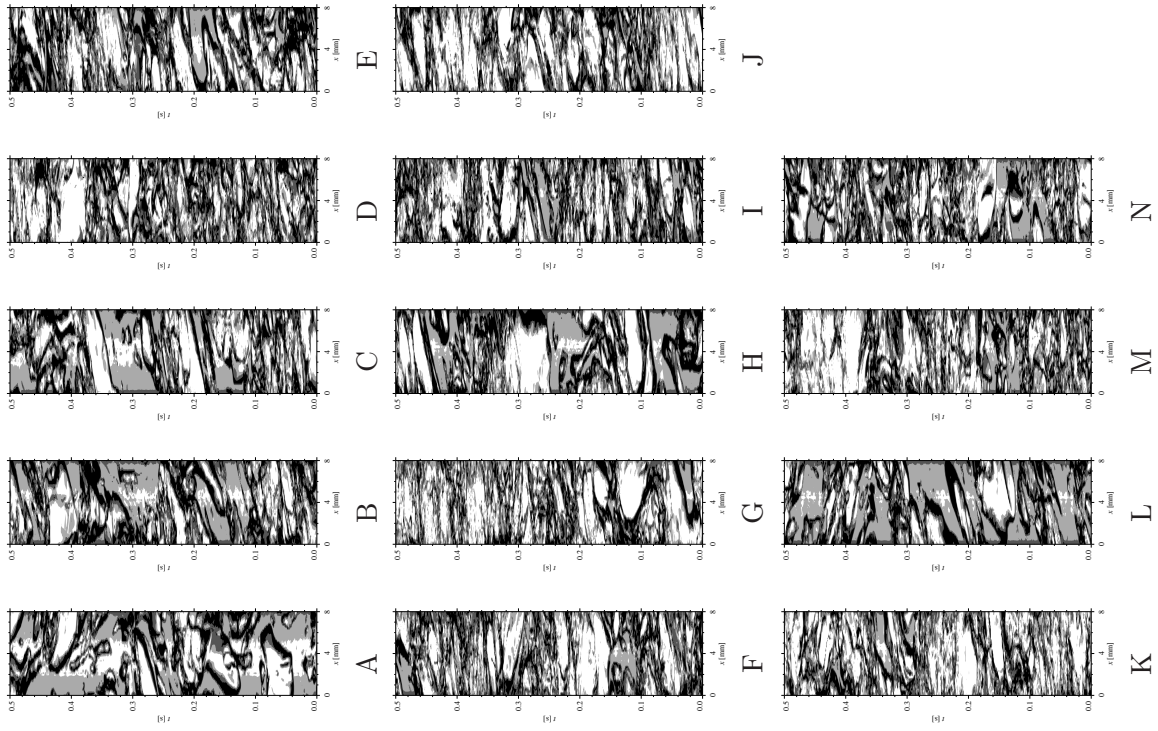
Figure D.17: Flow visualization, $q=12000\,[W/m^2]$, R134a, $T_{sat}=10\,°C$
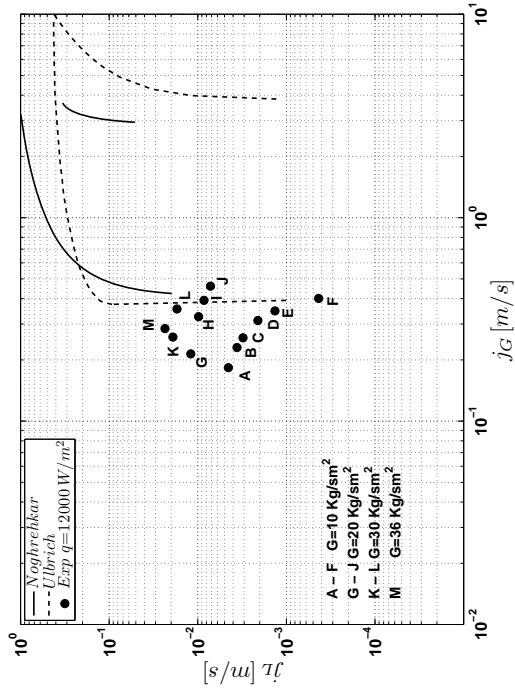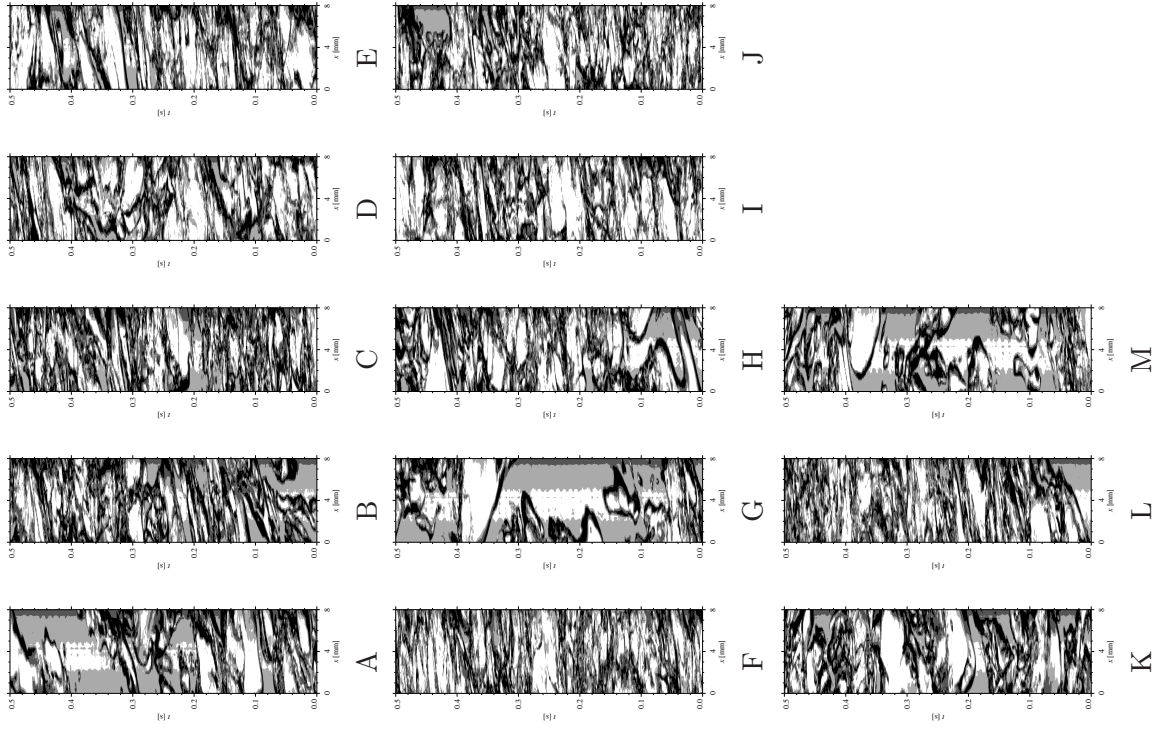
Figure D.18: Flow visualization, $q{=}12000\,[W/m^2]$, R134a, $T_{sat}{=}10\,^{\circ}\mathrm{C}$
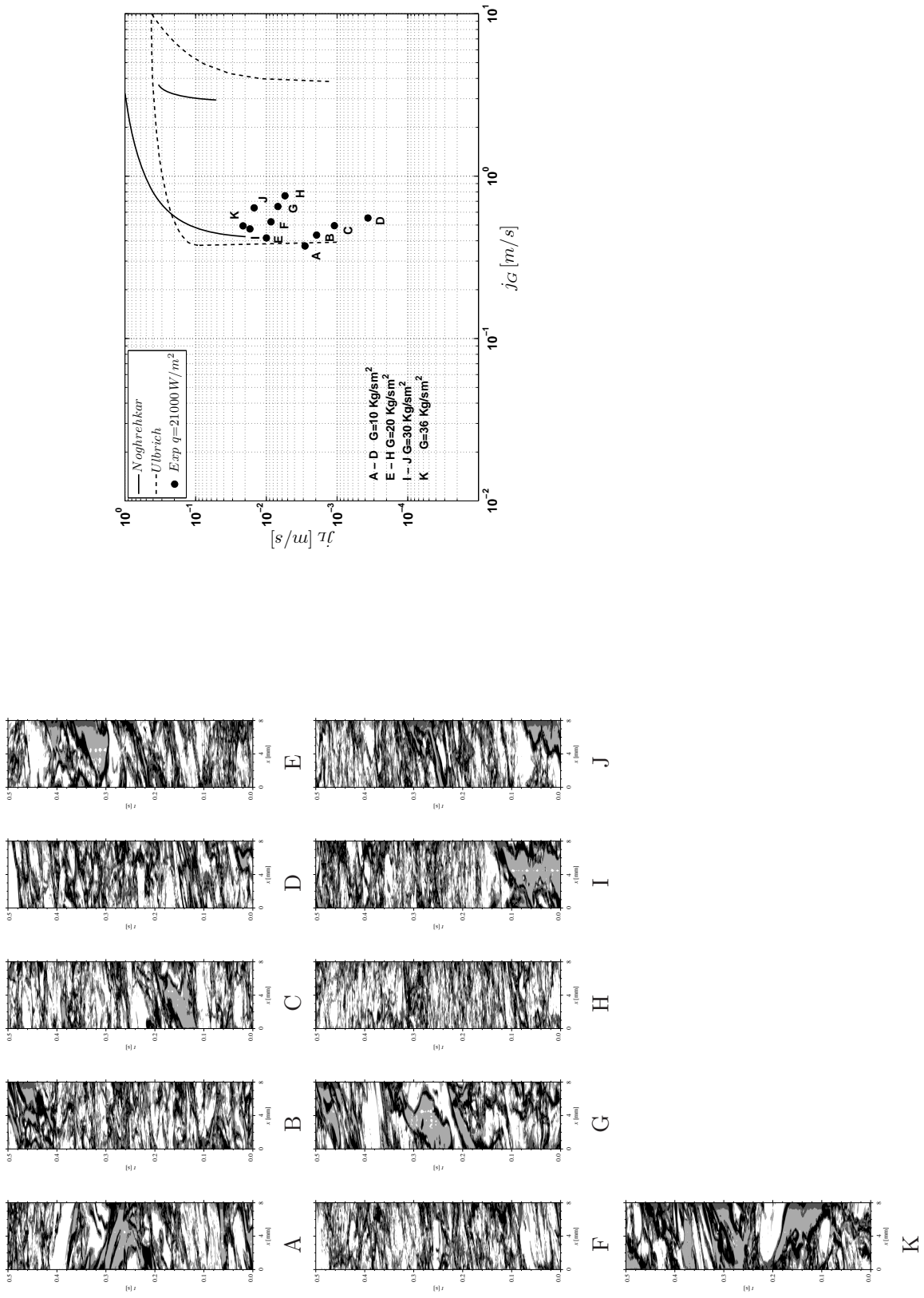
Figure D.19: Flow visualization, q=21000 $[W/m^2]$, R134a, T_{sat}=5 °C
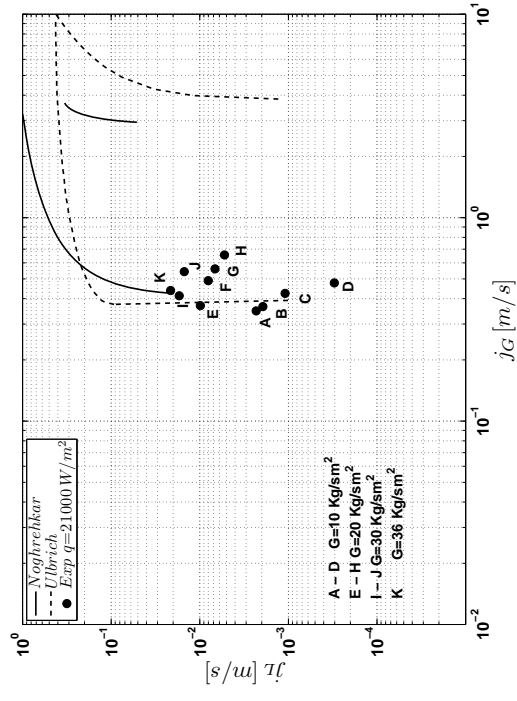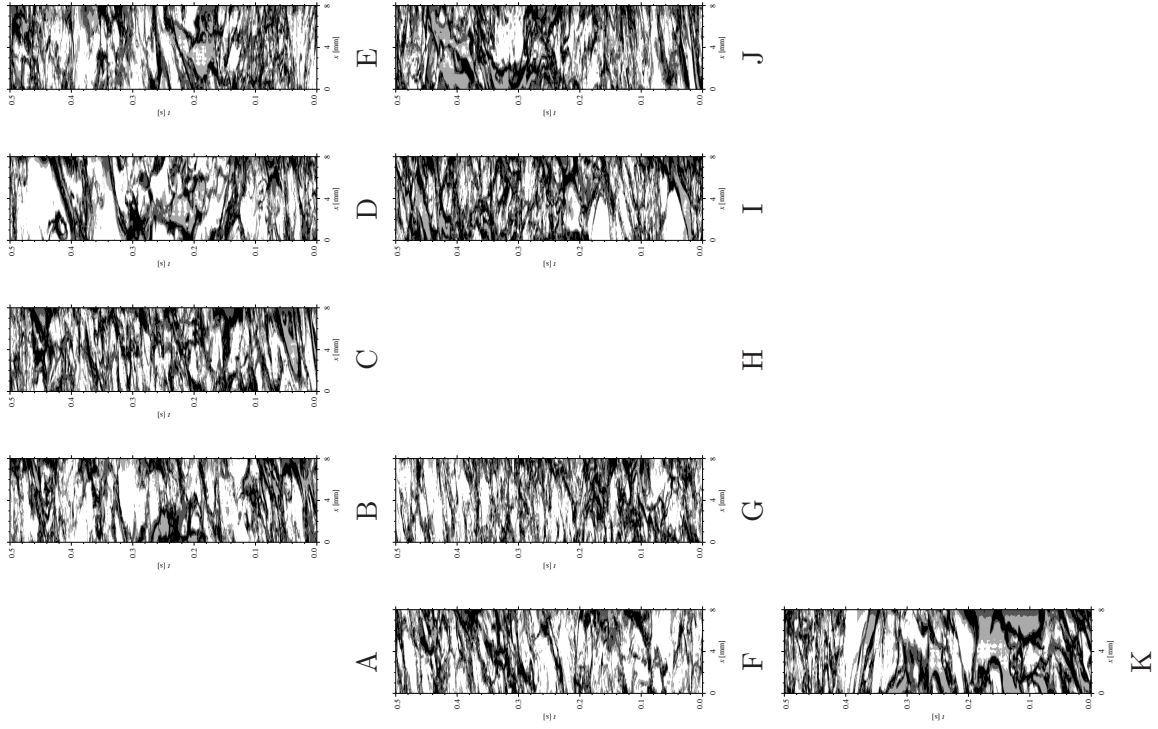
Figure D.20: Flow visualization, q=21000 $[W/m^2]$, R134a, T_{sat}=10 °C
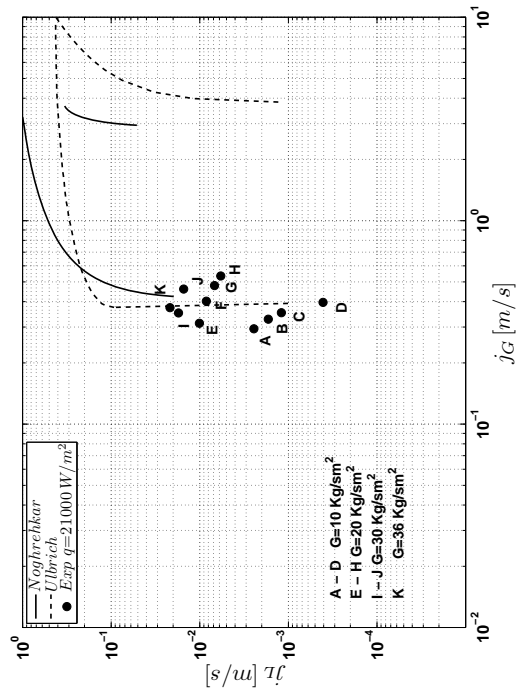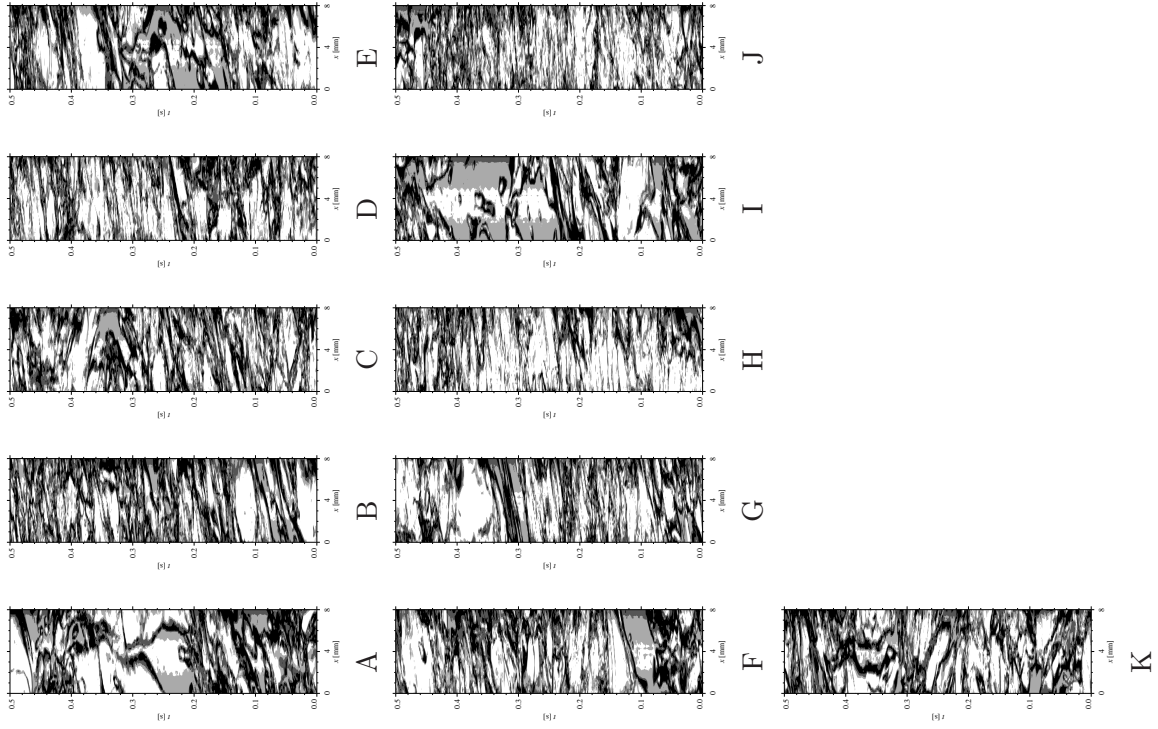
Figure D.21: Flow visualization, $q=21000\,[W/m^2]$, R134a, $T_{sat}=15\,°C$

Appendix E

Thermal Resistance Model: Conduction Cylinder

Consider the geometry Fig. (E.1).
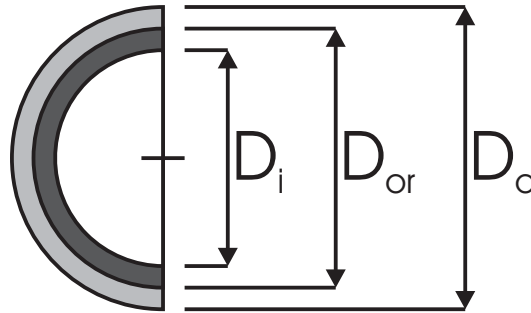
Figure E.1: Tube geometry

$$\frac{1}{r}\left(\lambda r \frac{dT}{dr}\right) = 0 \tag{E.1}$$

$$\lambda r \frac{dT}{dr} = C^{te} \tag{E.2}$$

$$Q_r = -\lambda A \frac{dT}{dr} = -\lambda(2\pi r L).\frac{dT}{dr} \tag{E.3}$$

$$Q_r = C^{te} \tag{E.4}$$

$$\lambda r \frac{dT}{dr} = \tilde{C}_1 \tag{E.5}$$

$$\frac{dT}{dr} = \frac{C_1}{r} \hookrightarrow T(r) = c_1 ln(r) + C_2 \tag{E.6}$$

Imposing as boundary conditions:

$$T(r_i) = T_1 \qquad T(r_{or}) = T_2 \tag{E.7}$$

$$T(r) = \frac{T_1 - T_2}{ln\left(\frac{r_1}{r_2}\right)} ln\left(\frac{r}{r_2}\right) + T_2 \tag{E.8}$$

$$Q_r = \frac{2\pi L \lambda (T_1 - T_2)}{ln\left(\frac{r_1}{r_2}\right)} \tag{E.9}$$

$$\tilde{R}_w = \frac{(T_1 - T_2)}{Q_r} = \frac{ln\left(\frac{r_1}{r_2}\right)}{2\pi L \lambda} \tag{E.10}$$

$$R_w = A\tilde{R}_w$$

$$= \frac{Dln\left(\frac{D_{or}}{D_i}\right)}{2\lambda} \tag{E.11}$$

Appendix F

Uncertainty analysis

A rigorous uncertainty analysis was applied starting from the approach proposed in [87].

$$\alpha_o = \left[\frac{T_{wat} - T_{sat}}{q_o} - R_w - \frac{1}{\alpha_i}\left(\frac{D_o}{D_i}\right)\right]^{-1} \tag{F.1}$$

$$\alpha_o = \alpha_o(T_{wat}, T_{sat}, q_o, R_w, \alpha_i, D_o, D_i)$$

$$\delta\alpha_o = \left[\underbrace{\left(\frac{\partial\alpha_o}{\partial T_{wat}}\delta T_{wat}\right)^2}_{A} + \underbrace{\left(\frac{\partial\alpha_o}{\partial T_{sat}}\delta T_{sat}\right)^2}_{B} + \underbrace{\left(\frac{\partial\alpha_o}{\partial q_o}\delta q_o\right)^2}_{C} + \underbrace{\left(\frac{\partial\alpha_o}{\partial R_w}\delta R_w\right)^2}_{D} \right.$$

$$\left. + \underbrace{\left(\frac{\partial\alpha_o}{\partial\alpha_i}\delta\alpha_i\right)^2}_{E} + \underbrace{\left(\frac{\partial\alpha_o}{\partial D_o}\delta D_o\right)^2}_{F} + \underbrace{\left(\frac{\partial\alpha_o}{\partial D_i}\delta D_i\right)^2}_{G}\right]$$

It is assumed that $(D, F, G) \ll$ other terms.

This equation is obtained considering the error propagation law and the hypothesis of completely independent and random errors to avoid an overestimate of the overall uncertainty. A quadratic summation is taken, see [88]. The various terms A, B, C, D, E, F, G will be discussed below.

In this preliminary phase, the following hypotheses are made:

Hyp 1 Geometric quantities are known exactly;

Hyp 2 Thermo-physical properties are known exactly;

Hyp 3 The exponent n of the pool boiling correlation is known exactly.

F.1   Term A

$$\frac{\partial\alpha_o}{\partial T_{wat}}\delta T_{wat}: \qquad \frac{\partial\alpha_o}{\partial T_{wat}} = -\left[\frac{T_{wat} - T_{sat}}{q_o} - R_w - \frac{1}{\alpha i}\left(\frac{D_o}{D_i}\right)\right]^{-2}\left(\frac{1}{q_o}\right)$$

$\delta T_{wat} :=$ this is known from the thermocouple calibration.

F.2   Term B

$$\frac{\partial \alpha_o}{\partial T_{sat}} \delta T_{sat} : \qquad \frac{\partial \alpha_o}{\partial T_{sat}} = + \left[\frac{T_{wat} - T_{sat}}{q_o} - R_w - \frac{1}{\alpha_i} \left(\frac{D_o}{D_i} \right) \right]^{-2} \left(\frac{1}{q_o} \right)$$

The same type of thermocouple is employed to measure T_{wat} and T_{sat}, so it is a good approximation consider that: $\delta T_{wat} \equiv \delta T_{sat} \hookrightarrow$ see section A.

F.3   Term C

$$\frac{\partial \alpha_o}{\partial q_o} \underbrace{\delta q_o}_{C1} : \qquad \frac{\partial \alpha_o}{\partial q_o} = + \left[\frac{T_{wat} - T_{sat}}{q_o} - R_w - \frac{1}{\alpha i} \left(\frac{D_o}{D_i} \right) \right]^{-2} \left(\frac{T_{wat} - T_{sat}}{q_o^2} \right)$$

F.3.1   Term C1

$$q_o = \frac{\dot{m}.c_p}{\pi.D_o} \frac{dT_{wat}}{ds}$$

$$\delta q_o = \left[\left(\frac{\partial q_o}{\partial \dot{m}} \delta \dot{m} \right)^2 + \left(\frac{\partial q_o}{\partial \left(\frac{dT_{wat}}{ds} \right)} \delta \left(\frac{dT_{wat}}{ds} \right) \right)^2 \right]^{0.5}$$

$$\frac{\partial q_o}{\partial \dot{m}} = \frac{c_p}{\pi D_o} \frac{dT_{wat}}{d_s}$$

$$\frac{\partial q_o}{\partial \left(\frac{dT_{wat}}{ds} \right)} = \frac{\dot{m} c_p}{\pi D_o}$$

$\delta \dot{m} :=$ this is known from the Coriolis flow-meter calibration. T_{wat} comes from a polynomial fit:

$$T_{wat} = a.s^2 + b.s + c$$

$$\hookrightarrow \frac{dT_{wat}}{ds} = 2.a.s + b$$

$$\hookrightarrow \delta \left(\frac{dT_{wat}}{ds} \right) = \delta(\varphi)$$

$$= \left[\left(\frac{\partial \varphi}{\partial a} \delta a \right)^2 + \left(\frac{\partial \varphi}{\partial s} \delta s \right)^2 + \left(\frac{\partial \varphi}{\partial b} \delta b \right)^2 \right]^{\frac{1}{2}}$$

The uncertainty in the curvilinear coordinate, δs, can be easily estimated. For a second order polynomial fit, it is not straightforward to calculate the uncertainties in the parameter a and b (δa and δb). From this point of view, the open literature gives the right approach to solve this problem: [93], [90], [89], [92].

A basic understanding of the problem is given in [88]. The method currently employed makes use of a mathematical software [91] that computes the confidence bound for a set of fitted coefficients. To calculate the confidence bound, that are given at a level of 95% of confidence, R^{-1} (the inverse R factor from QR decomposition of the Jacobian), the degree of freedom for error, and the root mean squared error are used. This means that the returned values are in a form like: $x = \bar{x} \pm 2.\delta x$, the confidence bounds is an interval of the type $[Min, Max]$. It means that $(Max - Min) = 4\delta x$ and that the uncertainty is: $\delta x = \frac{(Max - Min)}{4}$. Alternatively, as stated inGstöhl [61], for a specific case of a second order polynomial fit through the thermocouples at three equidistant locations, the heat flux in the middle of the tube can be re-written as:

$$q_o|_{s=L/2} = \frac{\dot{m}c_p}{\pi D_o L}(T_{wat,o} - T_{wat,i})$$

In this case, the uncertainty in the heat flux can be computed as:

$$\delta q_o|_{s=L/2} = \left[\left(\frac{\partial q_o}{\partial \dot{m}}\delta \dot{m}\right)^2 + 2\left(\frac{\dot{m}c_p}{\pi D_o L}\delta T_w\right)^2\right]^{\frac{1}{2}}$$

F.4   Term E

$$\frac{\partial \alpha_o}{\partial \alpha_i}\delta \alpha_i \qquad \frac{\partial \alpha_o}{\partial \alpha_i} = -\left[\frac{T_{wat} - T_{sat}}{q_o} - R_w - \frac{1}{\alpha_i}\left(\frac{D_o}{D_i}\right)\right]^{-2}(-1)\left(\frac{D_o}{D_i}\right)(-1)\left(\frac{1}{\alpha_i^2}\right)$$

$$= -\left[\frac{T_{wat} - T_{sat}}{q_o} - R_w - \frac{1}{\alpha_i}\left(\frac{D_o}{D_i}\right)\right]^{-2} \cdot \left(\frac{D_o}{D_i}\right)\left(\frac{1}{\alpha_i^2}\right)$$

$$\alpha_i = C_i \alpha_{Gni}$$

$$\hookrightarrow \delta \alpha_i = \left[\left(\frac{\partial \alpha_i}{\partial C_i} \cdot \underbrace{\delta C_i}_{E1}\right)^2 + \left(\frac{\partial \alpha_i}{\partial \alpha_{Gni}}\underbrace{\delta \alpha_{Gni}}_{E2}\right)^2\right]^{\frac{1}{2}}$$

$$\frac{\partial \alpha_i}{\partial C_i} = \alpha_{Gni}$$

$$\frac{\partial \alpha_i}{\partial \alpha_{Gni}} = C_i$$

Considering that the accuracy of the heat transfer coefficient is mainly dependent on the accuracy of the corrective multiplier C_i, see Gstöhl [61], it is possible to assume that:

$$\delta \alpha_i \approx \left|\frac{\partial \alpha_i}{\partial C_i}\delta C_i\right|$$

F.4.1   E1

The technique to compute δC_i is relative to the technique applied in the lab:

$$\underbrace{\left[\frac{1}{U_o} - R_w\right].q_o^n}_{y} = \underbrace{\frac{1}{C_o}}_{b} + \underbrace{\frac{1}{C_i}}_{a}\underbrace{\left[\frac{q_o^n}{\alpha_{Gni}}\frac{D_o}{D_i}\right]}_{x}$$

$$y = ax + b$$

The curve fits n pairs of observations (x_j, y_j). We are interested in determining δC_j, so that:

$$C_j = \frac{1}{a}$$

$$\delta C_j = \left|\frac{\partial C_j}{\partial a}\delta a\right| = \left|\frac{1}{a^2}\delta a\right|$$

It is now necessary to determine the uncertainty in the fitting parameters: $\delta a, \delta b$. One possible way is to determine these quantities numerically through mathematical software, as was presented for the quadratic fit in C1. A much more elegant way is the method presented in [93]. For the case of linear regression, the analytical expressions of the uncertainties δa and δb are obtained. More details about the available methodologies are presented in [94]. Before going through this method the uncertainties in the observations x_j and y_j are computed here.

Considering first the variable y_j:

$$y_j = \left[\frac{1}{U_o} - R_w\right].q_o^n$$

$$U_o = \frac{q_o}{(T_{wat} - T_{sat})}$$

$$\hookrightarrow y_j = (T_{wat} - T_{sat})q_o^{n-1} - R_w q_o^n$$

$$\delta y_j = \left[\left(\frac{\partial y_j}{\partial T_{wat}}\delta T_{wat}\right)^2 + \left(\frac{\partial y_j}{\partial T_{sat}}\delta T_{sat}\right)^2 + \left(\frac{\partial y_j}{\partial q_o}\delta q_o\right)^2 + \left(\frac{\partial y_j}{\partial R_w}\delta R_w\right)^2\right]^{0.5}$$

$$\frac{\partial y_j}{\partial T_{wat}} = q_o^{n-1}$$

$$\frac{\partial y_j}{\partial T_{sat}} = -q_o^{n-1}$$

$$\frac{\partial y_j}{\partial q_o} = (n-1).q_o^{n-2}(T_{wat} - T_{sat}) - n.R_w q_o^{n-1}$$

$$\delta q_o \quad \text{see C}$$

Anylyzing now x_j:

$$x_j = \frac{q_o^n}{\alpha_{Gni}}.\left(\frac{D_o}{D_i}\right)$$

$$\delta x_j = \left[\left(\frac{\partial x_j}{\partial q_o}\delta q_o\right)^2 + \left(\frac{\partial x_j}{\partial \alpha_{Gni}}\delta \alpha_{Gni}\right)^2\right]^{0.5}$$

$$\frac{\partial x_j}{\partial q_o} = n.\frac{q_o^{n-1}}{\alpha_{Gni}}\frac{D_o}{D_i}$$

$$\frac{\partial x_j}{\partial \alpha_{Gni}} = (-1)\frac{q_o^n}{\alpha_{Gni}^2}\frac{D_o}{D_i}$$

$$\delta q_o \quad \text{see C}$$

$$\delta \alpha_{Gni} \quad \text{see E2}$$

Skipping the methodology to determinate the parameters a and b, already presented in [93], here the focus on the procedure to determinate δa. The vertical distance between the jth point and the fitting curve at the abscissa x_j is:

$$d_j \;=\; y_j - (ax_j + b)$$

where a and b are determined minimize the sum of the squared distances d_j weighted on the squared uncertainty of each distance w_j as follows:

$$\varphi(a,b) \;=\; \sum_j w_j d_j^2$$

The method presented in [93] directly gives an analytical solution for the linear regression:

$$w_j \;=\; \frac{1}{\delta d_j^2}$$

$$\delta d_j^2 \;=\; \left[\left(\frac{\partial d_j}{\partial y_j}\delta y_j\right)^2 + \left(\frac{\partial d_j}{\partial x_j}\delta x_j\right)^2\right]$$

$$=\; \delta y_j^2 + \left(\frac{\partial(ax_j + b)}{\partial x_j}\delta x_j\right)^2$$

$$=\; \delta y_j^2 + (a\delta x_j)^2$$

$$\delta a^2 \;=\; \sum_j\left[\left(\frac{\partial a}{\partial x_j}\delta x_j\right)^2 + \left(\frac{\partial a}{\partial y_j}\delta y_j\right)^2\right]$$

$$\delta b^2 \;=\; \sum_j\left[\left(\frac{\partial b}{\partial x_j}\delta x_j\right)^2 + \left(\frac{\partial b}{\partial y_j}\delta y_j\right)^2\right]$$

$$F_j \;=\; x_j + \left(b.d_j w_j \delta x_j^2\right)$$

$$A \;=\; -\sum_j w_j$$

$$B \;=\; -\sum_j\left(w_j F_j\right)$$

$$C \;=\; \sum_j\left[\left(\delta x_j d_j w_j\right)^2 - \left(w_j F_j^2\right)\right]$$

$$\frac{\partial a}{\partial x_j} \;=\; \frac{d_j}{AC - B^2}\left[bC + B\left(d_j - bF_j\right)\right]$$

$$\frac{\partial a}{\partial y_j} \;=\; \frac{d_j}{A.C - B^2}\left(BF_j - C\right)$$

$$\frac{\partial b}{\partial x_j} \;=\; \frac{-d_j}{A.C - B^2}\left[b.B + A.\left(d_j - b.F_j\right)\right]$$

$$\frac{\partial b}{\partial y_j} \;=\; \frac{d_j}{A.C - B^2}\left(B - AF_j\right)$$

Substituting the partial derivatives of the fitting parameter to the expressions for δa^2 and δb^2, the analytical expressions of the uncertainties δa and δb are determined.

Bibliography

[1] Diehl, J.E., 1957, *Calculate condenser pressure drop*, Petroleum Refiner, 36(10), 147-153

[2] Sutherland, L.A., Murray, I., 1969, *Pressure-drop and heat-transfer on the shell-side of model heat exchanger with two-phase flow*, NEL Report No 395, National Engineering Laboratory, East Kilbride, Glasgow

[3] Grant, I.D.R., Murray, I., 1972, *Pressure drop on the shell-side of a segmentally buffled shell-and-tube heat exchanger with vertical two-phase flow*, NEL Report No 500, National Engineering Laboratory, East Kilbride, Glasgow

[4] Grant, I.D.R., Murray, I., 1974, *Pressuredrop on the shell-side of a segmentally buffled shell-and-tube heat exchanger with horizontal two-phase flow*, NEL Report No 560, National Engineering Laboratory, East Kilbride, Glasgow

[5] Report of a meeting at NEL 28 November 1973, 1975, *Advances in thermal and mechanical design of shell-and tube heat exchangers*, NEL Report No 590, National Engineering Laboratory, East Kilbride, Glasgow

[6] Grant, I.D.R., Chisholm, D., 1979, *Two-phase flow on the shell-side of a segmentally buffled shell-and-tube heat exchanger*, Journal of Heat Transfer, 101, 38-42

[7] Kondo, M., Nakajima, K.I, 1980, *Experimental investigation of air-water two phase upflow across horizontal tube bundles (Part I, Flow pattern and void fraction*, Bull. of JSME, 23(177),385-393

[8] Kondo, M., 1984, *Experimental investigation of air-water two phase upflow across horizontal tube bundles (Part II, Pressure drop*, Bull. of JSME, 27(230), 1616-1624

[9] Pettigrew, M.J., Taylor, C.E., Kim, B.S., 1989, *Vibration of tube bundles in two-phase cross-flow: Part 1-Hydrodynamic mass and damping*, Journal of Pressure Vessel Technology, 111, 466-477

[10] Pettigrew, M.J., Tromp, J.H., Taylor, C.E., Kim, B.S., 1989, *Vibration of tube bundles in two-phase cross-flow: Part 2-Fluid-elastic instability*, Journal of Pressure Vessel Technology, 111, 478-487

[11] Pettigrew, M.J., Tromp, J.H., Taylor, C.E., Kim, B.S., 1989, *Vibration of tube bundles in two-phase cross-flow: Part 3-Turbulence-induced excitation*, Journal of Pressure Vessel Technology, 111, 488-500

[12] Ulbrich, R., Mewes, D., 1994, *Vertical, upward gas-liquid two-phase flow across a tube bundle*, International Journal of Multiphase Flow, 20(2), 249-272

[13] Lian, H.Y., Chan, A.M.C., Kawaji, M., 1992, *Effects of void fraction on vibration of tubes in tube bundles under two-phase cross flow*, HTD-Vol. 230/NE-Vol. 9, Symposium on flow-induced vibration and noise - Volume 1, ASME

[14] Xu, G.P., Tso, C.P., Tou, K.W., 1998, *Hydrodynamics of two-phase flow across a horizontal tube bundle*, International Journal of Multiphase Flow, 24(8), 1317-1342

[15] Xu, G.P., Tou, K.W., Tso, C.P., 1998, *Two-phase void fraction and pressure drop in horizontal crossflow across a tube bundle*, Journal of Fluids Engineering, 120, 140-145

[16] Noghrehkar, G.R., Kawaji, M., Chan, A.M.C., 1999, *Investigation of two-phase flow regimes in tube bundles under cross-flow conditions*, International Journal of Multiphase Flow, 25(5), 854-874

[17] Umeda, S., Yang, D., 1999, *Interaction of von Karman vortices and intersecting main streams in staggered tube bundles*, Experiments in Fluids, 26(5), 389-396

[18] Burnside, B.M., Miller, K.M., McNeil, D.A., Bruce, T., 2005, *Flow velocities in an experimental kettle reboiler determined by particle image velocimetry*, International Journal of Heat and Mass Transfer, 48(5), 1000-1016

[19] Iwaki, C., Cheong, K.H., Monji, H., Matsui, G., 2005, *Vertical, bubbly, cross-flow characteristics over tube bundle*, Experiments in Fluids, 39(6), 1024-1039

[20] Khushnood, S., Khan, Z.M., Malik, M.A., Koreshi, Z.U., Khan, M.A., 2004, *A review of heat exchanger tube bundle vibrations in two-phase cross-flow*, Nuclear Engineering and Design, 230(1-3), 233-251

[21] Ribatski, G., Thome, J.R., 2004, *Dynamics of two-phase flow across horizontal tube bundles - a review* Proceedings of the 10th Brazilian Congress of Thermal Sciences and Engineering, ENCIT 2004, Braz. Soc. of Mechanical Sciences and Engineering, ABCM, Rio de janeiro, Brazil, CIT04-0036

[22] Jones, O.C. Jr, 1973, *Statistical considerations in heterogeneous two-phase flowing systems*, PhD Thesis, Rensselaer Polytechnic Institute, Troy, New York

[23] Jones, O.C. Jr, Zuber, N., 1974, *Statistical methods for measurement and analysis in two-phase flow*, Heat Transfer 1974: Proceedings of the 5th International Heat Transfer Conference, September 3 - September 7, Tokyo/Japan Society Of Mechanical Engineers, Society of Chemical Engineers, Japan, 4, 200-204

[24] Jones, O.C. Jr, Zuber, N., 1975, *The interrelation between void fraction fluctuations and flow patterns in two-phase flow*, International Journal of Multiphase Flow, 2(3), 273-306

[25] Tutu, N.K., 1982, *Pressure fluctuations and flow pattern recognition in vertical two-phase liquid flow*, International Journal of Multiphase Flow, 8(4), 443-447

[26] Beers, Y., 1957, *Introduction to the theory of error*, Addison-Wesley Publishing Company Inc.

[27] Matsui, G., 1984, *Identification of flow regimes in vertical gas-liquid two-phase flow using differential pressure fluctuations*, International Journal of Multiphase Flow, 10(6), 711-720

[28] Vince, M.A., Lahey, R.T.Jr., 1982, *On the development of an objective flow regime indicator*, International Journal of Multiphase Flow, 8(2), 93-124

[29] Hubbard, M.G., Dukler, A.E., 1966, *The characterization of flow regimes for horizontal two phase flow*, Proceedings Heat Transfer and Fluid Mechanics Institute, Stantford University Press

[30] Liebenberg, L., Thome, J.R., Meyer, J.P., 2005, *Flow visualization and flow pattern identification with power spectral density distributions of pressure traces during refrigerant condensation in smooth and microfin tubes*, Journal of Heat Transfer, 127(3), 209-220

[31] Alekseev, G.V., Ibragimov, M.G., Nevstrueva, E.I., Ryabtsev, V.A., Sabelev, G.I., Tyutyaev, V.V. , 1978, *Some spectral characteristics of two-phase non-equilibrium flows*, 6th International Heat Transfer Conference, Toronto (Canada), Hemisphere Washington DC, FB-11, 333-338

[32] Weisman, J., Duncan, D., Gibson, J., Crawford, T., 1979, *Effects of fluid properties and pipe diameter on two-phase flow patterns in horizontal lines*, International Journal of Multiphase Flow, 5(6), 437-462

[33] Lin, P.Y., Hanratty, T.J., 1987, *Detection of slug flow from pressure measurements*, International Journal of Multiphase Flow, 13(1), 13-21

[34] Matsui, G., 1986, *Automatic identification of flow regimes in vertical two-phase flow using differential pressure fluctuations*, Nuclear Engineering and Design, 95, 221-231

[35] Rajković, M., Riznić, J.R., Kojasoy, G., 1996, *Dynamical characteristics of flow pattern transitions in horizontal two-phase flow*, 2nd European Thermal-Science and 14th UIT National Heat Transfer Conference, Rome, Italy, Ed. ETS, 1403-1408

[36] Ito, K., Inoue, M., Ozawa, M., Shoji, M., 2004, *A simplified model of gas-liquid two-phase flow pattern transition*, Heat Transfer-Asian Research, 33(7), 445-461

[37] Jain, P.K., Roy, R.P., 1983, *Stochastic characteristics of vapor and wall pressure fluctuations in boiling flows*, International Journal of Multiphase flow, 9(5), 463-489

[38] Bertola, V., 2003, *Experimental characterization of gas-liquid intermittent subregimes by phase density function measurements*, Experiments in Fluids, 34(1), 122-129

[39] Tutu, N.K., 1984, *Pressure drop fluctuations and bubble-slug transition in a vertical two-phase air-water flow*, International Journal of Multiphase Flow, 10(2), 211-216

[40] Pike, R.W., Wilkins, B.Jr., Ward,H.C., 1965, *Measurement of the void fraction in two-phase flow by X-ray attenuation*, AiChE Journal, 11(5), 794-800

[41] Matsui, G., 1985, *Identification of flow patterns in horizontal gas-liquid two-phase flow using differential pressure fluctuations*, International Symposium on Fluid Control and Measurements, FLUCOME '85, Tokyo, 2-5 September 1985, Society of Instrument and Control Engineers

[42] Nishikawa, K., Sekoguchi, K., Fukano, T., 1969, *On the pulsation phenomena in gas liquid two-phase flow*, Bulletin of JSME, 12(54), 1410-1416

[43] Akagawa, K., Hamaguchi, H., Sakaguchi, T., Ikari, T., 1971, *Studies on the fluctuation of pressure drop in two-phase flow (1st Report, Experimental study)*, Bulletin of JSME, 14(71), 447-454

[44] Akagawa, K., Hamaguchi, H., Sakaguchi, T., Ikari, T., 1971, *Studies on the fluctuation of pressure drop in two-phase flow (2nd Report, Theoretical analysis)*, Bulletin of JSME, 14(71), 455-461

[45] Akagawa, K., Hamaguchi, H., Sakaguchi, T., Ikari, T., 1971, *Studies on the fluctuation of pressure drop in two-phase flow (3rd Report, Pressure recovery behind a bubble, and lengths of bubble and liquid slug)*, Bulletin of JSME, 14(71), 462-469

[46] Franca, F., Acikgoz, M., Lahey, R.T.Jr., Clausse, A., 1991, *The use of fractal techniques for flow regime identification*, International Journal of Multiphase Flow, 17(4), 545-552

[47] Lowe, D.C., Rezkallah, K.S., 1999, *Flow regime identification in microgravity two-phase flows using void fraction signals*, International Journal of Multiphase Flow, 25(3), 433-457

[48] Press, W.H., Teukolsky, S.A., Vetterling, W.T., Flannery, B.P., 1992, *Numerical Recipes in C. The Art of Scientific Computing. Second Edition*, Cambridge University Press

[49] Ribastski, G., Thome, J.R., 2007, *Two-phase flow and heat transfer across horizontal tube bundles - A review*, Heat Transfer Engineering, 28(6), 508-524

[50] Feenstra, P.A., Weaver, D.S., Judd R.L., 2000, *An improved void fraction model for two-phase cross-flow in horizontal tube bundles*, International Journal of Multiphase flow, 26(11), 1851-1873

[51] Consolini, L., Robinson, D., Thome, J.R., 2008, *Void fraction and two-phase pressure drops for evaporating flow over horizontal tube bundles*, Heat Transfer Engineering, 27(3), 5-21

[52] Žukauskas, A., Ulinskas, R., 1983, *Banks of plain and finned tubes*, Heat Exchanger Design Handbook, Chapter 2.2.4, Hemisphere Publishing Corporation

[53] Gaddis, E.S., Gnielinski, V., 1985, *Pressure drop in cross flow across tube bundles*, International Chemical Engineering, 25(1), 1-15

[54] Thome, J.R., Robinson, D., 2006, *Prediction of local bundle boiling heat transfer coefficients: pure refrigerant boiling on plain, low fin, and Turbo-BII HP tube bundles*, Heat Transfer Engineering, 27(10), 20-29

[55] Shah, M.M., 2007, *A general correlation for heat transfer during saturated boiling with flow across tube bundles*, HVAC&R Research, 27(10), 20-29

[56] Chae, H.B., Schmidt, J.W., Moldover, M.R., 1990, *Alternative refrigerants R123a, R134a, R141b, and R152a: critical temperature, refractive index, surface tension, and estimates of liquid, vapor, and critical densities*, The Journal of Physical Chemistry, 94(25),8840-8845

[57] Aprin, L., 2003, *Etude expérimentale de l'ébullition d'hydrocarbures sur un faisceau de tubes horizontaux. Influence de la nature du fluide et de l'état de surface*, PhD Thesis, Université de Provence Aix-Marseille I

[58] Ishihara, K., Palen, J.W., Taborek, J., 1980, *Critical review of correlations fro predicting two-phase flow pressure drop across tube banks*, Heat Transfer Engineering, 1(3), 23-32

[59] Gnielinski, V., 1976, *New equations for heat and mass transfer in turbulent pipe and channel flow*, Advances in Heat Transfer, 16(2), 359-368

[60] Petukhov, B.S., 1970, *Heat transfer and friction in turbulent pipe flow with variable physical properties*, Advances in Heat Transfer, 6, 503-564

[61] Gstöhl, D.,2004, *Heat transfer and flow visualization of falling film condensation on tube arrays with plain and enhanced surfaces*, PhD Thesis, Swiss Federal Institute of Technology, Lausanne

[62] Styrylska, T.B., Lechowska, A.A., 2003, *Unified Wilson Plot Method for determining heat transfer correlations for heat exchangers*, Journal of Heat Transfer, 125(4), 752-756

[63] Robinson, D., Thome, J.R., 2003, *Flooded evaporation heat transfer performance for tube bundles including the effects of oil using R-410A and R-507A*, ASHRAE Research Project RP-1089

[64] Cooper, M.,G., 1984, *Heat flow rates in saturated nucleate pool boiling. A wide-ranging examination using reduced properties*, Advances in Heat Transfer, Academic Press, Orlando, 16, 157-239

[65] Kim, N.,-H., Cho, J.,-P., Youn, B., 2002, *Forced convective boiling of pure refrigerants in a bundle of enhanced tubes having pores and connecting gaps*, Internationaal Journal of Heat and Mass Transfer, 45(12), 2449-2463

[66] Wilson, E.E., 1915, *A basis for rotational design of heat transfer apparatus*, Trans. ASME, 37, 47-82

[67] Rose, J.W., 2004, *Heat-transfer coefficients, Wilson plots and accuracy of thermal measurements*, Experimental Thermal and Fluid Science, 28(2004), 77-86

[68] El Sherbini, A.I., Joardar, A., Jacobi, A.M., 2004, *Modified Wilson-Plot Technique for heat exchanger performance: strategies for minimizing uncertainty in data reduction*, International Refrigeration and Air Conditioning Conference at Pordue, R069, 1-8

[69] Winterton, R.H.S., 1998, *Where did the Dittus-Boelter equation come from?*, International Journal of Heat and Mass Transfer, 41(4-5), 809-810

[70] Buckingham, E., 1914, *On phisically similar systems; illustrations of the use of dimensional equations*, Physical Review, IV(4), 345-376

[71] Khartabil, H.F., Christensen, R.N., Richards, D.E., 1988, *A modified Wilson plot technique for determining heat transfer correlations*, Proc. 2nd UK National Heat Transfer Conference, C168/88, 1331-1357

[72] Briggs, D.E., Young, E.H., 1969, *Modified Wilson plot technique for obtaining heat transfer correlations for shell and tube heat exchangers*, Chemical Engineering Progress Symposium Series, 65(92), 35-45

[73] Mayhew, Y.R., 1981, *Additional observations on vapour shear and condensate inundation*, Power Condenser Heat Transfer Technology, (eds) Marto, P.J., Nunn, R.H., Hemisphere, 243-257

[74] Shah, R.K., 1990, *Assesment of modified Wilson plot techniques for obtaining heat exchanger design data*, 9th International Heat Transfer Conference Jerusalem, Israel, 19-24 August, Paper 14-HX-9, 51-56

[75] Wójs, K., Tietze, T., 1997, *Effects on the temperature interface on the results obtained using the Wilson plot technique*, Heat and Mass Transfer, 33(3), 241-245

[76] Kumar, R., Varma, H.K., Agrawal, K.N., Mohanty, B., 2001, *A comprehensive study of modified Wilson plot technique to determine the heat transfer coefficient during condensation of steam and R134a over single horizontal plain and finned tubes*, Heat Transfer Engineering, 22(2), 3-12

[77] Roetzel, W., Na Ranong, C., 2002, *On the application of the Wilson plot technique*, Compact Heat Exchanger Symposium - A Festschrift on the 60th Birthday of Ramesh K. Shah, S 151-156 (Extended version of: Roetzel, W., Na Ranong, C., 2000, *Zur anwendung der Wilson-plot-methode*, Wärmeaustausch und erneuerbare energiequellen, Tagunsband VIII Internationales Symposium Szcecin-Leba, Poland, 18-20.09.2000, 317-326)

[78] Roetzel, W., Spang, B., 1995, *Measurement of heat transfer coefficients in heat exchangers - an alternative to the Wilson plot technique*, Proceedings of the 2nd Baltic Heat Transfer Conference, 589-596

[79] Agostini, F., 2007, *Design of experiments: "Modified Wilson plot method"*, LTCM Report, Swiss Federal Institute of Technology, Lausanne

[80] Cohen, D.K., Potts, J.E., 1978, *Light transmission through reflecting cylindrical tubes*, American Journal of Physics, 46(7), 727-728

[81] Lion, Y., Renotte, Y., 1992, *Interference of light by reflection on the inner walls of cylindrical tubes*, European Journal of Physics, 13(1), 47-52

[82] Carey, Van. P., 1992, *Liquid-Vapor Phase-Change Phenomena: an introduction to the thermophysics of vaporization and condensation processes in heat transfer equipment*, 206-211, Taylor & Francis, Hemisphere, Whasington DC

[83] Zuber, N., 1962, *Nucleate boiling. The region of isolated bubbles and the similarity with natural convection*, International Journal of Heat and Mass Transfer, 6(1), 53-78

[84] Fossa, M., Guglielmini, G., 1998, *Indagine sperimentale sullo sviluppo della struttura del moto nel flusso bifase orizzontale in regime intermittente*, Proceedings of the 16th UIT National Heat Transfer Conference, Siena, Italy, 18-19 June, 1, Ed. ETS, Pisa, Italy, 313-324

[85] Zobeiri, A., 2006, *Flow pattern characterization for air-water flow by high speed visualization, optical measurement and dynamic pressure signal*, Master Project, Swiss Federal Institute of Technology, Lausanne

[86] Barnea, D., 1987, *A ubified model for predicting flow-pattern transitions for the whole range of pipe*, International Journal of Multiphase Flow, 13(1),1-12

[87] Kline, S.J., McClintock, F.A., 1953, *Describing uncertainties in sinlge-sample experiments*, ASME Mechanical Engineering, 75(1), 3-8

[88] Taylor, J.R., 1997, *An introduction to error analysis: the study of uncertainties in physical measurements*, University Science Books

[89] Lira, I., Cordero R.R., François, M., Vial-Edwards, C., 2004, *The uncertainty of experimental derivatives: application to strain measurements*, Measurement Science and Technology, 15, 2381-2388

[90] Lira, I., 2000, *Curve adjustment by the least-square method*, Metrologia, 37, 677-681

[91] *Curve fitting toolbox User's Guide. For use with MATLAB*, The MathWorks

[92] Scarpa, F., 1998, *Evaluation of reliable bounds for sensor calibration curves*, Metrologia, 35, 1-5

[93] Cecchi, G.C., 1991, *Error analysis of the parameters of a least-squares determined curve when both variables have uncertainties*, Measurement Science and Technology, 2, 1127-1128

[94] Neri, F., Saitta, G., Chiofalo, S., 1989, *An accurate straighforward approach to line regression analysis of error-affected experimental data*, Journal of Physics E: Scientific Instruments, 22, 215-217

Curriculum Vitae

PERSONAL DATA

Name	**Francesco AGOSTINI**
Date of birth	23rd December, 1978
Birthplace	Gazzaniga (Bergamo), Italy
Nationality	Italian

EDUCATION

2004-2008   **Doctoral Student and Assistant**, Laboratory of Heat and Mass Transfer, Swiss Federal Institute of Technology Lausanne (EPFL), Switzerland

2003-2004   **Diploma Course in Fluid Dynamics**, von Karman Institute for Fluid Dynamics (VKI), Turbomachinery Department, Rhode Saint Genèse, Belgium

1997-2003   **Laurea di Dottore in Ingegneria Meccanica**, Università degli Studi di Bergamo, Bergamo, Italy (2001, one year obligatory military service)

1992-1997   **High School Certificate (specialization in constructions and surveying)**, Istituto Tecnico Andrea Fantoni, Clusone, Bergamo, Italy

WORKING EXPERIENCE

2004-2008   **Swiss Federal Institute of Technology (EPFL), Laboratory of Heat and Mass Transfer, Lausanne**, research project development, industrial contract, laboratory activity, students supervision and training:
- Boiling on a tube bundle. Heat transfer, pressure drop and flow patterns. Work supervised by Prof. John R.Thome;
- TURBO ELP, bundle boiling tests with R123 (Industrial contract);
- Two-phase flow (air-water) flow pattern recognition: supervisor of Master/Diploma projects.

2003-2004   **von Karman Institute for Fluid Dynamics (VKI), Turbomachinery department, Belgium**, research project and laboratory activity:
- Conjugate heat transfer investigation of rib-roughened cooling channels. Work supervised by Prof. Tony Arts. ASME TURBO EXPO 2005, Reno, Nevada, USA (GT-2005-68166)

2002-2003   **Università degli Studi di Bergamo, Italy**, research project and laboratory activity:
- Thermochromic liquid crystal technique applied on a film cooled nozzle vane - Adiabatic effectiveness and heat transfer coefficient. Work supervised by Prof. Giovanna Barigozzi

ADDITIONAL TRAINING

2007	**Short Course on Hydraulic Machinery Engineering**, Laboratory of Hydraulic Machines (LMH), Swiss Federal Institute of Technology (EPFL, Lausanne
Summers 1992-1996	**Architectural Office**, Vertova, Bergamo, Italy. Constructions and surveying.